



Mechanistic and structural study of GAP-catalysed hydrolase activity in small G proteins

Patrick Baumann

Cardiff University
School of Chemistry

Thesis submitted to Cardiff University for the degree of
Doctor of Philosophy

November 2021

I. Abstract

Small G proteins are a multifaceted class of enzymes and a major hub for signal transduction. In humans, dysregulation of this process can be the driver of a myriad of diseases, most prominently cancer. The first part of this work examines the newly discovered cSrc-mediated Switch-phosphorylation of the small G protein Ras. Conflicting literature reports exist regarding the Ras phosphorylation site and the impact the phosphorylation has on the interaction with its effectors. This work identifies Tyr64 to be the primary target of cSrc and examines structural implications the Ras phosphorylation has on the interaction with its effector RasGAP. Furthermore, this chapter provides an updated model for the only available HRas/RasGAP crystal structure and addresses misconceptions about this structural model, which is still widely used for computational studies. In the second part of this project the hydrogen bonding network of the small G protein RhoA in the transition state analog complex with its RhoGAP^{R85A} effector is investigated. Through the application of a polyspecific tRNA/tRNA synthetase pair, a series of site-specifically labelled fluorotyrosine-RhoA variants were generated. This enables the selective tuning of a single hydrogen bond, donated by Tyr34 to the transferring phosphoryl group. This effect was quantified by investigating the MgF₃⁻ transition state analogue complex between the fluorotyrosine-RhoA variants and RhoGAP^{R85A} using ¹⁹F-NMR. Protein X-ray crystallography confirmed that the active site integrity was unperturbed by the fluorotyrosine incorporation. The kinetic parameters for the GTP hydrolysis of the fluorotyrosine-RhoA variants were measured using an HPLC-based assay under single-turnover conditions. Together these data reveal an impaired ability to stabilise the build-up of negative charge during the phosphoryl transfer transition state with decreasing Tyr34 hydroxyl pK_a. This has implications for related systems such as the small GTPase Ran and establishes a methodology for probing single hydrogen bonds in enzyme active sites.

II. Acknowledgments

First and foremost, I want to express my gratitude to Dr Yi Jin. Not only for the opportunity to undertake this multifaceted doctoral project in her group, but also for her constant guidance in these last few years and for supporting my scientific development from the very first day to the last.

I also want to thank Dr Glyn Hemsworth and Dr Youcef Mehellou for kindly agreeing to take on the roles of examiners. I'm also grateful to Dr Louis Luk for providing a welcoming atmosphere in our shared lab space and for adopting me into his group towards the end of my PhD. Also, I want to thank Cardiff University, the Royal Society of Chemistry, and the Diamond Light Source for contributing to the funding of this doctoral project.

Further I want to thank the Cardiff University technical staff around Dr Rob Jenkins for all their help over the years and for always making sure everything kept running smoothly. A special mention goes out to mass spectrometry wizard Dr Tom Williams. He is one of the many amazing people who provided an incredibly supportive scientific environment and who I have had the pleasure of sharing uncountable pints and pies with during my time in Cardiff. These also include: the Quiztal Structure team, Luke Spear and Dr Emily Mills; the Brew club, Heather Hayes and Davide Zappalà; the Brilliant Club, Davide Cardella and Dr Alex Nödling.; my desk and lab bench neighbours, Victoria Barlow and Dr Helen Bell; the out-of-towners, Dr Simon Tang and Alex Lander; the master chefs Mia Dong and Muge Ma; as well as the many others I forgot.

Honorable mentions go out to my mainland friends for supporting me from afar, i.e. my fellow pigeon enthusiasts, Dr Philip Horx and Joeri Pepels, and my two favourite gal pals Lara Schleifenbaum and Kerrin Schwarze.

Finally, I want to thank my wonderful sisters and my ever-supportive parents for always being there for me. Together, through interesting dinner conversations, innumerable travel adventures and unwavering love and support, they have made me the person that I am today.

III. Table of Contents

I.	Abstract	II
II.	Acknowledgments	III
III.	Table of Contents	IV
IV.	List of Figures	VIII
V.	List of Tables	XI
VI.	Abbreviations	XII
1	Introduction	1
1.1	G Proteins Structure and Family	1
1.2	Signalling and Regulation	4
1.3	Turning off the Switch: GTP Hydrolysis	6
1.3.1	Hydrolysis of Phosphoester Bonds	6
1.3.2	GTPase Activating Protein (GAP)	8
1.3.3	The beating heart of cancer: A New Hope	10
1.4	Metal Fluorides: Powerful Transition State Analogues for Phosphoryl Transfer Enzymes	11
1.4.1	Structure of the Phosphoryl Transfer Transition State	11
1.4.2	Analysing Metal Fluoride Complexes: ^{19}F -NMR	12
1.4.3	Ras/RasGAP: AlF_3^0 or MgF_3^- ?	13
1.5	Phosphorylation of Ras proteins	14
1.5.1	cSrc-catalysed phosphorylation of HRas Switch regions	15
1.6	GAP-catalysed GTP hydrolysis for Rho proteins	17
1.6.1	Hydrogen Bonds in enzymatic Catalysis	20
1.6.2	Fluorinated Amino Acids as Biological Probes	20
1.6.3	Incorporation of Fluorotyrosine (FY) into Proteins	22
1.6.4	Literature Examples: Ribosomal Site-specific Fluorotyrosine Incorporation	23
1.7	Aims and Objectives	26
1.7.1	Ras	26
1.7.2	RhoA	26
2	Materials and Methods	28
2.1	Equipment and Materials	28
2.2	High Performance Liquid Chromatography (HPLC)	28
2.3	Nuclear Magnetic Resonance (NMR) Spectroscopy	28
2.4	Mass spectrometry	29
2.5	Gravity and Fast Protein Liquid Chromatography Column	29
2.6	Software	30
2.7	Gel Electrophoresis	30
2.8	Concentration, Buffer Exchange and Protein handling	32
2.9	Growth Media	32
2.10	Competent Cell Method	33
2.11	Heat-shock Transformation	34
2.12	Thin Layer Chromatography (TLC)	35
2.13	Cloning	35
		IV

2.14	Primers	35
2.15	Plasmids	36
2.16	Activity Assay of Tyrosine Phenol Lyase (TPL)	37
2.17	Fluorotyrosine Synthesis: General Procedure	37
2.17.1	2-Fluorotyrosine (F^2Y)	38
2.17.2	3-Fluorotyrosine (F^3Y)	38
2.17.3	2,5-Difluorotyrosine ($F^{25}Y$)	39
2.17.4	3,5-Difluorotyrosine ($F^{35}Y$)	39
2.17.5	2,6-Difluorotyrosine ($F^{26}Y$)	39
2.17.6	2,3,5-Trifluorotyrosine ($F^{235}Y$)	39
2.18	Synthesis 2,3,5,6-Tetrafluorotyrosine ($F^{2356}Y$)	40
2.19	Recombinant Protein Production	41
2.19.1	cSrc(251–533)	41
2.19.2	RasGAP(714–1047)	42
2.19.3	HRas(1–166)	42
2.19.4	hSOS1(564–1049)	43
2.19.5	RhoGAP(198–439) ^{R85A}	44
2.19.6	Usp2-cc	44
2.19.7	Tyrosine Phenol Lyase (TPL)	45
2.19.8	FY-RhoA	45
2.20	Screening Conditions for the Expression of RhoA-plasmid Constructs	46
2.21	Optimisation of cSrc Phosphorylation	47
2.22	Stability of cSrc-catalysed HRas phosphorylation	47
2.23	RhoA Nucleotide Exchange	47
2.24	Protein X-ray Crystallography	48
2.25	¹⁹ F-NMR Signal Assignment	51
2.26	pK _a Titration of incorporated FY Residues	51
2.27	RhoA Single-Turnover HPLC assay	52
2.28	Determination of Kinetic Parameters of FY-RhoA variants	52
3	HRas/RasGAP Complex and Implications of cSrc-mediated Tyrosine Phosphorylation of HRas Switch Regions	54
3.1	Results and Discussion	54
3.1.1	Crystallisation of HRas/MgF ₃ ⁻ /RasGAP Complex	54
3.1.2	cSrc-catalysed Phosphorylation of HRas	63
3.1.3	RasGAP-Dimer Interaction	70
4	Tyrosine-mediated Hydrogen Bonding and its Role in the catalytic Activity of RhoA	72
4.1	Results and Discussion	72
4.1.1	Site-specific Incorporation of Fluorotyrosine (FY)	72
4.1.2	¹⁹ F-NMR Analysis of RhoA/MgF ₃ ⁻ /RhoGAP ^{R85A} TSA Complex	81
4.1.3	Structural Analysis of FY-RhoA/RhoGAP ^{R85A} using X-ray Crystallography	88
4.1.4	Assessing Kinetic Profiles of Fluorinated RhoA Variants in the Context of RhoA/RhoGAP ^{R85A}	95
5	Summary	107

5.1	Summary: Chapter 3	107
5.2	Summary: Chapter 4	108
6	References	110
7	Appendix	126
7.1	Protein Sequences	126
7.1.1	HRas (1–166)	126
7.1.2	hSOS1 (564–1049)	126
7.1.3	YoPH	126
7.1.4	p120 RasGAP (714–1048)	127
7.1.5	USP2 (259–605)	127
7.1.6	Trigger factor - Ubiquitin - RhoA	127
7.1.7	RhoA – F25N	128
7.1.8	sfGFP - N150TAG	128
7.1.9	hDbs (622–966)	128
7.1.10	p50 RhoGAP(198–439) - R85A	129
7.1.11	MjTyrRS – Y32L, L65G, H70N, D158S, I159Y, L162H	129
7.1.12	TPL	129
7.1.13	cSrc (251–533)	129
7.2	Gene Sequences	131
7.2.1	Gene Fragment: USP2-cc	131
7.2.2	hSOS1	131
7.2.3	hDbs	132
7.2.4	Gene Fragment: Trigger factor-Ubiquitin	133
7.3	NMR Spectra	134
7.3.1	^1H -NMR spectra of synthesised Fluorotyrosines	134
7.3.2	^{19}F -NMR spectra of FY-RhoA/MgF ₃ ⁻ /RhoGAP ^{R85A} TSA complexes	138
7.4	Mass Spectroscopy	141
7.4.1	HRas(1–166)	141
7.4.2	Monophosphorylated HRas(1–166)	141
7.4.3	Diphosphorylated HRas(1–166)	142
7.4.4	HRas(1–166) ^{Y32F}	142
7.4.5	HRas(1–166) ^{Y64F}	143
7.4.6	RasGAP (714–1047)	143
7.4.7	sfGFP-N150F ^{35Y}	144
7.4.8	Truncated GST-RhoA	144
7.4.9	F ³ Y-RhoA	145
7.4.10	F ³⁵ Y-RhoA	145
7.4.11	F ²⁵ Y-RhoA	146
7.4.12	F ²³⁵ Y-RhoA	146
7.4.13	2-Fluorotyrosine (F ^{2Y})	147
7.4.14	3-Fluorotyrosine (F ^{3Y})	147
7.4.15	2,5-Difluorotyrosine (F ^{25Y})	148
7.4.16	3,5-Difluorotyrosine (F ^{35Y})	148

7.4.17	2,6-Difluorotyrosine (F ²⁶ Y)	149
7.4.18	2,3,5-Trifluorotyrosine (F ²³⁵ Y)	149
7.4.19	2,3,5,6-Tetrafluorotyrosine (F ²³⁵⁶ Y)	150
7.5	SDS-PAGE	151
7.6	Measured and predicted Small Molecule ¹⁹ F-NMR Shifts	153
7.7	Statistical Parameters for FY pK _a Determination	155
7.8	Pulse Programme for F ⁻ Suppression in ¹⁹ F-NMR Spectra	157
7.9	Single-Turnover Kinetics of GTP-loaded FY-RhoA	158
7.9.1	RhoGAP ^{R85A} -catalysed Hydrolysis of GTP-F ³ Y-RhoA	158
7.9.2	RhoGAP ^{R85A} -catalysed Hydrolysis of GTP-F ²⁵ Y-RhoA	159
7.9.3	RhoGAP ^{R85A} -catalysed Hydrolysis of GTP-F ³⁵ Y-RhoA	160
7.9.4	RhoGAP ^{R85A} -catalysed Hydrolysis of GTP-F ²³⁵ Y-RhoA	161
7.10	Supplementary Data for HPLC Analysis of FY-RhoA-GTP Hydrolysis	162

IV. List of Figures

Figure 1: GTP-induced conformational change of a G protein.....	1
Figure 2: Topology diagram for the G-domain of the Ras superfamily.....	3
Figure 3: Ras proteins cycle between a GDP- and a GTP-bound state. Interconversion is mediated by two classes of regulatory proteins called GAP and GEF.....	4
Figure 4: GTP-induced conformational changes in the G domain.....	5
Figure 5: Ras effector signalling interactions and their downstream pathways.....	6
Figure 6: Hydrolysis of a phosphoester bond via a trigonal bipyramidal transition state	7
Figure 7: Energy diagram for enzyme-catalysed reaction in comparison with an uncatalysed reaction	7
Figure 8: Key interactions during the Ras/RasGAP catalysed hydrolysis of GTP.....	9
Figure 9: Acrylamide-based covalent Ras ^{G12C} inhibitors	10
Figure 10: Geometries of AlF ₄ ⁻ and MgF ₃ ⁻ complexes compared to the phosphoryl transfer transition state.	12
Figure 11: Active site of HRas/RasGAP metal fluoride TSA complex (PDB: 1WQ1).	14
Figure 12: Active site hydrogen bond model of RhoA/GTP/RhoGAP ^{R85A} during the phosphoryl transfer transition state.....	18
Figure 13: Comparison of conserved Tyr residue of superimposed structures of metal fluoride complexes for HRas/RasGAP (PDB: 1WQ1), Cdc42/Cdc42GAP (PDB: 1GRN), RhoA/RhoGAP (PDB: 1OW3), RhoA/RhoGAP^{R85A} (PDB: 5M6X), Rap/RapGAP (PDB: 3BRW) and Ran/RanGAP (PDB: 1K5G).	19
Figure 14: Substitution patterns of fluorinated tyrosine derivates and their respective pK _a values.	22
Figure 15: Orthogonal tRNA charged with fluorotyrosine (FY) is incorporated through ribosomal translation at a non-coding codon leading to the site-specific labelling of the polypeptide chain.	23
Figure 16: TPL-catalysed cleavage of SOPC.....	37
Figure 17: Protein crystal images (A) HRas/MgF ₃ ⁻ /RasGAP crystals (left) visible light image (middle) UV light image (right) protein crystal during data acquisition (B) phospho-HRas crystals (C) visible light image of RasGAP dimer crystals (D) UV light image of RasGAP dimer crystal, the relatively faint intensity is due to the fact that RasGAP has relatively few Trp and Tyr residues. (E) Three iterations of microseeding conditions for the F ²³⁵ Y-RhoA/MgF ₃ ⁻ /RhoGAP ^{R85A} complex to improve crystal morphology.....	50
Figure 18: Electron density map for key active site residues of the newly generated HRas/MgF ₃ ⁻ /RasGAP complex.....	57
Figure 19: Overlay HRas/RasGAP TSA complexes from PDB:1WQ1 and the newly generated structure.....	58
Figure 20: Active site of HRas/ AlF₃⁰ /RasGAP and active site of HRas/ MgF₃⁻ /RasGAP from section 3.3.1.	61
Figure 21: Hydrogen bonding network surrounding the MgF ₃ ⁻ species of HRas/MgF ₃ ⁻ /RasGAP complex.....	62
Figure 22: Phosphorylation alters matrix migration during SDS-PAGE, by charge-charge repulsion.....	64
Figure 23: Optimisation of cSrc-catalysed HRas phosphorylation conditions.....	65
Figure 24: (A) Q column chromatogram of the separation of HRas, (B) Deconvoluted ESI-MS spectrum of unphosphorylated HRas (18853 Da) (C) Deconvoluted ESI-MS spectrum of monophosphorylated HRas (18933 Da) (D) Deconvoluted ESI-MS spectrum of diphosphorylated HRas (19013 Da)....	66
Figure 25: Time course testing the stability of phosphorylated HRas.....	67
Figure 26: (A) Crystal structure of dimeric RasGAP(714–1047). (B) Crystal structure of phospho-HRas(1–166).....	68

Figure 27: Overlay of unphosphorylated HRas-GDP (PDB: 4Q21, yellow) and phospho-HRas-GDP (blue). Switch2 regions are shown in orange and red	69
Figure 28: (A) Domain architecture of GAP1 family (adapted from SCHEFFZEK et al.). ¹¹⁹ (B) Binding interface of RasGAP(714–1047) dimer crystal structure. Highlighted residues are binding interactions identified by PISA analysis.	71
Figure 29: Chemoenzymatic synthesis of fluorinated L-tyrosine derivates.	72
Figure 30: Proposed reaction mechanism for the synthesis of L-tyrosine from phenol, pyruvate and ammonium catalysed by TPL using PLP as coenzyme. ¹⁸⁵	73
Figure 31: Synthesised FYs with their corresponding yields.	74
Figure 32: (A) Overview of site-specific ncAA incorporation by hijacking a non-coding codon. (B): cell pellets with FY-labelled GFP (left) and the no FY control (right). (C) Mass spectrum showing the successful incorporation of F ³⁵ Y into GFP.....	75
Figure 33: Plasmid Map. Folding chaperone Trigger factor and ubiquitin fused to RhoA.....	77
Figure 34: Screening of expression conditions for the incorporation of F ³⁵ Y into RhoA at 18°C (A), 25°C (B) and 30°C (C). For each temperature concentrations of 1–5 mM of F ³⁵ Y were screened. Lanes 1, 5 and 9 show the no FY control.....	79
Figure 35: ¹⁹ F-NMR spectrum of 0.5 mM WT-RhoA, 0.5 mM RhoGAP ^{R85A} , 100 mM NaCl, 10 mM MgCl ₂ , 20 mM NaF and 50 mM Tris-HCl buffered to pH = 7.5. The chemical shifts for WT-RhoA are –150.5 ppm (F ¹), –155.0 ppm (F ²) and –172.8 ppm (F ³).	81
Figure 36: ¹⁹ F-NMR spectrum of 0.5 mM F ²³⁵ Y-RhoA, 0.5 mM RhoGAP ^{R85A} , 100 mM NaCl, 10 mM MgCl ₂ , 20 mM NaF and 50 mM Tris-HCl buffered to pH = 7.5. The chemical shifts for F ²³⁵ Y-RhoA are –140.3 ppm (F _A), –148.1 ppm (F _B) and –160.1 ppm (F _C).....	82
Figure 37: (A) ¹⁹ F-NMR spectra of the pH dependant formation of the F ²³⁵ Y-RhoA/MgF ₃ ⁻ /RhoGAP ^{R85A} complex.). The free F ²³⁵ Y-RhoA (F ^A , F ^B , F ^C) and the complexed F ²³⁵ Y-RhoA (F ^{A'} , F ^{B'} , F ^{C'}) are shown in black while MgF ₃ ⁻ signals (F ¹ , F ² , F ³) are shown in black. (B) Model representation of F ²³⁵ Y-RhoA/MgF ₃ ⁻ /RhoGAP ^{R85A}	83
Figure 38: (A) Calibrated ¹⁹ F-NMR spectra of the pH dependant formation of the F ₂₃₅ Y-RhoA/MgF ₃ ⁻ /RhoGAP ^{R85A} complex.) buffered to pH values from 6.0 to 9.5. The free F ²³⁵ Y-RhoA (F _A , F _B , F _C) and the complexed F ²³⁵ Y-RhoA (F _{A'} , F _{B'} , F _{C'}) are shown in black while MgF ₃ ⁻ signals (F ¹ , F ² , F ³) are shown in black. (B) Chemical shift values for free F ²³⁵ Y-RhoA (F _A (●), F _B (■), F _C (▲)) plotted against the pH. The sigmoidal curves fitted to the three datasets yielded an average pK _a value of 6.3.	84
Figure 39: (A) Calibrated ¹⁹ F-NMR spectra of F ²⁵ Y-RhoA buffered to pH values from 6.0 to 9.5 (B) Chemical shift values for free F ²⁵ Y-RhoA (F _A , F _B) plotted against the pH. The sigmoidal curves fitted to the dataset yielded a pK _a value of 7.9 (see 2.26).....	86
Figure 40: (A) The electron density map of F ³⁵ Y-RhoA/MgF ₃ ⁻ /RhoGAP ^{R85A} contoured at 1.0 σ (0.253 e Å ⁻³) shows the incorporation of F ³⁵ Y at position 34 of the RhoA active site. Primed residues are part of RhoGAP ^{R85A} . Ligand omit maps for F ³⁵ Y-RhoA/MgF ₃ ⁻ /RhoGAP ^{R85A} complex. Difference Fourier map contoured at 3σ: (B) GDP (C) catalytic magnesium with two coordinating waters (D) MgF ₃ ⁻	89
Figure 41: The electron density map of F ²³⁵ Y-RhoA/MgF ₃ ⁻ /RhoGAP ^{R85A} contoured at 1.0 σ (0.320 e Å ⁻³) shows the incorporation of F ²³⁵ Y at position 34 of the RhoA active site. Ligand omit maps for F ²³⁵ Y-RhoA/MgF ₃ ⁻ /RhoGAP ^{R85A} complex. Primed residues are part of RhoGAP ^{R85A} . Difference Fourier map contoured at 3σ: (B) GDP (C) catalytic magnesium with two coordinating waters (D) magnesium trifluoride.....	90
Figure 42: (A) Alignment of RhoGAP ^{R85A} (grey) complexed with WT-RhoA (yellow), F ³⁵ Y-RhoA (green) and F ²³⁵ Y-RhoA (blue). (B) Bond lengths of hydrogen bond between Tyr34-hydroxyl group and F ³ of MgF ₃ ⁻ TSA plotted against the Tyr34 side chain pK _a . For the complexes each of the two protein assemblies in the asymmetric unit were measured.....	92
Figure 43: Comparison of metal fluoride TSA complex structures to show the position of a conserved tyrosine residue involved in GTP hydrolysis. (A) WT-RhoA/MgF ₃ ⁻ /RhoGAP ^{R85A} (B) F ³⁵ Y-RhoA/MgF ₃ ⁻ /RhoGAP ^{R85A} (C) F ²³⁵ Y-RhoA/MgF ₃ ⁻ /RhoGAP ^{R85A} (D) Ran/AlF ₃ ⁰ /RanGAP (PDB:1K5G).....	94

Figure 44: Overview of catalytic steps relevant for the RhoGAP ^{R85A} catalysed GTP hydrolysis by RhoA. These are GTP binding (k_1), RhoA/GTP/RhoGAP ^{R85A} complex formation (k_2), cleavage of the γ -phosphoester bond (k_3), phosphate release (k_4) as well as the intrinsic RhoA catalysed GTP hydrolysis(k_{intr}).	95
Figure 45: RhoGAP ^{R85A} catalysed GTP hydrolysis of 5 μM mant-GTP-loaded (A) WT-RhoA (green: 0 μM RhoGAP ^{R85A} ; blue: 5 μM RhoGAP ^{R85A}) or (B) F ²³⁵ Y-RhoA (purple: 0 μM RhoGAP ^{R85A} ; orange: 5 μM RhoGAP ^{R85A}). (C) mant-GTP (D) cy3-GTP (E) No change in fluorescence is detected for the RhoA-catalysed mant-GTP hydrolysis (adapted from AMIN et al.). ¹⁹⁸	97
Figure 46: ³¹ P-NMR spectrum of WT-RhoA-GTP 0.5 mM, BisTris:HCl 50 mM pH = 6.0, NaCl 150 mM, MgCl ₂ 5 mM / D ₂ O 10%) recorded on a 600 MHz spectrometer with 512 scans.....	98
Figure 47: Workflow measuring the hydrolysis rate of RhoA-bound GTP using HPLC.....	99
Figure 48: (A) UV trace showing the separation of guanine nucleotides GTP and GDP. (B) GTP loading of the RhoA enzyme over time fitted to a single exponent decay function to yield the intrinsic GTP hydrolysis rate of $2.2 \times 10^{-5} \text{ s}^{-1}$	100
Figure 49: Kinetic analysis of the of RhoGAP ^{R85A} -catalysed hydrolysis of GTP-loaded RhoA using single turnover kinetics. 50 μM of GTP-loaded ^{WT} RhoA are turned over with (A) 10 μM , (B) 25 μM , (C) 50 μM , (D) 100 μM or (E) 250 μM of RhoGAP ^{R85A} . All runs were run in duplicates (1: ●, 2: ▲) (F) Rates were obtained by fitting a two-exponential decay function, plotted against the RhoGAP ^{R85A} concentration, and fitted with a hyperbolic curve (see section 2.28).	101
Figure 50: Rates for (A) F ³ Y-RhoA, (B) F ²⁵ Y-RhoA, (C) F ³⁵ Y-RhoA and (D) F ²³⁵ Y-RhoA, obtained from fitting decay functions analogous to WT-RhoA (Fig.49), plotted against the RhoGAP ^{R85A} concentration, and fitted with a hyperbolic curve (see section 2.28).	102
Figure 51: (A) Intrinsic rate of hydrolysis of GTP-loaded FY-RhoA plotted against the Tyr34 side chain pK _a . Error bars represent the 95% confidence interval for the fitted values. (B) Proposed mechanism for the intrinsic RhoA-GTP hydrolysis. ^{27,208}	103
Figure 52: k_{cat} and $\log_{10}(k_{\text{cat}} \times 10^4)$ of RhoGAP ^{R85A} -catalysed hydrolysis of GTP-RhoA plotted against Tyr34 side chain pK _a . Error bars represent the 95% CI of the fitted curves.....	104
Figure 53: K_m for substrate complex FY-RhoA/GTP/RhoGAP ^{R85A} plotted against FY-Tyr34 pK _a . Error bars represent a 95% confidence interval for the fitted values.	105
Figure 54: SDS-PAGE gels (A) and (B): Optimisation of expression conditions for non-fluorotyrosine labelled RhoA. (C) Representative SDS-PAGE gel of a failed fluorotyrosine incorporation. Expression trials for trigger factor construct in BL21(DE3) AI cells using (D) 3-fluorotyrosine, (E) 3,5-difluorotyrosine, (F) 2,3,5-trifluorotyrosine and (G) 2,3,5,6-tetrafluorotyrosine.	152
Figure 55: GTP-loading of F ³ Y-RhoA during the RhoGAP ^{R85A} -catalysed hydrolysis of GTP. 50 μM of GTP-loaded F ³ Y-RhoA are turned over with (A) 0 μM , (B) 10 μM , (C) 25 μM , (D) 50 μM , (E) 100 μM or (F) 250 μM of RhoGAP ^{R85A} . All runs were run in duplicates (1: ●, 2: ▲). Rates were obtained by fitting a two-exponent decay function (section 2.3.14).	158
Figure 56: GTP-loading of F ²⁵ Y-RhoA during the RhoGAP ^{R85A} -catalysed hydrolysis of GTP. 50 μM of GTP-loaded F ²⁵ Y-RhoA are turned over with (A) 0 μM , (B) 10 μM , (C) 25 μM , (D) 50 μM , (E) 100 μM or (F) 250 μM of RhoGAP ^{R85A} . All runs were run in duplicates (1: ●, 2: ▲). Rates were obtained by fitting a two-exponent decay function (section 2.3.14).	159
Figure 57: GTP-loading of F ³⁵ Y-RhoA during the RhoGAP ^{R85A} -catalysed hydrolysis of GTP. 50 μM of GTP-loaded F ³⁵ Y-RhoA are turned over with (A) 0 μM , (B) 10 μM , (C) 25 μM , (D) 50 μM , (E) 100 μM or (F) 250 μM of RhoGAP ^{R85A} . All runs were run in duplicates (1: ●, 2: ▲). Rates were obtained by fitting a two-exponent decay function (section 2.3.14).	160
Figure 58: GTP-loading of F ²³⁵ Y-RhoA during the RhoGAP ^{R85A} -catalysed hydrolysis of GTP. 50 μM of GTP-loaded F ²³⁵ Y-RhoA are turned over with (A) 0 μM , (B) 10 μM , (C) 25 μM , (D) 50 μM , (E) 100 μM or (F) 250 μM of RhoGAP ^{R85A} . All runs were run in duplicates (1: ●, 2: ▲). Rates were obtained by fitting a two-exponent decay function (section 2.3.14).	161

V. List of Tables

Table 1: Ras superfamily of small G proteins. ³	2
Table 2: Protein LC-MS chromatography parameters.....	29
Table 3: Buffer and solutions for SDS-PAGE	31
Table 4: Genotypes of E.coli strains.....	34
Table 5: Screened conditions for the cSrc-mediated phosphorylation of HRas	47
Table 6: Crystallisation condition for HRas/RasGAP (PDB: 1WQ1).	54
Table 7: Data collection and refinement statistics for HRas/MgF ₃ ⁻ /RasGAP	55
Table 8: Data collection and refinement statistics for phospho-HRas and dimeric RasGAP ...	69
Table 9: Plasmid constructs for screening expression conditions for FY-RhoA incorporation.	76
Table 10: Protein yields after the ncAA incorporation of FY into RhoA.....	80
Table 11: ¹⁹ F-NMR chemical shifts of RhoA/MgF ₃ ⁻ /RhoGAP ^{R85A} TSA complexes and the pK _a values of the (F)-Tyr ³⁴ sidechains. ^{176,203}	87
Table 12: Crystallisation parameters for WT-RhoA/MgF ₃ ⁻ /RhoGAP ^{R85A} complex	88
Table 13: Data collection and refinement statistics for F ³⁵ Y-RhoA/MgF ₃ ⁻ /RhoGAP ^{R85A} and F ²³⁵ Y-RhoA/MgF ₃ ⁻ /RhoGAP ^{R85A}	91
Table 14: Intrinsic (k_{intr}) as well as RhoGAP ^{R85A} -catalysed (k_{cat}) GTP hydrolysis rates for FY-RhoA	102
Table 15: Measured and predicted ¹⁹ F-NMR shifts of fluorophenols used in this work and their respective fluorotyrosine derivates.	153
Table 16: Sigmoidal fit parameters for ¹⁹ F-NMR signals for F ²³⁵ Y-RhoA.	155
Table 17: Sigmoidal fit parameters for ¹⁹ F-NMR signal of F _A for F ²⁵ Y-RhoA. No significant pH dependant shift in ¹⁹ F NMR signal detected for F _B	156
Table 18: GTP-loading [%] for FY-RhoA at various timepoints.....	162
Table 19: Curve fit parameters for the intrinsic hydrolysis of FY-RhoA-GTP	164
Table 20: Curve fit parameters for the RhoGAP ^{R85A} catalysed hydrolysis of WT-RhoA-GTP	165
Table 21: Curve fit parameters for the RhoGAP ^{R85A} catalysed hydrolysis of F ³ Y-RhoA-GTP	166
Table 22: Curve fit parameters for the RhoGAP ^{R85A} catalysed hydrolysis of F ²⁵ Y-RhoA-GTP	167
Table 23: Curve fit parameters for the RhoGAP ^{R85A} catalysed hydrolysis of F ³⁵ Y-RhoA-GTP	168
Table 24: Curve fit parameters for the RhoGAP ^{R85A} catalysed hydrolysis of F ²³⁵ Y-RhoA-GTP	169

VI. Abbreviations

2-ME	2-mercaptoethanol
Å	Ångström (1 Å = 0.1 nm)
Amp	ampicillin
APS	ammonium persulfate
BTP	bis-tris propane
cfu	colony forming units
Chl	chloramphenicol
CI	confidence interval
CV	column volume
DTT	dithiothreitol
EDTA	2-ethylenediaminetetraacetic acid
FPLC	fast protein liquid chromatography
GST	glutathione-S-transferase
GppCp	5'-guanylylmethylenediphosphonate
GppNHP	5'-guanylylimidodiphosphate
HEPES	4-(2-hydroxyethyl)-1-piperazineethanesulfonic acid
HSQC	heteronuclear single quantum coherence spectroscopy
Kan	kanamycin A
mantGTP	2'/3'-O-(<i>N</i> -Methylanthraniloyl)-guanosine-5'-triphosphate
MOPS	3-(<i>N</i> -morpholino)propanesulfonic acid
ncAA	non-canonical amino acid
NTA	nitrilotriacetic acid
OD _{600nm}	optical density at 600 nm
PCR	polymerase chain reaction
PLP	pyridoxal 5-phosphate
PMSF	phenylmethanesulfonyl fluoride
RMS	root mean square
RS	tRNA synthetase
sfGFP	superfolder green fluorescent protein
SOPC	S-(2-nitrophenyl)-L-cysteine
Str	streptomycin
TEMED	tetramethylethylenediamine
ε	molar extinction coefficient

1 Introduction

1.1 G Proteins: Structure and Family

G proteins are ubiquitous regulatory proteins that are involved in a vast variety of cellular functions including hormone response, protein synthesis, apoptosis signalling and many others.^{1–3} Their common feature is a conserved guanine nucleotide binding domain, which functions as a molecular switch. Through the binding and the subsequent hydrolysis of guanosine triphosphate (GTP) the protein is able to cycle between an ‘ON’ and ‘OFF’ state. When GTP is bound, a conformational shift in a flexible region occurs and alters the mode of interaction with other proteins (Fig.1).^{4,5}

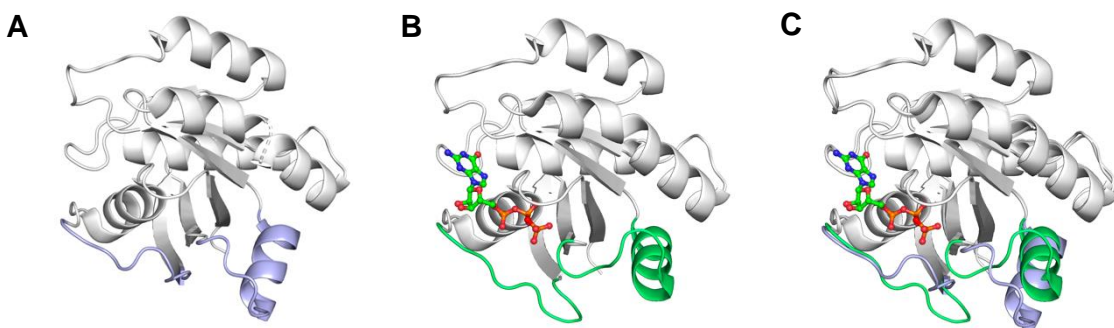


Figure 1: GTP-induced conformational change of a G protein. The flexible region is highlighted in blue/magenta. (A) GTP-free G protein (PDB:6MBU) (B) GTP-bound G protein (PDB:6MBC) (C) Overlay of (A) and (B).

G proteins are divided into three major classes. The first being ribosome-associated GTPases involved in protein synthesis, e.g., EF-Tu a prokaryotic elongation factor responsible for catalysing the binding of aminoacyl-tRNA to the ribosome.^{1,6} The second class are the large or heterotrimeric G proteins. This family consists of numerous signalling proteins that mediate cellular responses to most hormones, metabolites, cytokines, and neurotransmitters.² They are located in the cell where they are activated by G protein coupled receptors (GPCRs), which are distributed across the cell membrane. It is estimated that around 700 FDA approved drugs target GPCRs, which makes up a third of all approved drugs.⁷ In this work the focus lies on the third group, the small G proteins.

Small G proteins, also known as the Ras superfamily, are between 20 and 25 kDa in size and are classified by a conserved structural G domain. In contrast to their larger counterparts, they occur as monomers.⁸ In humans alone the Ras superfamily has over 150 members which are grouped into five subfamilies based on their function, localisation and structure.³ While these proteins belong to one of the most conserved genes in the human genome, subtle differences in their structure and post-translational modifications (PTM) causes them to execute a variety of functions within the cell (Tab.1).⁹

Table 1: Ras superfamily of small G proteins.³

Subfamily	Members	Biological Functions
Ras	HRas, KRas4A/4B, NRas, RRas, Rap1A/B, Rap2A/B, TalA/B, TC21	growth survival differentiation
Rho	RhoA/RhoB/RhoC Rac1/2, Cdc42/G25K, RhoG, TC10	cytoskeletal organisation integrin activity stress response
Rab	Rab1 to Rab26	vesicle transport
Arf	Arf1 to Arf6	vesicle transport
Ran	Ran1	nuclear import

The defining feature of small G proteins is their conserved nucleotide-binding domain, called the G domain, and it consists of approximately 170 residues, with insertions and N- and C-terminal extensions, depending on the subfamily (Fig.2A).³ It is made up of a central beta sheet which is flanked by five alpha helices. Five conserved fingerprint motifs (G1–G5) are present around the nucleotide binding site (Fig.2B). The first, the so-called P-loop (G1, GxxxxGKS/T), is a phosphate-binding site, where a conserved Ser/Thr hydroxyl group together with a neighbouring Lys residue binds the GTP β - and γ -phosphate. This is also known as the Walker A motif and can be widely found in many nucleotide binding proteins.^{10,11} The effector region Switch1 (G2) is one of the two loop regions that changes conformation upon GTP binding. It contains a conserved Thr residue, which interacts with the GTP γ -phosphate, contributing to the conformational shift. The DxxG motif (G3) can be found in the Switch2 region and is involved in sensing GTP binding. The N/TKxD motif (G4) is associated with guanidine base binding and the amide backbone of the SAK motif (G5) interacts with the guanine base oxygen.

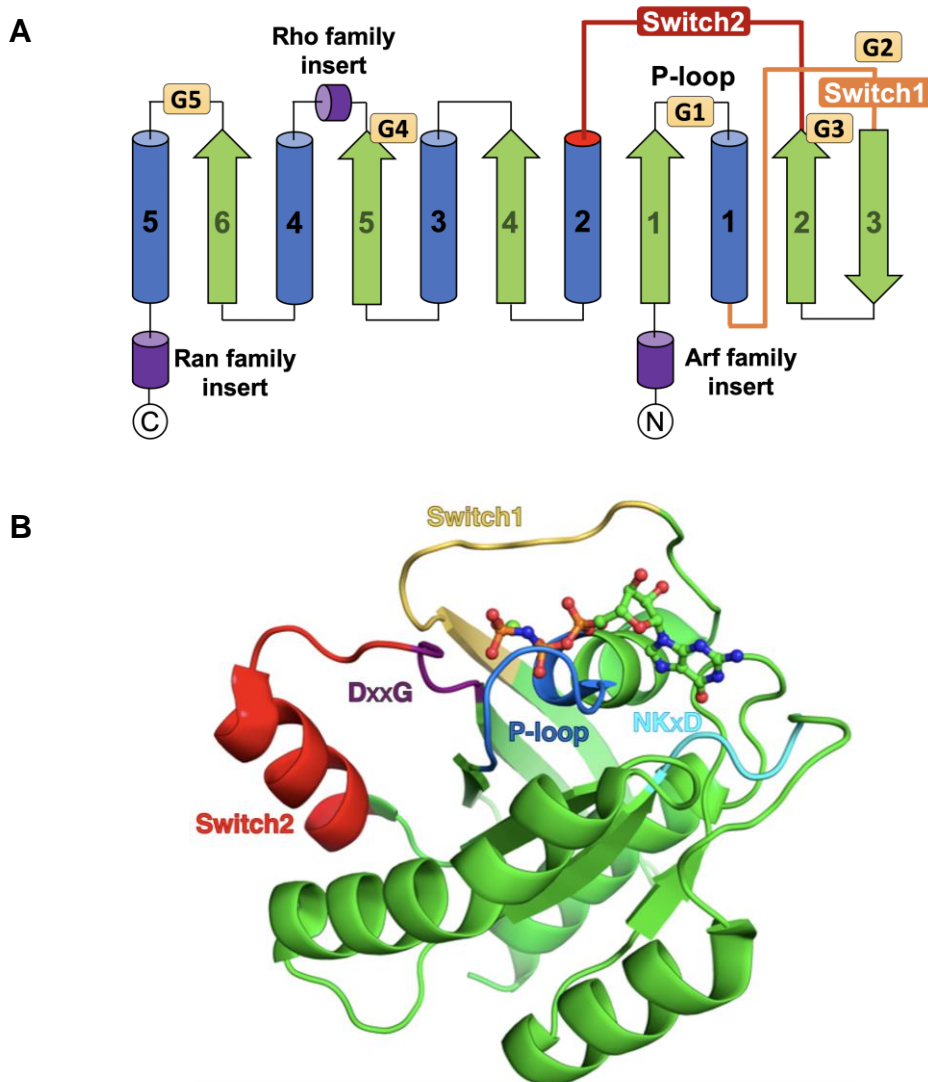


Figure 2: (A) Topology diagram for the G-domain of the Ras superfamily. The subfamily specific inserts are shown in purple. (B) Structural features of the G domain visualised using the structure of HRas-GppNHp (PDB: 5UFE).

Especially within the individual subfamilies, members exhibit a high level of sequence similarity within the G domain. Isoforms of the human Ras family for example have a sequence identity of around 95%.¹² Small G proteins differ primarily in the last 20 C-terminal amino acids which is known as the hypervariable region (HVR). Specific sequences in this region lead to post-translational modifications, for example in the form of various lipid groups.¹³ This results in differences in membrane trafficking and localisation that are thought to contribute to isoform-specific signalling. The Ras protein is the prototypical member of the small G proteins, has been thoroughly characterised and has thus led to many insights into the mechanistic properties of G proteins.¹⁴

1.2 Signalling and Regulation

The members of the Ras superfamily cycle between an GTP-bound (ON state) and GDP-bound state (OFF state), which differ by the conformations of their Switch1 and Switch2 regions. The ON/OFF cycle of small GTPases is tightly controlled by three types of regulatory proteins: 1) Guanine nucleotide exchange factors (**GEF**) accelerate GDP/GTP nucleotide exchange 2) GTPase-accelerating proteins (**GAP**) and 3) Guanine nucleotide dissociation inhibitors (**GDI**).

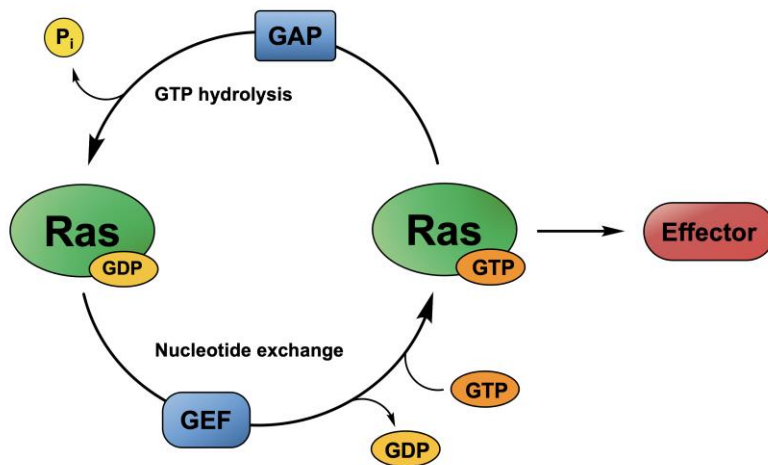


Figure 3: Ras proteins cycle between a GDP- and a GTP-bound state. Interconversion is mediated by two classes of regulatory proteins called GAP and GEF.

Small G proteins have a high binding affinity to GDP and GTP, HRas for example binds these guanine nucleotides with an affinity of $K_D = 10^{-12}$ M.¹⁵ This makes the release of GDP a comparatively slow process.¹⁶ While small G proteins predominantly remain in the GDP-loaded state, a swift nucleotide exchange is necessary for efficient signalling. GEF proteins accelerate GDP dissociation by several orders of magnitude and allow loading with GTP.^{17,18} As GEFs increase the dissociation of any bound nucleotide and GTP is in 10- to 50-fold excess in living cells, the effect of the GEF interaction is the loading of the protein with GTP.¹⁹ In the GTP-bound ON state, Ras proteins interact with downstream effectors which are proteins with high affinity to the GTP- and low affinity to the GDP-bound state.²⁰

The first step of the exchange reaction is the docking of GEF onto the GDP-bound small GTPase, forming a low affinity ternary intermediate.²¹ Dissociation of GDP then converts this complex into a high affinity nucleotide-free complex allowing for GTP to bind.²¹ All complexes feature a very large GTPase/GEF interface, in which

the GEF clamps the Switch2 region and displaces the Switch1 region away from the nucleotide-binding site.^{2,21} Apart from these general traits, the mechanisms whereby each GEF domain stimulates GDP dissociation vary considerably between families.²⁰

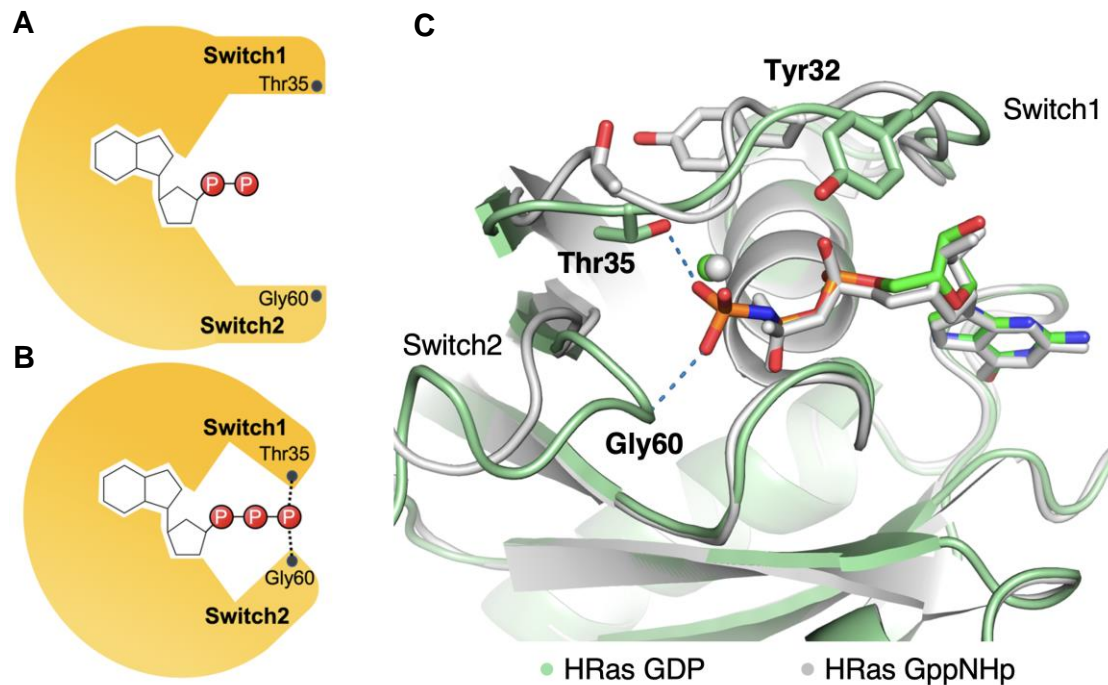


Figure 4: GTP-induced conformational changes in the G domain. The two Switch regions shift from a flexible conformation in the GDP-bound state (**A**) to a ‘closed’ conformation in the GTP-bound state (**B**). The key interactions occur between the GTP γ -phosphate and Thr35 (Sw1) and Gly60 (Sw2), as seen in (**C**) an overlay of HRas bound to GDP (grey, PDB:4Q21) and the GTP analogue GppNHp (green, PDB:5P21).

GTP-binding induces structural changes, where a conserved threonine of Switch1 and the amide backbone of a Switch2 glycine are held in place by the GTP γ -phosphate oxygens.²² This results in a reduction in flexibility, which is observed in numerous crystal structures as well as NMR experiments.²³ In this fixed state Switch1 and Switch2 can interact with downstream effectors as well as GAP effectors which in turn catalyses the hydrolysis of the bound GTP and thus causes a termination of the signal. Growing insight into Ras signal transduction reveals that more than ten pathways with distinct functions have been identified to be mediated through Ras effectors (Fig.5).^{24–26} These are generally defined as proteins with a strong affinity to Ras-GTP and regulate a number of cellular responses including apoptosis, differentiation, proliferation and many more.^{25,27–29}

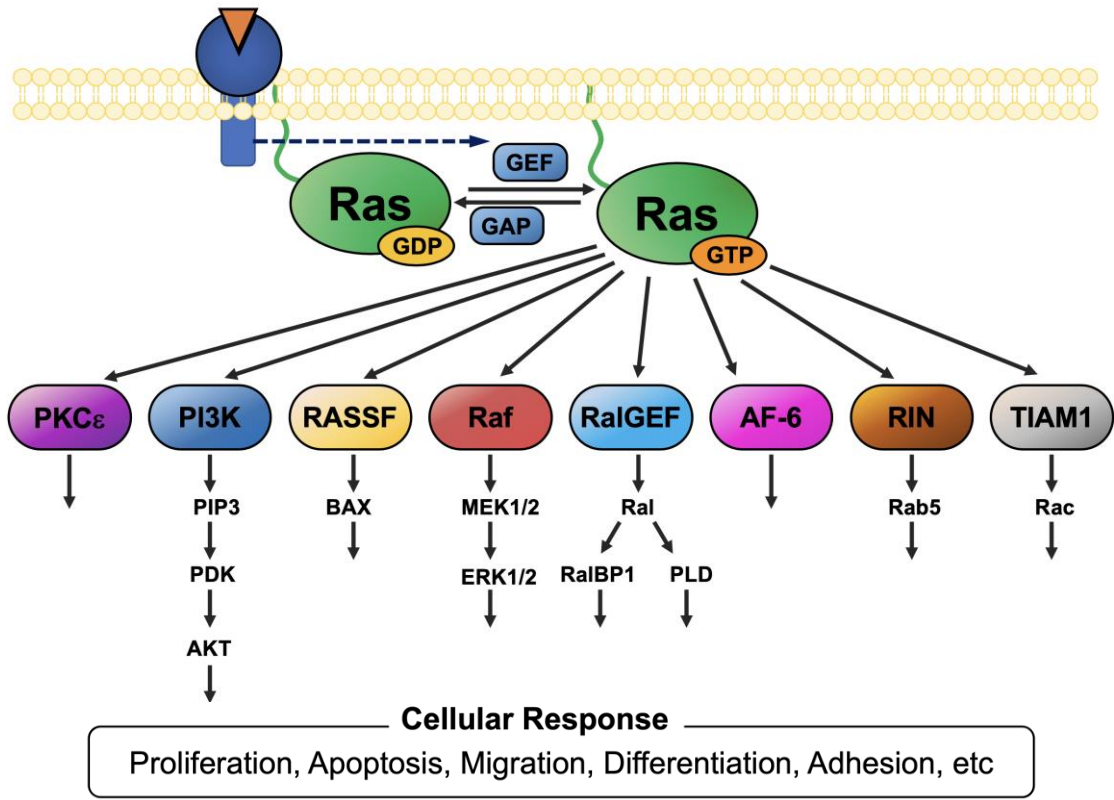


Figure 5: Ras effector signalling interactions and their downstream pathways.

1.3 Turning off the Switch: GTP Hydrolysis

1.3.1 Hydrolysis of Phosphoester Bonds

Phosphoryl transfer reactions play an integral role in metabolism, DNA synthesis, signalling and many other cellular processes.³⁰ Arguably the most prominent example is adenosine triphosphate (ATP), which is used by the cell as a short-term storage unit of chemical energy in the form of a phosphoester bond.³¹ In spite of the relatively high ΔG of around 30 kJ/mol, the bond exhibits a tremendous stability in aqueous media.³² As phosphate has three pK_a values of around 2, 7 and 12, phosphoesters carry one to two negative charges at physiological pH.³³ Due to electronegative shielding the nucleophilic attack of water molecules, which would lead to the bond cleavage, is slowed down significantly. Therefore, the typical half-life of phosphoester bonds is on the timescale of 10^{12} years.³⁴ This property is crucial for e.g., the DNA/RNA phosphate backbone, and thus genomic stability.³⁵

In enzymes, phosphoryl transfer reactions often proceed via a concerted trigonal bipyramidal transition state step, where the attacking oxygen and the leaving group

oxygen are oriented linearly (Fig.6), leading to an inversion of the stereochemistry at the phosphorus atom.

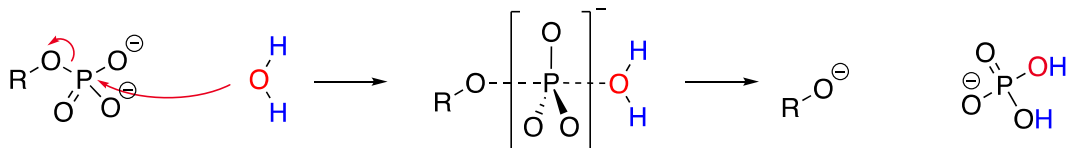


Figure 6: Hydrolysis of a phosphoester bond via a trigonal bipyramidal transition state.

Enzymes create tailored environments in their active sites, where steric and electrostatic constraints position phosphoester substrates in a way, which facilitates the nucleophilic attack and thus significantly lowers the activation energy of their substrates. This is achieved via different means. Positive residues, i.e., Arg or Lys, as well as bound cation cofactors can compensate the build-up of negative charge during the transition state. Furthermore, beneficial alignment of residues surrounding the nucleophilic water, orient it through orbital steering.^{36,37}

Instead of a single transition state, enzyme-catalysed phosphoester hydrolysis progresses *via* several intermediates. For the phosphoester cleavage involved in the hydrolysis of GTP a schematic representation is shown in Fig.7.

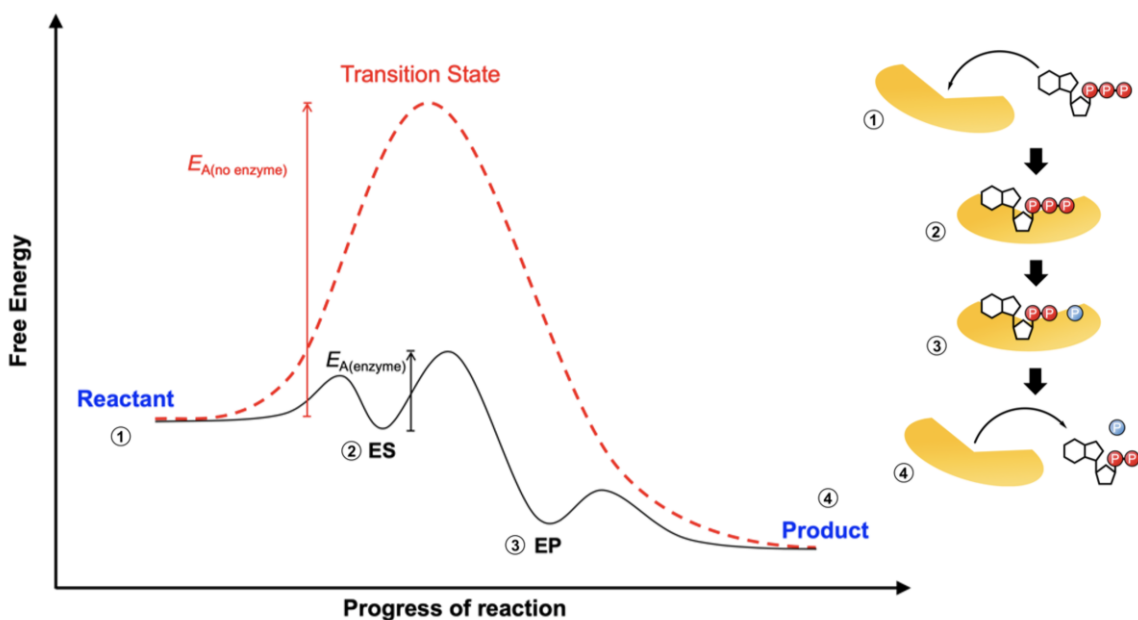


Figure 7: Energy diagram for enzyme-catalysed reaction (black) in comparison with an uncatalysed reaction (red). Instead of a large activation energy barrier, the enzyme-catalysed phosphoester hydrolysis progresses via several intermediary steps. Typically, these include substrate binding (1→2), phosphoester bond cleavage (2→3) and product release (3→4).

1.3.2 GTPase Activating Protein (GAP)

Although G proteins are also called GTPases, the intrinsic GTP hydrolysis reaction is in fact very slow, and efficient hydrolysis requires the interaction with a GAP, which accelerates the cleavage step by several orders of magnitude.¹⁹ Several structural and biophysical studies have examined this reaction mechanism, where a water molecule is positioned optimally for an in-line nucleophilic attack on the γ -phosphate opposite to the leaving group (Fig.8).^{21,22,38} Effective catalysis of phosphoryl transfer by GAPs consists of several elements: the proper orientation of the attacking water molecule and its polarisation, occlusion of water from the active site, and the stabilisation of the transition state.³⁷ However, as with GEFs, GAPs for the different Ras-protein families are not conserved. They approach the G protein from different angles and use various ways to enhance the GTPase activity.¹⁹ In the case of Ras proteins, which is a model system for many small G proteins, RasGAP stabilises the position of Gln61 of Ras, which in turn coordinates the attacking water. In addition, RasGAP provides an arginine residue, called the arginine finger. This residue is positioned into the phosphate-binding site and stabilises the transition state by neutralising negative charge at the γ -phosphate. The arginine finger fulfils a function similar to the arginine found in the helical insertion of α -subunits of large G proteins.³⁹ This mechanism of catalysis is supported by biochemical and mutational studies. For instance, mutation of Gln61, abolishes GAP-induced hydrolysis, by disrupting the coordination of the water molecule necessary for GTP hydrolysis. Mutations at position Gly12 and Gly13 of Ras sterically block the proper orientation of both the arginine finger and Gln61.⁴⁰

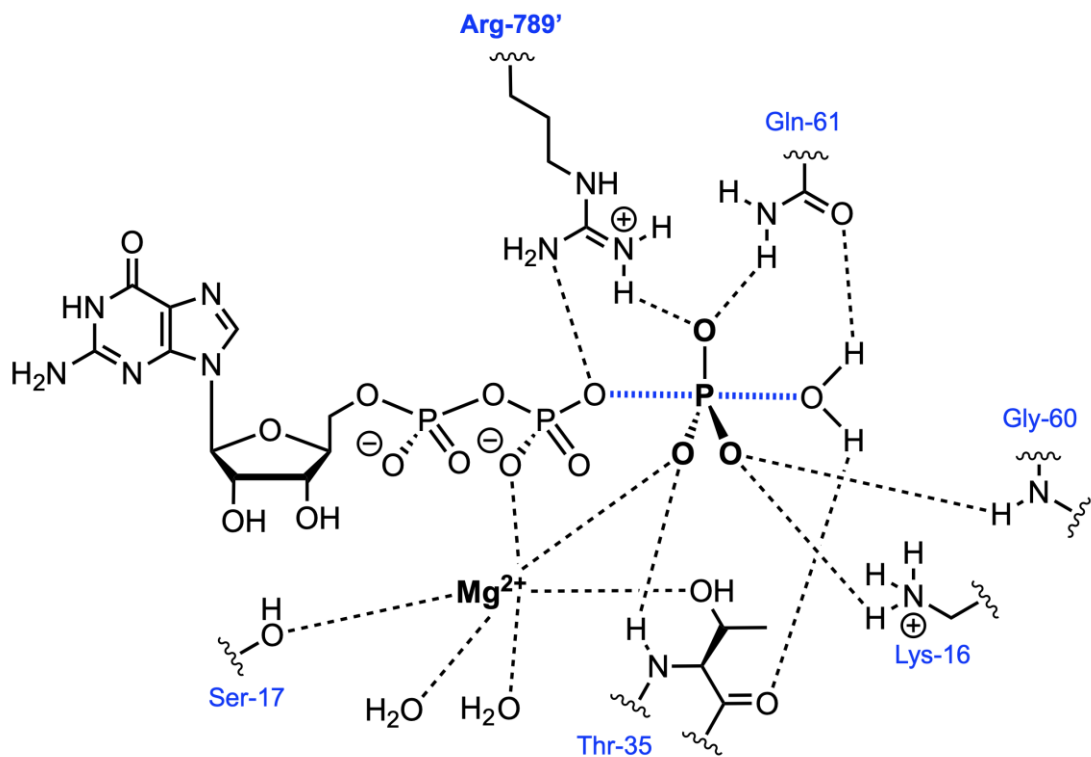


Figure 8: Key interactions during the Ras/RasGAP catalysed hydrolysis of GTP. Arg-789' represents the arginine finger provided by RasGAP.

With their vital roles in the cell, dysregulation of the activity of the Ras protein has been linked to a wide range of diseases. The most famous examples are the three isoforms HRas, KRas and NRas. They are highly homologous and mainly differ in their C-terminal region, which controls the localisation within the cell. While, due to screening bias, their often-quoted mutation rate of 30% in all human tumours is likely too high, with the real value, being closer to 15–20%, *ras* is nonetheless one of the most frequently mutated oncogenes in human cancers. The aforementioned mutations for residues Gly12, Gly13 and Gln61 account for >99% of oncogenic *ras* mutations.⁴¹ They lead to Ras becoming constitutively active, which causes an uncontrolled overactivation of downstream effectors. Ever since the function/disfunction of Ras and other small G proteins in the cell have become known, they have been an attractive drug target.⁴² However directly targeting Ras proteins has been proven difficult so far, despite many decades of research. The lack of obvious drug binding pockets,⁴³ its high affinity for guanine nucleotides⁴⁴ and the failures of indirect targeting strategies like farnesyl transferase inhibitors,⁴⁵ have led to it being dubbed as ‘undruggable’.

1.3.3 The beating heart of cancer: A New Hope

After decades of failed strategies, recent years have seen a renaissance starting with one common mutant. KRas^{G12C} is an oncogenic mutant found in a broad spectrum of cancers and a hallmark in lung adenocarcinoma caused by the exposure to tobacco smoke.^{46,47} The SHOKAT group demonstrated that the nucleophilicity of the cysteine sidechain can be used to tether an inhibitor to the oncogenic mutant causing it to be permanently deactivated.⁴⁸ The thiol group covalently binds to the acrylamide moiety, allowing for a tighter binding of the inhibitor. While many other proteins in the cell carry reactive cysteine residues, here the covalent attachment is being catalysed by Lys16 allowing to specifically target KRas^{G12C}. Based on these initial findings, numerous groups started developing drug candidates for clinical studies.

Initial optimisations led to the development of ARS-1620 (Fig.9), which showed big improvements in terms of binding and pharmacological properties.⁴⁹ AMGEN's AMG-510 was the first G12C inhibitor to start phase I clinical trials in late 2018 (NCT03600883). MIRATI THERAPEUTICS shortly followed with MRTX-849 (NCT03785249). In June 2021 AMG-510 was approved by the FDA under the trade name *Sotorasib*, marking a milestone in a research effort spanning several decades.

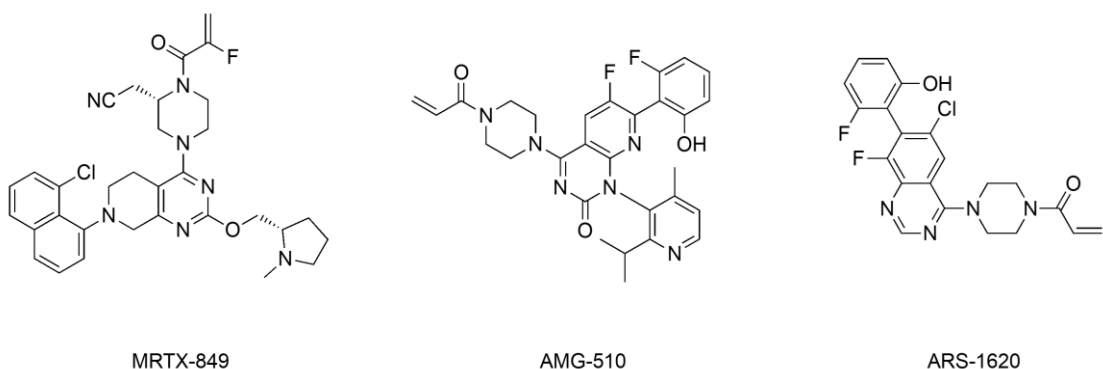


Figure 9: Acrylamide-based covalent Ras^{G12C} inhibitors.

While this is a great step forward in the treatment of a significant fraction of Ras cancers, it is only applicable when the G12C mutation is present. In the last few years fragment-based screenings have identified molecules that are able to bind to a pocket located between the Switch1 and Switch2 region.⁵⁰ It is present in both the GDP- and GTP-bound form of the protein, but due to its shallow and polar nature has been difficult to target. BOEHRINGER INGELHEIM used a fragment-based approach to develop a pan-KRas inhibitor BI-2852 with nanomolar affinity (e.g., $K_D(KRas^{G12D})$

= 740 nM).⁵¹ The compound was able to inhibit several oncogenic Ras mutants *in vivo*. Recently, the company started clinical trials on a further optimised version of the compound (NCT04111458). As of now, the exact structure has not been disclosed. These breakthroughs are the result of an improved mechanistic understanding of the molecular mechanism of small G proteins in a cellular context. A key tool was the application of metal fluoride transition state analogues, which will be discussed in the next section.

1.4 Metal Fluorides: Powerful Transition State Analogues for Phosphoryl Transfer Enzymes

In 1994 COLEMAN *et al.* published the structure GDP·AlF₄⁻ in complex with the G protein G_{iα1} marking the first of many stable analogues for phosphoryl transfer transition states.⁵² Due to their stability towards hydrolysis and their similarity to phosphoryl transfer transition states they have been enabling mechanistic studies in the solid state as well as in solution.⁵³ Since the initial findings with aluminium, many other complexes with metal fluorides, such as magnesium, have been reported.⁵⁴ These transition state analogues (TSA) have become one of the most powerful tools for studying enzymatic phosphoryl transfer reactions.^{53,55}

1.4.1 Structure of the Phosphoryl Transfer Transition State

Non-hydrolysable GTP analogues, like GppNHp or GppCp, bound to small G proteins are widely used to study the GTP-complex properties.⁵⁶ They can deliver valuable insights by providing a transition state precursor structure in the so-called near attack conformation (NAC).⁵⁷ For studying the transition state however these models are limited. The GTP γ-phosphate group adopts a tetragonal geometry and thus the active hydrogen bonding network is not arranged as during the phosphoryl transfer transition state. While the NAC can convey some mechanistic insight, more complete information can be obtained using metal fluoride TSAs. The two metal fluorides predominantly used for small G proteins involve aluminium and magnesium.⁵³ While several geometries exist for MF_x protein complexes, the prevalent ones are octahedral for AlF₄⁻ and trigonal bipyramidal for MgF₃⁻ (Fig.10).

Both species have been widely utilised for mechanistic studies and validated via computational analysis.⁵³

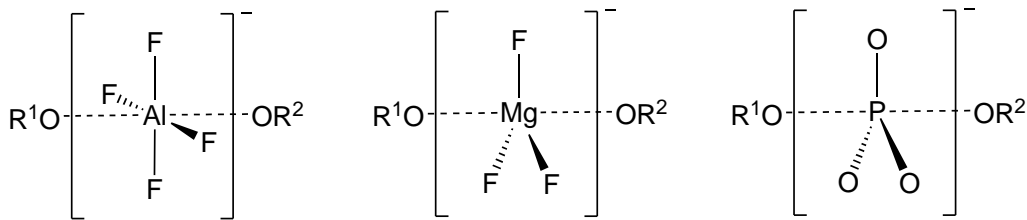


Figure 10: Geometries of AlF_4^- and MgF_3^- complexes compared to the phosphoryl transfer transition state.

Aluminium(III)fluoride complexes formed in water are highly dependent on the pH. AlF_4^- complexes with GDP constitute isoelectronic but non-isosteric mimics of GTP in small G proteins. Looking at the relevant PDB structures gives an average ‘in-line’ O–Al–O angle of $172.88 \pm 7.18^\circ$ and with aluminium midway between the axial oxygen atoms that are $4.07 \pm 0.23 \text{ \AA}$ apart.⁵³

Magnesium is normally six-coordinate and gives octahedral complexes (like AlF_4^-) with oxygen ligands. In contrast, trifluoromagnesate is five-coordinate, and has ideal characteristics to mimic the phosphoryl group as it is isoelectronic with PO_3^- and has the same tbp geometry. They have an axial O–Mg–O distance of $4.19 \pm 0.08 \text{ \AA}$, with an in-line angle of $171.48 \pm 3.98^\circ$. The axial Mg–O bonds are $2.13 \pm 0.10 \text{ \AA}$, with Mg–F bonds of $1.83 \pm 0.06 \text{ \AA}$.⁵³

Aside from geometrical considerations, charge in the active site plays an important role during enzyme catalysis. Based on the charge balance hypothesis, the enzyme active site is optimised to compensate charge build-up during the transition state.^{58,59} Thus, any TSA greatly benefits from an ideally identical charge distribution.

1.4.2 Analysing Metal Fluoride Complexes: $^{19}\text{F-NMR}$

The broad application of $^{19}\text{F-NMR}$ to the study of enzymology stems from a multitude of properties.^{60,61} ^{19}F -nuclei exhibit a high natural abundance, a large chemical shift range of over 800 ppm as well as a high gyromagnetic ratio, which results in a high sensitivity of fluorine containing compounds in NMR measurements.⁶² Furthermore, due to its rare occurrence in biological systems, the technique profits from a high signal to noise ratio. Hence NMR studies of proteins

are made possible, in spite of the usual size constraints.⁶³ The perhaps greatest advantage of ¹⁹F-NMR is its ability to probe proteins in their native state and concomitantly being able to collect data on kinetics and molecular dynamics in real-time.⁶⁴

The combination of X-ray crystallography, ¹⁹F-NMR spectroscopy and DFT calculations has proved powerful in elucidating the nature of transition states in enzyme-catalysed phosphoryl group (PO_3^-) transfer reactions.⁵⁴ For TSAs, the chemical shifts of ¹⁹F resonances provide a key measure of interactions between MF_x moieties and their protein hosts. They are reliable reporters of the electronic environment in the vicinity of the fluorine nuclei. When combined with calculations, they can also act as indirect reporters of the changes in the electronic environment experienced by phosphoryl oxygen atoms at the TS for the transfer reaction.⁶⁵ ¹⁹F resonances display a high degree of dispersion and can be predicted with good precision from quantum calculations of electronic distribution. The high sensitivity of ¹⁹F chemical shifts to the surrounding environment can be used to show e.g., how enzymes control the influence of changes in the protonation state.⁶⁵

1.4.3 Ras/RasGAP: AlF_3^0 or MgF_3^- ?

In 1997 the WITTINGHOFER group solved a 2.5 Å structure for the HRas/RasGAP TSA complex.³⁸ It revealed the role of a catalytic Arg residue, which is responsible for the hydrolysis rate acceleration. The insights provided a great leap in the mechanistic understanding of small G protein regulation. While not a high-resolution structure, it is still widely used as a source of initial atomic coordinates for modelling the enzymatic reactions for the Ras/RasGAP protein complex with trapped GTP as no other HRas/RasGAP TSA complexes have been reported to date.^{66–68}

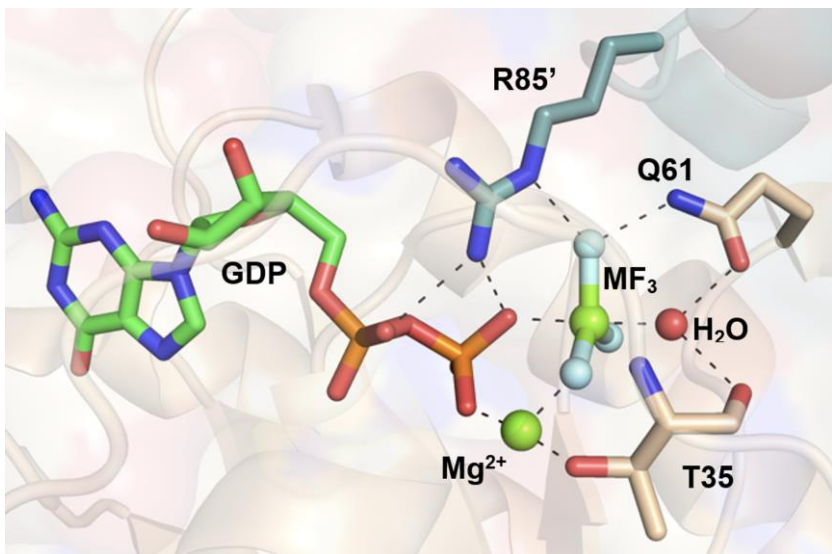


Figure 11: Active site of HRas/RasGAP metal fluoride TSA complex (PDB: 1WQ1). Arg-85' represents the arginine finger provided by RasGAP-334.

In the 1WQ1 structure, the authors assigned the maximum of electron density of the TSA as an AlF_3^0 moiety. However, doubts have emerged over the identity of the MF_x species. As the resolution of the structure is not sufficient for definitive assignment, e.g., an AlF_4^- species is conceivable. Computational studies point to a MgF_3^- species instead of AlF_3^0 .⁶⁹ This is supported by studies on the pH dependence of the solubility of the aluminium ion. Al(OH)_3 precipitates at pH = 8, thereby resulting in replacement of aluminium by magnesium in the protein complexes, with a consequent change to the tbp geometry.⁷⁰ Similarities are present to pH-dependent ¹⁹F-NMR analyses for other enzymes.⁷¹

1.5 Phosphorylation of Ras proteins

To fulfil their numerous biological functions, Ras proteins have a large number of regulatory proteins. In regards to achieving the required signalling specificity (and differentiate them from other similar small G proteins), Ras superfamily small GTPases are also modified posttranslationally to modulate their subcellular localisations, their interactions with positive and negative regulators, chaperones, downstream effector targets, and consequently their biological activities.⁷² Functionally relevant posttranslational modifications (PTMs) of small GTPases can be generally grouped into those that regulate their abundance, their location or their activation. Examples for abundance regulation are polyubiquitination and SUMOylation, leading to proteasomal degradation.⁷³ Localisation regulating PTMs

include prenylation by farnesyl or geranylgeranyl lipids, a modification that is required for membrane binding and that coordinate traffic between the plasma membrane, endomembrane structures, and especially the Golgi network. These occur at the C-terminal hypervariable regions, which is highly specific to the individual isoforms.⁷⁴ PTMs involved in activity regulation include S-nitrosylation, ADP-ribosylation, acetylation and phosphorylation.^{75,76}

Protein phosphorylation is a reversible PTM that is mediated by kinases and phosphatases, which phosphorylate and dephosphorylate substrates, respectively, thus regulating various cellular processes. In biological systems proteins get predominantly modified on the three amino acids Ser, Thr or Tyr.⁷⁷ In small G proteins, research has been focused on the phosphorylation of the HVR in the context of membrane localisation. In recent years studies reported the phosphorylation of effector binding interfaces and consequently a modulation of activity.^{75,78,79}

1.5.1 cSrc-catalysed phosphorylation of HRas Switch regions

cSrc is a non-receptor tyrosine kinase involved in cell growth, division, migration, and survival signalling pathways.⁸⁰ Despite the well-established connection between Ras and cSrc, until recently there was no evidence for direct interaction between the two proteins. In 2014 BUNDA *et al.* reported that cSrc binds to and phosphorylates GTP-loaded Ras on a Switch1 tyrosine residue, which leads to diminished binding to the key effector Raf as well as a stronger binding to RasGAP.⁸¹ With MS trypsin digest experiments they identified Tyr32, Tyr64, Tyr96 and Tyr157 of Ras to be phosphorylated by cSrc *in vitro* and suggested Tyr32 and Tyr64 to be the main sites on the basis of spectral count. Immunoprecipitation assays, where HEK293 cells were transfected with plasmids containing either wildtype Ras, Ras^{Y32F} or Ras^{Y64F}, showed diminished Ras phosphorylation when Tyr32 was mutated and no change in Ras phosphorylation levels when Tyr64 was mutated. From this the authors concluded, Tyr32 to be the main phosphorylation site. Using immunoprecipitation pull-down assays *in vivo* and *in vitro*, the authors showed that cSrc-mediated Ras phosphorylation decreased binding with the downstream effector Raf, while it increased binding with RasGAP. Subsequently, based on crystal structure of the non-phosphorylated Ras-Raf complex, the authors hypothesised the phosphorylation of Tyr32 could lead to electrostatic repulsion

against two negatively charged residues Asp38' and Asp57' on the binding interface of Raf, thus causing a conformational shift in the effector region.⁸¹ Regarding the interaction between phosphorylated Ras and RasGAP, the authors postulated that the electrostatic interaction between the phosphorylated Tyr32 and the negatively charged Arg903' of RasGAP leads to tighter binding.

In a follow-up study protein tyrosine phosphatase (PTP) SHP2 was found to dephosphorylate tyrosyl-phosphorylated Ras, which restores binding of Ras to Raf and reactivates downstream signalling.⁸² In addition, pharmacological inhibition of SHP2 activity was shown to increase the level of phosphorylated Ras and to attenuate cell proliferation in mammalian cells. This supports the notion that one of the functions of SHP2 is that of a direct activator of Ras.

KANO *et al.* further investigated cSrc-mediated phosphorylation of ¹⁵N-labelled Ras using 2D-NMR to examine *in vitro* phosphorylation-induced conformational changes.⁸³ Upon phosphorylation they observed major shifts for residues around Tyr32 (Switch1) and Tyr64 (Switch2). LC-MS/MS sequencing of trypsin-digested phosphorylated KRAS identified a tryptic peptide containing phosphorylated Tyr64 as the most abundant tyrosyl phosphorylated species, followed by a fragment containing phosphorylated Tyr32. To investigate how these findings apply *in vivo*, the authors performed immunoprecipitation experiments, which showed no significant Ras tyrosine phosphorylation when HEK293 cells were transfected with a plasmid containing Ras^{Y64F} and reduced levels when transfected with Ras^{Y32F}. In the next step, using a real-time HSQC ¹H-¹⁵N-NMR assay, the authors examined how phosphorylation affects effector binding, nucleotide exchange and the intrinsic rate of hydrolysis. They reported a 2.6-fold increase in intrinsic GTP/GDP nucleotide exchange and a 3-fold decrease of the intrinsic rate of GTP hydrolysis, compared to the unphosphorylated protein. When examining the interaction with effectors, they reported attenuated effects for the interaction with GEF and GAP. The rate of GEF acceleration dropped from a 17-fold increase for the unphosphorylated, to a 3-fold increase for the phosphorylated Ras. Similarly, for RasGAP the authors reported a >300% hydrolysis rate increase for the unphosphorylated Ras and only a <20% rate increase for the phosphorylated Ras protein.

Together this contradicts the earlier study which found Ras phosphorylation could accelerate RasGAP-catalysed GTP hydrolysis. Instead, the authors suggest a model where, upon phosphorylation, Ras is shifted to a 'dark state' in which the Ras cycle is suspended, until normal Ras function is restored by the relevant

phosphatase.⁸³ cSrc-mediated phosphorylation appears to play an important role in Ras regulation, however further clarification is still needed to understand its mechanistic details.

1.6 GAP-catalysed GTP hydrolysis for Rho proteins

Rho is one of the five small G protein families with a unique Rho insert region of 13 amino acids (124–136) and, like all small G protein families, is operating via a GDP/GTP cycle.⁸⁴ It is involved in essential cellular functions, like actin formation, cell motility, cell cycle progression, vesicular transport and gene expression.^{85–89} The human Rho GTPases family consists of twenty protein isoforms, with RhoA, Cdc42 and Rac1 being the most extensively studied and characterised members.⁹⁰ The human genome contains over 80 Rho family GEFs, over 80 Rho family GAPs, as well as three Rho family GDIs.^{91–93} Activation of RhoA, Cdc42 and Rac1 promotes fibroblast movement by regulating filopodias, membrane ruffles, focal adhesion and stress fibers.^{91,94} Dysregulation of Rho activity is linked to numerous diseases and disorders, among them cancer.⁹⁵

With Rho being involved in a variety of human diseases, slow Rho GTP hydrolysis is a logical way to attenuate Rho activity in the case of overactivation. A better understanding of GAP-catalysed GTP hydrolysis has therefore been the target of extensive research over the past decades. As mentioned in section 1.3, efficient catalysis includes a number of key elements, such as orientation and polarisation of the nucleophilic water, exclusion of solvent water from the active site and adequate stabilisation of intermediates and transition states during the phosphoryl transfer.³⁷ For the Ras superfamily, GAPs accelerate GTP hydrolysis by either participating directly in the catalysis, e.g. through the so-called ‘Arg-finger’ or via allosteric regulation.⁹⁶ RhoGAPs have been found to catalyse γ -phosphoester bond hydrolysis via a similar mechanism.^{65,97} The TSA complexes RhoA/MgF₃[−]/RhoGAP and RhoA/AIF₄[−]/RhoGAP have been invaluable in elucidating core mechanistic features, for example the stabilisation of Gln63 by the ‘Arg-finger’, which allows for the correct alignment of the nucleophilic water.^{65,158,98} Similar principles are observed for other small G proteins. While Cdc42 and Ras function via similar mechanisms,^{38,99} in Rab the conserved Gln92 is displaced from the active site and both residues are provided by RabGAP.¹⁰⁰ For the Sar/ArfGAP complex GAP catalysis is assisted by the ‘Arg-Finger’, while the role of the Gln is taken over by

His77.¹⁰¹ These are just a few examples that show the importance of the ‘Arg-Finger’ and while it is a wide-spread structural motif, other factors play a role as well. This is evident when considering that the ‘Arg-Finger’ deficient GAP mutants for the prototypical Rho GTPases RhoA and Cdc42 still retain a significant portion of their activity. Specifically, Cdc42GAP^{R305A} is able to accelerate GTP hydrolysis 10-fold and RhoGAP^{R85A} provides 160-fold acceleration compared to the intrinsic rate.^{151,102} Together with the fact that small G proteins have an intrinsic GTPase activity, this shows that other contributions to the catalytic activation are involved, aside from the ‘Arg-Finger’. Some GAPs lack this catalytic Arg residue altogether. In the case of Rap/RapGAP, instead of an Arg residue the GAP provides an Asn residue which takes the role of the previously mentioned catalytic Gln residue.¹⁰³ For Ran/RanGAP an Asn residue stabilises the positioning of Ran-Gln69 and the Switch1 Ran-Tyr39 donates a hydrogen bond to the γ -phosphate group of GTP instead a ‘Arg-Finger’. This Tyr is widely conserved in small G proteins.¹⁰⁴

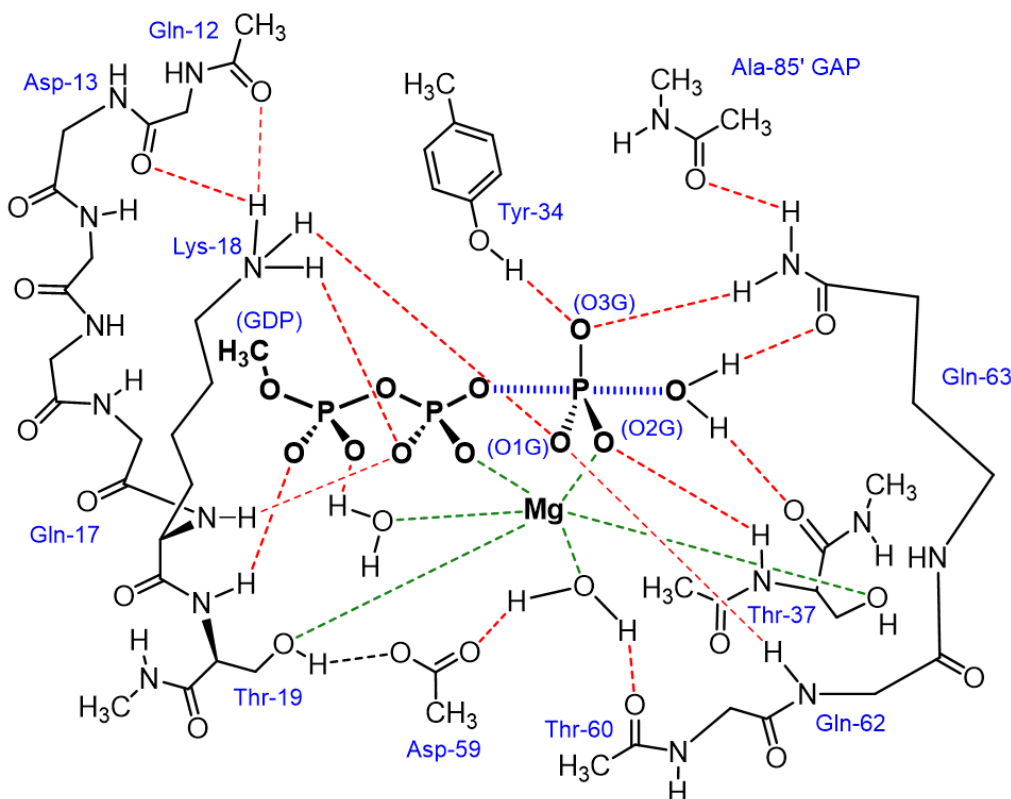


Figure 12: Active site hydrogen bond model of RhoA/GTP/RhoGAP^{R85A} during the phosphoryl transfer transition state (adapted from JIN *et al.*).¹⁵⁷ Ala85' is donated by RhoGAP^{R85A}.

Though the RhoGAP^{R85A} mutant is not particularly relevant clinically, it is nonetheless an interesting system to study. When assessing the influence of the deletion of the catalytic ‘Arg-Finger’ in the RhoA/RhoGAP system, JIN *et al.* found

that RhoA-Tyr34 fills the cavity of the deleted Arg side chain and coordinates to the GTP γ -phosphate group (Fig.25).¹⁵⁷ RhoA and RhoGAP readily form a TSA complex with MgF₃⁻ in solution and as a crystal structure. Together with ¹⁹F-NMR, protein X-ray crystallography and DFT calculations, the authors could characterise the differences in the active site resulting from the deletion of the ‘Arg-Finger’. They found that the attenuated catalytic activity for RhoGAP^{R85A} mainly stems from the reduced stabilisation of the transferring phosphoryl group and the removal of the positively charged Arg residue from the active site hydrogen network. For many small G proteins, the conserved Tyr in the Switch1 region coordinates the γ -phosphate group during the GTP hydrolysis. For small G Protein active sites with proteins like RasGAP, RhoGAP or Cdc42GAP, the ‘Arg-Finger’ displaces this residue, causing the Tyr sidechain to be rotated away from the γ -phosphate group. GAP systems without a catalytic Arg residue, like RapGAP, RanGAP or RhoGAP^{R85A}, exhibit a hydrogen bond contact between the Switch1 Tyr and the γ -phosphate group (Fig.25). To date only low resolution (<2.7 Å) crystal structures of these small-G-protein-GAP complexes without ‘Arg-Finger’ have been reported. Therefore, RhoA/RhoGAP^{R85A} lends itself as a well-behaved substitute model system.

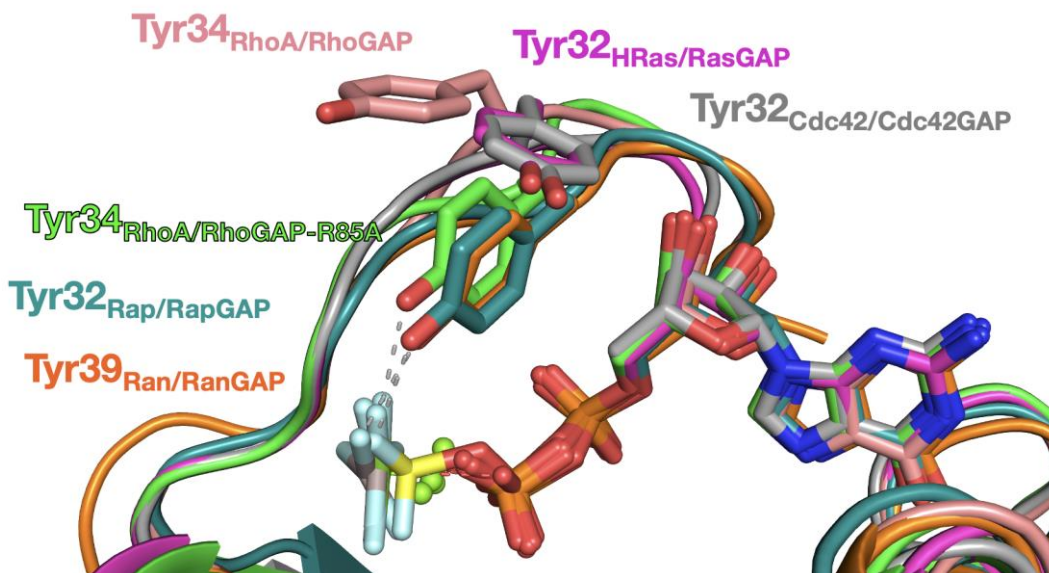


Figure 13: Comparison of conserved Tyr residue of superimposed structures of metal fluoride complexes for **HRas/RasGAP** (PDB: 1WQ1), **Cdc42/Cdc42GAP** (PDB: 1GRN), **RhoA/RhoGAP** (PDB: 1OW3), **RhoA/RhoGAP^{R85A}** (PDB: 5M6X), **Rap/RapGAP** (PDB: 3BRW) and **Ran/RanGAP** (PDB: 1K5G).

1.6.1 Hydrogen Bonds in enzymatic Catalysis

Hydrogen bonds are crucial for all biological systems. They hold together DNA base pairs, by highly specific amine proton donors and carbonyl acceptor groups. They are the most important non-covalent interaction for the formation of structural motifs in proteins and peptides like α -helices and β -sheets. Furthermore, they provide valuable contributions in enzyme catalysis through substrate recognition, orientation and/or activation.¹⁰⁵

They span a large range (~10–150 kJ/mol) from strong hydrogen bonds which have covalent character to weak ones which are energetically just above van der Waals interactions.^{106–108} They occur between a hydrogen bound to an electronegative atom and the lone pair of another electronegative atom. The strength depends mainly on the length, geometry and how closely the pK_a values of the participating heavy atom conjugate acids are matched.¹¹³ Even today, the exact nature of hydrogen bonding is not fully understood. Previously it had been thought to be a purely electrostatic interaction between a partially positively charged hydrogen atom and a partially negatively charged acceptor atom. However, other energy components, like π -resonance assistance, charge transfer interactions and dispersion interactions appear to play a role as well, especially for shorter hydrogen bonds.^{109–112} Average lengths (hetero atom distance) are between 2.7–3.0 Å and generally independent of the solvent environment.¹¹³ Stronger, and therefore shorter, hydrogen bonds occur, when the pK_a value of the two hetero atoms are closely matched. These strong hydrogen bonds (>2.5 Å) play a key role in enzyme catalysis and are often referred to as low barrier hydrogen bonds (LBHB).¹¹⁴ While generally the proton is associated with the more electronegative heteroatom, protons in a LBHB can move freely between the two hetero atoms, shown by neutron diffraction experiments.¹¹⁵ These bonds have an increased covalent character and have been shown to be integral to catalysis for serine proteases, ketosteroid isomerase, citrate synthase and many other systems.¹¹⁴

1.6.2 Fluorinated Amino Acids as Biological Probes

Fluorine is the element with the highest electronegativity, while being the smallest of the halogens, bringing with it unique properties.¹¹⁶ Fluorine substituents impact physicochemical properties of a compound by affecting the lipophilicity, dipole moment and electrostatic potential. In drug discovery these factors impact, among

other things, rate of metabolism, tissue distribution and binding properties. Well over 20% of pharmaceuticals have at least one fluorine substituent.¹¹⁷ While for longest time synthetic fluorine chemistry was extremely dangerous to work on, due to the high reactivity of elemental fluorine, in the recent decades it has become more accessible due to the discovery of safer reagents like Selectfluor, diethyl aminosulfur trifluoride (DAST) and many others.¹¹⁸ This has facilitated the broad application of fluorinated amino acids as a way to examine biological systems. Ranging from positron emission tomography to fluorinated metabolites, which can be studied using ¹⁹F-NMR without much background signal. Due to its relatively low abundance in biological systems and the high C–F bond strength, most organisms have not evolved ways to break down these bonds, therefore metabolic degradation is slowed down. While fluorine (van der Waals radius: 1.47 Å) is slightly larger than hydrogen (van der Waals radius 1.20 Å) it can generally be employed as a mimic of the respective canonical amino acid.¹¹⁹ While there are fluorinated examples for all 20 canonical amino acids in the literature, here the focus lies on fluorotyrosine (FY).¹²⁰ In biological systems tyrosine, with its phenol motif, is central to many molecular interactions and one of the major targets of post-translational modifications.¹²¹ Due to the electron withdrawing effect of fluorine substituents, the aromatic ring potential is reversed upon fluorination. As the van der Waals radius of fluorine and hydrogen is similar, single incorporations generally do not lead to destabilisation of the protein structure.¹²² Higher numbers of fluorine substituents however, increase the side chain volume by a larger margin (molecular volume for C₆H₆: 104 Å³ and C₆F₆ 141 Å³).¹²³ In contrast to phenylalanine fluorine substitution of the aromatic side chain leads to an increase in polarity. The electron withdrawing inductive effect causes the pK_a of the hydroxyl functional group to lower which in turn makes it a better hydrogen bond donor. The exact pK_a depends on the substitution pattern as seen in Fig.14.¹²⁴

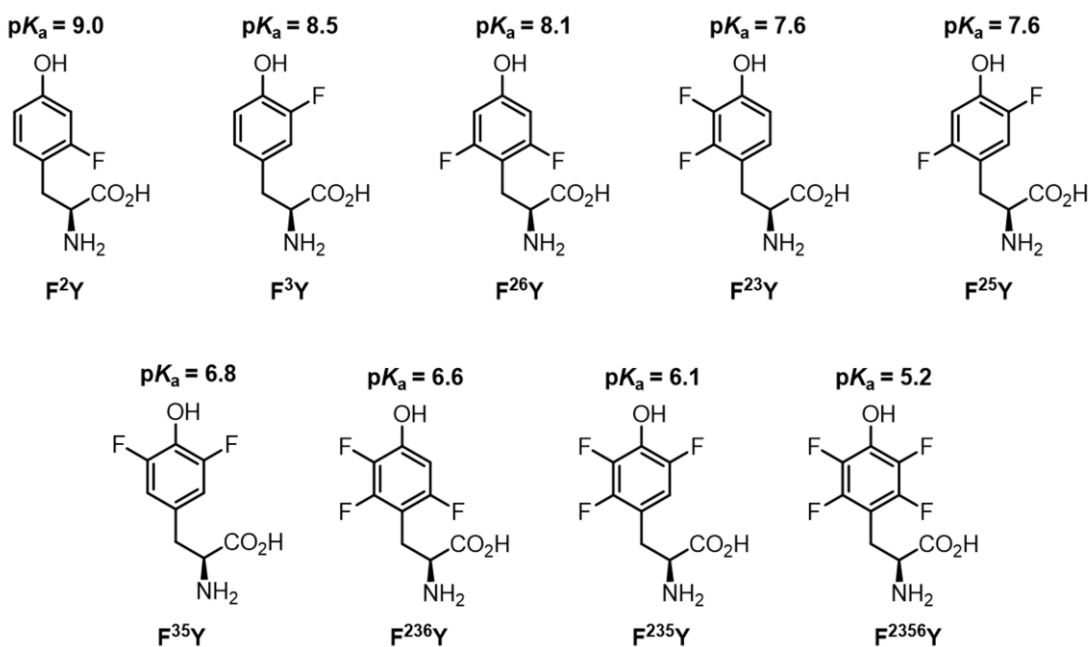


Figure 14: Substitution patterns of fluorinated tyrosine derivates and their respective pK_a values.¹²⁴

1.6.3 Incorporation of Fluorotyrosine (FY) into Proteins

Compared to many other fluorinated amino acids, FYs are readily accessible via a one-step chemoenzymatic reaction using tyrosine phenol lyase (TPL) from the respective fluorophenol, ammonia and pyruvate.¹²⁵ Three main strategies for the incorporation are used in the literature. (1) All Tyr residues are replaced globally by supplementing a Tyr free growth medium with either F^2Y or F^3Y . Auxotrophic *E.coli* strains can then incorporate FY using the tyrosine tRNA synthetase (RS).¹²² However, this strategy lacks the option to differentiate different Tyr residues and only works for monofluorinated amino acids, due to their similarity to Tyr. (2) In order to achieve site specificity expressed protein ligation was developed where an incomplete protein is ligated to a manually synthesised peptide to generate a semisynthetic protein.^{124,126} While this gives access to a great number of accessible chemical groups, it cannot readily be applied to positions in the interior of the protein. (3) Recently the STUBBE group has evolved an aminoacyl-tRNA/RS pair which is able to polyspecifically incorporate several fluorotyrosine residues.¹²⁷ This strategy utilises a blank TAG codon in the gene of interest to site-specifically incorporate the fluorotyrosine *in vivo* (Fig.15). They achieved this by evolving the new pair based on the known structure of Tyr-bound *MjTyrRS* by a double-sieve selection process. This methodology was then used to extensively study tyrosyl radical transfer mechanisms in ribonucleotide reductase.¹²⁸⁻¹³² Many other

examples can be found in the literature where this approach has been used to study a wide range of biological systems.

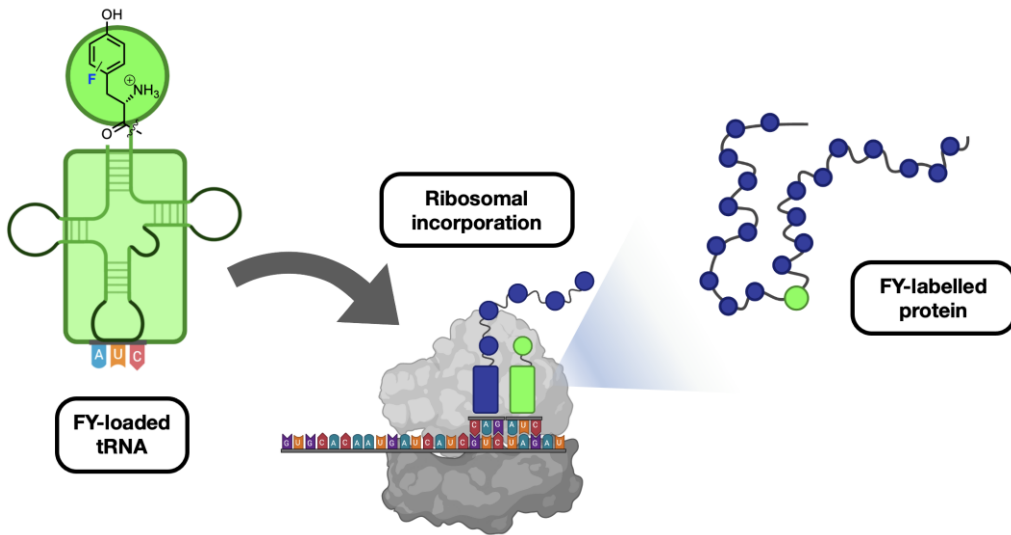


Figure 15: Orthogonal tRNA charged with fluorotyrosine (FY) is incorporated through ribosomal translation at a non-coding codon leading to the site-specific labelling of the polypeptide chain.

1.6.4 Literature Examples: Ribosomal Site-specific Fluorotyrosine (FY) Incorporation

1.6.4.1 FY Incorporation in Flavoproteins

AppA is a flavin dependant blue light photoreceptor with a Tyr²¹ residue involved in the hydrogen bonding network around the chromophore. By incorporating a series of fluorinated tyrosines Gil *et al.* studied the effects on light activation and the light independent dark state recovery.¹³³ The fast forward photoreaction was examined using time-resolved infrared techniques and only small rate changes were observed. For the dark state recovery, they found that the Tyr²¹ acidity increase of 3.5 pK_a units leads to a 4000-fold rate acceleration, confirming the role of Tyr in the recovery mechanism. A follow-up study applied the same strategy to the related protein PixD.¹³⁴ There the authors found a reversed effect, where the rate of recovery is significantly reduced, thus highlighting the mechanistic differences between two similar flavin chromophore proteins. Liu *et al.* incorporated a number of fluorotyrosines into the fluorescent flavoprotein iLovU to develop a novel class of genetically coded photo-induced electron transfer sensors.¹³⁵ Depending on the pK_a of the incorporated fluorotyrosine, these variants were able to sense pH changes *in vivo*.

1.6.4.2 FY Incorporation into Membrane Proteins

HE *et al.* developed a method where site-specifically incorporating F³⁵Y into membrane binding proteins can help elucidate the binding mode.¹³⁶ They differentiate between cation-π interactions, where the aromatic side chain interacts with the positively charged phospholipid head group, and membrane insertion where the aromatic side chain is inserted into hydrophobic part of membrane. Replacing all surface Tyr residues and measuring the binding of the F³⁵Y variants to small unilamellar vesicles allowed them to elucidate the binding mode. β-arrestin-1 recruits downstream proteins based on GPCR mediated signalling. To determine how phosphorylation patterns on signalling peptides affected the conformation of β-arrestin-1, YANG *et al.* incorporated F³⁵Y at the seven phosphate-binding sites of the protein as well as other strategic positions.¹³⁷ After adding a number of functional phospho-peptides, they monitored the shift in ¹⁹F-NMR signals and could thereby decipher which phosphorylation patterns lead to which conformational change. LI *et al.* used the same strategy to investigate F³⁵Y as a ¹⁹F-NMR probe for tyrosine phosphorylation.¹³⁸

1.6.4.3 Tuning the Electronic Properties of the GFP chromophore

VILLA *et al.* incorporated five different fluorotyrosine residues directly into the chromophore of the green fluorescent protein (GFP) beta barrel.¹³⁹ The measured absorbance maxima exhibited a significant blue-shift correlating with the decreasing pK_a value of the phenol side chain. ROMEI *et al.* expanded this work to determine the steric and electrostatic contributions of the bond photoisomerization in GFP and incorporated electron donating tyrosine derivate (3-Me-Tyr, 3-MeO-Tyr) as well as a series of fluorotyrosine residues into the GFP chromophore.¹⁴⁰ The resulting variants were analysed in terms of their absorption maxima, fluorescence quantum yield and how they relate to rotation around specific bonds after photoexcitation.

1.6.4.4 Other Examples

BLATTER *et al.* used site-specific incorporation of F²³⁵Y to modulate the pK_a of a KlenTaq DNA Polymerase Tyr671 residue.¹⁴¹ Using a series of activity assays they could establish the importance of the side chain for the repair of abasic DNA damage.

Because of the rarity of fluorine in biological systems only few other enzymatic C–F cleavage reactions have been reported.¹⁴² F³⁵Y has been site-specifically incorporated into cysteine dioxygenase to investigate the post-translationally generated cross linkage between Cys93 and Tyr157.¹⁴³ For the wildtype this oxygen dependant cross linkage occurs between the Cys93 sulphydryl group and the C³ hydrogen of the Tyr153 sidechain. Due to the fluorine substitution and the more stable C–F bond, the authors managed to capture the first structure of the uncrosslinked active site using X-ray crystallography under anaerobic conditions. Interestingly, upon treatment with oxygen the cleavage of the C–F bond was observed.

Yu *et al.* examined the role of a conserved Tyr residue found in oxidases and how the phenol ring pK_a affects the O₂ reduction activity.¹⁴⁴ They observed an inverse correlation between phenol sidechain pK_a and oxidase activity. Furthermore, they employed electron paramagnetic resonance measurements of the incorporated FY residue to examine the role of a tyrosine radical in the reaction mechanism.

1.7 Aims and Objectives

1.7.1 HRas

The first aim of this project is to improve on the only currently available X-ray crystal structure of the HRas/RasGAP complex (PDB:1WQ1), which has no structure factor available for inspection. Doubts have emerged over the identity of the assigned metal fluoride species (see section 1.5.3) and while this structure revolutionised our understanding of Ras biology at the time of its publication in 1997, the low resolution (2.5 Å) has an incomplete coordination sphere for its catalytic magnesium and has left some mechanistic questions unclear. For example, the participation of a second water molecule in the GTP hydrolysis mechanism has been suggested to assist in the deprotonation of the nucleophilic water.¹⁴⁵ While there are many computational studies on this topic, so far, no high-resolution crystal structures available. Given that this structure is still widely used for many computational and bioinformatic studies, it would be a great benefit to have a structure with improved resolution and density for the key ligands in the active site.^{66–68} Therefore, HRas and RasGAP need to be expressed recombinantly and purified, followed by screening for suitable crystallisation conditions to obtain an improved crystal structure.

The second aim of the project is to clarify the discrepancy in the literature regarding the structural and mechanistical implications of cSrc-mediated phosphorylation of HRas switch regions. As a first step, the role of the two key residues Tyr32 and Tyr64 in this PTM needs to be examined. For that the mutants HRas^{Y32F} and HRas^{Y64F} need to be generated and examined in terms of their interaction with cSrc. In order to gain the necessary structural insight into the interaction of phosphorylated HRas, metal fluorides are a valuable tool to study the Ras/RasGAP complex. Using ¹⁹F-NMR and an X-ray crystallography to examine the phosphorylated HRas/MgF₃⁻/RasGAP TSA complex would then provide valuable information on the structural impact of cSrc-mediated Switch phosphorylation of Ras.

1.7.2 RhoA

Recent findings revealed that in the RhoA/RhoGAP^{R85A} complex the Switch1 residue Tyr34 stabilises the phosphoryl transfer transition state, via a hydrogen bond. This project aims to precisely isolate the effect of this H-bond among the

active site hydrogen bonding network of this small G protein model system by selectively modulating the strength of this single hydrogen bond, to gain insights into the chemistry of phosphoryl activation. The modulation will be achieved by generating a range of fluorinated Tyr34 RhoA variants, with altered Tyr34 hydroxyl pK_a . The work can be divided into four areas:

1. Express and purify a series of FY-RhoA variants in which Tyr34 is site-specifically replaced by an array of fluorotyrosines. This will be achieved by using a polyspecific tRNA/tRNA synthetase pair, which allows incorporation of different FYs at a ribosomal level.
2. Utilising magnesium fluoride as a transition state analogue (TSA), the influence of the FY incorporation on electronics of the transition state will be investigated. This will be achieved by formation of the FY-RhoA/ MgF_3^- /RhoGAP^{R85A} TSA complex and examining the altered ¹⁹F chemical shift of the magnesium fluoride species.
3. Determine high-resolution X-ray crystal structures for FY-RhoA/ MgF_3^- /RhoGAP^{R85A} TSA complexes in order to ensure that the introduction of the fluorine substituents has not perturbed the overall arrangement of hydrogen bonding interactions in the catalytic core of the fluorinated enzyme.
4. Measure kinetic parameters of FY-RhoA variants to quantify the effect of pK_a modulation and to validate findings from (2) and (3).

2 Materials and Methods

2.1 Equipment and Materials

Water for buffers, media and experiments was purified using a PURELAB Chorus 2 system to a purity of $> 15 \times 10^6 \Omega \text{ cm}$. Unless otherwise stated, all experiments were performed at room temperature, in a temperature-controlled environment (20°C). pH values were determined at room temperature using a JENWAY 3510 pH Meter together with a general-purpose SJ 113 pH electrode. The electrode was stored in 3 M KCl and calibrated daily using a 3-point calibration method at pH = 4.0 (phthalate buffer, FISHER SCIENTIFIC., J/2820/15), pH = 7.0 (phosphate buffer, FISHER SCIENTIFIC., J/2855/15) and pH = 10.0 (borate buffer, FISHER SCIENTIFIC., J/2885/15). pD was measured in accordance with the literature.¹⁴⁶

2.2 High Performance Liquid Chromatography (HPLC)

HPLC was performed on an AGILENT infinity II HPLC system, using a SHIMADZU Shim-pack GIST C18 column ($150 \times 4.6 \text{ mm}, 5 \mu\text{m}$) with a linear gradient from 8% to 30% MeOH over 22 min. GTP-loadings were calculated by converting the HPLC peak areas of the 254 nm UV chromatogram corresponding to GDP and GTP into nucleotide ratios. Retention times were confirmed using commercial standards.

2.3 Nuclear Magnetic Resonance (NMR) Spectroscopy

NMR spectra in this work have been recorded on the following instruments: BRUKER DPX 400 MHz (9.3 Tesla; ^1H and ^{13}C), BRUKER Avance 500 MHz (11.7 Tesla; multinuclear) BRUKER DRX 600 MHz with cryoprobe (14.0 Tesla; ^1H , ^{13}C , ^{19}F , ^{31}P). Chemical shifts (δ) are given in parts per million (ppm) and are taken from the centre of the coupling pattern. Coupling constants are given in Hertz. For ^1H NMR, residual solvent peaks were used as internal standard (D_2O : ^1H : $\delta = 4.79 \text{ ppm}$). All spectra were recorded at 20°C . For the presaturation of the free fluoride signal, elective ^{19}F irradiation was achieved with a continuous wave (power level of 42 dB) applied over the 1 s recycle delay at the frequency of free fluoride peak (-119.5 ppm). For samples with 90% D_2O , this frequency was adjusted to -121.5 ppm . The pulse

programme used can be found in section 5.7. Unless stated otherwise, all protein ^{19}F -NMR spectra were calibrated to an internal fluorobenzene standard at -113.79 ppm.¹⁴⁷

2.4 Mass spectrometry

Liquid chromatography-mass spectrometry (LC-MS) was performed on a WATERS Synapt G2-Si quadrupole time-of-flight mass spectrometer coupled to a WATERS Acquity H-Class ultraperformance liquid chromatography (UPLC) system. The column was a WATERS Acquity UPLC protein BEH C4 (300 Å, 1.7 µm × 2.1 mm × 100 mm) operated in reverse phase and held at 60 °C. The gradient employed was 95% A to 35% A over 50 min, where A is water with 0.1% HCO_2H and B is acetonitrile with 0.1% HCO_2H (Tab. 2). Spectra were collected in positive ionisation mode and analysed using WATERS MassLynx software version 4.1. Deconvolution of protein charged states was obtained using the maximum entropy 1 processing software.

Table 2: Protein LC-MS chromatography parameters

Time (min)	A% (H_2O 0.1% CHOOH)	B% (ACN 0.1% CHOOH)
0	95	5
3	95	5
50	35	65
52	3	97
54	3	97
56	95	5
60	95	5

2.5 Gravity and Fast Protein Liquid Chromatography Column

Columns and resins were packed and regenerated following the respective manufacturing guidelines. All columns were stored in 20% (v/v) ethanol at either 4 or 20 °C. FPLC was performed using either ÄKTA purifier or ÄKTA start systems with stationary phase columns from GE Healthcare.

2.6 Software

Polyacrylamide and agarose gels were processed and analysed using BIO-RAD Laboratories Image Lab version 6.0.1. NMR data was acquired, processed, and analysed using BRUKER Topspin versions 3.5 and 4.0.7. For general data processing and visualisation MATHWORKS Matlab version R2019b, ORIGINLAB Origin 2019 and PERKINELMER ChemDraw version 16.0 were used. Structural protein data files were analysed and visualised using SCHRÖDINGER PyMOL version 2.0.6. Plate reader assays were run and analysed using BMG LABTECH Optima version 2.20R2. PISA queries were performed with PDBePISA v1.52.¹⁴⁸

2.7 Gel Electrophoresis

Sodium dodecyl sulfate polyacrylamide gel electrophoresis (SDS-PAGE): Solutions and buffers used for SDS-PAGE are listed in table 3. Hand cast SDS-PAGE gels (1 mm × 80 mm × 100 mm) were run using the BIO-RAD Mini-Protean vertical electrophoresis cells at a constant current of 35 mA for 50 min. The gels were prepared fresh and stored at 4 °C for a maximum of five days. 3 µL of THERMO SCIENTIFIC PageRuler protein ladder were run alongside protein samples to estimate protein size. Protein samples for SDS-PAGE were prepared by mixing the appropriate volume of protein sample with 4× SDS Loading Buffer and heating the sample at 2–5 min to denature the proteins. Native PAGE gels were run under identical conditions while omitting SDS from all buffers. Gels were imaged and processed using a BIO-RAD ChemiDoc imaging system.

Agarose Gel Electrophoresis: Agarose gel electrophoresis were used to assess integrity of DNA plasmids as well as analyse reactions involving DNA fragments. For 1% (w/v) agarose gels 0.5 g agarose are suspended in 50 mL TAE buffer (Tris-HCl 40 mM, pH = 8.3, AcOH 20 mM, EDTA 1 mM) and heated until the agarose was dissolved. 1 µL of INVITROGEN SYBR Safe DNA gel stain was added and the solution was poured into a 7 cm × 7 cm gel tray and cooled until it solidified. Gels were run in TAE buffer on a BIO-RAD Mini-Sub Cell GT System at 120 V for 30 min. DNA samples were mixed with THERMO SCIENTIFIC FastDigest Green Buffer before loading. Gel images were imaged and processed using a BIO-RAD ChemiDoc imaging system.

Table 3: Buffer and solutions for SDS-PAGE

4 × Resolving Buffer	Tris-HCl	1.5 M (pH = 8.8)
	SDS	0.4 % (w/v)
4 × Stacking Buffer	Tris-HCl	0.5 M (pH = 6.8)
	SDS	0.4% (w/v)
4 × SDS Loading Buffer	Tris-HCl	200 mM (pH = 6.8)
	DTT	400 mM
	SDS	8% (w/v)
	Bromophenol blue	0.4% (w/v)
	Glycerol	40%
	Tris-HCl	25 mM
SDS Running Buffer	Glycine	20 mM
	SDS	0.1% (w/v)
Stacking Gel	Acrylamide/bisacrylamide (37.5:1)	5% (w/v)
	4 × Stacking Buffer	25% (v/v)
	APS	5 mM
	TEMED	7 mM
10% Resolving Gel	Acrylamide/bisacrylamide (37.5:1)	10% (w/v)
	4 × Resolving Buffer	25% (v/v)
	APS	5 mM
	TEMED	7 mM
12% Resolving Gel	Acrylamide/bisacrylamide (37.5:1)	12% (w/v)
	4 × Resolving Buffer	25% (v/v)
	APS	5 mM
	TEMED	7 mM
15% Resolving Gel	Acrylamide/bisacrylamide (37.5:1)	15% (w/v)
	4 × Resolving Buffer	25% (v/v)
	APS	5 mM
	TEMED	7 mM
Coomassie Blue Stain	Coomassie brilliant blue G-250	0.06‰ (w/v)
	HCl	50 mM

2.8 Concentration, Buffer Exchange and Protein handling

Protein solutions were concentrated at 4 °C using MERCK Amicon centrifugal filters with a molecular weight cut-off between 3 and 50 kDa depending on the molecular weight of the target protein. The tubes were centrifuged at 5500g using a HETTICH Rotina 420R centrifuge.

Protein concentrations c were determined via the Beer-Lambert law (Eq.1). The absorbance was measured at 280 nm using a THERMO SCIENTIFIC NanoDrop One^C. The protein extinction coefficient was calculated using Eq.2 by inputting the amino acid sequence into Expasy-ProtParam.^{149,150} Small G proteins are copurified with the nucleotide GDP, therefore the extinction factor of $7950 \text{ M}^{-1} \text{ cm}^{-1}$ was added to the final calculated extinction factors.¹⁵¹ All Protein concentrations were measured in triplicate.

$$c = A / (\varepsilon \times d) \quad (1)$$

c : concentration of solute in mol L⁻¹ A: absorbance value

d : path length [cm] ε : molar extinction coefficient [$\text{M}^{-1} \text{ cm}^{-1}$]

$$\varepsilon = (5500 \times nW) + (1490 \times nY) + (125 \times nC) \quad (2)$$

ε : Molar extinction coefficient [$\text{M}^{-1} \text{ cm}^{-1}$] nW: number of W residues

nY: number of Y residues nC: number of C residues

2.9 Growth Media

Lysogeny Broth (LB) medium: For 1 L of LB medium 10 g tryptone, 10 g yeast extract and 5 g NaCl were dissolved to a volume of 1 L with water. The media was sterilised by steam autoclaving for at least 15 min at a temperature of 121°C and a pressure of 2.0 bar.

2xYT medium: For 1 L of 2xYT medium 16 g tryptone, 5 g yeast extract and 10 g NaCl were dissolved to a volume of 1 L with water. The media was sterilised by steam autoclaving for at least 15 min at a temperature of 121°C and a pressure of 2.0 bar.

Terrific Broth (TB) medium: For 1 L of TB medium 20 g tryptone, 24 g yeast extract and 4 mL glycerol were dissolved to a volume of 900 mL with water. The media was sterilised by steam autoclaving for at least 15 min at a temperature of 121 °C and a pressure of 2.0 bar. Prior to use 100 mL of sterile potassium phosphate buffer (0.17 mM KH₂PO₄/0.73 mM K₂HPO₄) were added to the medium.

Super Optimal Broth (SOB) medium: For 1 L of SOB medium 20 g tryptone, 5 g yeast extract, 0.5 g NaCl and 0.19 g KCl were dissolved to a volume of 1 L with water. The pH was adjusted to 7.0 with 5 M NaOH solution and the media was sterilised by steam autoclaving for at least 15 min at a temperature of 121 °C and a pressure of 2.0 bar. Prior to use 5 mL of sterile 2 M MgCl₂ were added to the medium.

Super Optimal broth with Catabolite repression (SOC) medium: For 1 L of SOC medium 20 mL of a sterile 20 % (w/v) D-glucose solution was added to 1 L of SOB medium.

LB agar plates: For 1 L of LB agar medium 10 g tryptone, 10 g yeast extract, 5 g NaCl and 15 g agar powder were mixed to a volume of 1 L with water. The suspension was sterilised by steam autoclaving for at least 15 min at a temperature of 121 °C and a pressure of 2.0 bar and cooled to approximately 50 °C. Under sterile conditions, the appropriate amount of antibiotic was added to the solution and the media was poured into sterile petri dishes to an approximate thickness of 5 mm. The plates were left to set at room temperature and stored at 4 °C for a maximum of three weeks.

Antibiotic Stocks: Antibiotic stocks for growth media and LB agar plates were prepared as 1000-fold stocks. These were prepared by dissolving the appropriate amount of antibiotic in water (or EtOH for Chl), filter sterilised and stored at -20 °C.

2.10 Competent Cell Method

Competent cells were prepared based on a method by ZHOU *et al.*¹⁵² 100 mL of LB growth medium were inoculated with 0.5 mL of an overnight culture (5 mL LB, 180 rpm, 16 h, 37 °C) and grown to an OD₆₀₀ between 0.3 and 0.6. Cultures were transferred to sterile 50 mL centrifuge tubes and centrifuged for 15 min at 4 °C (4000 rpm, 5500g). The supernatant was decanted, and the residual cell pellets were resuspended in a total of 100 mL of sterile transformation buffer (MOPS

10 mM pH = 6.8, CaCl₂ 25 mM, MgCl₂ 50 mM, MnCl₂ 25 mM) at 4 °C. After incubating on ice for 1 h, the cell suspension was centrifuged for 15 min at 4 °C (4000 rpm, 5500g) and the supernatant was discarded. Cell pellets were resuspended in a total of 1.5 mL of cold storage buffer (MOPS 10 mM pH = 6.8, CaCl₂ 25 mM, MgCl₂ 50 mM, MnCl₂ 25 mM, DMSO 7% (v/v)). Aliquots of 50 µL were flash frozen in liquid nitrogen and stored at –80 °C. Transformation efficiencies were tested using PUC18 and typically ranged from 10^{–6} to 10^{–9} cfu/µg.¹⁵³ Genotypes for the cell strains used are listed in table 4.

Table 4: Genotypes of *E. coli* strains

XL1-Blue	endA1 gyrA96(nal ^R) thi-1 recA1 relA1 lac glnV44 F' [::Tn10 proAB ⁺ lacI ^q Δ(lacZ)M15] hsdR17(rK [–] mK ⁺)
DH5α	F [–] endA1 glnV44 thi-1 recA1 relA1 gyrA96 deoR nupG purB20 φ80dlacZΔM15 Δ(lacZYA-argF)U169, hsdR17(rK [–] mK ⁺), λ [–]
BL21 DE3	F [–] ompT hsdS _B (r _B [–] m _B [–]) gal dcm (DE3)
BL21(DE3) AI	F [–] ompT hsdS _B (r _B [–] m _B [–]) gal dcm araB::T7RNAP-tetA
Top10	F [–] mcrA Δ(mrr-hsdRMS-mcrBC) φ80lacZΔM15 Δ lacX74 recA1 araD139 Δ(araleu)7697 galU galK rpsL (Str ^R) endA1 nupG
Rosetta(DE3) pLysS	F [–] ompT hsdS _B (r _B [–] m _B [–]) gal dcm pRARE2 (Cam ^R)
C41(DE3)	F [–] ompT hsdSB (r _B [–] m _B [–]) gal dcm (DE3)

2.11 Heat-shock Transformation

40–100 ng of plasmid were added to an aliquot of competent *E. coli* cells, followed by incubation on ice for 5 min. The cells were subject to heat-shock in a water bath at 42 °C for 45 s, then immediately returned to ice for 2 min. 600 µL of either LB or SOC medium were added to the heat-shocked *E. coli*, then incubated at 37 °C for 45 min. 200 µL of the *E. coli* culture were then spread on LB agar plates (Ø = 9 cm) containing the corresponding antibiotic for selection and incubated at 37 °C overnight (16–20 h).

2.12 Thin Layer Chromatography (TLC)

For TLC, MERCK 60 F₂₅₄ silica gel aluminium TLC plates were used. Detection was achieved by following the fluorescence quenching at $\lambda = 254$ nm or by staining with ninhydrin solution (*n*-BuOH 100 mL, AcOH 4 mL, ninhydrin 350 mg) and subsequent heating of the TLC plate.

2.13 Cloning

Custom oligonucleotides were purchased from MERCK SIGMA ALDRICH. Buffers, nucleotide triphosphate, and PrimeSTAR HS DNA polymerase were purchased from TAKARA. All restriction enzymes were purchased from THERMOFISHER SCIENTIFIC. NEBuilder HiFi DNA assembly master mix was purchased from NEW ENGLAND BIOLABS. All commercial gene sequences were optimised for gene expression in *E. coli*.

2.14 Primers

	Nucleotide sequence
primer_Y32to32F_f	5'-tgtggacgaattgaccggcac
primer_Y32to32F_r	5'-ggtaaaattcgccacaaaatgg
primer_Y64to64F_f	5'-caggaggagtttagcgcgcatgc
primer_Y64to64F_r	5'-catggcgctaaactccctcgttgg
primer_wttotag_f	5'-gttcccagagggttagtgccacagtg
primer_wttotag_r	5'-caccgttggacacctacactccggaaac
primer_removeGST_f	5'-cattccatggctgccattcgaaaaagcttgtga
primer_removeGST_r	5'-ccccaaatcgagccatggtaattccctcc
primer_husp2-cc_f	5'-cctctagaataattgttaactttaagaaggagataccatgg
primer_husp2-cc_r	5'-ggctgctaacaagccccaaagg
primer_pbad-rho_a_f	5'-ctaacaggaggaattaccatgtctccgattttggatattg
primer_pbad-rho_a_r	5'-gtaccagctgcagatctcgagttaatggtagatgtg
primer_pET28_f	5'-taaggatccgaattcgagctccgtcgac
primer_pET28_r	5'-gcccatggtatatctccctttaaagttaaacaaaattttctagagg

	ggaattgttatccgc
primer_rhoa_f	5'-gctgccattcgaaaaag
primer_rhoa_r	5'-agctcgaattcgatccttataagaccaggcaaccactc
primer_tf-tagtowt_f	5'-gttcccggaaagtgtatgtcccaacg
primer_tf-tagtowt_r	5'-cgttggacatacactccggaaac

2.15 Plasmids

pGEX_RasGAP334(714–1047) and ptac_HRas(1–166) were kindly provided by the WITTINGHOFER lab.¹⁵⁴ ptac_HRas(1–166)-Y32F and ptac_HRas(1–166)-Y64F were generated by SDM from ptac_HRas(1–166) using PrimeStarMax with primer_Y32to32F_f, primer_Y32to32F_r, primer_Y64to64F_f and primer_Y64to64F_r. hSOS1(564–1049) was purchased in a PUC19 vector,¹⁵³ digested with BamHI and Xhol, and ligated into a pET28a vector to generate pET28a-hSOS1(564–1049).¹⁵⁵ pET28_cSrc(251–533) and pCDFDUET_YoPH were present in the lab.

pBAD-sfGFP-N150TAG was kindly provided by the TSAI lab.¹⁵⁶ Plasmids pGEX-2T-RhoGAP-R85A and pGEX-2T-RhoA were already present in the lab.¹⁵⁷ The *rhoa* gene used in this work, carries a point mutation to improve protein stability (F25N).¹⁵⁸ The *rhoa* gene was amplified using primer_pbad-rhoa_f and primer_pbad-rhoa_r and subsequent Gibson Assembly yielded pBAD-GST-RhoA-His10 using the vector backbone from pBAD-sfGFP-N150TAG, which had been extracted using Ncol and Xhol digest. pBAD-GST-RhoA-His10-Y34TAG was generated by SDM from pBAD-GST-RhoA-His10 using PrimeStarMax with primer_wttotag_f and primer_wttotag_r. pGEX-2T-RhoA-Y34TAG was generated by SDM from pGEX-2T-RhoA using PrimeStarMax with primer_wttotag_f and primer_wttotag_r. A *rhoa* containing fragment was amplified from pBAD-GST-RhoA-His10 using primer_removeGST_f and primer_removeGST_r and was then ligated with the pBAD vector backbone to yield pBAD-RhoA-His6. pBAD-RhoA-His6-Y34TAG was generated by SDM from pBAD-RhoA-His6 using PrimeStarMax with primer_wttotag_f and primer_wttotag_r. pET32-GST-RhoA-His10-Y34TAG was created from a commercial pET32 vector and pBAD-GST-RhoA-His10-Y34TAG created by restriction digest using NdeI and Xhol. pET32-GST-RhoA-His10 was generated by SDM from pET32-GST-RhoA-His10-Y34TAG using PrimeStarMax with primer_tf-tagtowt_f and primer_tf-tagtowt_r. The gene fragment

for Usp2-cc was purchased from THERMO FISHER SCIENTIFIC (see 5.2.1) and amplified using PrimeSTAR Max DNA Polymerase with primer_HUsp2-cc_f and primerHUSp2-cc_r. The PCR product was then assembled into a pET15b vector backbone using Gibson Assembly to yield pET15b-Usp2-cc.¹⁵⁹ The gene fragment containing trigger factor (TF) and ubiquitin (Ub) was purchased from THERMO FISHER SCIENTIFIC (see 5.2.4). The vector backbone was amplified from pET28-cSrc using PrimeSTAR Max DNA Polymerase with primer_pET28_f and primer_pET28_r. The RhoA gene fragment was amplified from pET32-GST-RhoA-His10-Y34TAG using PrimeSTAR Max DNA Polymerase with primer_rhoa_f and primer_rhoa_r. The three gene fragments were assembled using Gibson Assembly to yield pET28a-TF-RhoA-Y34TAG. pET28a-TF-RhoA was generated by SDM from pET28a-TF-RhoA-Y34TAG using PrimestarMax with primer_tf-tagtowt_f and primer_tf-tagtowt_r. pEVOL-F3Y-RS-E3 was kindly provided by the STUBBE lab.¹⁶⁰

2.16 Activity Assay of Tyrosine Phenol Lyase (TPL)

Enzyme activity during purification was measured routinely with an assay based on the cleavage of SOPC (Fig.16). For the assay a 1.0 mL cuvette with 0.6 mM SOPC buffered with 50 mM potassium phosphate at pH = 8.0 was incubated with a known amount of TPL at 25°C, while following the decrease in absorbance at $\lambda = 370$ nm ($\Delta\epsilon = -1860 \text{ M}^{-1} \text{ cm}^{-1}$).¹⁶¹ A unit of enzyme activity was defined as the amount of TPL precipitate producing 1 μmol of pyruvate per minute.

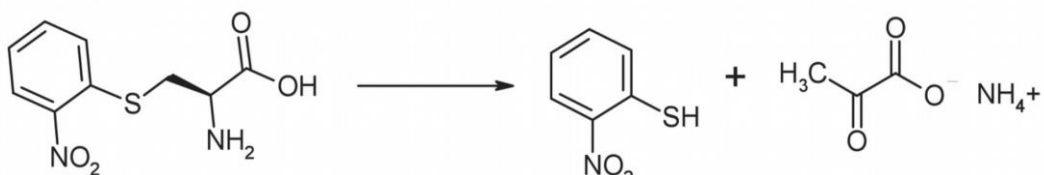


Figure 16: TPL-catalysed cleavage of SOPC.

2.17 Fluorotyrosine Synthesis: General Procedure

Ammonium acetate (15.4 g, 200 mmol, 10 eq), sodium pyruvate (11.0 g, 100 mmol, 5 eq), 2-ME (350 μL , 5.0 mmol, 0.25 eq) and the appropriate fluorophenol (5.0 mmol, 0.25 eq) were dissolved into 900 mL of deionised water. After adjusting to pH = 8.2 with 2.0 M ammonium hydroxide solution the volume was filled to 1.0 L

with deionised water. PLP (13 mg, 50 µmol, 0.25 mol%) and TPL (30 units) were added, and the reaction was stirred at room temperature in the dark. After two days more fluorophenol (5.0 mmol, 0.25 eq) was added and the pH adjusted if necessary. After an additional two days fluorophenol (5.0 mmol, 0.25 eq) and TPL (30 units) were added, and the pH was adjusted if necessary. After an additional two days fluorophenol (5.0 mmol, 0.25 eq) was added and the pH was adjusted if necessary. The reaction progress was regularly monitored via TLC or ^{19}F -NMR. After completion of the reaction the solution was adjusted to pH = 2 with 6 M hydrochloric acid. The resulting precipitation was filtered over celite, and the filtrate was extracted with 500 mL EtOAc. The aqueous layer was degassed and loaded on a 200 mL (3 cm × 60 cm) AG50W-X8 (50–100 mesh) cation-exchange resin in the protonated state. After washing the column with 10 volumes of deionised water the product was eluted with a 5 M ammonium hydroxide solution. The eluted fractions were analysed using TLC and a ninhydrin staining solution. The fluorotyrosine containing fractions were combined and evaporated to dryness under reduced pressure. After recrystallisation from EtOH/water the product was isolated as a white powder.

2.17.1 2-Fluorotyrosine (F^2Y)

Isolated as white solid in 86% yield.¹⁶²

TLC R_f = 0.4 (*n*-BuOH/AcOH/H₂O 3:1:1).

$^1\text{H-NMR}$ (600 MHz, D₂O): δ = 7.19 (dd, $^4J_{\text{HF}}$ = 8.4 Hz, $^3J_{\text{HF}}$ = 9.1 Hz, 1H), 6.74–6.69 (m, 2H), 3.96 (dd, 3J = 5.3 Hz, 3J = 7.6 Hz, 1H), 3.28 (dd, 3J = 5.3 Hz, 2J = 14.8 Hz, 1H), 3.07 (dd, 3J = 7.9 Hz, 2J = 14.8 Hz, 1H) ppm.

HR-MS (ESI) for C₉H₁₁NO₃F⁺ [M+H⁺]: calc.: 200.0723, found: 200.0722.

2.17.2 3-Fluorotyrosine (F^3Y)

Isolated as white solid in 82% yield.¹⁶²

TLC R_f = 0.4 (*n*-BuOH/AcOH/H₂O 3:1:1).

$^1\text{H-NMR}$ (500 MHz, D₂O): δ = 7.00 (d, 3J = 11.9 Hz, 1H), 6.94–6.86 (m, 2H), 3.86 (dd, 3J = 5.3 Hz, 3J = 7.6 Hz, 1H), 3.11 (dd, 3J = 5.1 Hz, 2J = 14.7 Hz, 1H), 2.97 (dd, 3J = 7.8 Hz, 2J = 14.7 Hz, 1H) ppm.

HR-MS (ESI) for C₉H₁₁NO₃F⁺ [M+H⁺]: calc.: 200.0723, found: 200.0723.

2.17.3 2,5-Difluorotyrosine (F²⁵Y)

Isolated as white solid in 77% yield.¹⁶²

TLC R_f = 0.4 (n-BuOH/AcOH/H₂O 3:1:1).

¹H-NMR (500 MHz, D₂O): δ = 7.00 (dd, ⁴J_{HF} = 7.9 Hz, ³J_{HF} = 10.0 Hz, 1H), 6.82 (dd, ⁴J_{HF} = 8.6 Hz, ³J_{HF} = 9.1 Hz, 1H), 3.94 (t, ³J = 6.1 Hz, 1H), 3.24 (dd, ³J = 5.1 Hz, ²J = 14.7 Hz, 1H), 3.04 (dd, ³J = 7.8 Hz, ²J = 14.6 Hz, 1H) ppm.

HR-MS (ESI) for C₉H₁₀NO₃F₂⁺ [M+H⁺]: calc.: 218.0629, found: 218.0631.

2.17.4 3,5-Difluorotyrosine (F³⁵Y)

Isolated as white solid in 92% yield.¹⁶²

TLC R_f = 0.4 (n-BuOH/AcOH/H₂O 3:1:1).

¹H-NMR (500 MHz, D₂O): δ = 6.84 (d, ³J_{HF} = 7.9 Hz, 2H), 3.86 (dd, ³J = 5.5 Hz, ³J = 7.4 Hz, 1H), 3.10 (dd, ³J = 5.2 Hz, ²J = 14.7 Hz, 1H), 2.96 (dd, ³J = 7.8 Hz, ²J = 14.7 Hz, 1H) ppm.

HR-MS (ESI) for C₉H₁₀NO₃F₂⁺ [M+H⁺]: calc.: 218.0629, found: 218.0626.

2.17.5 2,6-Difluorotyrosine (F²⁶Y)

Isolated as white solid in 45% yield.¹⁶³

TLC R_f = 0.4 (n-BuOH/AcOH/H₂O 3:1:1).

¹H-NMR (400 MHz, D₂O): δ = 6.52 (d, ³J_{HF} = 8.9 Hz, 2H), 3.88 (t, ³J = 6.4 Hz, 1H), 3.20 (dd, ³J = 5.2 Hz, ²J = 14.8 Hz, 1H), 3.09 (dd, ³J = 7.5 Hz, ²J = 14.8 Hz, 1H) ppm.

HR-MS (ESI) for C₉H₁₀NO₃F₂⁺ [M+H⁺]: calc.: 218.0629, found: 218.0628.

2.17.6 2,3,5-Trifluorotyrosine (F²³⁵Y)

Isolated as white solid in 71% yield.¹⁶²

TLC R_f = (*n*-BuOH/AcOH/H₂O 3:1:1).

¹H-NMR (400 MHz, D₂O): δ = 6.70 (ddd, ⁵J_{HF} = 2.2 Hz, ⁴J_{HF} = 7.1 Hz, ³J_{HF} = 11.3 Hz, 1H), 3.88 (dd, ³J = 4.9 Hz, ³J = 8.2 Hz, 1H), 3.21 (dd, ³J = 4.6 Hz, ²J = 14.9 Hz, 1H), 2.95 (dd, ³J = 8.2 Hz, ²J = 14.8 Hz, 1H) ppm.

HR-MS(ESI) for C₉H₉NO₃F₃⁺ [M+H⁺]: calc.: 236.0535, found: 236.0535.

2.18 Synthesis 2,3,5,6-Tetrafluorotyrosine (F²³⁵⁶Y)

Ammonium acetate (15.4 g, 200 mmol, 10 eq), sodium pyruvate (11.0 g, 100 mmol, 5.0 eq), 2-ME (350 μ L, 5.0 mmol, 0.25 eq) and 2,3,5,6-tetrafluorophenol (0.83 g, 5.0 mmol, 0.25 eq) were dissolved in 900 mL of deionised water. After adjusting the pH to 8.2 with 2 M ammonium hydroxide solution the volume was filled to 1.0 L with deionised water. PLP (13 mg, 50 μ mol, 0.25 mol%) and TPL (30 units) were added, and the reaction was stirred at room temperature in the dark. After one week more 2,3,5,6-tetrafluorophenol (5.0 mmol, 0.25 eq) and TPL (30 units) was added and the pH was adjusted if necessary. After an additional week further 2,3,5,6-tetrafluorophenol (0.83 g, 5.0 mmol, 0.25 eq) and TPL (30 units) were added, and the pH was adjusted if necessary. After an additional two days fluorophenol (0.83 g, 5.0 mmol, 0.25 eq) was added and the pH adjusted if necessary. The reaction progress was regularly monitored via TLC or ¹⁹F-NMR. After completion of the reaction the solution was adjusted to pH = 2 with 6 M hydrochloric acid. The resulting precipitation was filtered over celite, and the filtrate was extracted with 500 mL EtOAc. The aqueous layer was degassed and loaded on a 200 mL (3 cm \times 60 cm) AG50W-X8 (50–100 mesh) cation-exchange resin in the protonated state. After washing the column with 10 volumes of deionised water the product was eluted with a 5 M ammonium hydroxide solution. The fluorotyrosine containing fractions were combined and evaporated to dryness under reduced pressure. After recrystallisation from EtOH/water the product was isolated as a white powder in 64% yield.¹⁶²

TLC R_f = 0.3 (*n*-BuOH/AcOH/H₂O 3:1:1).

¹H-NMR (500 MHz, D₂O): δ = 3.91 (t, ³J = 6.9 Hz, 1H), 3.28 (dd, ³J = 6.4 Hz, ²J = 14.9 Hz, 1H), 3.18 (dd, ³J = 7.4 Hz, ²J = 14.8 Hz, 1H) ppm.

HR-MS(ESI) for C₉H₈NO₃F₄⁺ [M+H⁺]: calc.: 254.0440, found: 254.0443.

2.19 Recombinant Protein Production

2.19.1 cSrc(251–533)

E. coli BL21(DE3) cells were transformed with pET28_cSrc and pCDFDuet_YoPH,¹⁶⁴ plated onto LB agar plates (50 µg/mL Kan and 50 µg/mL Str) and grown overnight at 37 °C. A single colony was used to inoculate 30 mL of LB media (50 µg/mL Kan and 50 µg/mL Str) and the culture was shaken at 180 rpm at 37 °C overnight. This culture was used to inoculate TB medium (50 µg/mL Kan and 50 µg/mL Str) at a 1:100 ratio. The culture was grown at 37 °C to an OD_{600nm} between 1.0 and 1.2 and expression was induced with 0.2 mM IPTG. The culture was incubated at 18 °C for 16 h and cells were harvested by centrifugation (7000g, 4°C, 20 min). The cell pellet was either processed directly after centrifugation or stored at –80°C. The cell pellet was resuspended in buffer A (Tris-HCl 50 mM, pH = 8.0, NaCl 500 mM, imidazole 25 mM, glycerol 5% (v/v)) and supplemented with 1 mM PMSF. The cells were lysed by sonication (4 min sonication time, pulsed 2 s on and 8 s off) and the cell debris was removed by centrifugation (40 min, 32000g, 4 °C). The supernatant was filtered and loaded on a Ni²⁺-NTA column (GE 5 mL FF HisTrap). After washing with 5 CV buffer A, the target protein was eluted by applying a gradient of 0–50% buffer B (Tris-HCl 50 mM, pH = 8.0, NaCl 500 mM, imidazole 500 mM, glycerol 5% (v/v)) over 30 CV. The eluted protein fractions were pooled, concentrated, and dialysed at 4°C overnight against 20 volumes of buffer C (Tris-HCl 20 mM, pH 8.0, 100 mM, DTT 1 mM, glycerol 5% (v/v)). The crude kinase was then loaded on a Q column (CYTIVA HiTrap FF 5 mL) equilibrated with buffer C. The target protein was then eluted by applying a gradient of 0–40% buffer D (Tris-HCl 20 mM, pH = 8.0, NaCl 1.0 M, DTT 1 mM, glycerol 5% (v/v)). Fraction containing the kinase were then pooled and concentrated to <1 mL and further purified on a SEC75 16/60 column (retention time t_R = 60 mL). Kinase fractions were concentrated to 0.25 mM and stored at –80°C.

2.19.2 RasGAP(714–1047)

E. coli BL21(DE3) cells were transformed with pGEX-2T_RasGAP(714–1047) plated onto LB agar plates (50 µg/mL Amp) and grown overnight at 37 °C. A single colony was used to inoculate 30 mL of LB media (50 µg/mL Amp) and the culture was shaken at 180 rpm at 37 °C overnight. This culture was used to inoculate LB media (Amp 50 µg/mL) at a 1:100 ratio. The culture was grown at 37 °C to an OD_{600nm} between 0.6 and 0.8 and expression was induced with 1.0 mM IPTG. The culture was incubated at 18 °C for 16 h and cells were harvested by centrifugation (7000g, 4 °C, 20 min). The cell pellet was either stored at –80°C or processed directly after centrifugation. The cell pellet was resuspended in buffer A (Tris-HCl 50 mM, pH = 7.6, NaCl 150 mM, MgCl₂ 5 mM, DTT 1 mM) and supplemented with 1 mM PMSF. The cells were lysed by sonication (4 min sonication time, pulsed 2 s on and 8 s off) and the cell debris was removed by centrifugation (40 min, 32000g, 4 °C). The supernatant was filtered and loaded on a GST column (CV = 25 mL). The beads were incubated on a tube roller at 4 °C for 60 min and washed with 5 CV buffer A. The target protein was eluted over 3 CV with buffer B (Tris-HCl 50 mM, pH = 7.6, NaCl 150 mM, MgCl₂ 5 mM, DTT 1 mM, glutathione 10 mM) and buffer exchanged into buffer A. To cleave the GST-tag the protein solution was incubated at 4 °C with 25 NIH units thrombin. Progress of the cleavage reaction was controlled via SDS-PAGE and further thrombin was added as required. Upon completion of the cleavage reaction, the protein solution was incubated with GST resin (CV = 25 mL) at 4 °C. After 60 min the flow-through was collected and concentrated to 4 mL. Finally, the target protein was purified on a SEC75 26/60 column (retention time t_R = 160 mL), concentrated to 0.5–1.0 mM and stored at –80°C.

2.19.3 HRas(1–166)

E. coli BL21(DE3) cells were transformed with ptac_HRas(1–166)¹⁵⁴ plated onto LB agar plates (100 µg/mL Amp) and grown overnight at 37 °C. A single colony was used to inoculate 30 mL of LB media (100 µg/mL Amp) and shaken at 180 rpm at 37 °C overnight. This culture was used to inoculate LB medium (100 µg/mL Amp) at a 1:100 ratio. The culture was grown at 37 °C to an OD_{600nm} between 0.6 and 0.8 and expression was induced with 1.0 mM IPTG. The culture was incubated at 25 °C for 18 h and cells were harvested by centrifugation (7000g, 4 °C, 20 min). The cell pellet was either stored at –80°C or processed directly after centrifugation. The cell

pellet was resuspended in buffer A (Tris-HCl 25 mM, pH = 7.6, MgCl₂ 5 mM, DTT 1 mM) and supplemented with 1 mM PMSF. The cells were lysed by sonication (4 min sonication time, pulsed 2 s on and 8 s off) and the cell debris was removed by centrifugation (40 min, 32000g, 4 °C). The supernatant was filtered and loaded on a DEAE column (CV = 45 mL), washed with 3 CV buffer A, and eluted by applying a gradient of 0–100% buffer B (Tris-HCl 25 mM, pH = 7.6, NaCl 200 mM, MgCl₂ 5 mM, DTT 1 mM) over 8 CV. The eluted protein fractions were pooled and concentrated to 4 mL. Finally, the target protein was purified on a SEC75 26/60 column (retention time t_R = 190 mL), concentrated to 1.0 mM, and stored at –80°C. The same procedure was used for HRas(1–166)^{Y32F} and HRas(1–166)^{Y64F}.

2.19.4 hSOS1(564–1049)

E. coli BL21(DE3) cells were transformed with pET28_hSOS1(564–1049),¹⁵⁵ plated onto LB agar plates (50 µg/mL Kan) and grown overnight at 37 °C. A single colony was used to inoculate 30 mL of LB media (50 µg/mL Kan) and shaken at 180 rpm at 37 °C overnight. This culture was used to inoculate LB medium (50 µg/mL Kan) at a 1:100 ratio. The culture was grown at 37 °C to an OD_{600nm} between 0.6 and 0.8 and expression was induced with 0.5 mM IPTG. The culture was incubated at 30 °C for 16 h and cells were harvested by centrifugation (7000g, 4 °C, 20 min). The cell pellet was either stored at –80°C or processed directly after centrifugation. The cell pellet was resuspended in buffer A (Tris-HCl 25 mM, pH = 7.5, NaCl 200 mM, imidazole 25 mM, 2-ME 2 mM) and supplemented with 1 mM PMSF. The cells were lysed by sonication (4 min sonication time, pulsed 2 s on and 8 s off) and the cell debris was removed by centrifugation (40 min, 32000g, 4 °C). The supernatant was filtered and loaded on a Ni²⁺-NTA column (GE 5 mL FF HisTrap). After washing with 5 CV buffer A, the target protein was eluted by applying a gradient of 0–100% buffer B (Tris-HCl 25 mM, pH = 7.5, NaCl 200 mM, imidazole 300 mM, 2-ME 2 mM) over 15 CV. The eluted protein fractions were pooled and concentrated to 4 mL. The target protein was further purified on a SEC75 26/60 column (retention time t_R = 160 mL), concentrated to 0.5–1.0 mM and stored at –80°C.

2.19.5 RhoGAP(198–439)^{R85A}

E. coli Rosetta(DE3) pLysS cells were transformed with pGEX-2T_RhoGAP-R85A¹⁵⁷, plated onto LB agar plates (35 µg/mL Chl and 100 µg/mL Amp) and grown overnight at 37 °C. A single colony was used to inoculate 30 mL of LB medium (35 µg/mL Chl and 100 µg/mL Amp) and shaken at 180 rpm at 37 °C overnight. This culture was used to inoculate 1 L LB medium (35 µg/mL Chl and 100 µg/mL Amp) at a 1:100 ratio. The culture was grown at 37 °C to an OD_{600nm} between 0.6 and 0.8 and expression was induced with 1.0 mM IPTG. The culture was incubated at 30 °C for 6 h and cells were harvested by centrifugation (7000g, 4 °C, 20 min). The cell pellet was either processed directly after centrifugation or stored at –80°C. The cell pellet was resuspended in buffer A (Tris·HCl 50 mM, pH = 7.6, NaCl 150 mM, MgCl₂ 5 mM, DTT 1 mM) supplemented with 1 mM PMSF. The cells were lysed by sonication (4 min sonication time, pulsed 2 s on and 8 s off) and the cell debris was removed by centrifugation (40 min, 32000g, 4 °C). The supernatant was filtered and loaded on a GST column (CV = 25 mL). The beads were incubated on a tube roller at 4 °C for 60 min and washed with 5 CV buffer B (Tris·HCl 50 mM pH = 8.0, NaCl 150 mM, MgCl₂ 5 mM, DTT 1 mM). 50 NIH units thrombin were added to the column and the beads were incubated on a tube roller at 4 °C overnight. The flow-through containing the crude RhoGAP^{R85A} was collected and further purified on a 26/60 S75 size exclusion column (Tris·HCl 50 mM, pH = 8.0, NaCl 150 mM, MgCl₂ 5 mM, DTT 1 mM, retention time t_R = 160 mL). The protein was concentrated to 0.6–0.9 mM and stored at –80°C.

2.19.6 Usp2-cc

E. coli BL21(DE3) cells were transformed with pET15b-Usp2-cc,¹⁵⁹ plated onto LB agar plates (100 µg/mL Amp) and grown overnight at 37 °C. A single colony was used to inoculate 30 mL of LB media (100 µg/mL Amp) and the culture was shaken at 180 rpm at 37 °C overnight. This culture was used to inoculate LB medium (100 µg/mL Amp) at a 1:100 ratio. The culture was grown at 37 °C to an OD_{600nm} between 0.6 and 0.8 and expression was induced with 0.5 mM IPTG. The culture was incubated at 37 °C for 5 h and cells were harvested by centrifugation (7000g, 4 °C, 20 min). The cell pellet was either stored at –80°C or processed directly after centrifugation. The cell pellet was resuspended in buffer A (NaH₂PO₄/Na₂PO₄ 50 mM pH = 7.4, NaCl 300 mM, imidazole 12 mM, 2-ME 20 mM, glycerol 30% (v/v))

and supplemented with 1 mM PMSF. The cells were lysed by sonication (4 min sonication time, pulsed 2 s on and 8 s off) and the cell debris was removed by centrifugation (40 min, 32000g, 4 °C). The supernatant was filtered and loaded on a Ni²⁺-NTA column (GE 5 mL FF HisTrap). After washing with 5 CV buffer A, the target protein was eluted by applying a gradient of 0–100% buffer B (NaH₂PO₄/Na₂PO₄ 50 mM pH = 7.4, NaCl 300 mM, imidazole 300 mM, 2-ME 20 mM, glycerol 30% (v/v)) over 25 CV. The deubiquitinase was buffer exchanged into buffer C (NaH₂PO₄/Na₂PO₄ 50 mM pH = 7.4, NaCl 200 mM, 2-ME 2 mM, glycerol 30% (v/v)), concentrated to 0.5 mM and stored at –80°C.

2.19.7 Tyrosine Phenol Lyase (TPL)

E. coli BL21(DE3) cells were transformed with pTZTPL, plated onto LB agar plates (100 µg/mL Amp) and grown overnight at 37 °C. A single colony was used to inoculate 30 mL of LB media (100 µg/mL Amp) and the culture was shaken at 180 rpm at 37 °C overnight. This culture was used to inoculate LB medium (100 µg/mL Amp) at a 1:1000 ratio. The large-scale culture was incubated at 37 °C for 20 h, after which the cells were harvested by centrifugation (7000g, 4°C, 20 min). The cell pellet was either stored at –80°C or processed directly after centrifugation. The cells were resuspended in buffer A (KH₂PO₄/K₂HPO₄ 100 mM, pH = 7.0, PLP 0.1 mM, EDTA 1 mM, 2-ME 5 mM) and lysed by sonication (4 min sonication time, pulsed 2 s on and 8 s off). Cell debris was removed by centrifugation (40 min, 32000g, 4 °C) and the supernatant was brought to 60% saturation of (NH₄)₂SO₄. The resulting precipitate was collected by centrifugation (30 min, 25000g, 4°C) and stored at 4 °C for up to 5 days. TPL activity was measured by following the absorbance decrease at 370 nm of buffer B (KH₂PO₄/K₂HPO₄ 50 mM, pH = 8.0, SOPC 0.6 mM) at 25°C upon enzyme addition.¹⁶¹

2.19.8 FY-RhoA

E. coli BL21(DE3) AI cells were transformed with pET28a-TF-RhoA-Y34TAG and pEVOL-F3Y-E3,¹⁶⁰ plated onto LB agar plates (50 µg/mL Kan and 35 µg/mL Chl) and grown overnight at 37 °C. A single colony was used to inoculate 30 mL of LB media (50 µg/mL Kan and 35 µg/mL Chl) and the culture was shaken at 180 rpm at 37 °C overnight. This culture was used to inoculate 1 L TB medium (35 µg/mL Chl

and 100 µg/mL Amp) at a 1:100 ratio. The culture was grown at 37 °C to an OD_{600nm} between 0.6–0.8 and supplemented with 1–2 mM FY and 0.05% (w/v) L-arabinose. The culture was grown further at 37 °C to an OD_{600nm} between 1.0–1.2 and expression was induced with 1.0 mM IPTG. The culture was further incubated at 25 °C for 16–18 h and cells were harvested by centrifugation (7000g, 4 °C, 20 min). The cell pellet was either stored at –80 °C or processed directly after centrifugation. The cells were resuspended in buffer A (Tris-HCl 50 mM, pH = 8.0, NaCl 150 mM, imidazole 25 mM, MgCl₂ 5 mM, DTT 1 mM) and lysed by sonication (4 min sonication time, pulsed 2 s on and 8 s off). The supernatant was filtered and loaded on a Ni²⁺-NTA column (GE 5 mL FF HisTrap). After washing with 5 CV buffer A, the target protein was eluted by applying a gradient of 0–100% buffer B (Tris-HCl 50 mM, pH = 8.0, NaCl 150 mM, imidazole 300 mM, MgCl₂ 5 mM, DTT 1 mM) over 25 CV. The purified protein contained a mixture of full-length TF-FY-RhoA and RhoA-Tyr34-truncated protein. The ratio of the two species varied according to the TAG-suppression efficiency achieved with the respective FY. Fractions were pooled, buffer exchanged into buffer A and incubated at 4 °C overnight with Usp2-cc (~1:100). The protein solution was then filtered over a Ni²⁺-NTA column (GE 5 mL FF HisTrap) and further purified on a 26/60 S75 size exclusion column (Tris-HCl 50 mM, pH = 8.0, NaCl 150 mM, MgCl₂ 5 mM, DTT 1 mM, retention time t_R = 190 mL). The protein was concentrated to 0.6–1.0 mM and stored at –80 °C.

2.20 Screening Conditions for the Expression of RhoA-plasmid Constructs

Expression tests were performed on a 10 mL scale. Media was inoculated from a 5 mL LB overnight culture with the appropriate antibiotics and grown to OD₆₀₀ = 0.6 before induction. The pET32-GST-RhoA-TEV-His10 plasmid was induced with IPTG (0.01 mM, 0.1 mM, 1.0 mM) and 0.05% (w/v) L-arabinose. Four different strains were tested C41(DE3), BL21(DE3), BL21(DE3) Gold and BL21(DE3) Star. The pBAD plasmids were tested with Top10 cells in 2xYT media and induced with L-arabinose (0.00002%, 0.0002%, 0.002%, 0.02%, 0.2% (w/v)). For different temperatures, different incubations times were used (16 °C 24 h, 25 °C 16 h, 30 °C 6 h). The cells were lysed using the BugBuster reagent. ε-Boc-Lys, F³Y or F³⁵Y were added to the cell culture once the OD₆₀₀ had reached 0.3.

2.21 Optimisation of cSrc Phosphorylation

500 µM HRas was incubated for two hours at either 25 or 30 °C in a buffer containing Tris 25 mM pH = 7.6, NaCl 150 mM, MgCl₂ 5 mM, DTT 1 mM, ATP 2–4 mM, cSrc 10–20 µM. SDS-PAGE with subsequent densitometrical analysis showed the highest level of HRas phosphorylation for condition 6 (Tab.5).

Table 5: Screened conditions for the cSrc-mediated phosphorylation of HRas

	# 1	# 2	# 3	# 4	# 5	# 6	# 7	# 8
[ATP]	2 mM	2 mM	2 mM	2 mM	4 mM	4 mM	4 mM	4 mM
[cSrc]	10 µM							
T	25 °C	25 °C	30 °C	30 °C	25 °C	25 °C	30 °C	30 °C

2.22 Stability of cSrc-catalysed HRas phosphorylation

Stability of phospho-HRas was determined by incubating 100 µM monophosphorylated HRas in crystallisation buffer (HEPES-Na 20 mM pH = 8.0, MgCl₂ 10 mM, NaF 20 mM). In regular intervals 30 µL aliquots were taken and mixed with 4× SDS-PAGE buffer (Tab.3), heated to 100 °C for 3 min and stored at –80 °C until all timepoints could be analysed by SDS-PAGE.

2.23 RhoA Nucleotide Exchange

Due to the high affinity for guanine nucleotides, small G proteins are usually copurified with GDP in an equimolar ratio. To exchange the bound GDP for GTP or mantGTP, 0.5–1 mM of the RhoA variant was incubated with 10 mM EDTA and a 10-fold excess of GTP or mantGTP at 4 °C for 30–45 min. To remove unbound nucleotides the mixture was loaded on a PD-10 desalting column, which had been equilibrated with the target buffer at 4 °C. 200 µL fractions were taken and the absorbance at 260 nm and 280 nm of each fraction was measured. Protein fractions were combined and stored at –80 °C. GTP loadings as determined by HPLC were generally between 90–95%.

2.24 Protein X-ray Crystallography

Protein crystallisation conditions were setup either by hand or using a DOUGLAS INSTRUMENTS ORYX4 system in either a hanging drop or sitting drop configuration. Microseeding was performed based on literature conditions.¹⁶⁵

An initial hit for HRas/MgF₃⁻/RasGAP was obtained for 2.0 µL sitting drop conditions with a 1:1 ratio of buffered protein solution (HRas 400 µM, RasGAP 400 µM, Na·HEPES 20 mM pH = 8.0, NaF 20 mM) and precipitant solution (Na·HEPES 100 mM, pH = 8.0, PEG3350 20% (w/v), (NH₄)₂SO₄ 20 mM, Gd·HCl 100 mM, NaF 20 mM). After two rounds of microseeding, crystals were obtained for 5.0 µL hanging drop conditions with a 1:1.2 ratio of buffered HRas/RasGAP solution (HRas 400 µM, RasGAP 400 µM, Na·HEPES 20 mM pH = 8.0, NaF 20 mM) and precipitant solution (Na·HEPES 100 mM, pH = 8.0, PEG3350 22% (w/v), (NH₄)₂SO₄ 20 mM, Gd·HCl 100 mM, NaF 20 mM). Crystals were harvested using cryoprotectant (80% precipitant, 20% glycerol (v/v)) and sent for data collection.

Using a commercial crystal screen (HAMPTON RESEARCH, HR2-130) yielded a hit for monophosphorylated HRas under sitting drop conditions (drop size 0.6 µL) with a 1:1 ratio of buffered protein solution (phospho-HRas 400 µM, RasGAP 400 µM, Na·HEPES 20 mM pH = 8.0, NaF 20 mM) and precipitant (Na·Citrate 100 mM pH = 5.6, Li₂SO₄ 1.0 M, CaCl₂ 200 mM). After three rounds of microseeding well-formed single crystals were obtained using 2 µL sitting drops and a 1:1 ratio of buffered protein solution (phospho-HRas 400 µM, RasGAP 400 µM, Na·HEPES 20 mM pH = 8.0, NaF 20 mM) and precipitant (Na·Citrate 100 mM pH = 5.6, Li₂SO₄ 800 mM, CaCl₂ 200 mM). These were harvested using cryoprotectant (80% precipitant, 20% glycerol (v/v)) and sent for data collection.

Conditions yielding the RasGAP homodimer were based on an initial hit under sitting drop conditions (drop size 3.0 µL) using a 1:1.2 ratio of buffered protein solution (phospho-HRas 400 µM, RasGAP 400 µM, Na·HEPES 20 mM pH = 8.0, NaF 20 mM) to precipitant (HEPES 0.1 M, pH 8.0, (NH₄)₂SO₄ 20 mM, MgCl₂ 5 mM, NaF 20 mM, PEG3350 21% (w/v)). Two subsequent rounds of microseeding yielded crystals under sitting drop conditions (drop size 3.0 µL) with a 1:0.8 ratio of buffered protein solution (phospho-HRas 400 µM, RasGAP 400 µM, Na·HEPES 20 mM pH = 8.0, NaF 20 mM) to precipitant (Na·HEPES 0.1 M, pH 8.0, (NH₄)₂SO₄ 20 mM, NaF 20 mM, PEG3350 19% (w/v), Gd·HCl 100 mM). The crystals were harvested using cryoprotectant (80% precipitant, 20% glycerol (v/v)) and sent for data collection.

The non-FY-labelled RhoA/MgF₃⁻/RhoGAP^{R85A} complex was crystallised under sitting drop conditions (drop size 2.0 µL) using a 1:1 ratio of buffered protein solution (RhoA 700 µM, RhoGAP^{R85A} 700 µM, 0.1 M BisTris·HCl pH = 6.0, NaCl 150 mM, MgCl₂ 5 mM, NaF 10 mM, DTT 1 mM) to precipitant (BisTris·HCl, 100 mM pH = 6.0, 23–26% (w/v)). These crystals were used as seed stocks to produce hits for the FY-labelled complex.

Crystals for the F³⁵Y-RhoA/MgF₃⁻/RhoGAP^{R85A} complex were obtained after three rounds of seeding using an initial seed stock of non-FY-labelled crystals under hanging drop conditions (drop size 4 µL). A 1:1 ratio of buffered protein solution (RhoA 700 µM, RhoGAP^{R85A} 700 µM, BisTris·HCl pH = 6.0, NaCl 150 mM, MgCl₂ 5 mM, NaF 10 mM, DTT 1 mM) to precipitant (0.1 M BisTris·HCl pH = 5.8, PEG3350 25% (w/v)) was used. The crystals were harvested using cryoprotectant (75% precipitant, 25% PEG400 (w/v)) and sent for data collection.

For the F²³⁵Y-RhoA/MgF₃⁻/RhoGAP^{R85A} complex, crystals were obtained after four rounds of seeding using an initial seed stock of non-FY-labelled crystals under hanging drop conditions (drop size 5 µL). A 1.2:1 ratio of buffered protein solution (RhoA 700 µM, RhoGAP^{R85A} 700 µM, BisTris·HCl pH = 6.0, NaCl 150 mM, MgCl₂ 5 mM, NaF 10 mM, DTT 1 mM) to precipitant (0.1 M BisTris·HCl pH = 5.8, PEG3350 26% (w/v)) was used. The crystals were harvested using cryoprotectant (75% precipitant, 25% PEG400 (w/v)) and sent for data collection.

Diffraction datasets were collected at Diamond Light Source (Oxfordshire, UK) on beamlines I-04 or I-03. Crystals were kept at 100 K in a cold nitrogen stream during data collection. Wavelengths used are listed in the respective crystal structure parameter tables. Data collection was either performed through remote access or by automated data collection.

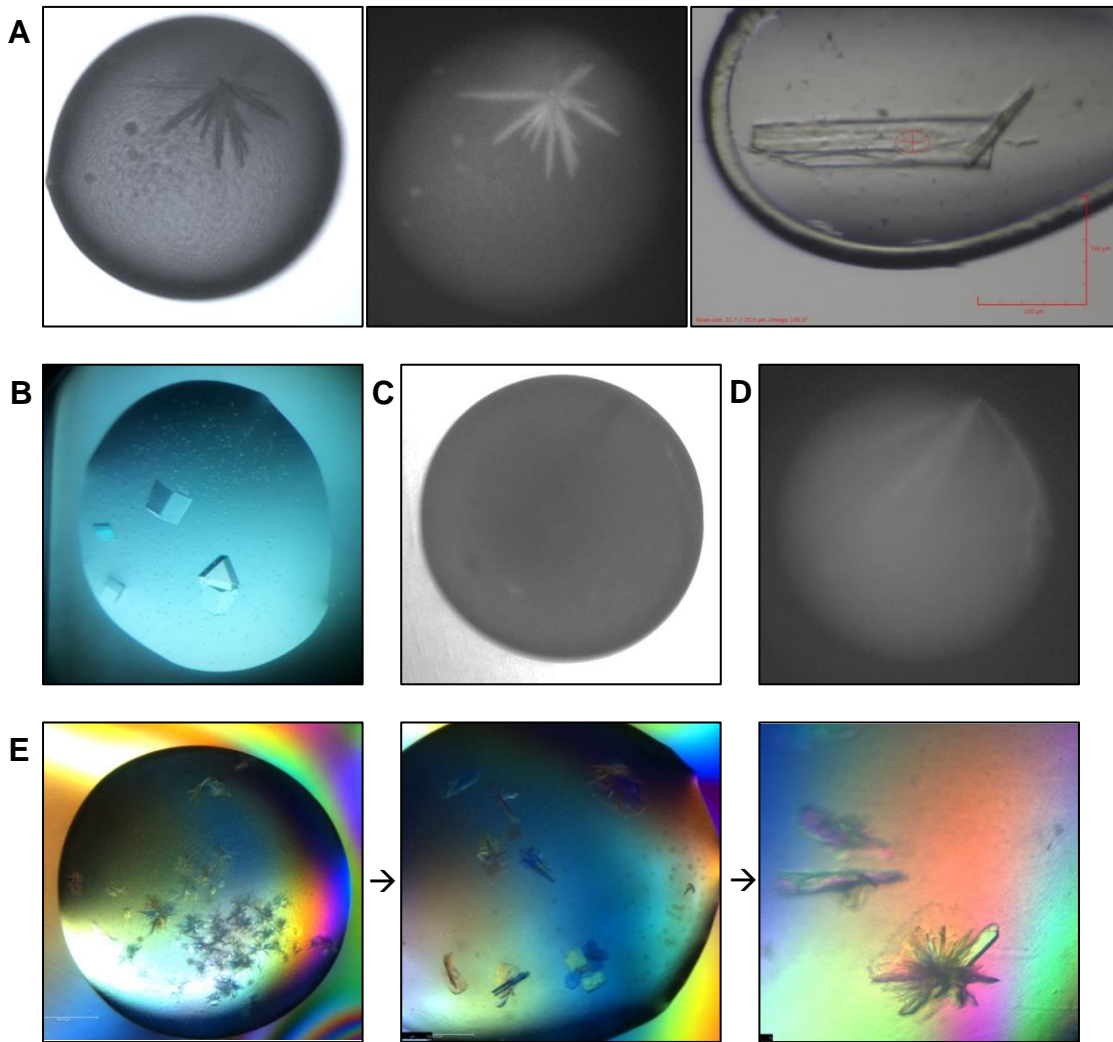


Figure 17: Protein crystal images (A) HRas/MgF₃⁻/RasGAP crystals (left) visible light image (middle) UV light image (right) protein crystal during data acquisition (B) phospho-HRas crystals (C) visible light image of RasGAP dimer crystals (D) UV light image of RasGAP dimer crystal, the relatively faint intensity is due to the fact that RasGAP has relatively few Trp and Tyr residues. (E) Three iterations of microseeding conditions for the F²³⁵Y-RhoA/MgF₃⁻/RhoGAP^{R85A} complex to improve crystal morphology.

Diffraction data for the HRas/MgF₃⁻/RasGAP complex were processed using the STARANISO web server, where an anisotropic cut-off of merged intensity data is performed, to obtain an Bayesian estimation of structure amplitudes.¹⁶⁶ General data analysis and processing was performed using CCP4.¹⁶⁷ Molecular replacement was performed using MOLREP with either HRas/RasGAP (PDB: 1WQ1) or RhoA/RhoGAP^{R85A} (PDB: 5M6X) as a search model.¹⁶⁸ Model building and structural refinements was achieved through alternate cycles of Coot and REFMAC5.¹⁶⁹ Structural models for fluorotyrosine residues were built using JLigand.¹⁷⁰

2.25 ^{19}F -NMR Signal Assignment

^{19}F -NMR signals of fluorinated aromatic compounds were assigned, based on predictions from statistical substituent chemical shift (SSCS) calculations. The chemical shift was calculated using Eq.3 with Z values from the literature.¹⁷¹

$$\delta_{\text{F}} \text{ (ppm)} = -113.9 + \sum Z_i \quad (3)$$

The predicted and measured chemical shifts are tabulated in Tab.15 in section 5.5.

2.26 $\text{p}K_{\text{a}}$ Titration of incorporated FY Residues

F^{235}Y -RhoA and RhoGAP^{R85A} were mixed in equimolar ratio in buffer containing BisTris-HCl 25 mM pH = 7.5, NaCl 150 mM, MgCl₂ 10 mM, NaF 20 mM and concentrated to 0.60 mL with both proteins at a concentration of 0.5 mM. The pH of the buffer was changed stepwise by diluting the sample until the desired pH was reached and concentrating the solution back to 0.5–0.6 mL. A 2048 scan spectrum was recorded at each pH.

F^{25}Y -RhoA was buffer exchanged into a buffer containing BTP-HCl 25 mM pH = 6.0, NaCl 150 mM, MgCl₂ 10 mM, NaF 20 mM and concentrated to 0.60 mL with both proteins at a concentration of 0.5 mM. The pH of the buffer was changed stepwise by diluting the sample until the desired pH was reached and concentrating the solution back to 0.5–0.6 mL. A 2048 scan spectrum was recorded at each pH.

For the determination of the $\text{p}K_{\text{a}}$ of the fluorinated Tyr34 residue ^{19}F -NMR chemical shifts were plotted against the pH value of the buffer. A sigmoidal curve based on the Henderson-Hasselbalch equation (Eq.4) was fitted to yield the $\text{p}K_{\text{a}}$ value. (δ_{obs} : observed chemical shift, δ_{OH} : chemical shift for protonated form, $\Delta\delta$: chemical shift changes upon deprotonation, n: Hill coefficient). Statistical parameters are tabulated in section 5.6.

$$\delta_{\text{obs}} = \delta_{\text{OH}} + \Delta\delta \frac{10^{n(\text{pH}-\text{p}K_{\text{a}})}}{1+10^{n(\text{pH}-\text{p}K_{\text{a}})}} \quad (4)$$

2.27 RhoA Single-Turnover HPLC assay

The HPLC based activity assays for WT- and FY-RhoA were performed at 4 °C in Buffer A (BisTris-HCl 25 mM pH = 6.0, NaCl 50 mM, MgCl₂ 5 mM). Stock solutions of GTP-loaded RhoA and RhoGAP^{R85A} were in Buffer A and cooled to 4 °C. Microcentrifuge tubes were cooled to 4 °C and RhoA was diluted with Buffer A to the appropriate concentration and the reaction was initiated by the addition of RhoGAP^{R85A} to a final volume of 170 µL. Protein concentrations for RhoA were 50 µM and for RhoGAP^{R85A} were 0–250 µM. At regular timepoints 22.5 µL aliquots were taken and mixed with 2.5 µL trichloroacetic acid (100% (w/v)) at 4 °C. After two minutes 10 µL 4 M NaOAc was added, the precipitated protein was removed by centrifugation at 4 °C and the sample was stored at –80°C. HPLC analysis was performed as described in section 2.2.

2.28 Determination of Kinetic Parameters of FY-RhoA variants

GTP/GDP loading was determined by comparing the peak area for the respective signal at 254 nm. Results for the intrinsic RhoA catalysis were fitted to a single exponent decay functions (Eq.5; y = %GTP-loading, t = time, k_{int} = intrinsic RhoA hydrolysis rate).

$$y = y_0 \times e^{-k_{int}t} \quad (5)$$

The intrinsic rates of GTP hydrolysis for the FY-RhoA variants were used to fit the data using non-linear regression (Eq.6; y = %GTP-loading, y_0 = initial %GTP-loading, $k_{R85Ax\mu M}$ = rate of RhoGAP^{R85A}-catalysed GTP hydrolysis, t = time, k_{int} = intrinsic RhoA hydrolysis rate).

$$y = y_0 \times e^{-k_{R85Ax\mu M}t} - y_0(1 - e^{-k_{int}t}) \quad (6)$$

The obtained rates were plotted against the RhoGAP_{R85A} concentration and fitted with a hyperbolic curve (Eq.7).

$$k_{R85Ax\mu M} = \frac{k_{cat} \times [\text{RhoGAP}_{R85A}]}{K_m + [\text{RhoGAP}_{R85A}]} \quad (7)$$

A list of all kinetic parameters used for fitting can be found in Tab.19. Error bars for rates are given as 95% confidence intervals.

3 HRas/RasGAP Complex and Implications of cSrc-mediated Tyrosine Phosphorylation of HRas Switch Regions

3.1 Results and Discussion

3.1.1 Crystallisation of HRas/MgF₃⁻/RasGAP Complex

3.1.1.1 Screening of Crystallisation Conditions

HRas(1–166) was expressed in *E.coli* BL21(DE3) cells and purified using DEAE chromatography and SEC as described in section 2.19.3. RasGAP(714–1047) was expressed in *E.coli* BL21(DE3) cells and purified using GST chromatography and SEC as described in section 2.19.2. As a starting point, screening crystal trays were set up based on crystallisation conditions for PDB:1WQ1, while omitting the addition of any aluminium containing additives (Tab.6).

Table 6: Crystallisation condition for HRas/RasGAP (PDB: 1WQ1).

Protein buffer		Precipitant	
HRas	400 µM	HEPES·Na pH = 8.0	100 mM
RasGAP	400 µM	PEG3350	15–20% (w/v)
HEPES·Na pH = 8.0	20 mM	(NH ₄) ₂ SO ₄	20 mM
AlCl ₃	2 mM	NaF	20 mM
NaF	20 mM	Gd·HCl	100 mM

The screening trays were setup using ‘sitting drop’ conditions with drop sizes between 0.8–1.3 µL. Experimental details can be found in section 2.24. However, only severe precipitation was observed, until the drop size was increased to 2 µL. Further parameter variation with the increased drop size yielded a hit using the following precipitant: HEPES·Na 100 mM pH = 8.0, PEG3350 20% (w/v), (NH₄)₂SO₄ 20 mM, Gd·HCl 100 mM, NaF 20 mM. Due to the thin needle shape of the obtained crystals, further screening was performed using seeding protocols to improve the crystal morphology. Unfortunately, continued screening could not achieve a significant change in morphology. Switching to a ‘hanging drop’ approach and increasing the drop size to 5 µL, also produced needle shaped crystals. However, significantly less protein precipitation was observed in the drops and the increased size of the crystals allowed the harvest and measurement of the crystal. The best

diffraction for HRas/MgF₃⁻/RasGAP crystals was obtained for a highly anisotropic dataset, processed using the Staraniso web server and solved using molecular replacement on the basis of PDB:1WQ1 (see Tab.7 and section 2.24).¹⁶⁶

Table 7: Data collection and refinement statistics for HRas/MgF₃⁻/RasGAP

HRas/MgF ₃ ⁻ /RasGAP	
Crystal Data	
Wavelength	0.976 Å
Space group	P 1 21 1
a, b, c (Å)	71.83, 41.56, 89.67
a, b, g (°)	90.00, 109.25, 90.00
Resolution (Å)	84.66–2.26, 3.24, 2.10*
R _{merge}	0.027
I / σI	35.9 / 1.7
CC(1/2)	0.996 / 0.552
Completeness (%)	99.1 / 72.2 (ellipsoidal)
Refinement	
Resolution (Å)	84.66–2.10
No. reflections	15962 / 791
R _{work} / R _{free}	0.200 / 0.279
<u>No. atoms</u>	
Protein	3878
Ligand/ion	36 / 1
Water	52
<u>B-factors</u>	
Protein	45.46
Ligand/ion	37.06 / 43.08
Water	31.72
<u>RMS deviations</u>	
Bond lengths (Å)	0.0066
Bond angles (°)	1.500

*Resolution limits of anisotropic ellipsoid fitted to diffraction cut-off surface along axes
 $-0.127 \mathbf{a}^* + 0.992 \mathbf{c}^* / -0.773 \mathbf{a}^* + 0.301 \mathbf{b}^* + 0.558 \mathbf{c}^* / 0.363 \mathbf{a}^* + 0.212 \mathbf{b}^* + 0.907 \mathbf{c}^*$

3.1.1.2 Structural Analysis of the Phosphoryl Transfer TSA for HRas/RasGAP

The previously mentioned uncertainties regarding the assigned metal fluoride species (MgF_3^- or AlF_3^0) of the 1WQ1 structure, in combination with the low resolution warrant a re-examination of the HRas/RasGAP TSA crystal structure. Even more than 20 years after its initial publication this structure is still used by many computational studies as a starting point for calculations regarding RasGAP catalysed GTP hydrolysis.^{66–68} Thus, the aluminium-free crystal structure solved in section 3.3.1.1, provides a more accurate active site model and will improve conclusions drawn from these studies. Shown in figure 18 is the refined electron density map for the Ras/ MgF_3^- /RasGAP active site (A), as well as the ligand omit maps for GDP (B), the catalytic magnesium (C) as well as the MgF_3^- species (D). These omit maps can be useful in validating the atomic models due to their inherent bias resulting from model building and refinement. By excluding the atoms in question from the model and calculating a residual map, they should then be visible as positive features in the map. This unmodelled electron density can be clearly seen in Figure 13B-D, thus confirming the ligand assignment.

Comparing this newly generated HRas/ MgF_3^- /RasGAP TSA structure with the one from PDB:1WQ1 reveals the same overall fold (Fig.19A), evidenced by the low RMSD of 0.436 Å (2089 to 2089 atoms). When taking a closer look, subtle changes become apparent (Fig.19 B). The better and more accurate electron density of the obtained structure therefore is likely to depict a more accurate representation of the HRas/RasGAP active site during the phosphoryl transfer transition state. This is of particular importance when examining the metal fluoride transition state analogue species. Here the ligand omit map (Fig.18D) clearly shows a trigonal coordination of the fluoride ligands around the magnesium centre. This is congruent with the PDB:1WQ1 structure. Unfortunately, no structure factors are available to compare the electron densities in the active site.

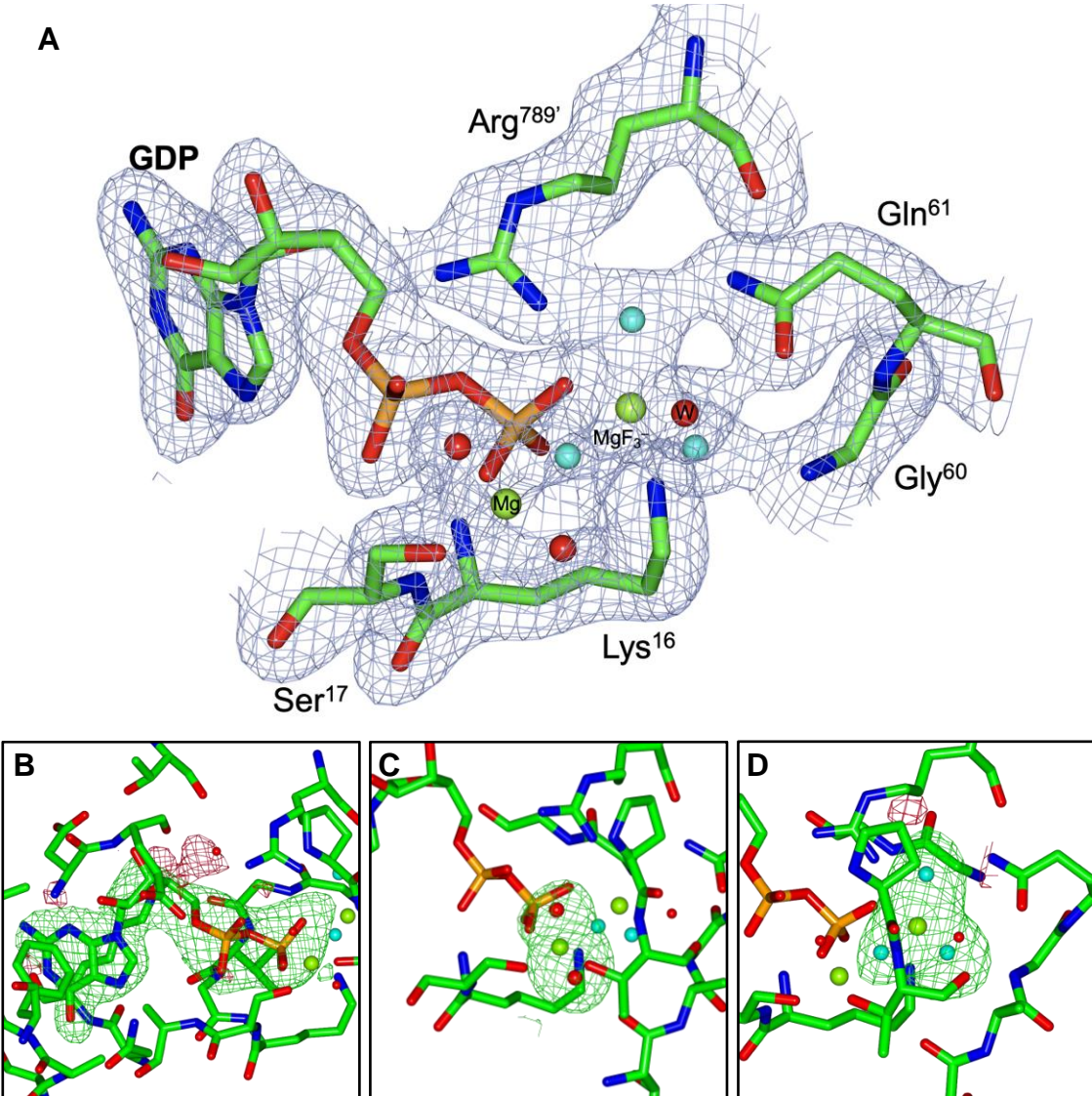


Figure 18: (A) Electron density map for key active site residues of the newly generated HRas/MgF₃⁻/RasGAP complex, contoured to 1σ (0.23 e^{-3}). Ligand omit maps for HRas/MgF₃⁻/RasGAP complex. Difference Fourier map $F_0 - F_c$, contoured at 3σ : (B) GDP (C) catalytic magnesium with two coordinating waters (D) MgF₃⁻.

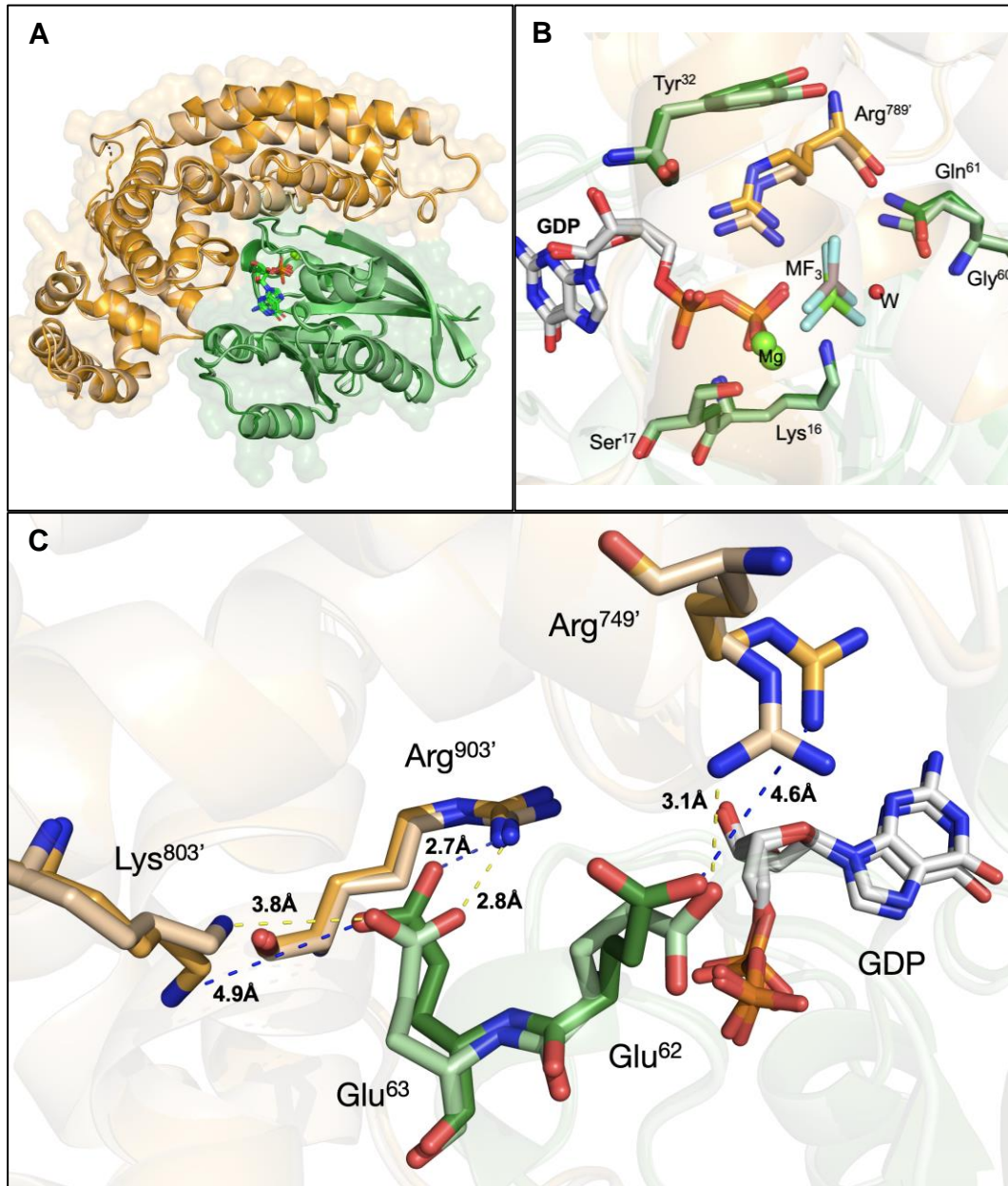


Figure 19: (A) Overlay HRas/RasGAP TSA complexes from PDB:1WQ1 (HRas: **dark green**, RasGAP: **dark orange**) and the newly generated structure (HRas: **light green**, RasGAP: **light orange**). (B) Active site of (A) with key residues highlighted for comparison. (C) Bond lengths of the salt bridges between the two proteins of the HRas/ MgF_3^- /RasGAP TSA as identified by PISA analysis. Primed residues are part of RasGAP.

PISA analysis of the improved HRas/ MgF_3^- /RasGAP TSA structure further identifies new salt bridge contacts between HRas and RasGAP (Fig.20C). Of these, in the 1WQ1 structure only the interaction between HRas-Glu62 and RasGAP-Arg903' is identified. The distance between HRas-Glu62 and RasGAP-Arg749' is 4.6 Å, too long for a salt bridge interaction. In comparison, in the new structure, the guanidinium moiety of RasGAP-Arg749' is rotated closer to HRas-Glu62, decreasing the distance to 3.1 Å. Similarly, the salt bridge identified between

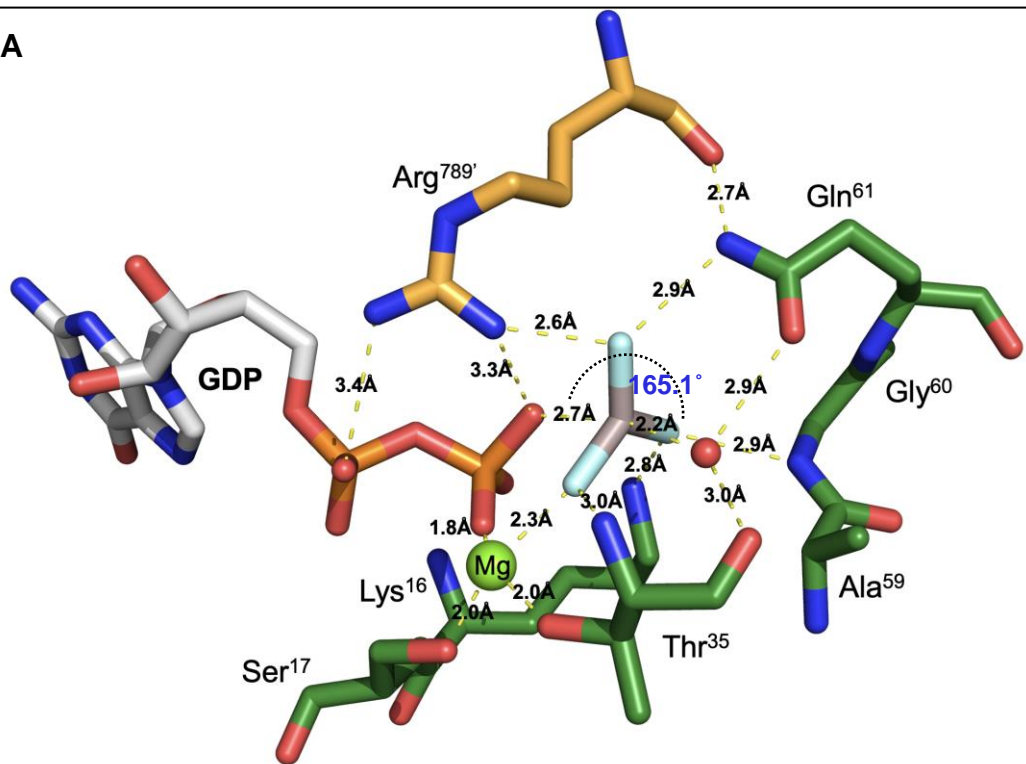
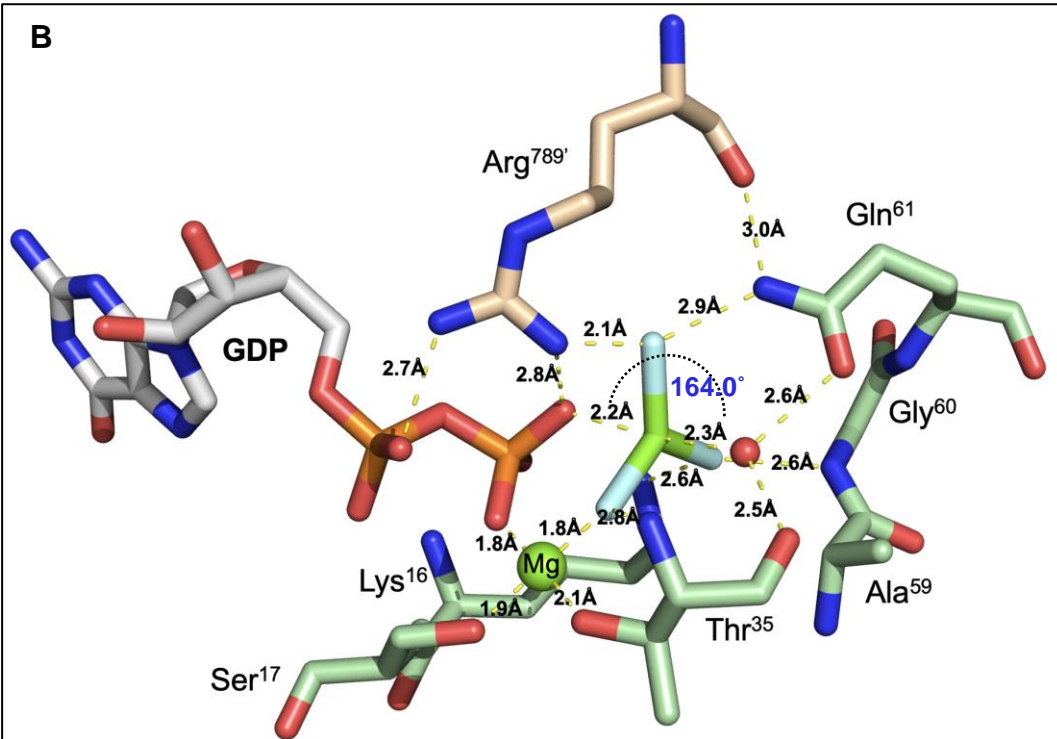
RasGAP-Lys803' and HRas-Glu62 shortens from 4.9 to 3.8 Å, when PISA takes dynamic distance into account.

When comparing interatomic distances of the active site, an overall shortening of bond distances is observed for the new structure (Fig.20A and B). Particularly the bond distances, between Arg789' and the GDP phosphates/MgF₃⁻ decreases on average by about 20%. Similarly, when considering the O–M–O distance between the nucleophilic water, the metal fluoride species and bridging oxygen, the distances in the 1WQ1 structure are well above the literature values of around 2.0–2.2 Å (Fig.20A and B), while the new structure has more accurate values.⁵³

Another significant difference is noticeable when comparing the complexation of the catalytic magnesium in both structures (Fig.20E and F). In the PDB:1WQ1 model, the magnesium coordination sphere is incomplete, as it lacks a water ligand, whereas in the structure generated in this work, the observed density allows for much higher confidence to fit in a magnesium with another water with the octahedral coordination fulfilled. This is an important step towards a more accurate Ras/RasGAP transition state model, meaning there are additional insights that can be gained on the role of active site water molecules during GTP hydrolysis.

Apart from water molecules' role in the coordination of the catalytic magnesium, the implications for the widely discussed 'one-water' or 'two-waters' mechanism are of particular interest.¹⁴⁵ It has been argued that a second water assists the proton transfer of the phosphoester hydrolysis, by directly abstracting a proton from the nucleophilic water in the enzyme active site.

As the resolution of 2.50 Å for the 1WQ1 structure is close to the resolution limit for identifying the ordered density for water molecules, uncertainties existed in regard to the number and position of water molecules in the active site. The higher resolution of this new structure reveals no 'second water' adjacent to the nucleophilic water in the TSA and the electron density of neighbouring residues do not leave sufficient space for it. Therefore, the catalytic mechanism involving activation of the nucleophilic water by a second adjacent water molecule seems unlikely.

A**B**

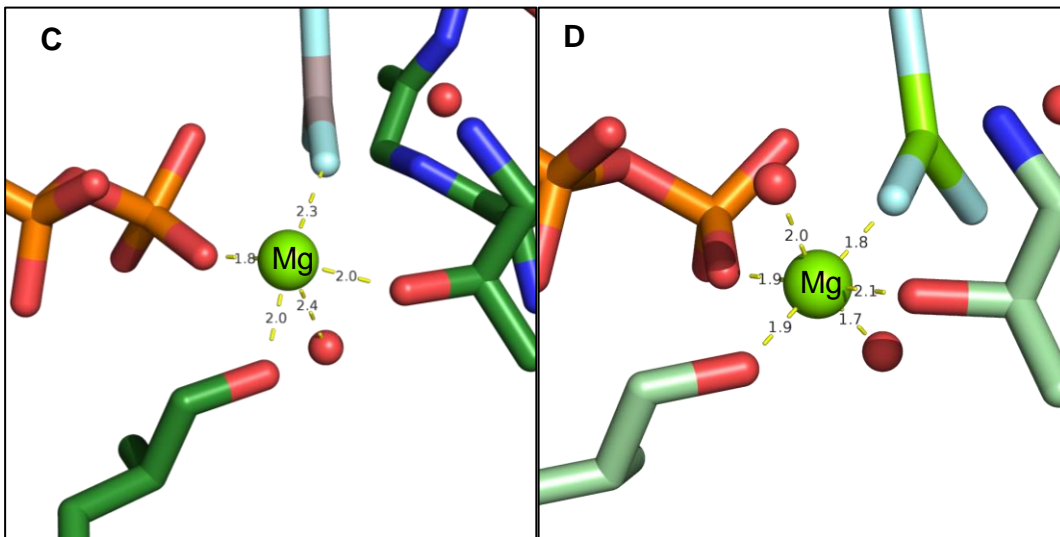
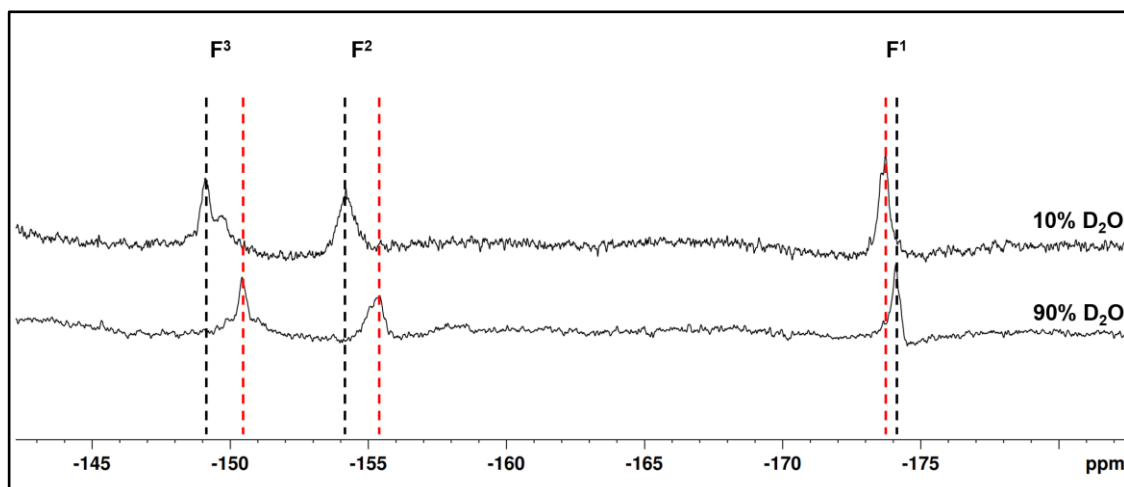
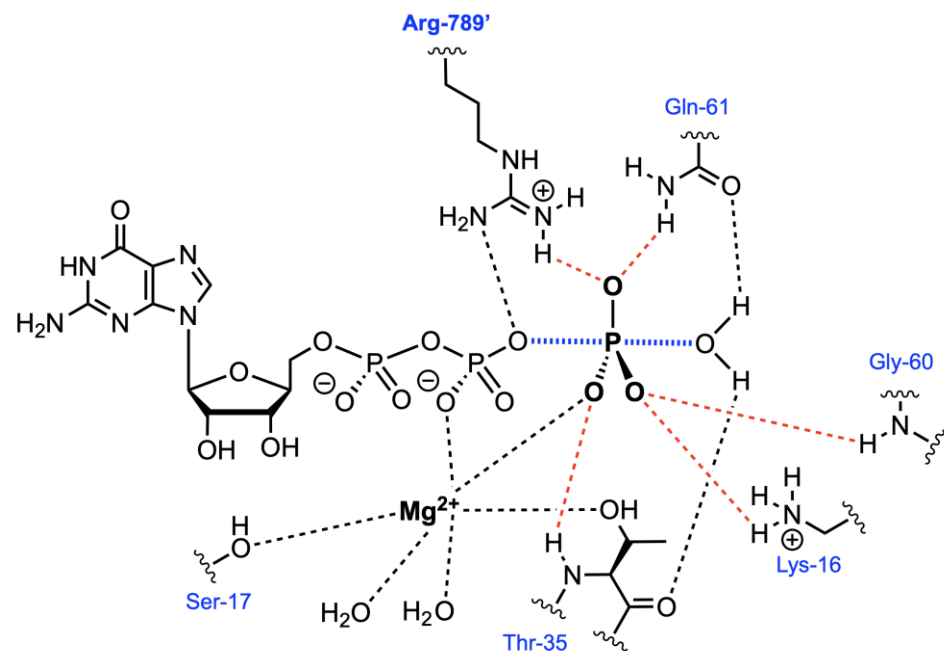


Figure 20: (A) Active site of HRas/ AlF_3^0 /RasGAP (PDB:1WQ1; HRas: **dark green**, RasGAP: **dark orange**). (B) Active site of HRas/ MgF_3^- /RasGAP from section 3.3.1 (HRas: **light green**, RasGAP: **light orange**). (C) Coordination sphere for the catalytic magnesium of HRas/ AlF_3^0 /RasGAP (PDB: 1WQ1). (D) Coordination sphere for the catalytic magnesium of HRas/ MgF_3^- /RasGAP. Primed residues are part of RasGAP.

To further prove the observation of no ‘second-water’ in our crystal structure, the HRas/ MgF_3^- /RasGAP TSA complex was further investigated by measuring the solvent-induced isotope shift (SIIS) in ^{19}F -NMR. This effect results from differences in the electric field transmission to the MgF_3^- species when comparing ^1H - and ^2H -hydrogen bonds.¹⁷² In the HRas/ MgF_3^- /RasGAP TSA complex, the obtained crystal structure indicates five hydrogen-bonding contacts to the MgF_3^- species (indicated in red in Fig.21A).

The HRas/ MgF_3^- /RasGAP TSA complex readily forms in solution when sufficient magnesium and fluoride is present. This complexed magnesium fluoride species can be observed using ^{19}F -NMR, showing three distinct peaks (Fig.21B, top spectrum). The most upfield and therefore most shielded signal corresponds to the fluorine atom coordinated to the catalytic magnesium of the active site (F^1). The signal at $\delta = -154.2$ ppm corresponds to the fluorine in contact with the Gly60 residue (F^2) and the most downfield signal at $\delta = -149.1$ ppm corresponds to the fluorine atom in contact with the ‘Arg-finger’ (F^3). These assignments are supported by DFT calculations and SIIS experiments of the related RhoA/ MgF_3^- /RhoGAP TSA complex.¹⁵⁷ After the initial ^{19}F -NMR spectrum of the complex was recorded in 10% D_2O (Fig.21B, top spectrum), the protein mixture was buffer exchanged into the same buffer with 90% D_2O and a second spectrum was recorded (Fig.21B, bottom spectrum).



[ppm]	Buffer 10% D ₂ O	Buffer 90% D ₂ O	Δ SIIS
F ¹	-173.7	-174.1	0.4
F ²	-154.2	-155.3	1.1
F ³	-149.2	-150.4	1.2

Figure 21: (A) Hydrogen bonding network surrounding the MgF_3^- species of HRas/ MgF_3^- /RasGAP complex. Primed residue Arg789' is donated by RasGAP. (B)¹⁹F-NMR spectra of HRas/ MgF_3^- /RasGAP: HRas 0.5 mM, RasGAP 0.5 mM, HEPES-Na 20 mM pH/pD = 7.5, NaCl 150 mM, DTT 1 mM, $MgCl_2$ 10 mM, NaF 20 mM (1024 scans).

The crystallographic data show one H-bond contact for F^1 ($Thr35_{N-H}$), two for F^2 ($Lys16_{NH4+}$ and $Gly60_{N-H}$) and two for F^3 ($Gln61_{NH2}$ and $Arg789'_{NH2}$). This is congruent with the ratio of the obtained SIIS values of $F^1 : F^2 : F^3 = 1 : 2 : 2$. The

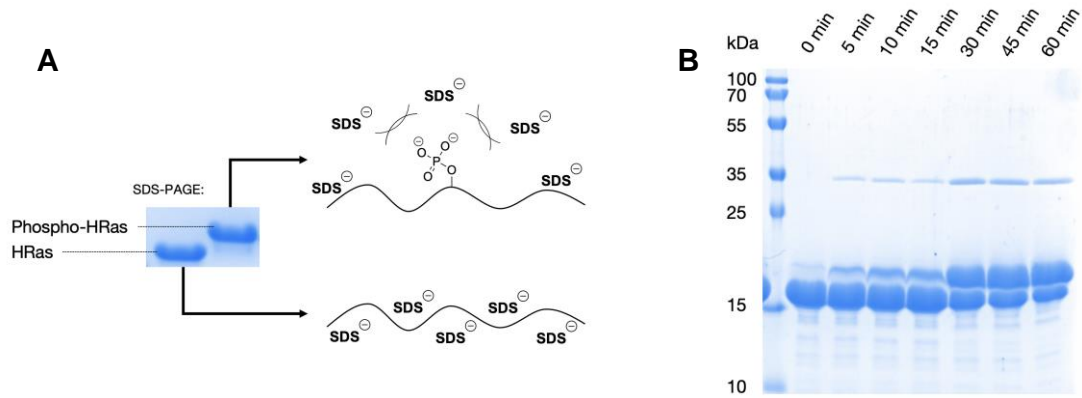
value of ~ 0.5 ppm per hydrogen bond is marginally below that of other magnesium fluoride SIIS experiments.^{157,173} This might be either because 90% D₂O was used instead of 100%, as is commonly done in the literature, or due to slow and therefore incomplete ¹H–²H exchange. Nevertheless, these SIIS results support that the structure of the H-bonding network observable in the crystal structure is also valid in solution.

Addressing the question which metal fluoride species is present in the 1WQ1 structure, this new structure strongly supports the hypothesis that MgF₃⁻ not AlF₃⁰ is the species in the TSA complex.⁶⁹ No aluminium was used during the crystallisation, thus the metal fluoride species in the newly produced structure can confidently be assigned to MgF₃⁻.

3.1.2 cSrc-catalysed Phosphorylation of HRas

3.1.2.1 Tyr32/Tyr64 – cSrc/SDM Studies

The plasmids for HRas(1–166)^{Y32F} and HRas(1–166)^{Y64F} were generated from ptac-HRas(1–166) using SDM as outlined in section 2.15. HRas(1–166)^{Y32F} and HRas(1–166)^{Y64F} were expressed in *E.coli* BL21(DE3) cells and purified using DEAE chromatography and SEC as described in section 2.19.3. Both mutants were validated using DNA sequencing of the plasmid as well as using SDS-PAGE and mass spectrometry analysis of the purified protein. The overall protein fold between the WT-HRas and the two mutants was checked using ¹H-NMR. cSrc(251–533) and hSOS1(564–1049) were expressed and purified based on literature conditions (see section 2.19.1 and 2.19.4).^{164,155}



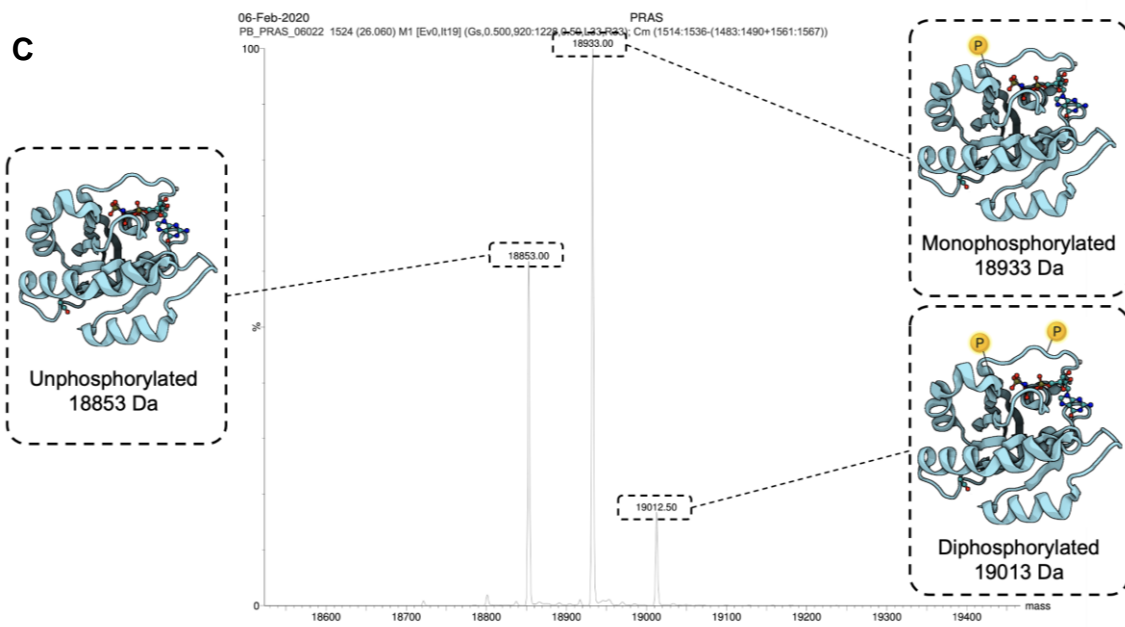


Figure 22: (A) Phosphorylation alters matrix migration during SDS-PAGE, by charge-charge repulsion.¹⁷⁴ (B) 500 μ M WT-HRas was incubated with ATP 3 mM, MgCl₂ 10 mM, NaCl 200 mM, DTT 1 mM, Tris-HCl 25 mM pH = 7.6, and cSrc 50 μ M. Timepoints taken over the course of 0–60 min (lanes 1–7). (C) Deconvoluted ESI-MS of HRas after cSrc phosphorylation. Peaks correspond to unphosphorylated HRas (18853 Da), monophosphorylated HRas (18933 Da) and diphosphorylated HRas (19013 Da).

The first step to examine cSrc-mediated HRas phosphorylation requires finding optimal conditions for the production of the phosphorylated protein. To test the activity of the purified cSrc, HRas was incubated with cSrc based on literature conditions.⁸³ SDS-PAGE was chosen to monitor the progress of the reaction. Protein phosphorylation was shown to alter the protein-SDS interaction and therefore alter the matrix migration during the electrophoresis, even for similarly sized proteins (Fig.22A).¹⁷⁴

Building on this initial assay, the reaction parameters were further optimised (Fig.23A, section 2.21). To interrogate the effect of the two mutations Y32F and Y64F have the cSrc interaction, WT-HRas, HRas^{Y32F} and HRas^{Y64F} were incubated overnight with the optimised phosphorylation conditions. In order to quantify the level of protein phosphorylation, ³¹P-NMR spectra of the three protein samples were recorded (Fig.23C). While the level of phosphorylation remained unchanged between WT-HRas and HRas^{Y32F} (Fig.23C, middle and bottom spectrum), the HRas^{Y64F} mutant showed a significantly reduced level of phosphorylation (Fig.23C, top spectrum). The low residual phospho-tyrosine peak is most likely due to non-specific phosphorylation of one of the other tyrosine residues present in the Ras

protein. This points towards Tyr64 being the primary target for cSrc phosphorylation under the conditions used for the phosphorylation. Interestingly, the signal for the α -phosphate of the bound GDP ligand showed a downfield shift of 0.3 ppm compared to both the wildtype and the Y64F mutant, which is in line with the strong influence of Tyr32 in regards to nucleotide binding (Fig.23B).¹⁷⁵ Previously, it has been shown that mutations at Ras-Tyr32 influence the ^{31}P resonance of bound guanine nucleotides by changing the conformational equilibrium between an open and a closed state.^{176,177}

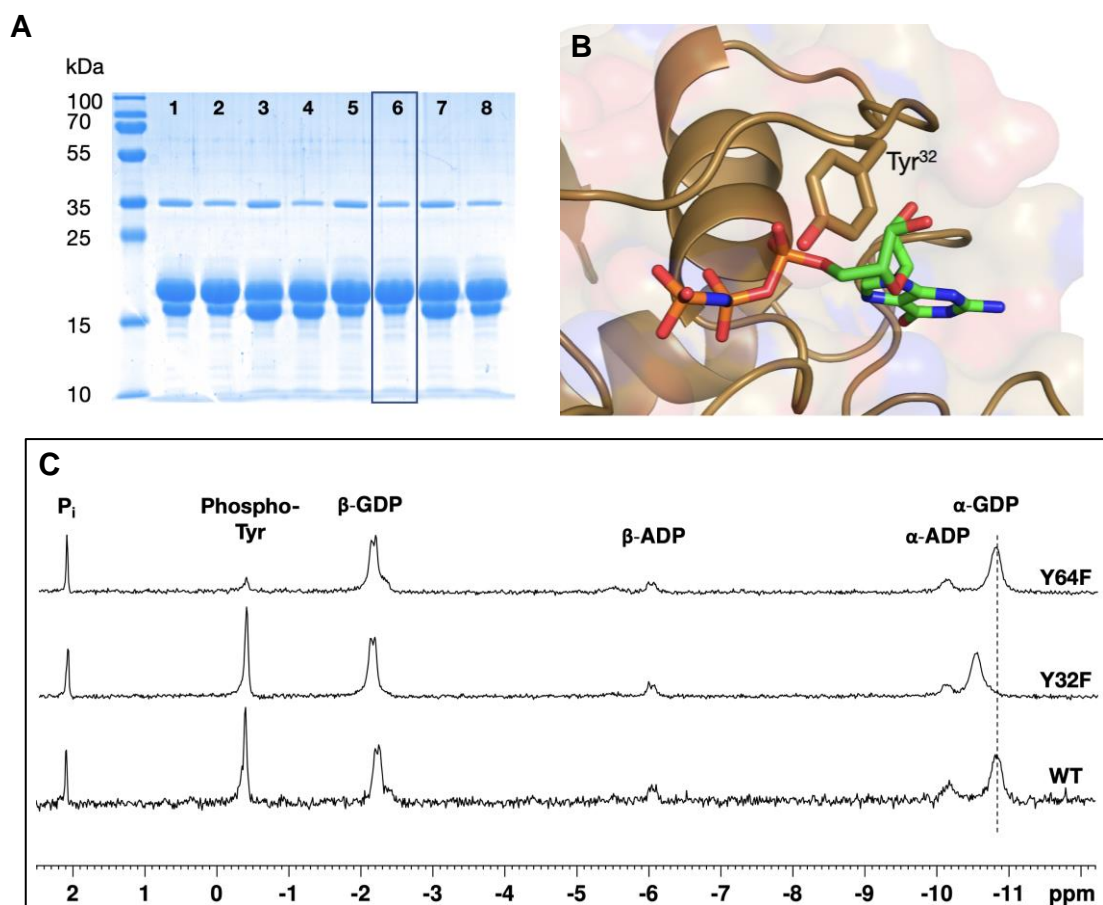


Figure 23: (A) Optimisation of cSrc-catalysed HRas phosphorylation conditions. Lane 6 shows the chosen optimised conditions: cSrc (100:1), ATP 4 mM, 25 °C (B) Crystal structure of HRas-GppNHp (PDB: 5P21) showing the vicinity of Tyr32 to the β -phosphate of the guanine nucleotide (C) ^{31}P -NMR spectra of phosphorylated WT-HRas (bottom), HRas^{Y32F} (middle) and HRas^{Y64F} (top).

3.1.2.2 Purification of monophosphorylated HRas

To better understand how the phosphorylation affects complex formation with RasGAP, X-ray crystallography gives unique insights by providing a structural

model. To ensure sample homogeneity necessary for protein crystallisation, monophosphorylated HRas needed to be separated from the unphosphorylated and diphosphorylated species. The only significant difference is their charge state, therefore ion-exchange chromatography was chosen. While smaller cartridge ion-exchange columns could not achieve adequate separation, a 16×100 mm Q FF 16/10 column, with a higher separating efficiency was able to separate the individual phosphorylation states of HRas (Fig.24A) as identified by MS (Fig.24B–D). The chromatogram shows a major monophosphorylated peak, as well as two diphosphorylated peaks.

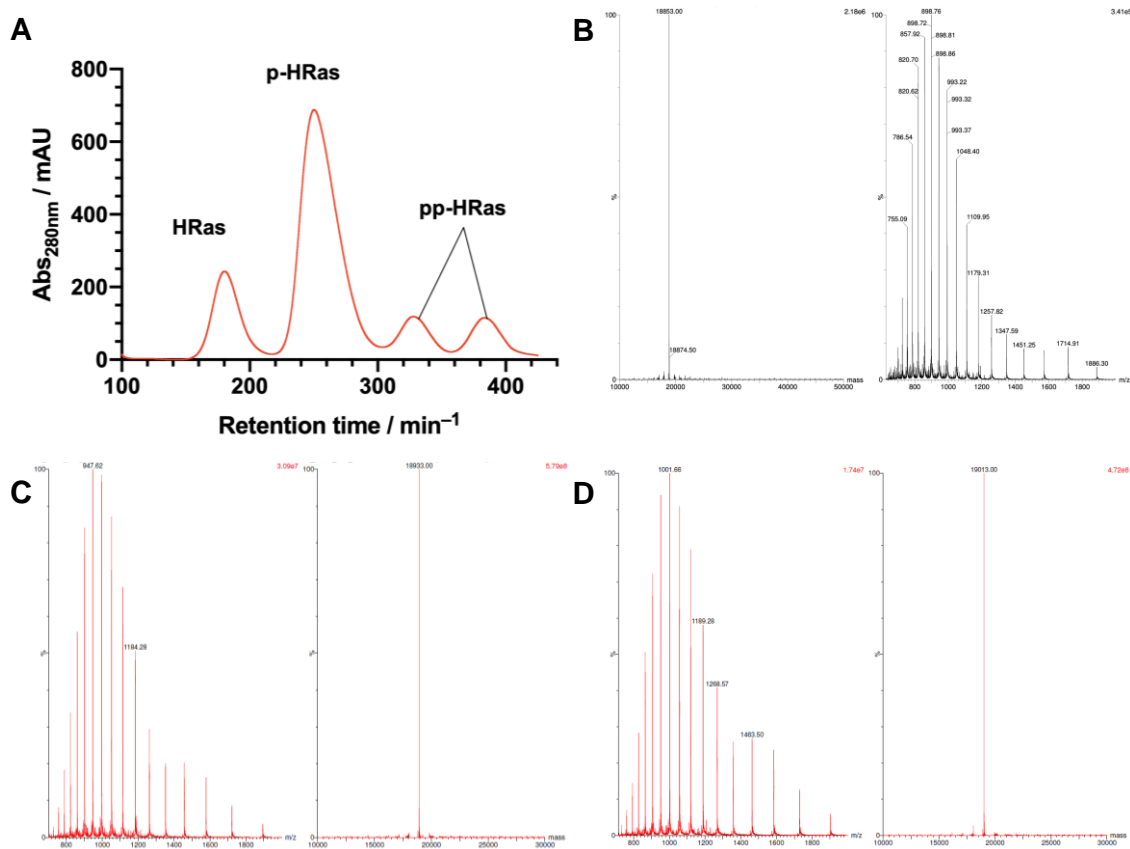


Figure 24: (A) Q column chromatogram of the separation of HRas, (B) Deconvoluted ESI-MS spectrum of unphosphorylated HRas (18853 Da) (C) Deconvoluted ESI-MS spectrum of monophosphorylated HRas (18933 Da) (D) Deconvoluted ESI-MS spectrum of diphosphorylated HRas (19013 Da).

After a method for the isolation of mono-phosphorylated HRas had been established, the stability of the phosphorylation had to be tested. This is important for the screening of crystallisation conditions, as it can take days or weeks for crystals to form. Therefore, mono-phosphorylated HRas was incubated in crystallisation buffer and the phosphorylation state was monitored over time (Fig.25,

see section 2.22). No significant dephosphorylation could be detected after one week. While the addition of precipitant could have an effect on the stability, these results show a generally good stability of the mono-phosphorylated HRas species.

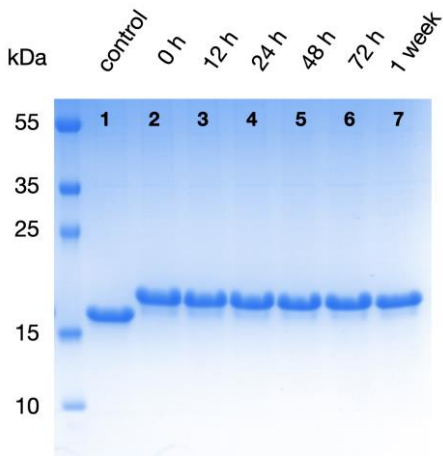


Figure 25: Time course testing the stability of phosphorylated HRas. Monophosphorylated HRas was incubated at 4 °C in crystallisation buffer (HEPES-Na, pH = 8.0, MgCl₂ 10 mM, NaF 20 mM) and aliquots were taken after 0, 0.5, 1, 2, 3 and 7 days (lanes 2–7). After an aliquot was taken it was mixed with 4× SDS-PAGE buffer and frozen at –80 °C. Unphosphorylated HRas was run as a control (lane 1).

3.1.2.3 Screening Crystallisation Conditions: phospho-HRas/MgF₃[−]/RasGAP

HRas/MgF₃[−]/RasGAP readily forms a complex in solution. To investigate phospho-HRas/MgF₃[−]/RasGAP complex formation in solution, mono-phosphorylated HRas was mixed with equal amounts of RasGAP in a buffer containing 10 mM MgCl₂ and 20 mM NaF and examined by ¹⁹F-NMR to confirm the complex formation, however no complexation was observed.

Initial screenings for the crystallisation of phospho-HRas/MgF₃[−]/RasGAP were based on the conditions for the phosphorylated HRas/RasGAP complex using drop sizes of 0.8–1.3 µL (Tab.6). However, only heavy protein precipitation could be observed. Crystal formation could only be observed when the drop size was increased to 3 µL (see 2.24). The crystals were sent to the Diamond Light Source Synchrotron and diffracted to a resolution of 3.05 Å and were solved using the CCP4i2 software suite based on the HRas/RasGAP complex (PDB: 1WQ1). Unfortunately, instead of the phospho-HRas/RasGAP complex, the crystallised protein turned out to be a dimeric form of RasGAP (Fig.26A).

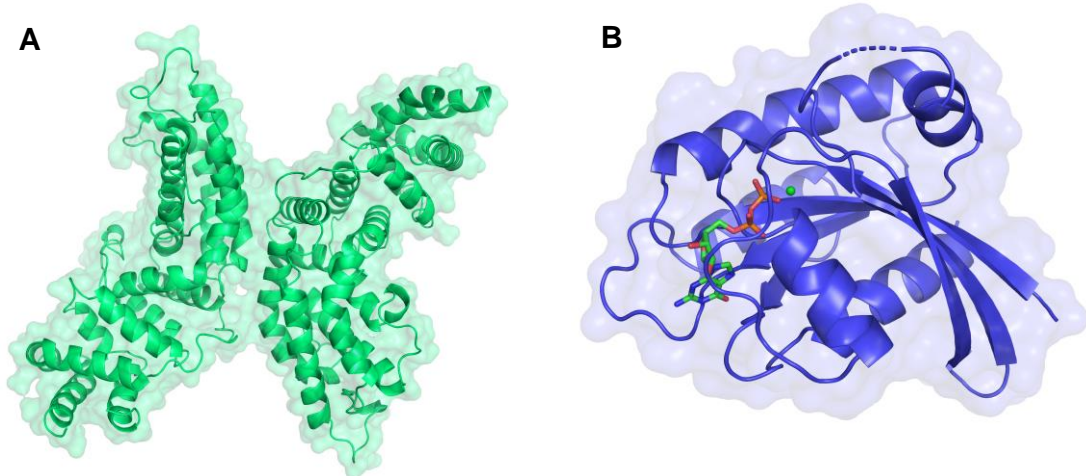


Figure 26: (A) Crystal structure of dimeric RasGAP(714–1047). (B) Crystal structure of phospho-HRas(1–166).

As the conditions for the unphosphorylated HRas complex had not been successful in producing crystals for the phosphorylated HRas/RasGAP complex. A broader range of crystallisation conditions was screened by using commercial crystal screens (see 2.24). While many conditions produced heavy precipitation of the protein, a condition was found to produce star shaped crystals with no precipitation (Precipitant 1: 0.1 M Na·Citrate pH = 5.6, Li₂SO₄ 1.0 M, (NH₄)₂SO₄ 0.5 M). Multiple rounds of seeding yielded well-formed single crystals which were sent to the Diamond Light Source Synchrotron and diffracted to a resolution of 1.32 Å. The structure of the phospho-HRas was solved by molecular replacement with 1WQ1 but was found only HRas could match the density. The structure was finalised by several rounds of refinement. Unfortunately, instead of the phospho-HRas/RasGAP complex, the crystallised protein turned out to be monomeric phospho-HRas protein (Fig.26B). Comparing the protein fold to an unphosphorylated HRas-GDP crystal structure (PDB: 4Q21) reveals an identical folding pattern (Fig.27), the only difference being the highly dynamic Switch2 region, which could not be resolved. This unfortunately also means that the phosphorylation of the Tyr64 residue is not discernible from the electron density. However, as every other tyrosine residue is well resolve and does not carry this PTM, it is likely that Tyr64 is the main phosphorylation site. This needs to be confirmed with further studies, using for example trypsin digest analysis or by further X-ray crystallographic studies with alternate guanine nucleotides.

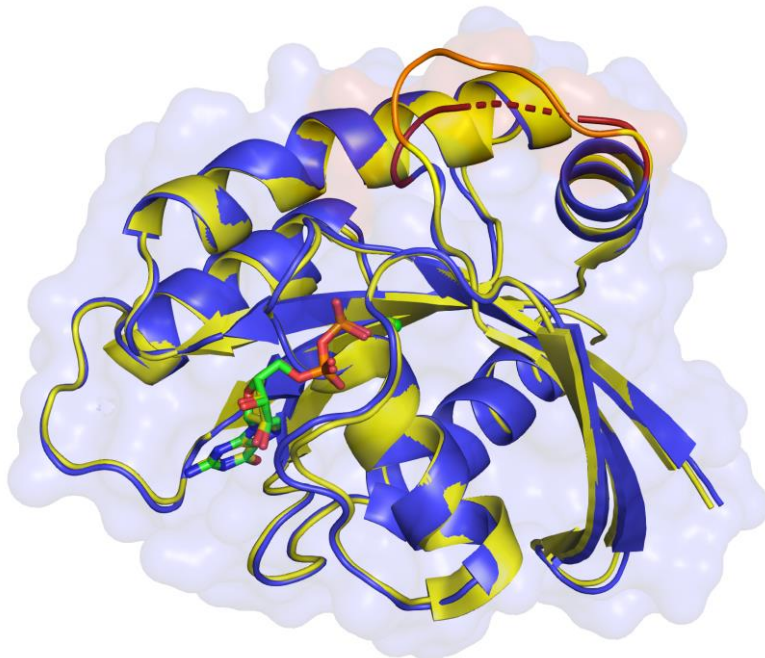


Figure 27: Overlay of unphosphorylated HRas·GDP (PDB: 4Q21, **yellow**) and phospho-HRas·GDP (**blue**). Switch2 regions are shown in **orange** and **red**.

Table 8: Data collection and refinement statistics for phospho-HRas and dimeric RasGAP

	phospho-HRas	dimeric RasGAP(714–1047)
Crystal Data		
Wavelength	0.976 Å	0.976 Å
Space group	H 3 2	P 1
<i>a</i> , <i>b</i> , <i>c</i> (Å)	92.66, 92.66, 119.32	38.17, 58.68, 75.90
<i>a</i> , <i>b</i> , <i>g</i> (°)	90.00, 90.00, 120.00	91.30, 103.72, 107.87
Resolution (Å)	47.88–1.32	36.67–3.05
<i>R</i> _{merge}	0.083	0.065
<i>I</i> / <i>σI</i>	124.6 / 1.1	20.5 / 1.0
CC(1/2)	0.999 / 0.577	0.997 / 0.530
Completeness (%)	87.2 / 91.0	98.8 / 98.0
Refinement		
No. reflections	35121 / 1683	11427 / 528
<i>R</i> _{work} / <i>R</i> _{free}	0.220 / 0.306	0.220 / 0.364
<u>No. atoms</u>		
Protein	1210	3966
Ligand/ion	44 / 1	- / -

Water	117	-
<u>B-factors</u>		
Protein	26.31	60.07
Ligand/ion	60.74 / 20.59	- / -
Water	36.43	-
<u>RMS deviations</u>		
Bond lengths (Å)	0.00163	0.0062
Bond angles (°)	2.030	1.593

3.1.3 RasGAP-Dimer Interaction

Obtaining the RasGAP(714–1047) dimer crystal structure has interesting implications for its activity *in vivo*. Other members of the GAP1 family have been reported to be regulated by homodimer formation (e.g., NF1).^{178–180} However, no structural data for the molecular interaction are known so far. RasGAP(714–1047) is a domain that is conserved in the GAP1 family as the GAP-related domain (GRD) (Fig.28A).¹⁸¹ Therefore, parallels between the members of this family can be drawn. An initial PISA analysis identified several residues involved in the binding interaction (Fig.28B), which was calculated to have a weak to moderate dimer interface energy of $\Delta^iG = -4.0$ kcal/mol. Conversely, based on retention times of size exclusion chromatography it is unlikely that this dimer forms in solution and is therefore only a crystal state dimer. Nevertheless, as RasGAP(714–1047) is only a single domain, these binding interactions might hold some significance for the fully assembled p120 RasGAP complex *in vivo*. While this is an interesting initial finding, more work is necessary to determine its mechanistic role in the context of cellular signalling. In order to assess the exact binding mode, the next step in future research should be to determine dimer forming parameters of the full-length p120 RasGAP protein, followed by site-directed mutagenesis to determine the contributions of these newly identified binding interactions.

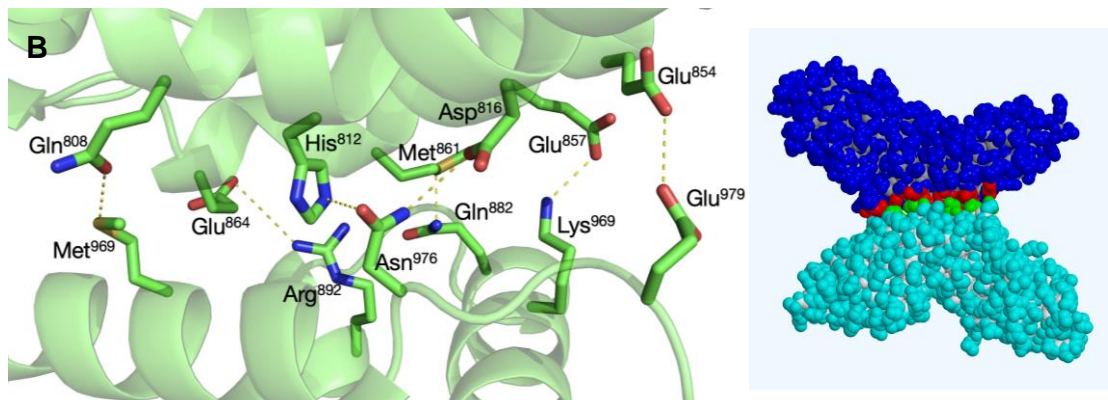
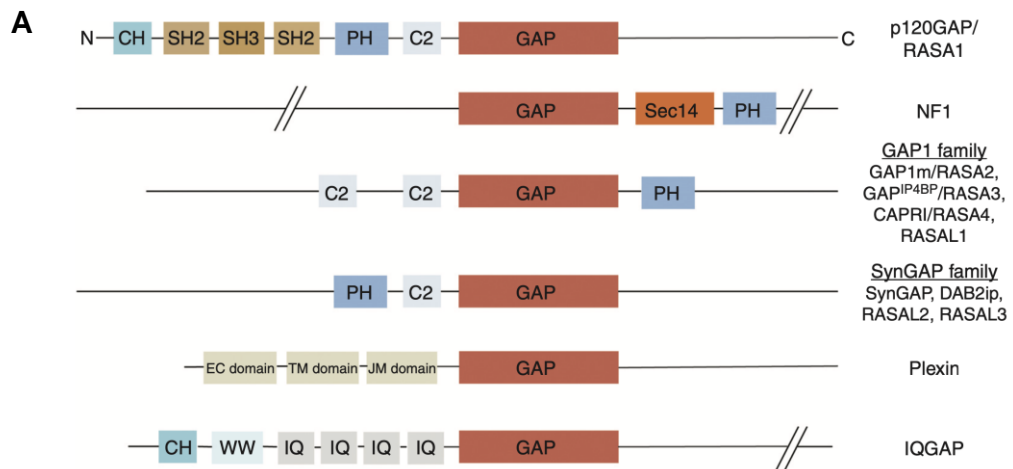


Figure 28: (A) Domain architecture of GAP1 family (adapted from SCHEFFZEK *et al.*).¹⁸¹ (B) Binding interface of RasGAP(714–1047) dimer crystal structure. Highlighted residues are binding interactions identified by PISA analysis.

4 Tyrosine-mediated Hydrogen Bonding and its Role in the catalytic Activity of RhoA

4.1 Results and Discussion

4.1.1 Site-specific Incorporation of Fluorotyrosine (FY)

4.1.1.1 Synthesis of Fluorotyrosines (FYs)

To generate the necessary FY-RhoA variants, the relevant FYs needed to be synthesised. This can be difficult when using classical organic synthesis,¹⁸² e.g., F²³⁵⁶Y can be obtained from hexafluorobenzene in five steps to afford a racemic mixture.¹⁸³ Syntheses of other FYs are similarly laborious when using standard routes. Separation and characterisation of the different stereoisomers is also challenging. Fortunately, the enzyme TPL can act as an efficient catalyst for the incorporation of substituted phenols into L-tyrosine derivates.¹²⁵ Here, the syntheses were based on literature conditions using recombinant TPL from *Citrobacter intermedius*, starting from the respective fluorophenols which were available commercially (Fig.29).¹⁸⁴ The detailed experimental procedures can be found in sections 2.17 and 2.18.

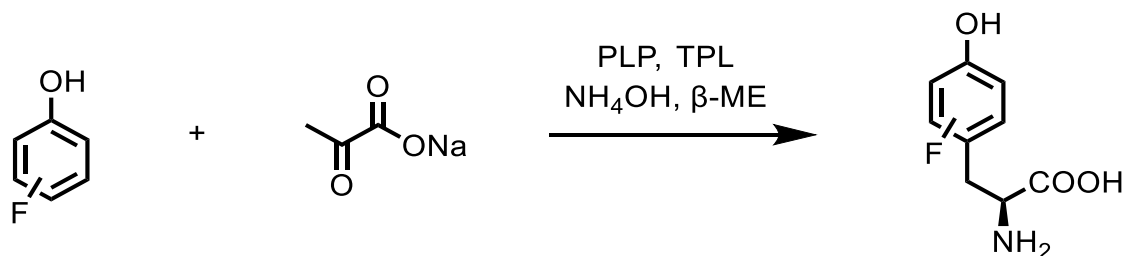


Figure 29: Chemoenzymatic synthesis of fluorinated L-tyrosine derivates.

The postulated mechanism involves several key steps, beginning with the formation of an amino acrylate intermediate from pyruvate and ammonium, which then proceeds to form a C-C-bond to the phenol moiety at the para position. C- γ proton abstraction by Tyr71 assisted by Arg381, with subsequent C- α protonation by Lys257 yields the aldimine intermediate, which goes on to form the final L-tyrosine amino acid.¹⁸⁵

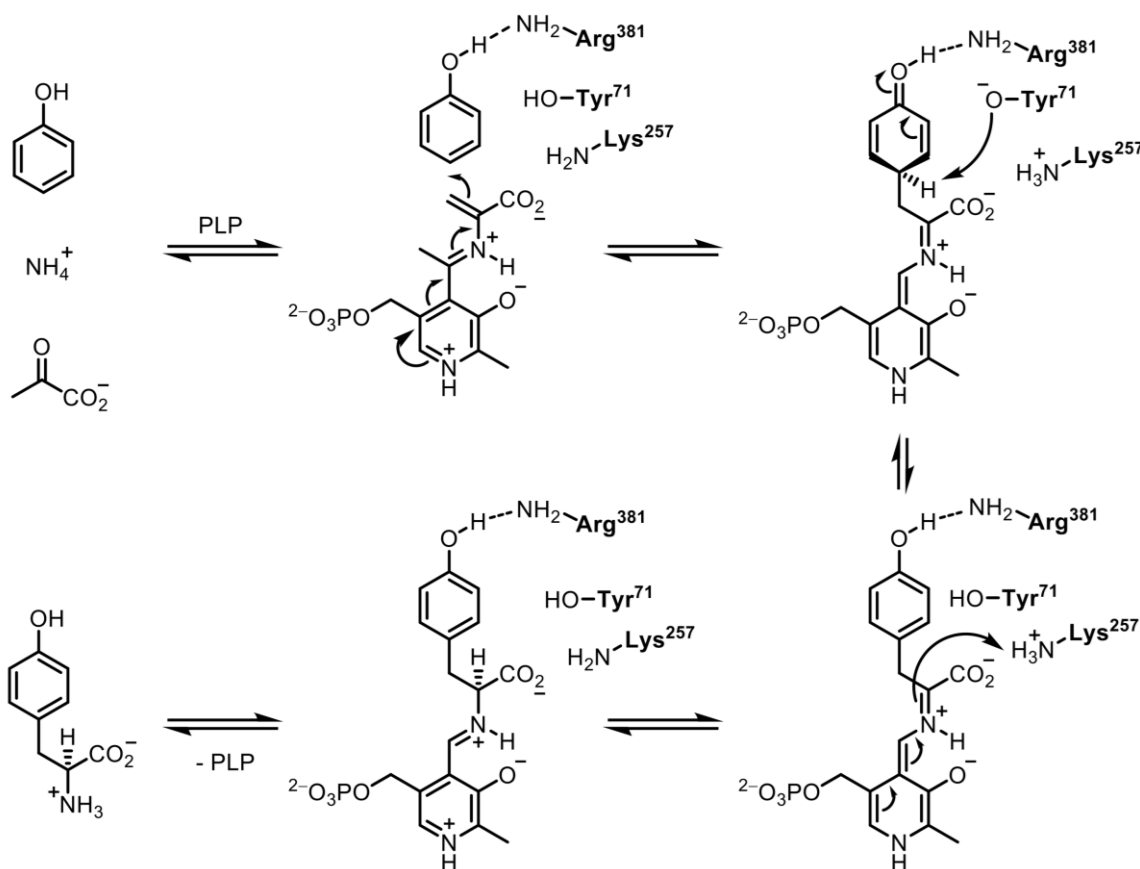


Figure 30: Proposed reaction mechanism for the synthesis of L-tyrosine from phenol, pyruvate and ammonium catalysed by TPL using PLP as coenzyme.¹⁸⁶

TPL was expressed in BL21(DE3) cells and purified using ammonium sulfate precipitation as described in section 2.19.7. The activity of the crude TPL extract was quantified spectrometrically using an SOPC assay as described in section 2.16. The duration of the reaction ranged from several days for the FYs with a lower number of fluorine substituents to several weeks for F²³⁵⁶Y. The reason, in addition to the slightly increased steric demand of the substrate, is likely due to a decreased stabilisation of the positive charge in the aryl group in the transition state.¹⁸⁶ The yields based on fluorophenol as starting material for the respective FYs are listed in Fig.31.

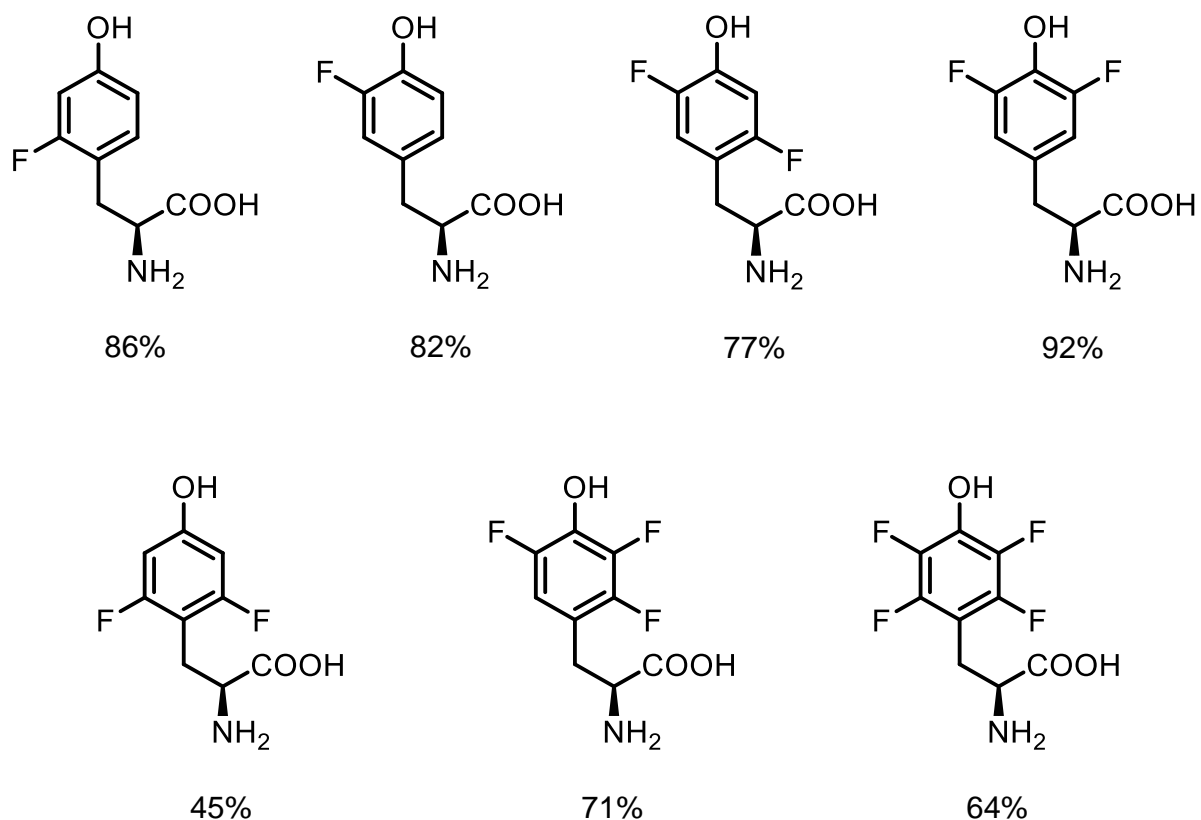


Figure 31: Synthesised FYs with their corresponding yields.

4.1.1.2 Fluorotyrosine (FY) Incorporation into RhoA – Construct Screening

With a range of FY compounds in hand, the next step was to incorporate them into RhoA at position 34 using a polyspecific tRNA/tRNA synthetase pair. The plasmid encoding the tRNA synthetase was a generous gift from the STUBBE lab.¹⁶⁰ In order to check the function of the FY incorporation with the tRNA/tRNA synthetase pair, the use of a green fluorescent protein provides a useful reporter system to visualise the expression level of the target protein (Fig.32A). For the initial test of our expression system, the plasmid contained the gene for a His₆-tagged GFP protein with a TAG codon at position 150.

Competent cells were cotransformed with pET32-sfGFP-N150TAG containing the gene for the GFP protein with an amber codon for residue 150 and pEVOL-F3Y-RS-E3 containing the tRNA/tRNA synthetase pair as described in section 2.19.8. After centrifugation, the distinct green colour of the GFP protein could be observed, indicating a successful incorporation of the FY (Fig.32B). After a subsequent protein purification step using Ni-NTA, the protein sample was analysed using MS, confirming a successful incorporation of F³⁵Y (Fig.32C).

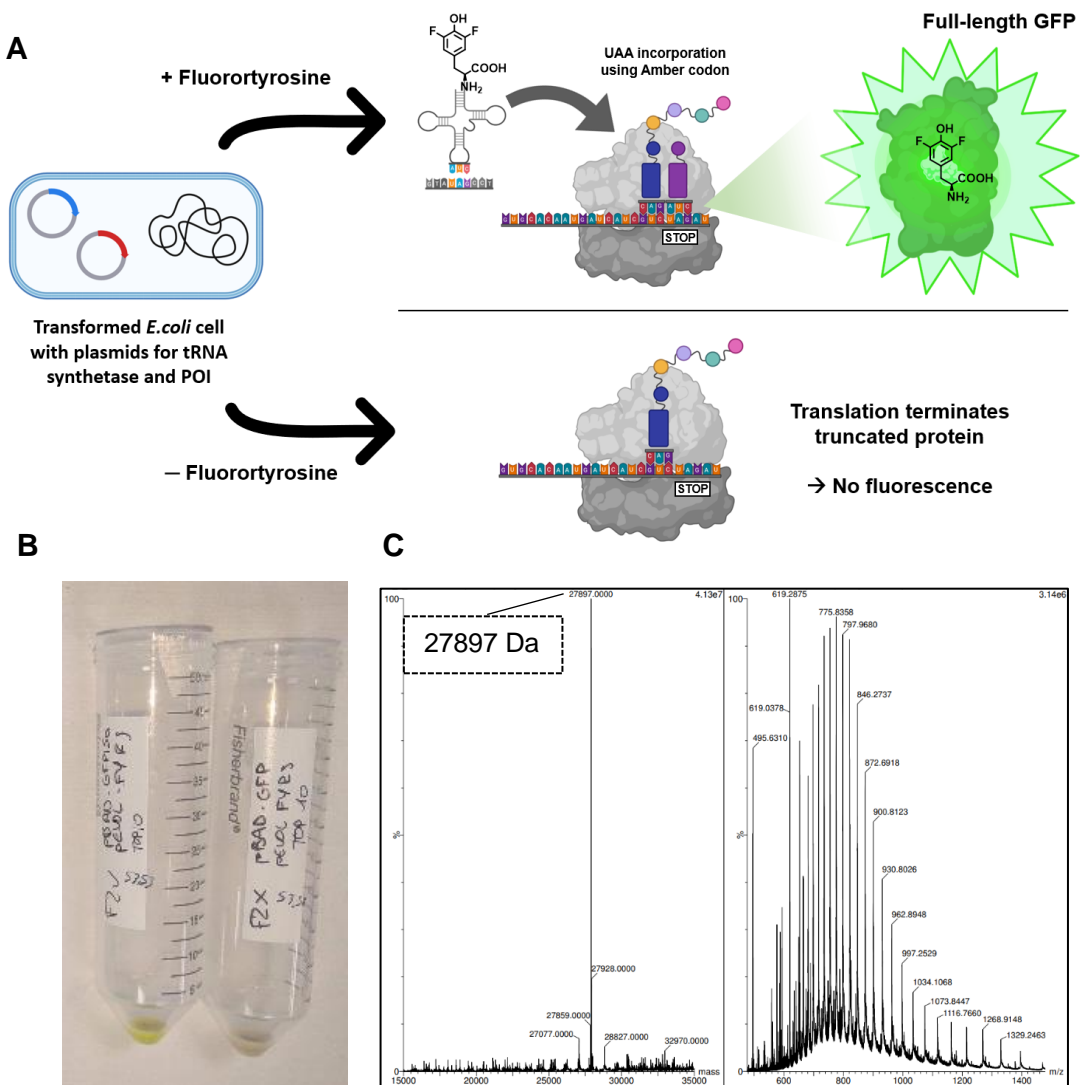


Figure 32: (A) Overview of site-specific ncAA incorporation by hijacking a non-coding codon. (B): cell pellets with FY-labelled GFP (left) and the no FY control (right). (C) Mass spectrum showing the successful incorporation of F^{35}Y into GFP.

After the successful F^{35}Y labelling of GFP, the next step was the FY incorporation into RhoA. The incorporation of non-canonical amino acids can lead to drastically reduced protein yields due to possible issues with the compatibility of the orthogonal pair with the translational machinery as well as the competition of suppressor tRNA with release factor for binding to nonsense codons.¹⁸⁷ Therefore, several vector constructs were prepared to optimise for a high protein yield. A variety of constructs with/without an amber codon were generated using different vector backbones (Tab.9) using either Gibson Assembly, restriction cloning or site-directed mutagenesis. The detailed experimental procedures can be found in section 2.13.

Table 9: Plasmid constructs for screening expression conditions for FY-RhoA incorporation.

Plasmid name	Y34TAG?	N-terminus	C-terminus
pBAD-GST-RhoA-His10	No	GST	His ₁₀
pBAD-GST-RhoA-His10-Y34TAG	Yes	GST	His ₁₀
pET32-GST-RhoA-His10	No	GST	His ₁₀
pET32-GST-RhoA-His10-Y34TAG	Yes	GST	His ₁₀
pGEX-2T-RhoA	No	GST	-
pGEX-2T-RhoA-Y34TAG	Yes	GST	-
pBAD-RhoA-His6	No	-	His ₆
pBAD-RhoA-His6-Y34TAG	Yes	-	His ₆

The pBAD plasmids were screened using *E. coli* TOP10 cells, while *E. coli* BL21(DE3), BL21(DE3) STAR and BL21(DE3) GOLD were screened for the pET32 and pGEX plasmids. Further screening parameters included the expression temperature (16 °C, 25 °C or 30 °C) and the concentration of the inducing agent, i.e., IPTG (0.01 mM to 1 mM) or L-arabinose (0.00002% to 0.2%). For 25 °C and 30 °C pBAD-GST-RhoA-His10 showed the best level of expression at L-arabinose concentrations of 0.002% to 0.2% (see section 7.5). Full experimental details can be found in section 2.3.9. With these optimised conditions the incorporation of F³Y and F³⁵Y were tested at concentrations ranging from 1–5 mM. However, no incorporation was observed.

To assay whether a different unnatural amino acid that generally give better yield incorporation yield can be incorporated into the Tyr34 position as a control, the pBAD-GST-RhoA-His10-Y34TAG plasmid was cotransformed with the plasmid encoding for the tRNA synthetase used for ε-Boc-Lys incorporation. Expression testing at 16 °C, 25 °C and 30 °C and at L-arabinose concentrations between 0.00002% and 0.2% gave no clear overexpression of the target protein. For both 25 °C and 30 °C, at L-arabinose concentrations higher than 0.002% a band was overexpressed at around 30 kDa. After GST-column chromatography and mass spectrometry analysis, the band was identified as the truncated protein, stalled at the mutation site. This indicates that it is the targeted position that causes problem at the protein synthesis.

4.1.1.3 Folding Chaperone assisted FY Incorporation

To solve the problem of protein truncation and low expression, a new approach was needed. Folding chaperones are found to help with protein folding. Thus, a new method was tried by generating a construct where the folding chaperone trigger factor (TF) is fused to the protein of interest. As with the GST-tag, TF needs to be removed to not interfere with the examination of RhoA. CATANZARITI *et al.* have used a construct where an additional ubiquitin fusion partner is added between the folding chaperone and the protein of interest.¹⁵⁹ This has the advantage that, in addition to its natural yield enhancement, the additional tags can easily be cleaved off by very specific deubiquitinases which do not cleave non-specific sequences. Furthermore, they do not leave any amino acid residues after the C-terminal glycine residue of ubiquitin. The authors have also engineered a mouse deubiquitinase, USP2-cc, which is readily expressed and purified as a His₆-tagged protein.¹⁵⁹

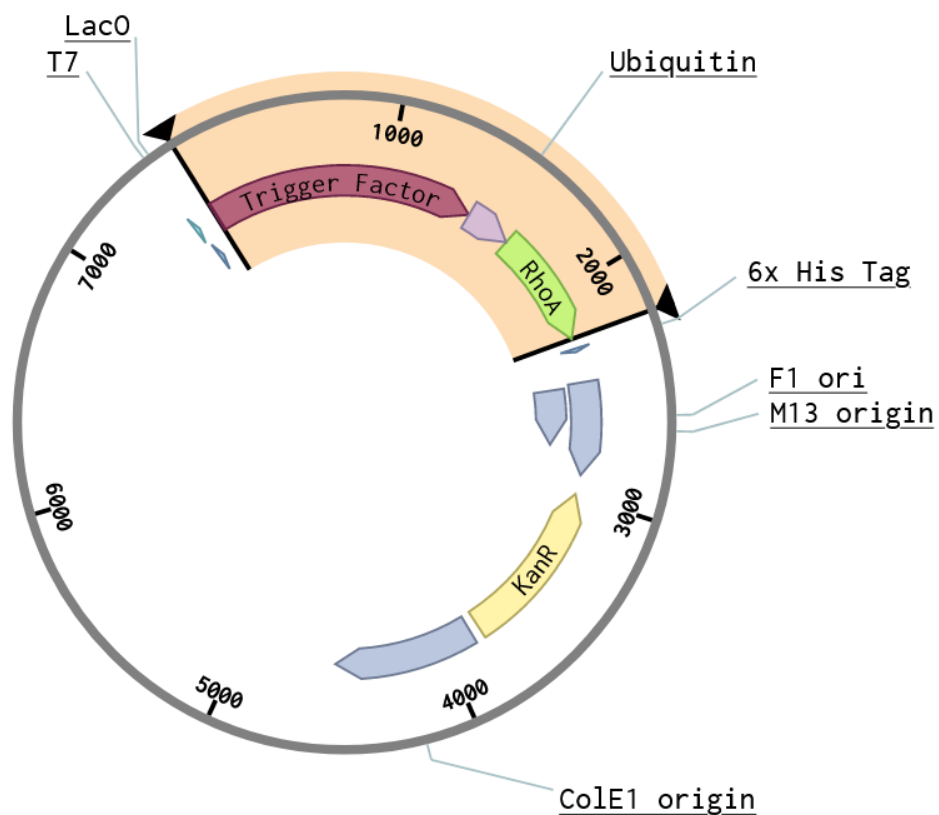


Figure 33: Plasmid Map. Folding chaperone Trigger factor and ubiquitin fused to RhoA.

The gene for the C-terminal His₆-tagged deubiquitinase necessary for the cleavage of TF-Ub fragment was purchased from LIFE TECHNOLOGIES Ltd and cloned into a pET15 plasmid vector (sequence: see 5.2.1). Details for the cloning procedure, expression and purification can be found in section 2.13.

The gene encoding the C-terminal His₆-tagged TF-Ub fragment was purchased from LIFE TECHNOLOGIES Ltd. (sequence: see 5.2.4). To generate the final plasmid (Fig.33) the purchased gene fragment was combined with a pET28a backbone fragment and a RhoA fragment. These last two fragments were amplified from laboratory stocks using PCR. The assembly procedure and the used primers are described in detail in section 2.13. The newly generated plasmid was sequenced confirming that the desired product was obtained. *E.coli* BL21(DE3) AI were transformed with pET28a-TF-RhoA-Y34TAG and plated for expression. *E.coli* BL21(DE3) AI cells were chosen, as these contains a chromosomal insertion of the gene encoding T7 RNA polymerase into the *araB* locus of the *araBAD* operon. Therefore, it places the T7 RNA polymerase under the control of the L-arabinose inducible *araBAD* promoter. This strain is usually used to produce toxic protein as this grants a tighter regulation over gene expression. Here it is used for its property to accommodate the two inducing agents IPTG and L-arabinose, which allows for temporal control over the induction of overexpression of the two genes. To screen for the optimal conditions *E.coli* BL21(DE3) AI cells were cotransformed with pEVOL-F3Y-RS and pET28a-TF-RhoA-Y34TAG and plated on LB agar plates containing the appropriate antibiotic. Many factors influence the incorporation and expression level when it comes to protein expression with ncAAs. In this case different temperatures, FY concentration in the medium as well as the type of culturing media were screened. As F³⁵Y can be produced with the highest yield, it was chosen for the initial screen. Fig.34 shows a number of conditions after the cells have been harvested. All lanes show an overexpressed band around the 70 kDa marker, where the fusion protein was truncated at position 34. The second overexpressed band just under the 100 kDa marker is the full-length protein with the F³⁵Y residue incorporated at position 34. The band intensity increases in a dose-dependent manner depending on the FY concentration present in the growth medium. The expression level for other media showed no significant improvement, however as TB media supports the highest cell density this media was chosen to proceed.

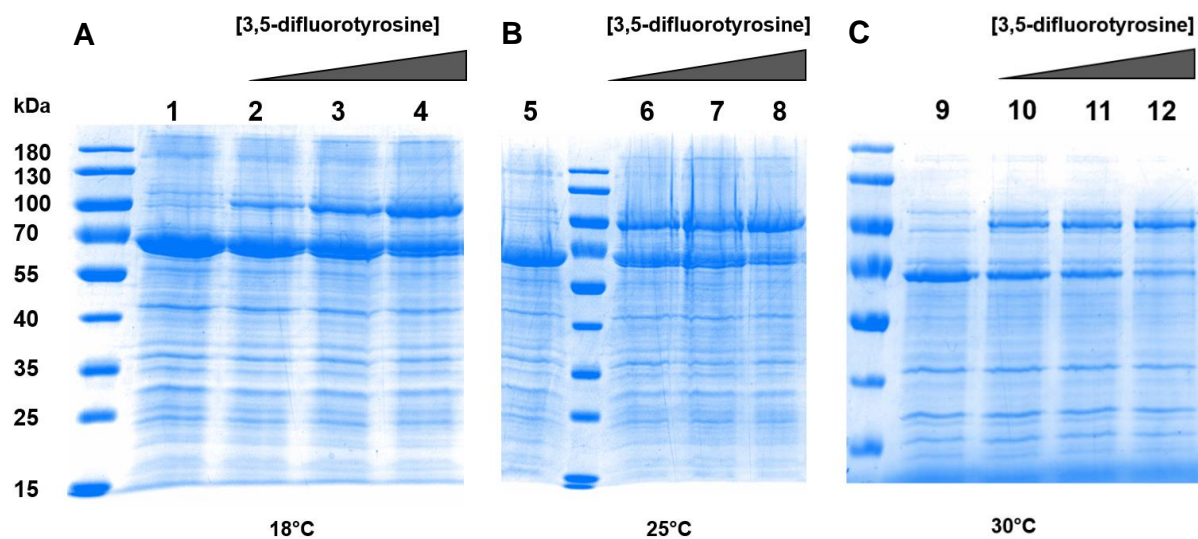
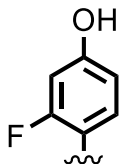
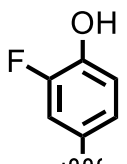
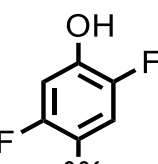
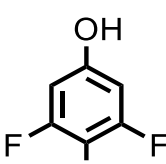
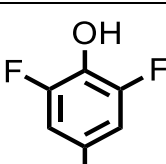
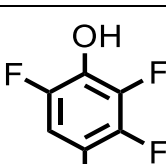
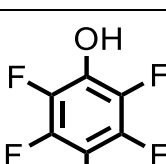


Figure 34: Screening of expression conditions for the incorporation of F³⁵Y into RhoA at 18°C (A), 25°C (B) and 30°C (C). For each temperature concentrations of 1–5 mM of F³⁵Y were screened. Lanes 1, 5 and 9 show the no FY control.

Scaling up the optimised expression conditions yielded a mixture of TF-F³⁵Y-RhoA and its truncated form. The mixture was purified using IMAC and subsequently incubated with the deubiquitinase Usp2-cc at a ratio of 20:1 at 4°C for 24 h. Finally, the cleaved F³⁵Y-RhoA was purified using SEC and the F³⁵Y incorporation was confirmed with mass spectrometry (see 5.4.10). This procedure was repeated for all synthesised FYs and all successful incorporations were confirmed by protein MS (see 5.4). The overall yields after purification are summarised in Tab.10. Based on the band intensity and overall protein yield, the fluorotyrosine with the highest incorporation rate is F²³⁵Y. This is likely due to the tRNA/tRNA synthetase pair having been evolved to incorporate this specific amino acid.¹⁶⁰ Incorporations using F²⁶Y and F²³⁵⁶Y (Tab.10, entry 4 and 7) could not be achieved. A possible explanation is that the two fluorine substituents in meta position to the hydroxyl group lead to steric clashes with the tRNA synthetase. F²Y could also not be incorporated into RhoA. Notably the hydroxyl pK_a value of this amino acid is the highest of all tested fluorotyrosines and therefore might be too high to be recognised by the tRNA synthetase, as it disrupts the hydrogen bonding network necessary for the substrate specificity. For the purposes of this project the pK_a values of the successfully incorporated FY residues span a range from 10.2 to 6.4 in regular intervals. The pK_a values of the incorporated FY side chains are addressed in section 4.3.2.

Table 10: Protein yields after the ncAA incorporation of FY into RhoA.

Entry No.	RhoA residue 34 side chain	Hydroxyl pK _a	Ø Yield [mg/L]
1		9.0	no incorporation
2		8.4	8
3		7.9	7
4		7.0	no incorporation
5		7.2	9
6		6.4	13
7		5.6	no incorporation

4.1.2 ^{19}F -NMR Analysis of RhoA/ MgF_3^- /RhoGAP $^{\text{R}85\text{A}}$ TSA Complex

4.1.2.1 Measurement of FY-RhoA/ MgF_3^- /RhoGAP $^{\text{R}85\text{A}}$ TSA Complexes using ^{19}F -NMR

To compare the FY-RhoA variants as a first step the formation of the WT-RhoA/ MgF_3^- /RhoGAP $^{\text{R}85\text{A}}$ TSA complex had to be repeated. WT-RhoA and RhoGAP $^{\text{R}85\text{A}}$ were produced and purified as described in section 2.19.8. The two proteins were then mixed in an equimolar ratio, based on literature conditions and a ^{19}F -NMR spectrum was recorded (Fig.35).¹⁵⁷ The chemical shift values for the MgF_3^- complex were in concurrence with the ones reported in the literature.¹⁵⁷

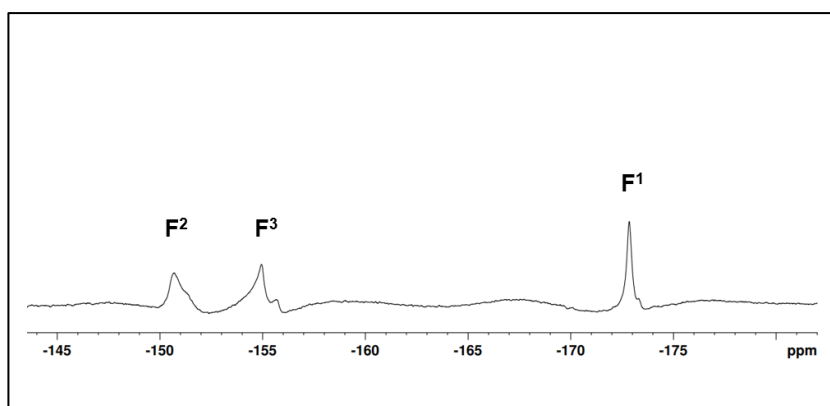


Figure 35: ^{19}F -NMR spectrum of 0.5 mM WT-RhoA, 0.5 mM RhoGAP $^{\text{R}85\text{A}}$, 100 mM NaCl, 10 mM MgCl $_2$, 20 mM NaF and 50 mM Tris-HCl buffered to pH = 7.5. The chemical shifts for WT-RhoA are –150.5 ppm (F¹), –155.0 ppm (F²) and –172.8 ppm (F³).

As a next step the complex formation between the F ^{235}Y -RhoA variant and RhoGAP $^{\text{R}85\text{A}}$ was to be examined. To study the MgF_3^- complex the two proteins were mixed in an equimolar ratio, based on literature conditions and a ^{19}F -NMR spectrum was recorded (Fig.36).¹⁵⁷ The spectrum shows five distinct peaks: fluoride (–119.6 ppm), MgF $^+$ (–156.5 ppm) and three signals (–140.3 ppm, –148.1 ppm and –160.1 ppm) belonging to the F ^{235}Y sidechain of the modified RhoA protein. Notably, no peaks corresponding to the F ^{235}Y -RhoA/ MgF_3^- /RhoGAP $^{\text{R}85\text{A}}$ TSA complex were observed.

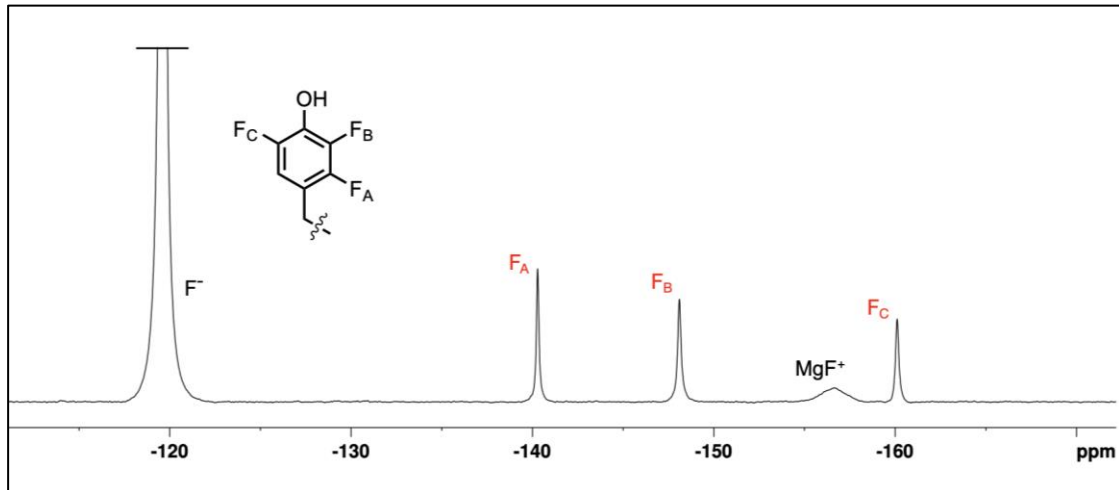


Figure 36: ¹⁹F-NMR spectrum of 0.5 mM F²³⁵Y-RhoA, 0.5 mM RhoGAP^{R85A}, 100 mM NaCl, 10 mM MgCl₂, 20 mM NaF and 50 mM Tris-HCl buffered to pH = 7.5. The chemical shifts for F²³⁵Y-RhoA are -140.3 ppm (F_A), -148.1 ppm (F_B) and -160.1 ppm (F_C).

The sample of the spectrum in Fig.36 was buffered to pH = 7.5. As the pK_a of the hydroxyl group of the F²³⁵Y sidechain is 6.4, it is in a predominantly deprotonated state. RhoA^{Y34F} does not form a MgF₃⁻ complex with RhoGAP^{R85A}. This means that the protonation state of the Tyr34 hydroxyl group is of critical importance for the complex formation. Thus, when the pH was gradually lowered, the emergence of a new set of six ¹⁹F-NMR peaks could be observed (Fig.37A). These six new peaks correspond to the newly formed F²³⁵Y-RhoA/MgF₃⁻/RhoGAP^{R85A} TSA complex (Fig.37B) and they maintain the same chemical shifts across the tested pH range. In contrast, the three peaks corresponding to the ‘free’ F²³⁵Y-RhoA protein show a downfield shift of about 2–4 ppm as the pH decreases, corresponding to the transition from the deprotonated state of the F²³⁵Y sidechain to the protonated one.

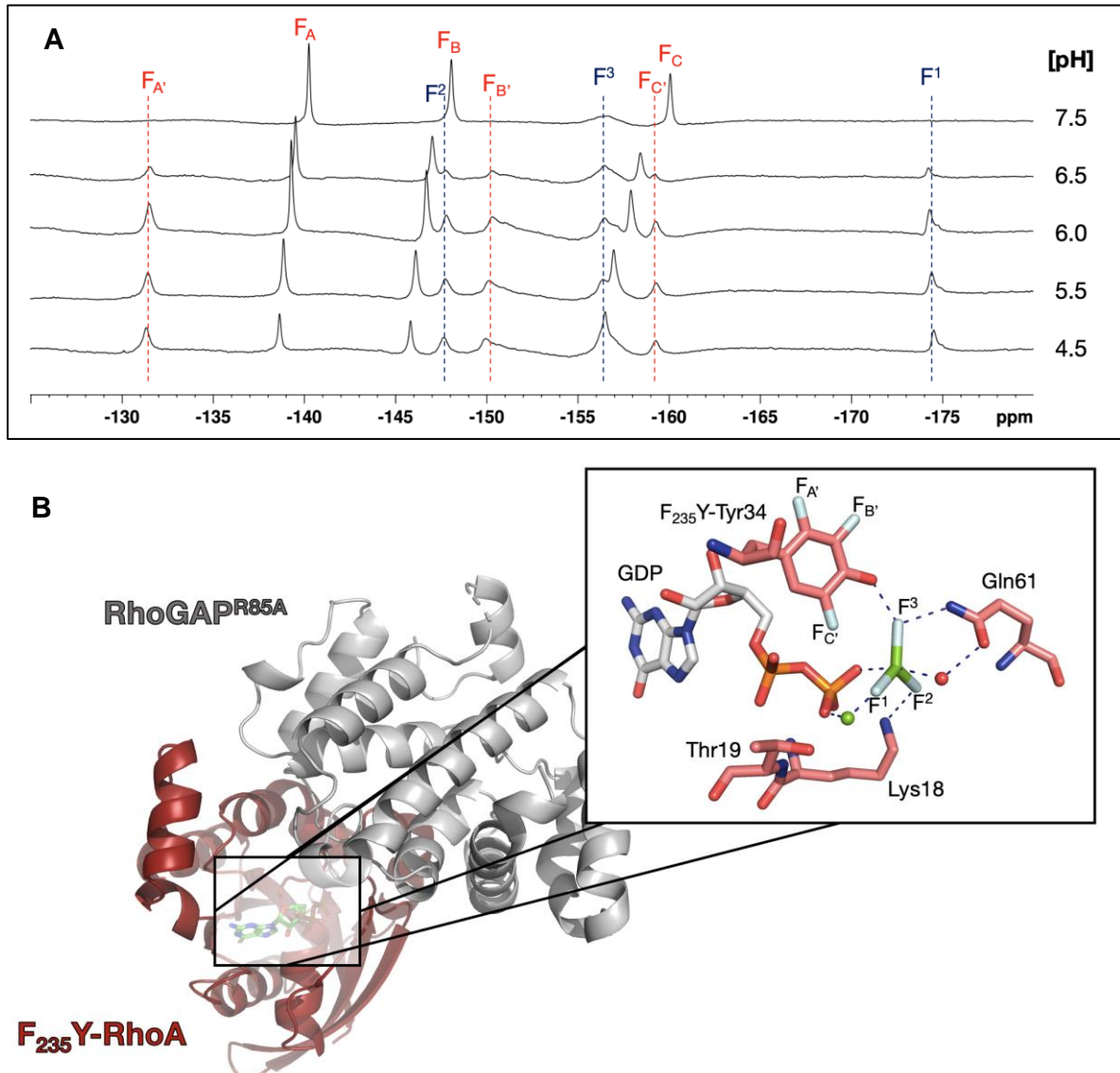


Figure 37: (A) ¹⁹F-NMR spectra of the pH dependant formation of the F²³⁵Y-RhoA/MgF₃⁻/RhoGAP^{R85A} complex.). The free F²³⁵Y-RhoA (F^A, F^B, F^C) and the complexed F²³⁵Y-RhoA (F^{A'}, F^{B'}, F^{C'}) are shown in black while MgF₃⁻ signals (F¹, F², F³) are shown in blue. (B) Model representation of F²³⁵Y-RhoA/MgF₃⁻/RhoGAP^{R85A}.

Two major challenges present themselves with the observation in Fig.37A. The first is the obfuscation of signals from the broad MgF⁺ peak at -157 ppm. This can be resolved through pre-saturation of the fluoride signal as outlined in section 2.3. The second stems from the calibration of ¹⁹F-spectra, which has become a major issue as the use of ¹⁹F-NMR spectroscopy has increased in the recent decades.¹⁴⁷ With subtle chemical shift changes, fluorobenzene was chosen as an internal reference, since a robust referencing system is required to reliably quantify the subtle differences in chemical shift. A second pH titration of the F²³⁵Y-RhoA/RhoGAP^{R85A} mixture was performed with these adjustments as outline in section 2.26. With these

adjusted conditions, accurate values for the fluorine signals involved in F^{235}Y -RhoA/ MgF_3^- /RhoGAP^{R85A} could be obtained (see Tab.11).

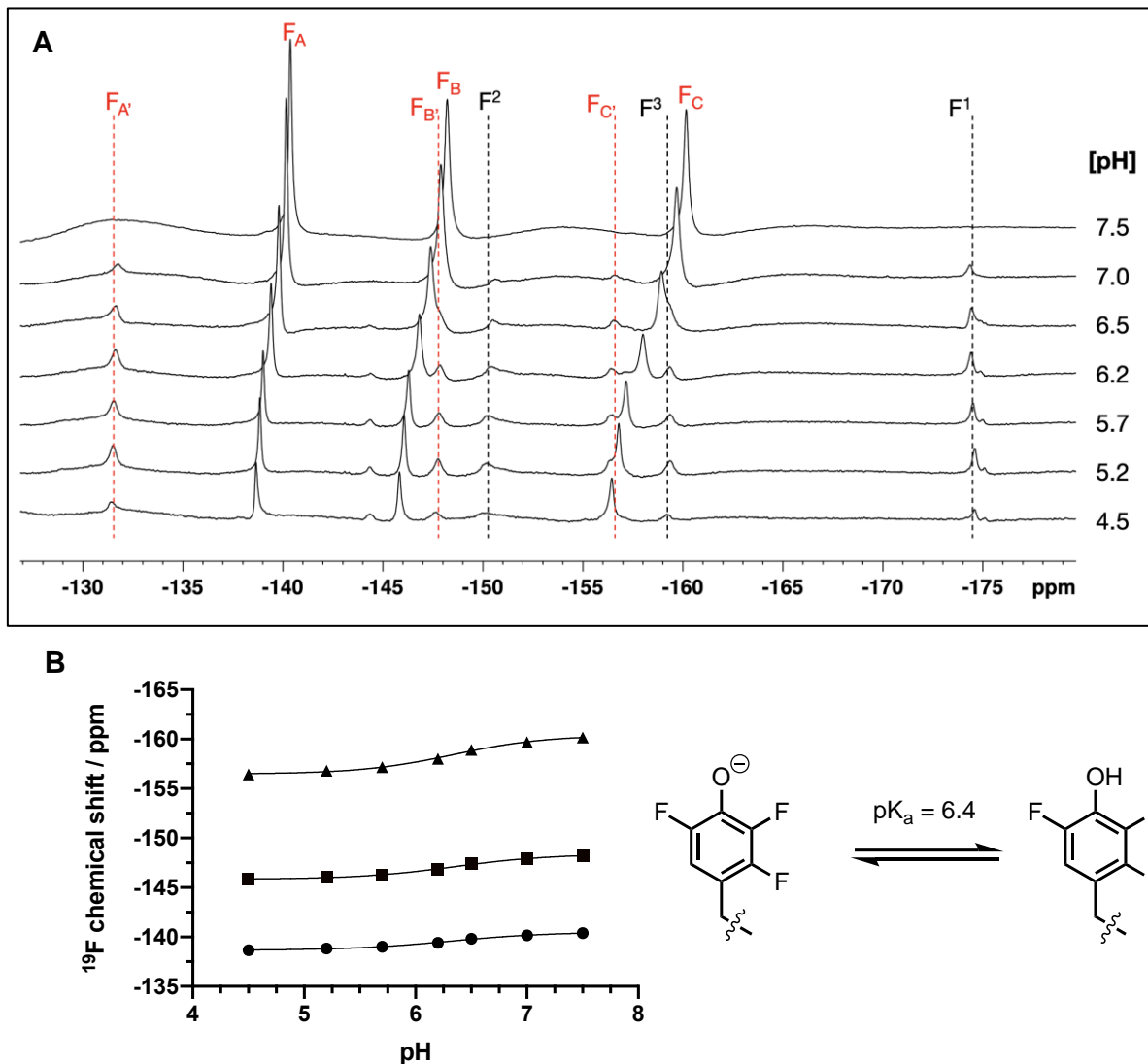


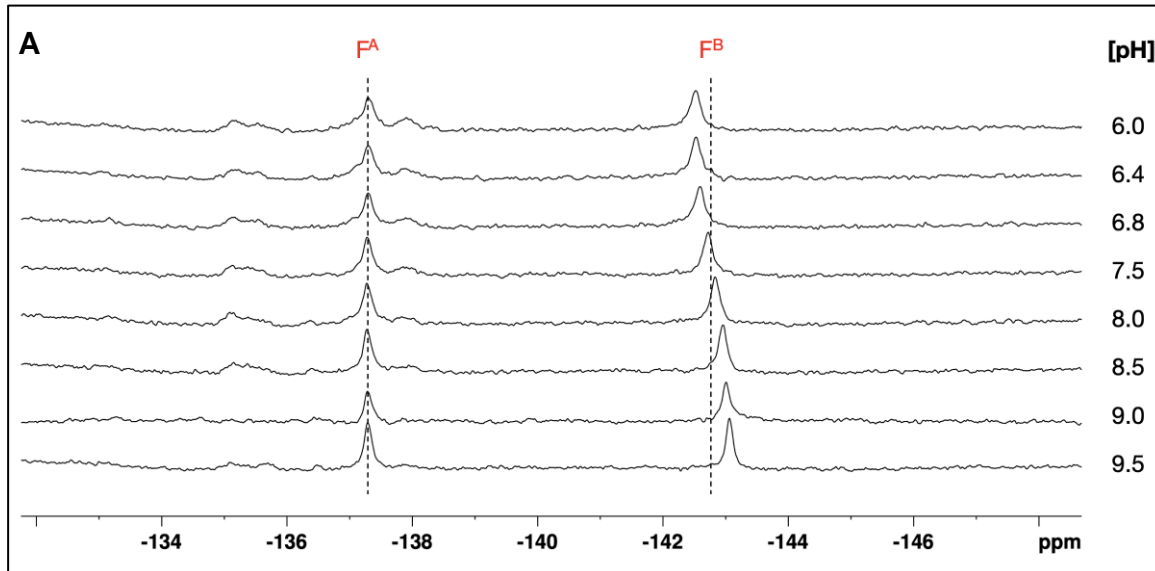
Figure 38: (A) Calibrated ${}^{19}\text{F}$ -NMR spectra of the pH dependant formation of the F^{235}Y -RhoA/ MgF_3^- /RhoGAP^{R85A} complex.) buffered to pH values from 6.0 to 9.5. The free F^{235}Y -RhoA (F_A , F_B , F_C) and the complexed F^{235}Y -RhoA (F_A' , F_B' , F_C') are shown in black while MgF_3^- signals (F^1 , F^2 , F^3) are shown in black. (B) Chemical shift values for free F^{235}Y -RhoA (F_A (●), F_B (■), F_C (▲)) plotted against the pH. The sigmoidal curves fitted to the three datasets yielded an average pK_a value of 6.3.

The signal intensity of the uncomplexed F^{235}Y -RhoA signals decreases as the pH is lowered. This is due to the increased complexation with RhoGAP^{R85A}, which should lead to the majority of the F^{235}Y -RhoA protein to be complexed. With an estimated K_D of $\sim 35 \mu\text{M}$ (see section 4.3.4), the complexation is expected to be $\sim 80\%$, for the conditions at pH = 5.7. However, protein precipitation was observed during the buffer exchange procedure. During the production and purification of both proteins,

RhoGAP_{R85A} was found to be less stable. It is therefore likely that it precipitates in a higher proportion under the buffer exchange condition, leading to an excess of F²³⁵Y-RhoA in the NMR tube.

As in Fig.37, the calibrated signals for the uncomplexed F²³⁵Y-RhoA signals in Fig.38A (F_A , F_B and F_C) show a downfield shift as the pH decreases. When plotted against the buffered pH, the signals can be fitted with a sigmoidal curve, yielding an average pK_a value of 6.3 (Fig.38B). This is in good agreement with the literature value of 6.4 determined for the *N*-acylated carboxyamide L-tyrosine derivate, indicating that these are a good approximation of the pK_a of the incorporated FY side chain.¹⁸⁸ While these literature values give good approximations for Tyr, F³Y-Tyr, F³⁵Y-Tyr and F²³⁵Y-Tyr sidechains, no literature value was available for the *N*-acylated carboxyamide L-tyrosine derivate of F²⁵Y-Tyr.¹⁸⁸

To assess values measured for the F²⁵Y-RhoA/MgF₃⁻/RhoGAP^{R85A} TSA complex, the pK_a was determined by measuring the ¹⁹F-NMR chemical shift transition as described in section 2.26. Interestingly, the signal of the fluorine atom in meta position to the hydroxyl group showed no significant difference between the protonated and the deprotonated species (Fig.39). Therefore, only the ¹⁹F-NMR chemical shift transition of F_B was plotted as a function of pH of the buffer solution and a sigmoidal curve was fitted (Fig.39, see 2.26). The obtained pK_a value of 7.9 is marginally higher than that of the free amino acid ($pK_a = 7.6$). This result is consistent with other examined FYs in the literature.¹⁸⁸



B

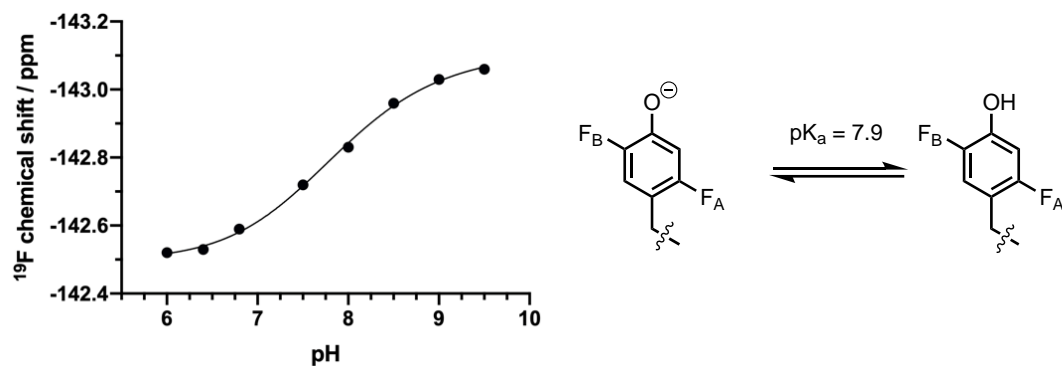
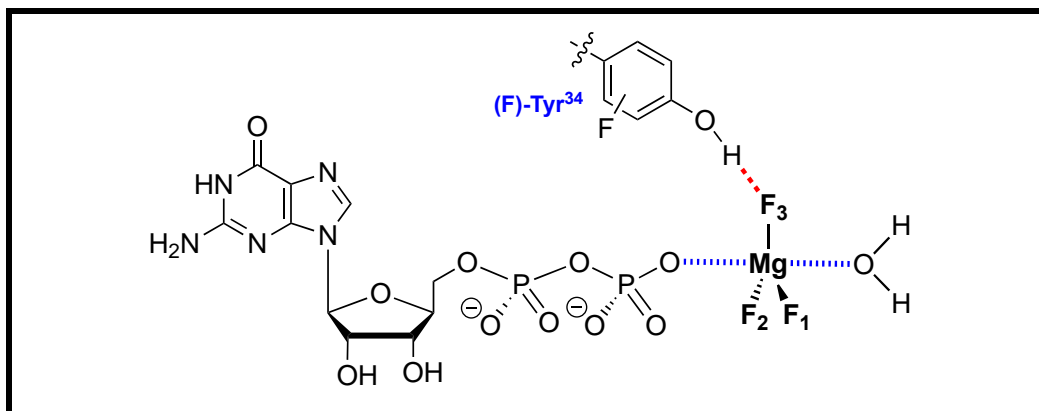


Figure 39: (A) Calibrated ¹⁹F-NMR spectra of F²⁵Y-RhoA buffered to pH values from 6.0 to 9.5 (B) Chemical shift values for free F²⁵Y-RhoA (F_A, F_B) plotted against the pH. The sigmoidal curves fitted to the dataset yielded a pK_a value of 7.9 (see 2.26).

The ¹⁹F-NMR spectra for the remaining MgF₃⁻ complexes were recorded with the same conditions as the ones for F²³⁵Y-RhoA/MgF₃⁻/RhoGAP^{R85A} (see section 2.3 and appendix 5.3). The chemical shifts for the MgF₃⁻ species are tabulated in Tab.11.

Table 11: ^{19}F -NMR chemical shifts of RhoA/MgF₃⁻/RhoGAP^{R85A} TSA complexes and the pK_a values of the (F)-Tyr34 sidechains.^{188,189}



$\delta\Delta$ in ppm	(F)-Tyr34 pK _a	F ¹	F ²	F ³
WT-RhoA	10.2	-172.83	-150.54	-154.99
F ³ Y-RhoA	8.4	-173.26	-151.10	-154.87
F ^{2,5} Y-RhoA	7.9	-173.20	-150.98	-155.03
F ^{3,5} Y-RhoA	7.2	-174.18	-150.01	-157.24
F ^{2,3,5} Y-RhoA	6.4	-174.51	-150.29	-159.35

4.1.2.2 Comparing ^{19}F -NMR Chemical Shifts of FY-RhoA/MgF₃⁻/RhoGAP^{R85A} Complexes

When comparing the ^{19}F -NMR chemical shift values for the FY-RhoA/MgF₃⁻/RhoGAP^{R85A} complexes obtained in section 4.4.2.1, the strongest trend can be observed for the F³ atom of the complex.

This signal had previously been assigned to the fluorine atom, which is in direct contact with the Tyr34 sidechain -OH as depicted in the top part of Tab.11 using QM calculations and solvent-induced isotope shift (SIIS) experiments.¹⁵¹ As such it is not surprising that the decreasing pK_a of the hydroxyl group has a relatively larger effect on the chemical shift. For F¹ a slight upfield shift is observed while no significant change in shielding occurs for F².

This increased shielding has implications for the phosphoryl transfer transition state. One of the major functions of the RhoA/RhoGAP complex in the GTP hydrolysis is

the compensation of the negative charge build-up during the attack of the nucleophilic water. This increased shielding at F³ indicates that increasing the Tyr34 side chain acidity alters the hydrogen bonding in a way that it increases the electron density on this fluorine atom. Therefore, during the phosphoryl transfer transition state, the negative charge at the corresponding oxygen would be stabilised less which could contribute to a slower rate of hydrolysis as the pK_a decreases.

4.1.3 Structural Analysis of FY-RhoA/RhoGAP^{R85A} using X-ray Crystallography

Introducing changes to active site residues always carries the risk of unforeseen consequences, e.g., unintentional changes of side chain conformations. A way to confirm that the active site integrity remains unperturbed, is to generate a structural model of FY-RhoA variants using protein X-ray crystallography.

4.1.3.1 Screening of Crystallisation Conditions

The initial crystallisation attempts were based on conditions used to crystallise WT-RhoA/MgF₃⁻/RhoGAP^{R85A} (PDB: 5M6X, 2.4 Å) as listed in Tab.12.¹⁵⁷

Table 12: Crystallisation parameters for WT-RhoA/MgF₃⁻/RhoGAP^{R85A} complex

Protein buffer		Precipitant	
WT-RhoA	700 µM	BisTris·HCl pH = 6.0	100 mM
RhoGAP ^{R85A}	700 µM	PEG3350	23–26%
BisTris·HCl pH = 6.0	50 mM		
NaCl	150 mM		
MgCl ₂	5 mM		
NaF	20 mM		
DTT	1 mM		

F²³⁵Y-RhoA and F³⁵Y-RhoA variants were chosen to be crystallised. Crystallisation parameters were screened as 1 µL drops in 48-well plates. However, no suitable conditions were found. To improve nucleation, crystallisation trays for the WT-RhoA/MgF₃⁻/RhoGAP^{R85A} was setup with conditions from Tab.12. Protein crystals were readily formed and were subsequently used to seed crystallisation trays for

F^{35}Y - and F^{235}Y -RhoA complexes. This led to crystal formation for both complexes, however due to the long needle shape and the small size, they were unsuitable for X-ray diffraction. Further rounds of seeding could not significantly alter the protein crystal shape for either of the complexes. Therefore, the crystallisation method was changed from a ‘sitting drop’ to a ‘hanging drop’ setup. Drops setup in a 48-well plate are limited to a maximum drop size of about 2 μL , due to the size of the drop pedestal and the vapour chamber. For the ‘hanging drop’ setup the drop volume can be multiple time larger, thus enabling a slower crystal growth as well as a bigger crystal size. After three generations of seeding, a batch of crystals for F^{35}Y -RhoA were harvested and sent to the Diamond Light Source Synchrotron. The crystals diffracted to a resolution of 2.25 \AA and the structure was solved using the CCP4i2 software suite.

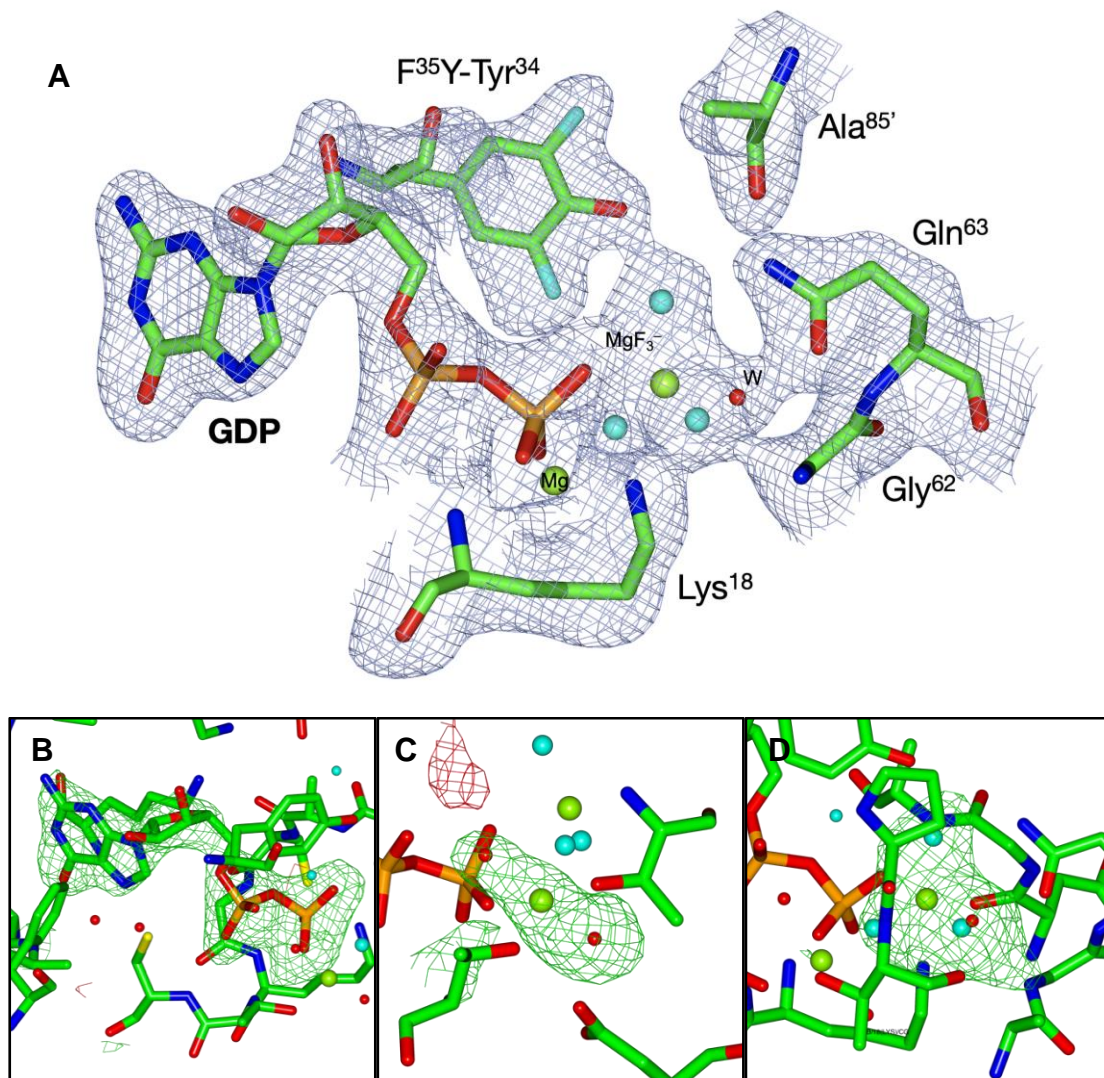


Figure 40: (A) The electron density map of F^{35}Y -RhoA/ MgF_3^- /RhoGAP^{R85A} contoured at 1.0 σ (0.253 e \AA^{-3}) shows the incorporation of F^{35}Y at position 34 of the RhoA active site. Primed residues are part of RhoGAP^{R85A}. Ligand omit maps for F^{35}Y -RhoA/ MgF_3^- /RhoGAP^{R85A} complex.

Difference Fourier map contoured at 3σ : (B) GDP (C) catalytic magnesium with two coordinating waters (D) MgF_3^- .

Using similar conditions, a structure was obtained for the F^{235}Y -RhoA/ MgF_3^- /RhoGAP^{R85A} TSA complex after three rounds of seeding (see section 2.24). The crystals diffracted to a resolution of 1.91 Å and were solved using the CCP4i2 software suite.

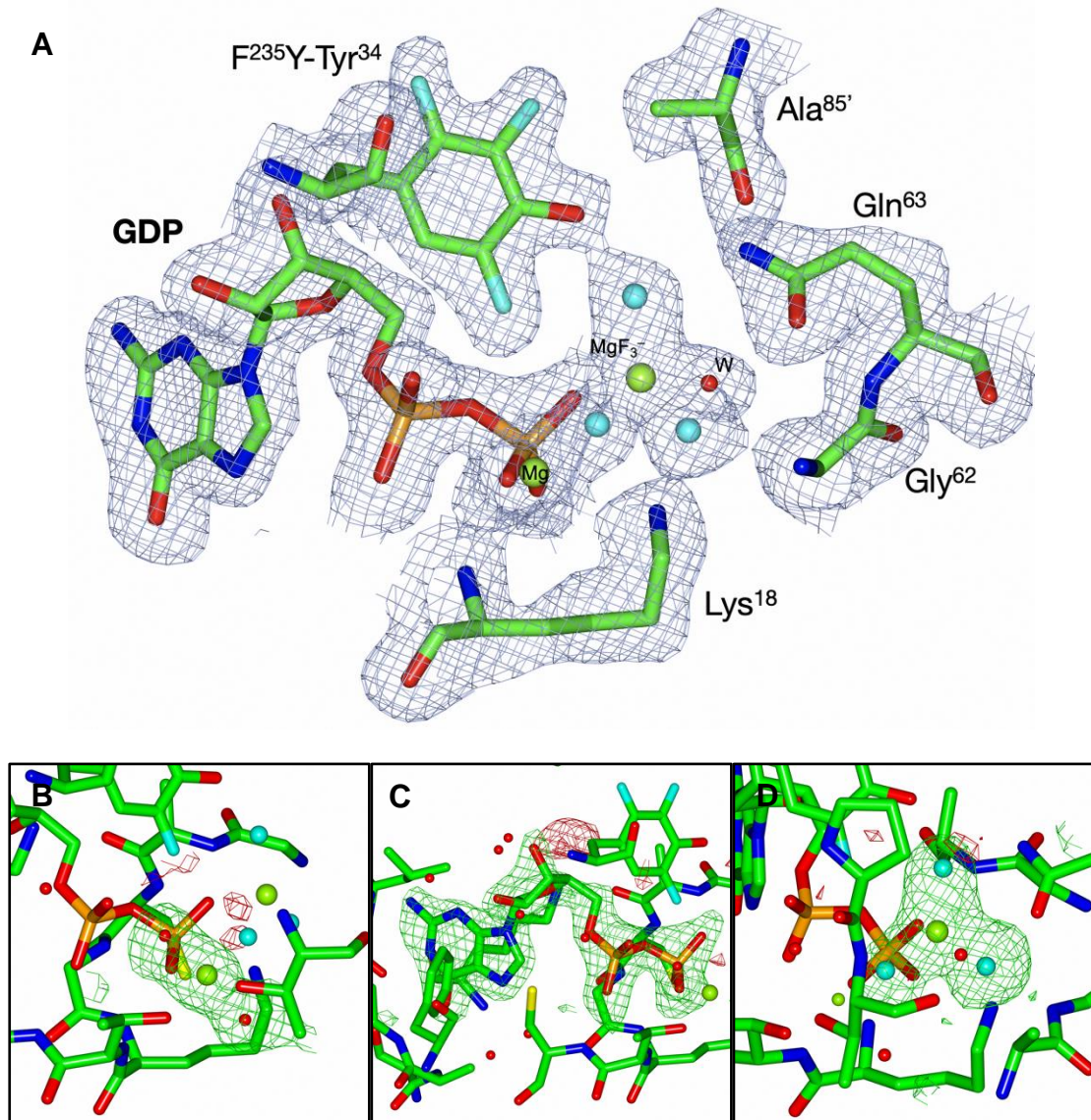


Figure 41: The electron density map of F^{235}Y -RhoA/ MgF_3^- /RhoGAP^{R85A} contoured at 1.0σ ($0.320 \text{ e } \text{\AA}^{-3}$) shows the incorporation of F^{235}Y at position 34 of the RhoA active site. Ligand omit maps for F^{235}Y -RhoA/ MgF_3^- /RhoGAP^{R85A} complex. Primed residues are part of RhoGAP^{R85A}. Difference Fourier map contoured at 3σ : (B) GDP (C) catalytic magnesium with two coordinating waters (D) magnesium trifluoride.

Table 13: Data collection and refinement statistics for F^{35}Y -RhoA/MgF₃⁻/RhoGAP^{R85A} and F^{235}Y -RhoA/MgF₃⁻/RhoGAP^{R85A}

	F^{35}Y -RhoA/RhoGAP ^{R85A}	F^{235}Y -RhoA/RhoGAP ^{R85A}
Crystal Data		
Wavelength	0.976 Å	0.976 Å
Space group	P 1 21 1	P 1 21 1
<i>a</i> , <i>b</i> , <i>c</i> (Å)	73.63, 66.60, 76.46	73.77, 66.49, 76.96
α , β , γ (°)	90.00, 95.02, 90.00	90.00, 95.27, 90.00
Resolution (Å)	55.31–2.25	55.64–1.91
R_{merge}	0.083	0.065
$I / \sigma I$	10.8 / 1.0	19.3 / 1.0
CC _(1/2)	0.988 / 0.530	0.999 / 0.649
Completeness (%)	99.2 / 100.0	99.4 / 100.0
Refinement		
No. reflections	35121 / 1683	57665 / 2918
$R_{\text{work}} / R_{\text{free}}$	0.220 / 0.306	0.242 / 0.293
<u>No. atoms</u>		
Protein	5814	5817
Ligand/ion	92 / 2	94 / 2
Water	134	225
<u>B-factors</u>		
Protein	42.57	30.78
Ligand/ion	35.92 / 32.63	25.01 / 18.54
Water	36.39	29.60
<u>RMS deviations</u>		
Bond lengths (Å)	0.0076	0.0145
Bond angles (°)	1.62	1.89

4.1.3.2 Comparative Analysis of FY-RhoA/MgF₃⁻/RhoGAP and Implications for other Small G protein Systems

When comparing the structures of the WT-RhoA/MgF₃⁻/RhoGAP^{R85A} TSA to the F³⁵Y-RhoA (Fig.40) and F²³⁵Y-RhoA (Fig.41) variants, the identical fold of the complexes is apparent (Fig.42A). This clearly indicates that no major conformational shifts occur as a result of the FY incorporation, a result of the relatively small size of the additional fluorine substituents. Therefore, effects from the FY incorporation on the polarisation of the MgF₃⁻ result from the shift in Tyr34 hydroxyl acidity. By extension this also relates to the differences in activity measured in section 4.3.4.

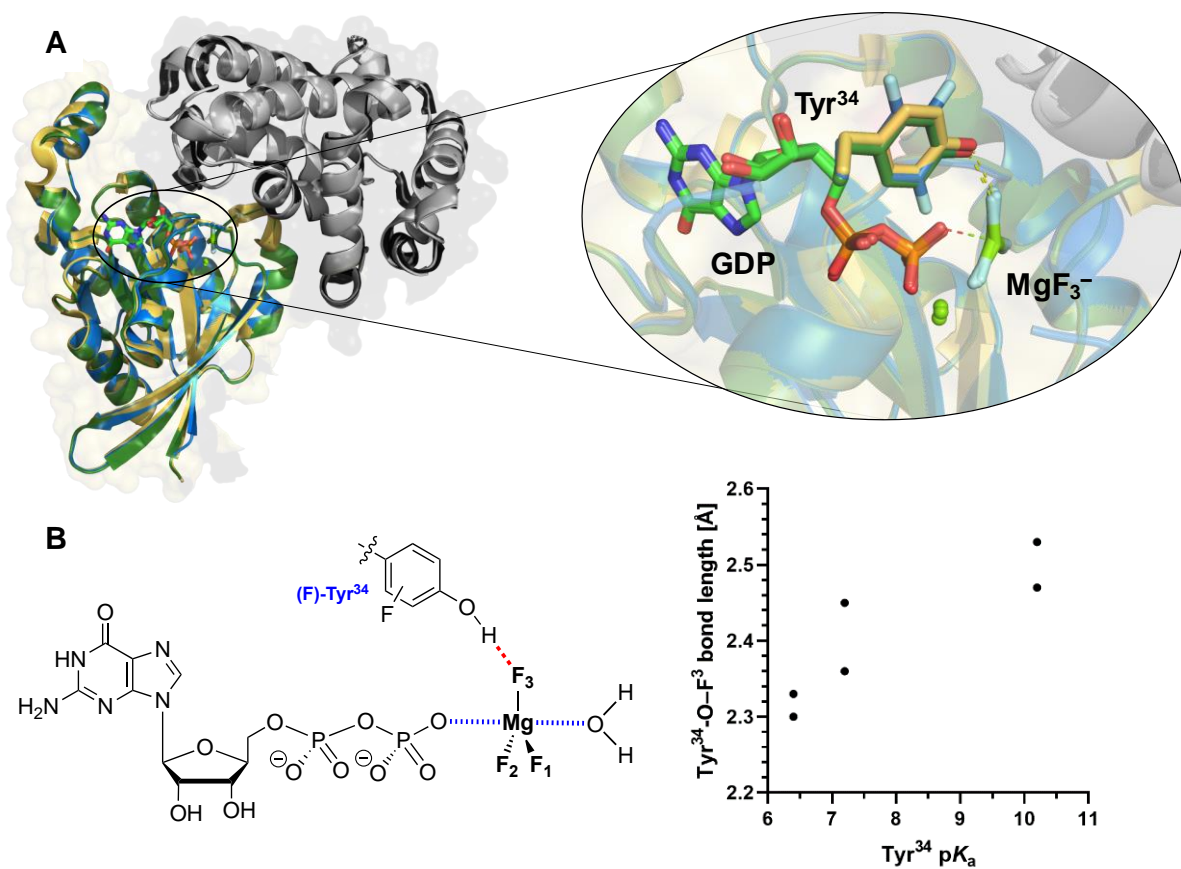


Figure 42: (A) Alignment of RhoGAP^{R85A} (grey) complexed with WT-RhoA (yellow), F³⁵Y-RhoA (green) and F²³⁵Y-RhoA (blue). (B) Bond lengths of hydrogen bond between Tyr34-hydroxyl group and F³ of MgF₃⁻ TSA plotted against the Tyr34 side chain pK_a. For the complexes each of the two protein assemblies in the asymmetric unit were measured.

Interestingly, while the overall conformation of the RhoGAP^{R85A} complexes did not show significant changes upon FY incorporation, a trend of Tyr34–MgF₃⁻ hydrogen bond length versus the pK_a of the FY can be found. With increasing acidity of the hydroxyl group, the heteroatom O–F³ bond distance shows a slight decrease from

around 2.5 Å for the WT-RhoA complex to 2.3 Å for the F²³⁵Y-RhoA complex (Fig.42B). The basis of this increased hydrogen bonding strength could be attributed to the improved pK_a matching of the two hetero atoms.¹¹³ As hydrogen bonds in proteins are generally in the area of 2.8 Å, a bond length of 2.5 Å is already relatively short. At these distances the energy barrier for the proton transfer between the two heteroatoms gets significantly lowered and the strength of the interaction increases. Hydrogen bonding interactions where the heteroatom distance is 2.3 Å are classed as ‘single-well hydrogen bond’ where the hydrogen is essentially equally associated with both hetero atoms.¹⁹⁰ To recognise the shortening of H-bonds in the FY-RhoA/RhoGAP^{R85A} structures, however, several factors need to be considered. As protein X-ray crystallography inherently introduces bias through the refinement process, due to different weighting applied to the structure restraints, the bond lengths and angles in the final structure model carry a certain error regarding the absolute bond length values.^{191,192} The higher the resolution, the more confident the position of the atoms is fitted. Thus, atoms in crystal structures with atomic resolution can be fitted with higher confidence. The three RhoA/MgF₃⁻/RhoGAP^{R85A} complexes examined here have resolutions between 1.9 and 2.5 Å and therefore there is a higher degree of uncertainty when it comes to interatomic distances. From this, it is difficult to determine the actual bond distances for the complexes, which is problematic as these small differences carry significant implications for the bonding energies. With only three structures for comparison, this can only provide a first indication of a trend between the Tyr34 side chain acidity and the strength of the donated hydrogen bond the F³ atom. In the case of the phosphoryl group in the transition state, it is likely that the Tyr34-O-H···O3G distance is longer, as the equatorial P–O bond (1.5 Å) is 0.3 Å shorter than the analogous Mg–F bond (1.8 Å).⁵³ Computational analysis of this model system could provide insights towards the validity of this trend.

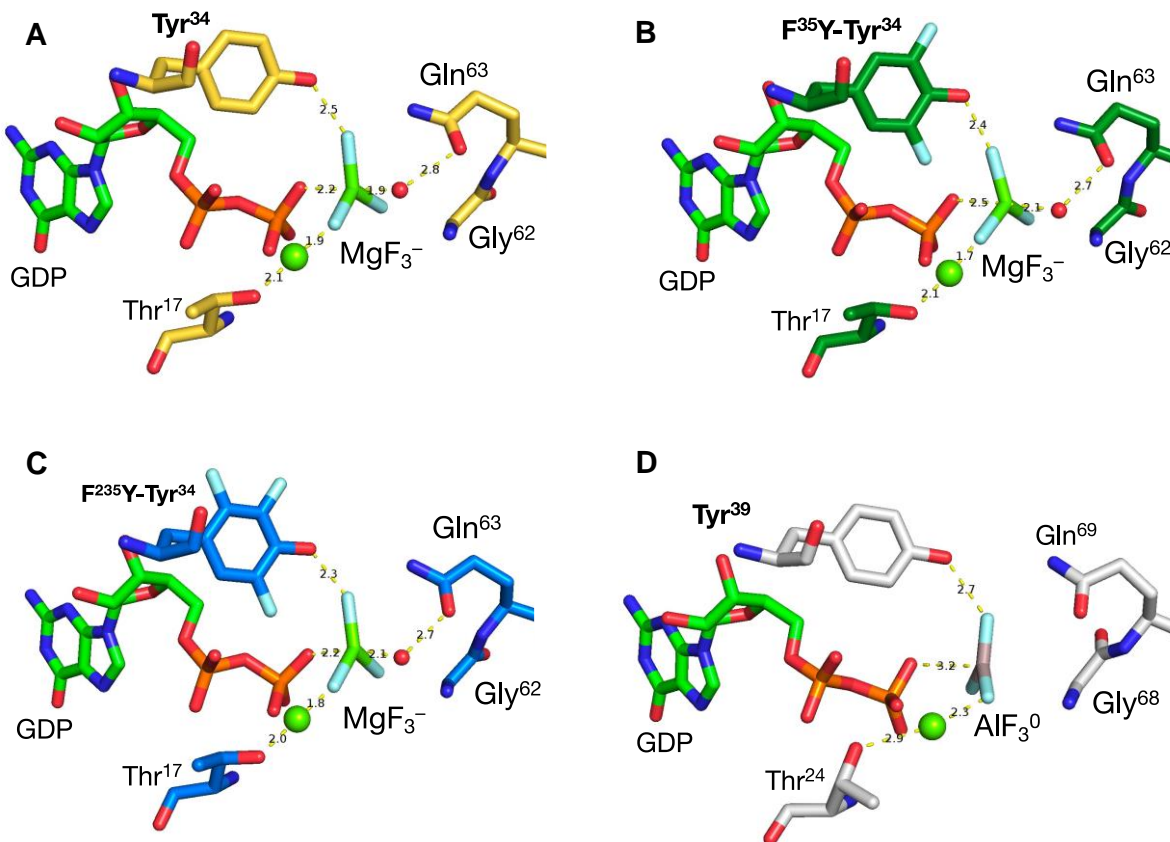


Figure 43: Comparison of metal fluoride TSA complex structures to show the position of a conserved tyrosine residue involved in GTP hydrolysis. (A) WT-RhoA/MgF₃⁻/RhoGAP^{R85A} (B) F³⁵Y-RhoA/MgF₃⁻/RhoGAP^{R85A} (C) F²³⁵Y-RhoA/MgF₃⁻/RhoGAP^{R85A} (D) Ran/AlF₃⁰/RanGAP (PDB:1K5G).

When comparing this system to other small G Protein/GAP complexes without a catalytic Arg residue, like Ran and Rap, these structures can be used as a good model to understand the role of tyrosine. Ran for example is a small G protein which controls nucleo-cytoplasmic transport through the nuclear pore complex as well as cell cycle progression through the regulation of microtubule polymerisation. It has been linked to various types of cancer and is therefore a therapeutic target.^{193,190} For these systems, only low-resolution structures exist in the literature (>2.7 Å). These structures lack important details, such as active site waters and exact orientations of amino acid side chains.¹⁰⁴ For example, there are no TSA crystal structures where the nucleophilic water is resolved (Fig.43D). This makes it difficult to draw conclusions about the exact mechanistic details.

Regarding the question of the ‘second water’ mechanism, the obtained electron density maps (Fig.40 and Fig.41) clearly show, that no additional water is in the

vicinity of the metal fluoride species. It is therefore unlikely, that these types of GTPase/GAP systems function via this mechanism.

4.1.4 Assessing Kinetic Profiles of Fluorinated RhoA Variants in the Context of RhoA/RhoGAP^{R85A}

A key characteristic when comparing enzymes are the kinetic properties. Several key steps are involved in the RhoA/RhoGAP catalysed GTP hydrolysis, which are outlined in Fig.44. Starting with the GTP nucleotide binding (k_1), followed by the RhoA/GTP/RhoGAP complex formation (k_2), the cleavage of the γ -phosphoester bond (k_3) and finally the phosphate release step (k_4). As RhoA on its own stabilises the GTP hydrolysis transition state, it has an intrinsic activity (k_{intr}).¹⁵⁸ However, as this rate is several orders of magnitude slower than the RhoGAP catalysis, it is often negligible. A further complication for the kinetics of small G proteins, is that sometimes not the GTP hydrolysis, but the release of the inorganic phosphate from the enzyme active site can be the rate-determining step.¹⁹⁵

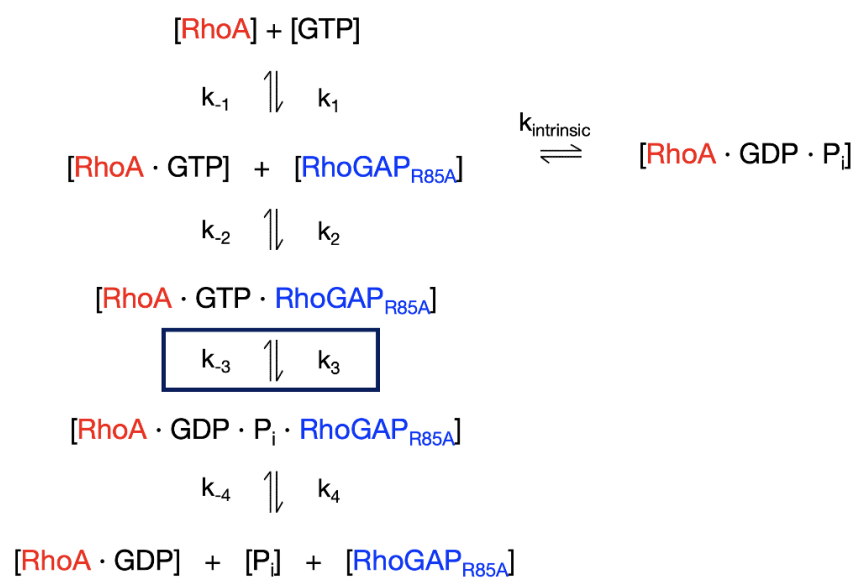


Figure 44: Overview of catalytic steps relevant for the RhoGAP^{R85A} catalysed GTP hydrolysis by RhoA. These are GTP binding (k_1), RhoA/GTP/RhoGAP^{R85A} complex formation (k_2), cleavage of the γ -phosphoester bond (k_3), phosphate release (k_4) as well as the intrinsic RhoA catalysed GTP hydrolysis (k_{intr}).

4.1.4.1 Hydrolysis of Fluorescently Labelled Nucleotide Mant-GTP

Assessing kinetic parameters of small G proteins is challenging. One of the most versatile strategy to overcome the challenges of measuring small G protein kinetics is the use of fluorescently labelled nucleotide, the most common of which is the methylanthraniloyl (mant) group.¹⁹⁶ This fluorescent nucleotide analogue can be excited at a wavelength of 360 nm, a wavelength at which proteins or nucleotides do not absorb, and fluoresce at 440 nm.¹⁹⁷ While they are weakly fluorescent in aqueous solutions, their fluorescence can be enhanced significantly upon binding to a small G protein. As previously mentioned, small G proteins have a high binding affinity to guanine nucleotides, preventing dissociation of the product. Therefore, RhoA needed to be preloaded with the relevant fluorescent nucleotide and the kinetics of the phosphoester bond cleavage can be investigated under single-turnover conditions analogous to literature conditions.¹⁹⁸ There, a difference in fluorescence is monitored as mant-GTP is hydrolysed to mant-GDP. Incubating a mant-GTP-loaded small G protein with varying concentrations of GAP can be used to determine kinetic parameters like K_m and k_{cat} . Based on this, an assay was designed where the loaded RhoA variant is mixed with varying concentrations of RhoGAP^{R85A} in a multi-well plate and the fluorescence is monitored in a plate reader.

The nucleotide exchange of bound GDP for GTP/mant-GTP is well documented in the literature and most commonly done by sequestering Mg²⁺ which is necessary for nucleotide binding with a chelating agent such as EDTA.^{196,199} This approach was performed based on literature conditions (section 2.23). In order to ensure loading of the fluorescent nucleotide, the 280/350nm ratio was monitored yielding a loading of >90%.

Mant-GTP-loaded WT-RhoA or F²³⁵Y-RhoA was incubated with increasing concentrations of RhoGAP^{R85A}, and the fluorescence was monitored. After several attempts, no significant difference could be detected between the RhoGAP^{R85A}-catalysed reactions and the control reaction without RhoGAP^{R85A} (Fig.45A). Further literature research revealed that while the transition from mant-GTP to mant-GDP can be monitored for many small G proteins, such as HRas and Rac1, RhoA shows no change in relative fluorescence between the two nucleotides.²⁰⁰ AMIN *et al.* found a cyanine-labelled guanine nucleotide which is able to monitor the hydrolysis of the γ -phosphoester bond when bound to RhoA (Fig.45E).²⁰⁰ While this alternative

fluorescent probe seems like a viable option, more economical approaches were pursued.

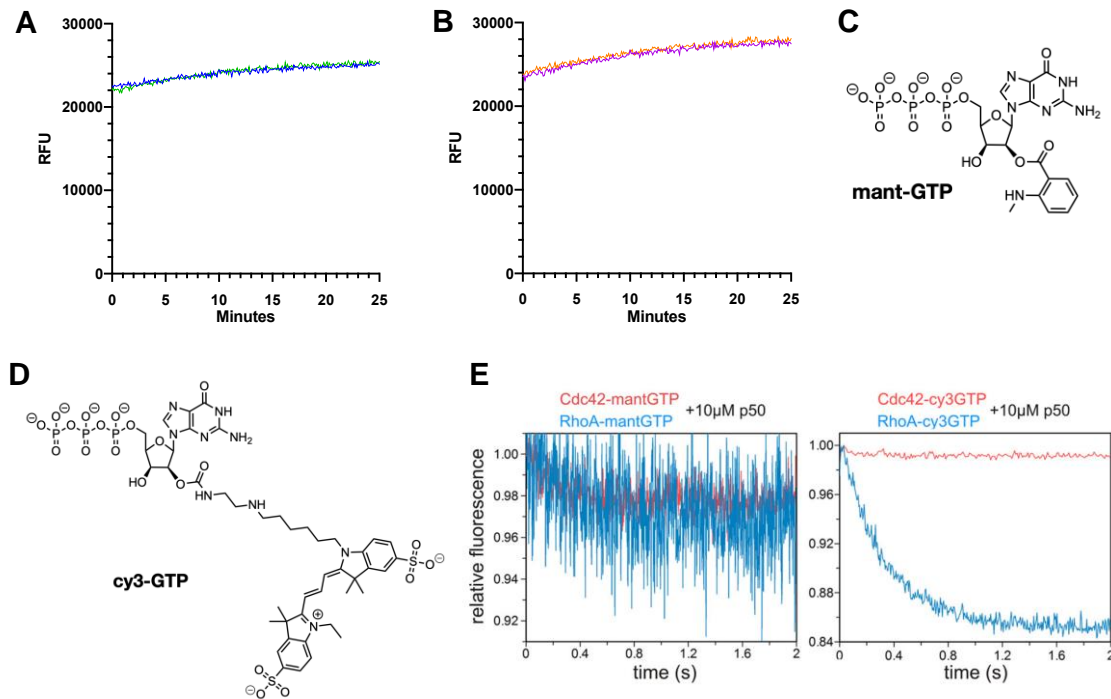


Figure 45: RhoGAP^{R85A} catalysed GTP hydrolysis of 5 μM mant-GTP-loaded (A) WT-RhoA (green: 0 μM RhoGAP^{R85A}; blue: 5 μM RhoGAP^{R85A}) or (B) F²³⁵Y-RhoA (purple: 0 μM RhoGAP^{R85A}; orange: 5 μM RhoGAP^{R85A}). (C) mant-GTP (D) cy3-GTP (E) No change in fluorescence is detected for the RhoA-catalysed mant-GTP hydrolysis (adapted from AMIN et al.).²⁰⁰

4.1.4.2 Measuring RhoA-catalysed GTP hydrolysis using ³¹P-NMR

As an alternative way to measure kinetic parameters, ³¹P-NMR was explored. This has previously been used extensively to assay the kinetics of enzyme-catalysed nucleotide hydrolysis.^{201,202} The advantage is that, with GTP, the actual substrate is being used instead of an analogue such as mant-GTP or cy3-GTP. Furthermore, the signals from the recorded spectrum directly report on the hydrolysis of the γ-phosphate group, without having to consider the kinetics of the phosphate release from the active site. However, there are some drawbacks when it comes to applying this methodology to small G proteins. While most kinetic studies on phosphorus containing substrate studies work with steady state conditions, the binding kinetics of small G proteins require single-turnover conditions, with RhoA being preloaded with GTP. This greatly reduces the concentration of available substrate, as well as increases the tumbling rate of the observed ³¹P-species.²⁰³ Additionally, ³¹P nuclei

are intrinsically less sensitive compared to others like ^1H or ^{19}F . A further complication arises due to the similar chemical shift of the α - and β -phosphates of GDP and the α - and γ -phosphates of GTP, which can cause an overlapping of the signals. Therefore, GTP-loaded WT-RhoA was prepared (see section 2.23) and a ^{31}P -NMR spectrum was recorded to assess whether the signal to noise ratio is sufficient for conducting kinetic studies.

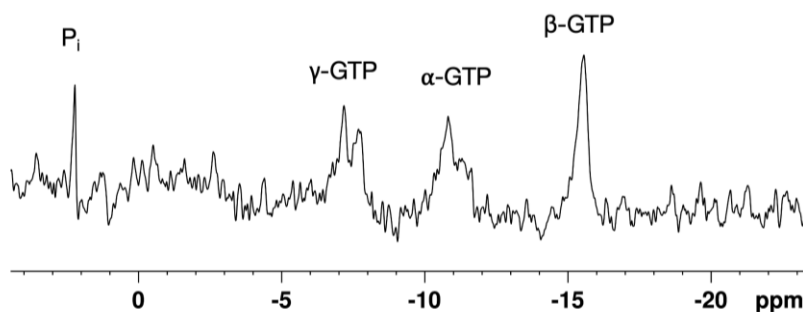


Figure 46: ^{31}P -NMR spectrum of WT-RhoA-GTP 0.5 mM, BisTris:HCl 50 mM pH = 6.0, NaCl 150 mM, MgCl₂ 5 mM / D₂O 10% recorded on a 600 MHz spectrometer with 512 scans.

To collect meaningful data for kinetic parameters, a significant level of signal intensity must be recorded in a short time span. This time span must be short enough to observe the transition from GTP-loaded RhoA to GDP-loaded RhoA. Unfortunately, the signal intensity obtained from a 256-scan spectrum is too low for kinetic measurements. While a higher number of scans make it possible to detect the signals of the bound GTP (Fig.46), the necessary acquisition time per spectrum prevents its use for the assessment of kinetic parameters of this RhoA/RhoGAP^{R85A} system.

4.1.4.3 Analysis of Kinetic Parameters for the RhoGAP^{R85A}-catalysed Hydrolysis of FY-RhoA-GTP

Due to the problems with the assay methods tried earlier, a new HPLC-based approach was chosen. Here, the rate of GTP hydrolysis is measured by mixing GTP-loaded RhoA with a series of RhoGAP^{R85A} concentrations and taking aliquots at various timepoints (Fig.47). These aliquots are immediately quenched using TCA/NaOAc and the GTP/GDP levels are determined using HPLC. For a detailed description of the assay procedure see section 2.27. This method was not the first choice, as it is very labour intensive and supplies fewer data points compared to a

continuous assay. However, as its working principle is very robust, it holds numerous advantages: (1) Only a few μL are needed for each HPLC injection, reducing the overall amount of required enzyme. (2) Using GTP as substrate prevents the slight errors introduced by using a non-natural GTP analogue such as mant-GTP. (3) The measured rate is not influenced by secondary factors such as the release of phosphate or its subsequent translation into a signal, i.e., using the enzyme PNP.

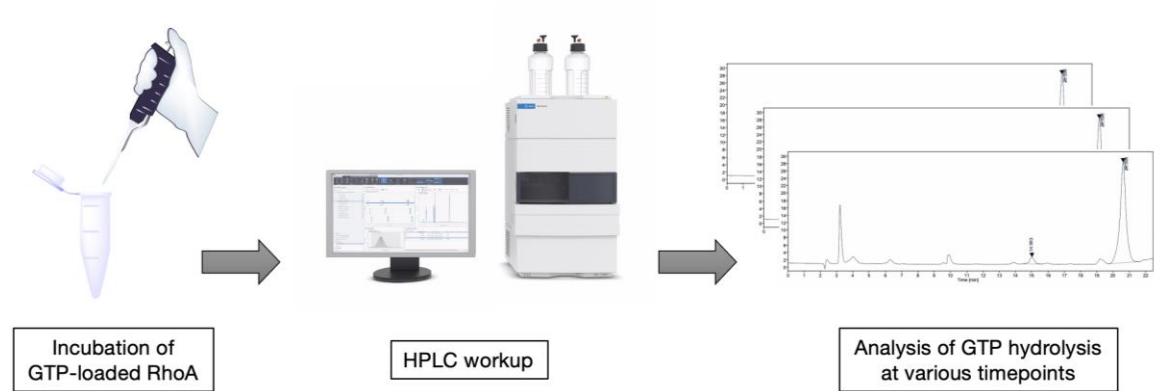


Figure 47: Workflow measuring the hydrolysis rate of RhoA-bound GTP using HPLC.

For the first step of this assay optimal conditions were screened for the separation of the GTP and GDP nucleotide using a C18 reverse phase column (Fig.48). Tetrabutylammonium was used as an ion-pairing reagent to improve the separation efficiency. The rate for RhoGAP^{R85A} catalysed GTP hydrolysis has been reported as $1.0 \times 10^{-2} \text{ s}^{-1}$ at 25°C , yielding a half-life of just under 70 s.¹⁵¹ Several seconds are needed for the taking and workup of each timepoint aliquot. To ensure an adequate number of data points for each GTP decay curve, all assays were performed at 4°C . This also improves enzyme stability for assays with durations of several hours, as is necessary for measuring the intrinsic GTP hydrolysis rate for the RhoA variants.

As outlined in section 4.4.4.1 the intrinsic RhoA GTP hydrolysis rate had to be determined. Therefore, GTP-loaded WT-RhoA was incubated at 4°C for several hours, and the GDP/GTP ratio was determined at various timepoints (Fig.48B). Based on the assumption that all guanine nucleotides are bound to RhoA, the recorded datapoints were fitted to a single exponent decay function (Fig.48C), yielding an intrinsic hydrolysis rate of $2.2 \times 10^{-5} \text{ s}^{-1}$. This is in line with the literature when accounting for the decreased temperature using the Van 't Hoff equation.^{151,204}

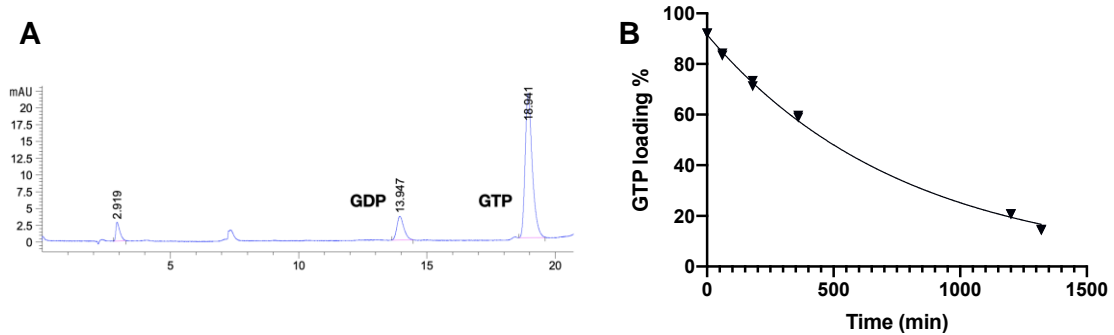


Figure 48: (A) UV trace showing the separation of guanine nucleotides GTP and GDP. (B) GTP loading of the RhoA enzyme over time fitted to a single exponent decay function to yield the intrinsic GTP hydrolysis rate of $2.2 \times 10^{-5} \text{ s}^{-1}$.

In order to determine the RhoGAP^{R85A}-catalysed rate of hydrolysis, GTP-loaded WT-RhoA (section 2.23) was incubated at 4°C for with various concentrations of RhoGAP^{R85A}, and the GDP/GTP ratio was determined at various timepoint (Fig.48). The observed rate for GAP catalysed GTP hydrolysis consists of two components (Eq.6), the intrinsic RhoA GTP hydrolysis rate (k_{int}) and the RhoGAP^{R85A}-catalysed GTP hydrolysis rate ($k_{\text{R85Ax}\mu\text{M}}$).

$$y = y_0 \times e^{-k_{\text{R85Ax}\mu\text{M}}t} - y_0(1 - e^{-k_{\text{int}}t}) \quad (6)$$

y: GTP loading %; y_0 : initial GTP loading %

This two-exponential decay function was fitted to the obtained data points for the tested RhoGAP^{R85A} concentrations (Fig.49A–E). The detailed fitting parameter and measured rates are tabulated in section 5.9. The plotted rates show a hyperbolic increase as a function of the RhoGAP^{R85A} concentration (Fig.49F). A corresponding curve was fitted to yield a K_M of 22 μM and a k_{cat} of $7.1 \times 10^{-3} \text{ s}^{-1}$ (Tab.14).

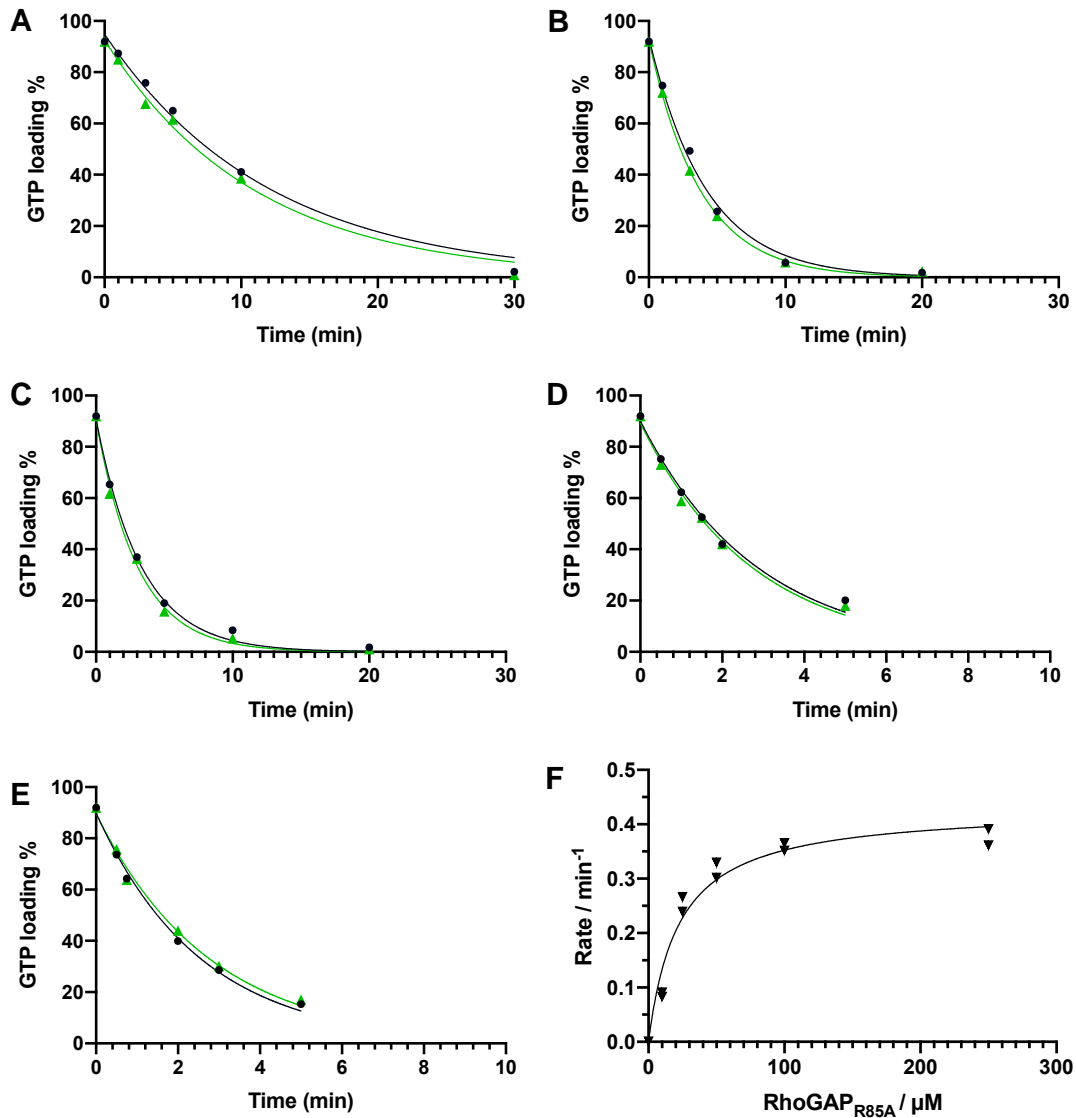


Figure 49: Kinetic analysis of the of RhoGAP^{R85A}-catalysed hydrolysis of GTP-loaded RhoA using single turnover kinetics. 50 µM of GTP-loaded ^{WT}RhoA are turned over with (A) 10 µM, (B) 25 µM, (C) 50 µM, (D) 100 µM or (E) 250 µM of RhoGAP^{R85A}. All runs were run in duplicates (1: ●, 2: ▲) (F) Rates were obtained by fitting a two-exponential decay function, plotted against the RhoGAP^{R85A} concentration, and fitted with a hyperbolic curve (see section 2.28).

This procedure was repeated for F³Y-RhoA, F³⁵Y-RhoA, F²⁵Y-RhoA and F²³⁵Y-RhoA. As these exhibited slower GTP hydrolysis rates, the intervals between timepoint aliquots were adjusted. The results are summarised in Fig.50.

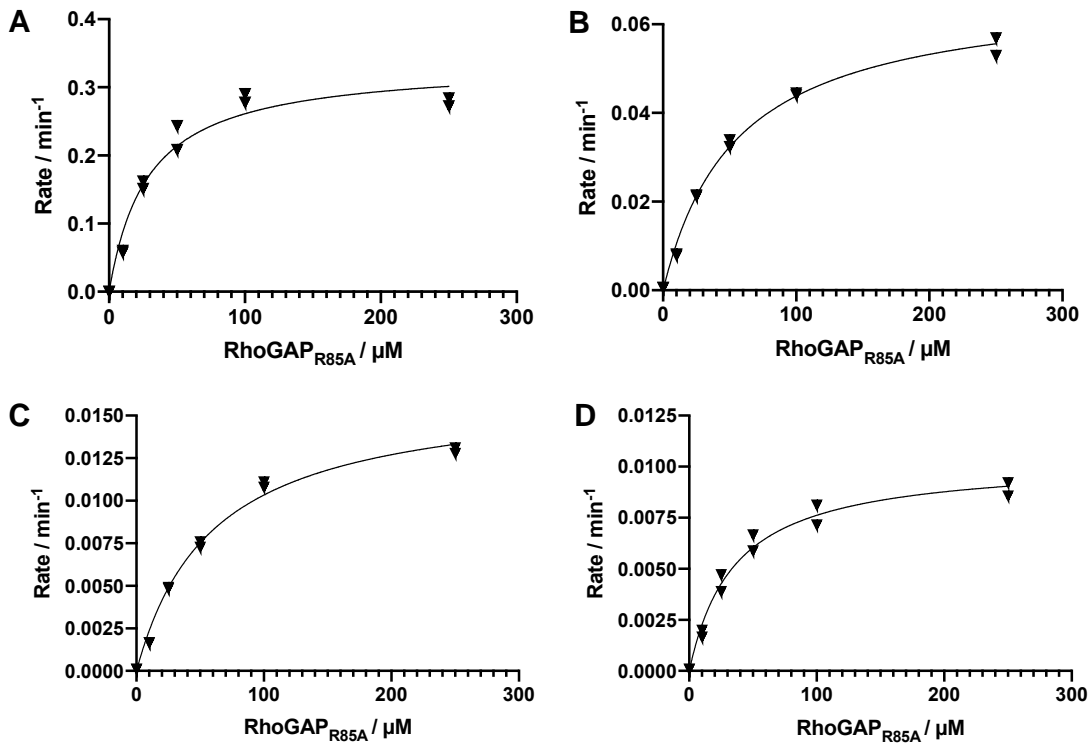


Figure 50: Rates for (A) F^3Y -RhoA, (B) F^{25}Y -RhoA, (C) F^{35}Y -RhoA and (D) F^{235}Y -RhoA, obtained from fitting decay functions analogous to WT-RhoA (Fig.49), plotted against the $\text{RhoGAP}^{\text{R85A}}$ concentration, and fitted with a hyperbolic curve (see section 2.28).

Table 14: Intrinsic (k_{intr}) and $\text{RhoGAP}^{\text{R85A}}$ -catalysed ($k_{\mu\text{M}}$) GTP hydrolysis rates for FY-RhoA. Errors give the 95% confidence interval of the fitted curve.

All values are given in min^{-1}	WT-RhoA	F^3Y -RhoA	F^{25}Y -RhoA	F^{35}Y -RhoA	F^{235}Y -RhoA
k_{intr}	1.3×10^{-3} $\pm 1.9 \times 10^{-4}$	7.7×10^{-4} $\pm 6.0 \times 10^{-2}$	7.3×10^{-4} $\pm 7.9 \times 10^{-5}$	1.4×10^{-4} $\pm 5.0 \times 10^{-5}$	1.1×10^{-4} $\pm 3.6 \times 10^{-5}$
$k_{10\mu\text{M}}$	8.8×10^{-2} $\pm 2.7 \times 10^{-2}$	6.0×10^{-2} $\pm 1.2 \times 10^{-2}$	8.1×10^{-3} $\pm 1.2 \times 10^{-3}$	1.7×10^{-3} $\pm 6.2 \times 10^{-4}$	1.9×10^{-3} $\pm 4.6 \times 10^{-4}$
$k_{25\mu\text{M}}$	2.5×10^{-1} $\pm 4.5 \times 10^{-2}$	1.6×10^{-1} $\pm 2.9 \times 10^{-2}$	2.1×10^{-2} $\pm 2.8 \times 10^{-3}$	4.9×10^{-3} $\pm 1.4 \times 10^{-3}$	4.3×10^{-3} $\pm 4.8 \times 10^{-4}$
$k_{50\mu\text{M}}$	3.2×10^{-1} $\pm 7.7 \times 10^{-2}$	2.3×10^{-1} $\pm 7.0 \times 10^{-2}$	3.3×10^{-2} $\pm 4.5 \times 10^{-3}$	7.5×10^{-3} $\pm 1.6 \times 10^{-3}$	6.3×10^{-3} $\pm 4.7 \times 10^{-4}$
$k_{100\mu\text{M}}$	3.6×10^{-1} $\pm 1.0 \times 10^{-1}$	2.8×10^{-1} $\pm 1.4 \times 10^{-1}$	4.4×10^{-2} $\pm 5.3 \times 10^{-3}$	1.1×10^{-2} $\pm 2.5 \times 10^{-3}$	7.7×10^{-3} $\pm 1.8 \times 10^{-3}$
$k_{250\mu\text{M}}$	3.8×10^{-1} $\pm 6.3 \times 10^{-2}$	2.7×10^{-1} $\pm 1.3 \times 10^{-1}$	4.8×10^{-2} $\pm 1.2 \times 10^{-2}$	1.3×10^{-2} $\pm 1.6 \times 10^{-3}$	8.9×10^{-3} $\pm 2.0 \times 10^{-3}$

k_{cat}	$4.3 \times 10^{-1} \pm 5.0 \times 10^{-2}$	$3.3 \times 10^{-1} \pm 4.2 \times 10^{-2}$	$5.8 \times 10^{-2} \pm 5.5 \times 10^{-3}$	$1.7 \times 10^{-2} \pm 1.4 \times 10^{-3}$	$1.0 \times 10^{-2} \pm 9.5 \times 10^{-4}$
K_{M}	$22 \pm 9 \mu\text{M}$	$28 \pm 12 \mu\text{M}$	$41 \pm 11 \mu\text{M}$	$59 \pm 12 \mu\text{M}$	$36 \pm 10 \mu\text{M}$

4.1.4.4 Analysis of Kinetic Parameters for the intrinsic Hydrolysis of FY-RhoA-GTP

When comparing the intrinsic GTP-hydrolysis rate for the FY-RhoA variants a similar trend can be observed (Fig.51A). The intrinsic RhoA GTP hydrolysis rate is the fastest for the WT and decreases as the Tyr34 side chain pK_a is lowered. This supports an involvement of the phenolic side chain in the non-GAP catalysed GTP hydrolysis through proton transfer to and from an additional active site water molecule. Similar mechanisms have been described for many small G proteins (Fig.51B).^{27,208-210}

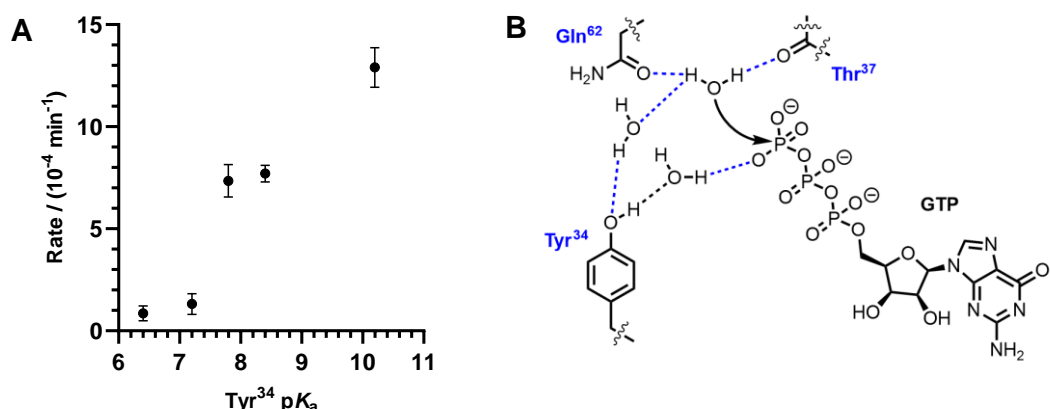


Figure 51: (A) Intrinsic rate of hydrolysis of GTP-loaded FY-RhoA plotted against the Tyr^{34} side chain pK_a . Error bars represent the 95% confidence interval for the fitted values. (B) Proposed mechanism for the intrinsic RhoA-GTP hydrolysis.^{27,210}

As is evidenced by the $^{19}\text{F-NMR}$ experiments in section 4.3.2, the Tyr^{34} protonation state for the uncomplexed FY-RhoA, depends heavily on the pH of the buffer system, due to its solvent accessibility. The proportion of deprotonated FY/Tyr34 increases as the hydroxyl pK_a decreases. It is therefore conceivable, that the increasingly negatively charged sidechain is less able to coordinate the γ -phosphate group due to charge-charge repulsion. Even small differences in the

highly flexible Switch1 region can cause major conformational changes and thus decrease the intrinsic GTPase activity.

4.1.4.5 Analysis of Kinetic Parameters for the RhoGAP^{R85A}-catalysed Hydrolysis of FY-RhoA-GTP

Comparing kinetic parameters obtained in table 14 a clear correlation between Tyr34 side chain pK_a and RhoGAP^{R85A}-catalysed rate acceleration is observed. As the acidity of the phenolic hydroxyl group increases, the rate of GTP hydrolysis decreases (Fig.52). Crystallographic evidence from (section 4.4.3) shows no perturbation to the active site of the TSA structure. Therefore, this change in activity is the result of the altered Tyr34 pK_a.

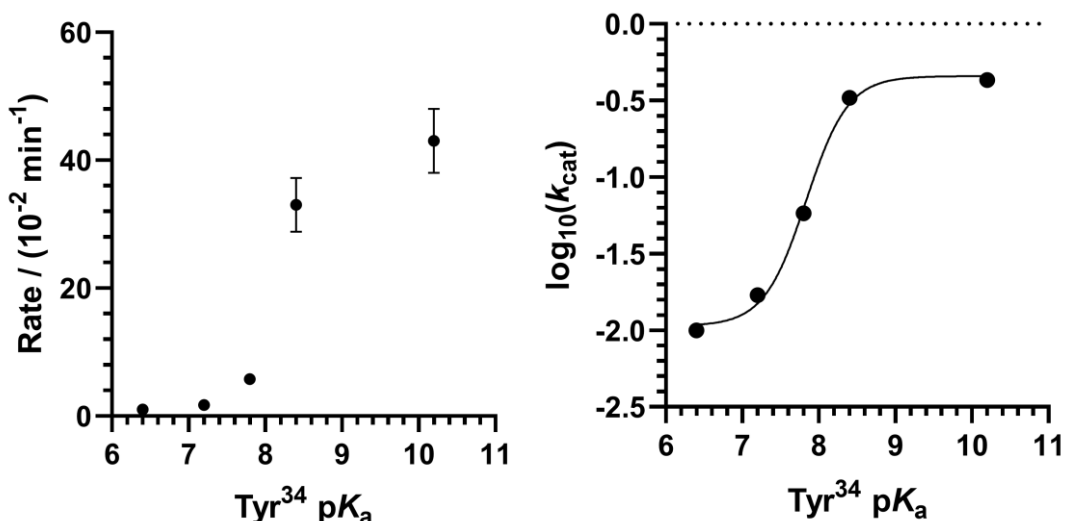


Figure 52: k_{cat} and $\log_{10}(k_{\text{cat}} \times 10^4)$ of RhoGAP^{R85A}-catalysed hydrolysis of GTP-RhoA plotted against Tyr34 side chain pK_a. Error bars represent the 95% CI of the fitted curves.

The protonated Tyr34 hydroxyl group seems to be essential for complex formation. When comparing the K_M values from the examined FY-RhoA variants, no significant trend can be observed and they are generally in line with literature values (Tab.14, Fig.53).^{151,206} The rate of dissociation of the RhoA/GTP/RhoGAP^{R85A} complex (k_{-2} , Fig.44) is comparatively fast, compared to the slow cleavage reaction. Thus, the K_D can be approximated to be similar to the K_M (Eq.8).

$$K_D = \frac{k_{\text{cat}}}{k_{-2}} \approx K_M \quad (8)$$

The observed rate decrease for the FY-RhoA variants is consequently not significantly impacted by RhoA/RhoGAP^{R85A} complex formation, but rather by the subsequent stabilisation of the transition state during the phosphoryl transfer.

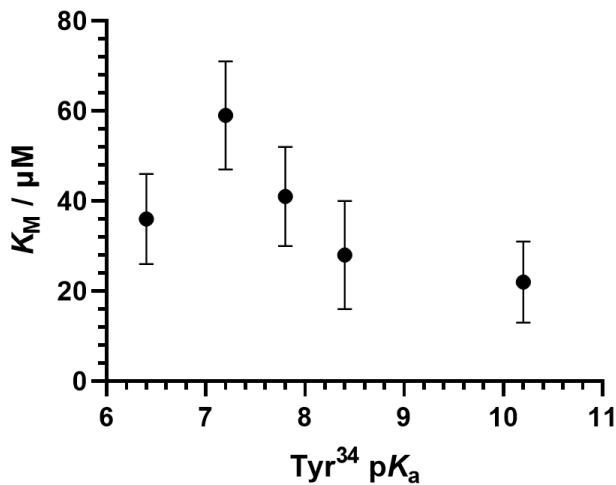


Figure 53: K_m for substrate complex FY-RhoA/GTP/RhoGAP^{R85A} plotted against FY-Tyr34 pK_a . Error bars represent a 95% confidence interval for the fitted values.

Section 4.4.2 shows that this pK_a decrease leads to a shielding of the ¹⁹F-NMR fluorine (F^3) signal of the MgF_3^- in contact with the Tyr34 side chain. The bonds in the MgF_3^- species have a highly ionic character.³⁷ It is therefore plausible that this increased electron density is localised at the F^3 atom and does not largely affect the neighbouring Mg^{2+} cation. In the case of the phosphoryl group in transfer, the negative charge is more delocalised, therefore an increase of electron density at one of the oxygens is distributed. The observation that the RhoGAP^{R85A}-catalysed GTPase activity decreases with increasing Tyr34 side chain acidity, can therefore be explained by the altered hydrogen bonding between the Tyr34 hydroxyl group and the O3G atom. When the level of fluorination increases, due to the better pK_a matching between the oxygen of PO_3^- and the decreased pK_a , the already short low barrier hydrogen bond (LBHB) gets shorter. The crystal structure for $F^{235}Y$ -RhoA/ MgF_3^- /RhoGAP^{R85A} shows a O–H··· F^3 bond length of 2.3 Å, which puts it in the range of single-well hydrogen bonds. Whether this is the case for the phosphoryl group needs to be confirmed by computational studies to overcome the limitation of the refinement process in crystallography. Never mind that, Mg–F bonds (1.9 Å) tend to be slightly longer than P–O bonds (1.5 Å) and therefore the F^3 atom would be pushed slightly towards the Tyr34 and Gln63 side chains. Regardless, this translates to a higher electron density at the oxygen in contact with the Tyr34 hydroxyl group during the transition state. From these data definitive conclusions

can be drawn as to how the electron density changes at the Mg²⁺ and by extension the γ-phosphorus atom during the transition state. If the increase of electron density at F³ is a result of pulling electron density from the magnesium ion, the latter would be more positive. This should lead to a deshielding and a decrease in electron density around F¹ and F². However, as the shielding around F¹ increases and remains unchanged for F², it is likely that the increased electron density at F³ comes from the Tyr34-OH H-bond. With this increased negative charge, the energy barrier for the nucleophilic water is increased due to electrostatic repulsion, therefore slowing down the catalytic rate.

Recent structural and QM/MM calculation findings revealed a substrate-assisted proton transfer step for the RhoGAP^{WT}-catalysed GTP hydrolysis, where a proton from the nucleophilic water is transferred to the O3G atom.²⁰⁵ A stronger H-bond between the Tyr and O3G is harder to break and therefore might slow down the subsequent proton transfer step, which is essential for completing the attack of the nucleophilic water. If the pK_a of the Tyr34 hydroxyl group drops below the pK_a for O3G, the donor-acceptor roles in this hydrogen bond could switch and the proton would be predominantly associated with O3G. This diminishes the ability to accept the proton from the nucleophilic water, thus slowing down the catalytic rate. A sigmoidal curve, fitted in Fig.52B puts the inflection point at 7.8, which can be interpreted as the pK_a of O3G in the RhoA/RhoGAP^{R85A} active site. A computational analysis of the energy profiles for these reaction pathways might provide further valuable insights.

5 Summary

5.1 Summary: Chapter 3

HRas(1–166), RasGAP(714–1047) and cSrc(251–533) were recombinantly expressed and purified. A method for the cSrc-mediated phosphorylation and subsequent purification of HRas was developed. A MgF₃[−] complex of HRas and RasGAP was successfully crystallised, and the structure was processed to a resolution of 2.1 Å. This is an improvement over the only other available low-resolution structure (PDB:1WQ1) and provides strong evidence for MgF₃[−] being the metal fluoride species of 1WQ1. With this improved structure as a starting point, the higher resolution has the potential to greatly increase the quality of future computational studies on this highly relevant HRas/MgF₃[−]/RasGAP TSA structure.

Site-directed mutagenesis on Switch1 and Switch2 regions of HRas found evidence pointing towards Tyr64 being the main phosphorylation site of cSrc.⁸³ In the attempt to crystallise the phospho-HRas/MgF₃[−]/RasGAP TSA complex, mono-phosphorylated HRas was crystallised on its own and showed no conformational difference to unphosphorylated HRas. However, as the flexible Switch2 region was disordered in the structure, as is often the case for GDP-loaded small G proteins, the phosphorylation could only be confirmed indirectly, due to the fact that, no other Tyr residue carried a phosphorylation modification. During the attempts to obtain a phospho-HRas/RasGAP complex, the structure for a previously unknown RasGAP dimer was found. Important binding residues for the dimer-dimer interface were identified and could hold biological significance for related RasGAP proteins. Although further studies are needed to confirm its biological relevance outside of a crystallographic environment.

¹⁹F-NMR experiments showed that monophosphorylated HRas does not form a MgF₃[−] complex with RasGAP and no crystal structure for the complex could be found. This supports the findings of KANO et al. that suggest that a phosphorylation of the switch regions lead to a decreased binding affinity towards RasGAP. Further investigations are needed to elucidate precise structural implications for other effectors such as hSOS1 and Raf, as well as determine K_D values for the phospho-HRas/RasGAP interaction.

5.2 Summary: Chapter 4

Several FYs were synthesised chemoenzymatically and site-specifically incorporated into RhoA at position 34, generating a range of FY-RhoA variants. Through the incorporation, the modified Tyr34 hydroxyl pK_a is reduced stepwise from 10.2 to 6.4, depending on the substitution pattern of the fluorine substituents.¹⁵⁷ RhoA and RhoGAP^{R85A} readily form a transition state analogue complex with MgF₃⁻ which had previously been crystallised in the literature. Based on these conditions, X-ray crystal structures for F³⁵Y-RhoA/MgF₃⁻/RhoGAP^{R85A} (2.25 Å) and F²³⁵Y-RhoA/MgF₃⁻/RhoGAP^{R85A} (1.91 Å) were solved. These confirmed that the fluorotyrosine residues were successfully incorporated at the target position and that no perturbation to the active site was caused by the additional substituents.

¹⁹F-NMR spectra of this array of FY-RhoA/MgF₃⁻/RhoGAP^{R85A} complexes show a stepwise increase of shielding for the fluorine atom (F³) of the MgF₃⁻ species in contact with the Tyr34 side chain as its hydroxyl pK_a decreases. This implies an attenuated ability of the Tyr34 sidechain to stabilise the build-up of negative charge during the transition state. Subsequently kinetic parameters of the RhoGAP^{R85A}-catalysed hydrolysis of the GTP-loaded FY-RhoA variants were measured and showed no significant trend in the obtained K_D values. For the k_{cat} values however, a clear dependence of the Tyr34 hydroxyl pK_a is observed. Namely, as the Tyr34 pK_a decreases, so does the catalytic rate.

This decrease is due to the impaired ability of the Tyr34 hydrogen bond to stabilise negative charge during the phosphoryl transfer, as evident by the pK_a dependent upfield shift of the MgF₃⁻ ¹⁹F-NMR signal. Previous computational studies of the RhoA/RhoGAP system have revealed a substrate assisted mechanism where the necessary proton transfer from the nucleophilic water is assisted by the transferring phosphoryl group. Here the dynamic H bond modulation diminishes ability of the phosphoryl oxygen to serve as general base during hydrolysis, thus reducing the catalytic activity.

Based on these experimental data, future computational work on this project can shed light on the energetic contributions of individual interactions to help draw parallels to related small G proteins like Ran.

Together these data reveal the utility of a combined approach using $^{19}\text{F-NMR}$, kinetic assays and X-ray crystallography. Thereby a methodology is established which can readily be applied to similar systems in the future.

6 References

- 1 Clementi, N.; Polacek, N. Ribosome-Associated GTPases: The Role of RNA for GTPase Activation. *RNA Biol.* **2010**, *7* (5), 521–527. <https://doi.org/10.4161/rna.7.5.12467>.
- 2 Rosenbaum, D. M.; Rasmussen, S. G. F.; Kobilka, B. K. The Structure and Function of G-Protein-Coupled Receptors. *Nature* **2009**, *459* (7245), 356–363. <https://doi.org/10.1038/nature08144>.
- 3 Cherfils, J. GEFs and GAPs: Mechanisms and Structures. In *Ras Superfamily Small G Proteins: Biology and Mechanisms* 1; Springer, **2014**; p.3–63. https://doi.org/10.1007/978-3-7091-1806-1_3.
- 4 Goricanec, D.; Stehle, R.; Egloff, P.; Grigoriu, S.; Plückthun, A.; Wagner, G.; Hagn, F. Conformational Dynamics of a G-Protein α Subunit Is Tightly Regulated by Nucleotide Binding. *Proc. Natl. Acad. Sci.* **2016**, *113* (26), E3629–E3638. <https://doi.org/10.1073/pnas.1604125113>.
- 5 Chung, K. Y.; Rasmussen, S. G. F.; Liu, T.; Li, S.; DeVree, B. T.; Chae, P. S.; Calinski, D.; Kobilka, B. K.; Woods, V. L.; Sunahara, R. K. Conformational Changes in the G Protein Gs Induced by the B2 Adrenergic Receptor. *Nature* **2011**, *477* (7366), 611–615. <https://doi.org/10.1038/nature10488>.
- 6 Noel, J. K.; Whitford, P. C. How EF-Tu Can Contribute to Efficient Proofreading of Aa-tRNA by the Ribosome. *Nat. Commun.* **2016**, *7* (1), 13314. <https://doi.org/10.1038/ncomms13314>.
- 7 Sriram, K.; Insel, P. A. G Protein-Coupled Receptors as Targets for Approved Drugs: How Many Targets and How Many Drugs? *Mol. Pharmacol.* **2018**, *93* (4), 251–258. <https://doi.org/10.1124/mol.117.111062>.
- 8 Gloerich, M.; Bos, J. L. Regulating Rap Small G-Proteins in Time and Space. *Trends Cell Biol.* **2011**, *21* (10), 615–623. <https://doi.org/10.1016/j.tcb.2011.07.001>.
- 9 Takai, Y.; Sasaki, T.; Matozaki, T. Small GTP-Binding Proteins. *Physiol. Rev.* **2001**, *81* (1), 153–208. <https://doi.org/10.1152/physrev.2001.81.1.153>.
- 10 Walker, J. E.; Saraste, M.; Runswick, M. J.; Gay, N. J. Distantly Related Sequences in the Alpha- and Beta-Subunits of ATP Synthase, Myosin, Kinases and Other ATP-Requiring Enzymes and a Common Nucleotide Binding Fold. *EMBO J.* **1982**, *1* (8), 945–951. <https://doi.org/10.1002/j.1460-2075.1982.tb01276.x>.
- 11 Koonin, E. V.; Tatusov, R. L.; Rudd, K. E. Sequence Similarity Analysis of Escherichia Coli Proteins: Functional and Evolutionary Implications. *Proc. Natl. Acad. Sci.* **1995**, *92* (25), 11921–11925. <https://doi.org/10.1073/pnas.92.25.11921>.
- 12 Buhrman, G.; O'Connor, C.; Zerbe, B.; Kearney, B. M.; Napoleon, R.; Kovrigina, E. A.; Vajda, S.; Kozakov, D.; Kovrigin, E. L.; Mattos, C. Analysis of Binding Site Hot Spots on the Surface of Ras GTPase. *J. Mol. Biol.* **2011**, *413* (4), 773–789. <https://doi.org/10.1016/j.jmb.2011.09.011>.
- 13 Gibbs, J. B. Lipid Modifications of Proteins in the Ras Superfamily, GTPases in Biology **1993**, 335–344. https://doi.org/10.1007/978-3-642-78267-1_22.
- 14 Cox, A. D.; Der, C. J. Ras History: The Saga Continues. *Small GTPases* **2010**, *1* (1), 2–27. <https://doi.org/10.4161/sgtp.1.1.12178>.

-
- 15 John, J.; Rensland, H.; Schlichting, I.; Vetter, I.; Borasio, G. D.; Goody, R. S.; Wittinghofer, A. Kinetic and Structural Analysis of the Mg(2+)-Binding Site of the Guanine Nucleotide-Binding Protein P21H-Ras. *J. Biol. Chem.* **1993**, *268* (2), 923–929. [https://doi.org/10.1016/S0021-9258\(18\)54022-9](https://doi.org/10.1016/S0021-9258(18)54022-9).
- 16 Baker, R.; Lewis, S. M.; Sasaki, A. T.; Wilkerson, E. M.; Locasale, J. W.; Cantley, L. C.; Kuhlman, B.; Dohlman, H. G.; Campbell, S. L. Site-Specific Monoubiquitination Activates Ras by Impeding GTPase-Activating Protein Function. *Nat. Struct. Mol. Biol.* **2013**, *20* (1), 46–52. <https://doi.org/10.1038/nsmb.2430>.
- 17 Haeusler, L. C.; Blumenstein, L.; Stege, P.; Dvorsky, R.; Ahmadian, M. R. Comparative Functional Analysis of the Rac GTPases. *FEBS Lett.* **2003**, *555* (3), 556–560. [https://doi.org/10.1016/S0014-5793\(03\)01351-6](https://doi.org/10.1016/S0014-5793(03)01351-6).
- 18 Lenzen, C.; Cool, R. H.; Prinz, H.; Kuhlmann, J.; Wittinghofer, A. Kinetic Analysis by Fluorescence of the Interaction between Ras and the Catalytic Domain of the Guanine Nucleotide Exchange Factor Cdc25 Mm. *Biochemistry* **1998**, *37* (20), 7420–7430. <https://doi.org/10.1021/bi972621j>.
- 19 Bos, J.; Rehmann, H.; Wittinghofer, A. GEFs and GAPs : Critical Elements in the Control of Small G Proteins. *Cell* **2007**, 865–877. <https://doi.org/10.1016/j.cell.200>.
- 20 Killoran, R. C.; Smith, M. J. Conformational Resolution of Nucleotide Cycling and Effector Interactions for Multiple Small GTPases Determined in Parallel. *J. Biol. Chem.* **2019**, *294* (25), 9937–9948. <https://doi.org/10.1074/jbc.ra119.008653>.
- 21 Cherfils, J.; Zeghouf, M. Regulation of Small GTPases by GEFs, GAPs, and GDIs. *Physiol. Rev.* **2013**, *93* (1), 269–309. <https://doi.org/10.1152/physrev.00003.2012>.
- 22 Vetter, I. R.; Wittinghofer, A. The Guanine Nucleotide-Binding Switch in Three Dimensions. *Science* **2001**, *294* (5545), 1299–1304. <https://doi.org/10.1126/science.1062023>.
- 23 Hall, B. E.; Bar-Sagi, D.; Nassar, N. The Structural Basis for the Transition from Ras-GTP to Ras-GDP. *Proc. Natl. Acad. Sci.* **2002**, *99* (19), 12138–12142. <https://doi.org/10.1073/pnas.192453199>.
- 24 McCormick, F. Raf: The Holy Grail of Ras Biology? *Trends Cell Biol.* **1994**, *4* (10), 347–350. [https://doi.org/10.1016/0962-8924\(94\)90075-2](https://doi.org/10.1016/0962-8924(94)90075-2).
- 25 Rajalingam, K.; Schreck, R.; Rapp, U. R.; Albert, Š. Ras Oncogenes and Their Downstream Targets. *Biochim. Biophys. Acta - Mol. Cell Res.* **2007**, *1773* (8), 1177–1195. <https://doi.org/10.1016/j.bbamcr.2007.01.012>.
- 26 Tanaka, T.; Rabbits, T. H. Interfering with Protein-Protein Interactions: Potential for Cancer Therapy. *Cell Cycle* **2008**, *7* (11), 1569–1574. <https://doi.org/10.4161/cc.7.11.6061>.
- 27 Buhrman, G.; Holzapfel, G.; Fetts, S.; Mattos, C. Allosteric Modulation of Ras Positions Q61 for a Direct Role in Catalysis. *Proc. Natl. Acad. Sci.* **2010**, *107* (11), 4931–4936. <https://doi.org/10.1073/pnas.0912226107>.
- 28 Csépányi-Kömi, R.; Lévay, M.; Ligeti, E. Small G Proteins and Their Regulators in Cellular Signalling. *Mol. Cell. Endocrinol.* **2012**, *353* (1–2), 10–20. <https://doi.org/10.1016/j.mce.2011.11.005>.
- 29 Keeton, A. B.; Salter, E. A.; Piazza, G. A. The RAS–Effector Interaction as a Drug Target. *Cancer Res.* **2017**, *77* (2), 221–226. <https://doi.org/10.1158/0008-5472.CAN-16-0938>.

-
- 30 Lassila, J. K.; Zalatan, J. G.; Herschlag, D. Biological Phosphoryl-Transfer Reactions: Understanding Mechanism and Catalysis. *Annu. Rev. Biochem.* **2011**, *80* (1), 669–702. <https://doi.org/10.1146/annurev-biochem-060409-092741>.
- 31 Bonora, M.; Patergnani, S.; Rimessi, A.; De Marchi, E.; Suski, J. M.; Bononi, A.; Giorgi, C.; Marchi, S.; Missiroli, S.; Poletti, F.; Wieckowski, M. R.; Pinton, P. ATP Synthesis and Storage. *Purinergic Signal.* **2012**, *8* (3), 343–357. <https://doi.org/10.1007/s11302-012-9305-8>.
- 32 Rosing, J.; Slater, E. C. The Value of ΔG° for the Hydrolysis of ATP. *Biochim. Biophys. Acta - Bioenerg.* **1972**, *267* (2), 275–290. [https://doi.org/10.1016/0005-2728\(72\)90116-8](https://doi.org/10.1016/0005-2728(72)90116-8).
- 33 Powell, K. J.; Brown, P. L.; Byrne, R. H.; Gajda, T.; Hefta, G.; Sjöberg, S.; Wanner, H. Chemical Speciation of Environmentally Significant Heavy Metals with Inorganic Ligands. Part 1: The Hg^{2+} Cl^- , OH^- , CO_3^{2-} , SO_4^{2-} , and PO_4^{3-} Aqueous Systems (IUPAC Technical Report). *Pure Appl. Chem.* **2005**, *77* (4), 739–800. <https://doi.org/10.1351/pac200577040739>.
- 34 Lad, C.; Williams, N. H.; Wolfenden, R. The Rate of Hydrolysis of Phosphomonoester Dianions and the Exceptional Catalytic Proficiencies of Protein and Inositol Phosphatases. *Proc. Natl. Acad. Sci.* **2003**, *100* (10), 5607–5610. <https://doi.org/10.1073/pnas.0631607100>.
- 35 Westheimer, F. Why Nature Chose Phosphates. *Science* **1987**, *235* (4793), 1173–1178. <https://doi.org/10.1126/science.2434996>.
- 36 Lad, C.; Williams, N. H.; Wolfenden, R. The Rate of Hydrolysis of Phosphomonoester Dianions and the Exceptional Catalytic Proficiencies of Protein and Inositol Phosphatases. *Proc. Natl. Acad. Sci.* **2003**, *100* (10), 5607–5610. <https://doi.org/10.1073/pnas.0631607100>.
- 37 Blackburn, G. M.; Bowler, M. W.; Jin, Y.; Walther, J. P. Reflections on Biocatalysis Involving Phosphorus. *Biochem.* **2012**, *77* (10), 1083–1096. <https://doi.org/10.1134/S000629791210001X>.
- 38 Scheffzek, K.; Ahmadian, M. R.; Kabsch, W.; Wiesmüller, L.; Lautwein, A.; Schmitz, F.; Wittinghofer, A. The Ras-RasGAP Complex: Structural Basis for GTPase Activation and Its Loss in Oncogenic Ras Mutants. *Science* **1997**, *277* (5324), 333–339. <https://doi.org/10.1126/science.277.5324.333>.
- 39 Goricanec, D.; Stehle, R.; Egloff, P.; Grigoriu, S.; Plückthun, A.; Wagner, G.; Hagn, F. Conformational Dynamics of a G-Protein α Subunit Is Tightly Regulated by Nucleotide Binding. *Proc. Natl. Acad. Sci.* **2016**, *113* (26), E3629–E3638. <https://doi.org/10.1073/pnas.1604125113>.
- 40 Shurki, A.; Warshel, A. Why Does the Ras Switch “Break” by Oncogenic Mutations? *Proteins Struct. Funct. Bioinforma.* **2004**, *55* (1), 1–10. <https://doi.org/10.1002/prot.20004>.
- 41 Prior, I. a; Lewis, P. D.; Mattos, C. A Comprehensive Survey of Ras Mutations in Cancer. *Cancer Res.* **2012**, *72* (10), 2457–2467. <https://doi.org/10.1158/0008-5472.CAN-11-2612>.
- 42 Lowy, D. R.; Willumsen, B. M. Function and Regulation of Ras. *Annu. Rev. Biochem.* **1993**, *62* (1), 851–891. <https://doi.org/10.1146/annurev.bi.62.070193.004223>.

-
- 43 Spiegel, J.; Cromm, P. M.; Zimmermann, G.; Grossmann, T. N.; Waldmann, H. Small-Molecule Modulation of Ras Signaling. *Nat. Chem. Biol.* **2014**, *10* (8), 613–622. <https://doi.org/10.1038/nchembio.1560>.
- 44 Waters, A. M.; Der, C. J. KRAS: The Critical Driver and Therapeutic Target for Pancreatic Cancer. *Cold Spring Harb. Perspect. Med.* **2018**, *8* (9), a031435. <https://doi.org/10.1101/cshperspect.a031435>.
- 45 Cox, A. D.; Der, C. J.; Philips, M. R. Targeting RAS Membrane Association: Back to the Future for Anti-RAS Drug Discovery? *Clin. Cancer Res.* **2015**, *21* (8), 1819–1827. <https://doi.org/10.1158/1078-0432.CCR-14-3214>.
- 46 Canon, J.; Rex, K.; Saiki, A. Y.; Mohr, C.; Cooke, K.; Bagal, D.; Gaida, K.; Holt, T.; Knutson, C. G.; Koppada, N.; Lanman, B. A.; Werner, J.; Rapaport, A. S.; San Miguel, T.; Ortiz, R.; Osgood, T.; Sun, J.-R.; Zhu, X.; McCarter, J. D.; Volak, L. P.; Houk, B. E.; Fakih, M. G.; O’Neil, B. H.; Price, T. J.; Falchook, G. S.; Desai, J.; Kuo, J.; Govindan, R.; Hong, D. S.; Ouyang, W.; Henary, H.; Arvedson, T.; Cee, V. J.; Lipford, J. R. The Clinical KRAS(G12C) Inhibitor AMG 510 Drives Anti-Tumour Immunity. *Nature* **2019**, *575* (7781), 217–223. <https://doi.org/10.1038/s41586-019-1694-1>.
- 47 Westcott, P. M. K.; Halliwill, K. D.; To, M. D.; Rashid, M.; Rust, A. G.; Keane, T. M.; Delrosario, R.; Jen, K.-Y.; Gurley, K. E.; Kemp, C. J.; Fredlund, E.; Quigley, D. A.; Adams, D. J.; Balmain, A. The Mutational Landscapes of Genetic and Chemical Models of Kras-Driven Lung Cancer. *Nature* **2015**, *517* (7535), 489–492. <https://doi.org/10.1038/nature13898>.
- 48 Ostrem, J. M., Peters, U., Sos, M. L., Wells, J. A., Shokat, K. M. K-Ras(G12C) inhibitors allosterically control GTP affinity and effector interactions. *Nature* **2013**, *503* (7477), 548–551. <https://doi.org/10.1038/nature12796>
- 49 Janes, M. R.; Zhang, J.; Li, L.-S.; Hansen, R.; Peters, U.; Guo, X.; Chen, Y.; Babbar, A.; Firdaus, S. J.; Darjania, L.; Feng, J.; Chen, J. H.; Li, S.; Li, S.; Long, Y. O.; Thach, C.; Liu, Y.; Zarieh, A.; Ely, T.; Kucharski, J. M.; Kessler, L. V.; Wu, T.; Yu, K.; Wang, Y.; Yao, Y.; Deng, X.; Zarrinkar, P. P.; Brehmer, D.; Dhanak, D.; Lorenzi, M. V.; Hu-Lowe, D.; Patricelli, M. P.; Ren, P.; Liu, Y. Targeting KRAS Mutant Cancers with a Covalent G12C-Specific Inhibitor. *Cell* **2018**, *172* (3), 578–589.e17. <https://doi.org/10.1016/j.cell.2018.01.006>.
- 50 Sun, Q., Burke, J. P., Phan, J., Burns, M. C., Olejniczak, E. T., Waterson, A. G., Lee, T., Rossanese, O. W., Fesik, S. W. Discovery of Small Molecules that Bind to K-Ras and Inhibit Sos-Mediated Activation. *Angew. Chem. Int. Ed.* **2012**, *51* (25), 6140–6143. <https://doi.org/10.1002/anie.201201358>
- 51 Kessler, D., Gmachl, M., Mantoulidis, A., Martin, L. J., Zoephel, A., Mayer, M., Gollner, A., Covini, D., Fischer, S., Gerstberger, T., Gmaschitz, T., Goodwin, C., Greb, P., Häring, D., Hela, W., Hoffmann, J., Karolyi-Oezguer, J., Knesl, P., Kornigg, S., McConnell, D. B. Drugging an undruggable pocket on KRAS. *Proc. Natl. Acad. Sci.* **2019**, *116* (32), 15823–15829. <https://doi.org/10.1073/pnas.1904529116>
- 52 Coleman, D.; Berghuis, A.; Lee, E.; Linder, M.; Gilman, A.; Sprang. Structures of Active Conformations of Gi Alpha 1 and the Mechanism of GTP Hydrolysis. *Science* **1994**, *265* (5177), 1405–1412. <https://doi.org/10.1126/science.8073283>.
- 53 Jin, Y.; Richards, N. G.; Walther, J. P.; Blackburn, G. M. Metal Fluorides as Analogues for Studies on Phosphoryl Transfer Enzymes. *Angew. Chem. Int. Ed.* **2017**, *56* (15), 4110–4128. <https://doi.org/10.1002/anie.201606474>.

-
- 54 Jin, Y.; Molt, R. W.; Blackburn, G. M. Metal Fluorides: Tools for Structural and Computational Analysis of Phosphoryl Transfer Enzymes. *Top. Curr. Chem.* **2017**, *375* (2), 36. <https://doi.org/10.1007/s41061-017-0130-y>.
- 55 Ge, M.; Molt, R. W.; Jenkins, H. T.; Blackburn, G. M.; Jin, Y.; Antson, A. A. Octahedral Trifluoromagnesate, an Anomalous Metal Fluoride Species, Stabilizes the Transition State in a Biological Motor. *ACS Catal.* **2021**, *11* (5), 2769–2773. <https://doi.org/10.1021/acscatal.0c04500>.
- 56 Korhonen, H. J.; Conway, L. P.; Hodgson, D. R. Phosphate Analogues in the Dissection of Mechanism. *Curr. Opin. Chem. Biol.* **2014**, *21*, 63–72. <https://doi.org/10.1016/j.cbpa.2014.05.001>.
- 57 Bruice, T. C. Some Pertinent Aspects of Mechanism as Determined with Small Molecules. *Annu. Rev. Biochem.* **1976**, *45* (1), 331–374. <https://doi.org/10.1146/annurev.bi.45.070176.001555>.
- 58 Bowler, M. W.; Cliff, M. J.; Walther, J. P.; Blackburn, G. M. Why Did Nature Select Phosphate for Its Dominant Roles in Biology? *New J. Chem.* **2010**, *34* (5), 784–794. <https://doi.org/10.1039/b9nj00718k>.
- 59 Williams, D. M.; Jakeman, D. L.; Vyle, J. S.; Williamson, M. P.; Blackburn, G. M. Synthesis and Binding of Stable Bisubstrate Ligands for Phosphoglycerate Kinase. *Bioorg. Med. Chem. Lett.* **1998**, *8* (18), 2603–2608. [https://doi.org/10.1016/S0960-894X\(98\)00466-1](https://doi.org/10.1016/S0960-894X(98)00466-1).
- 60 Danielson, M. A.; Falke, J. J. Use of ¹⁹F NMR to Probe Protein Structure and Conformational Changes. *Annu. Rev. Biophys. Biomol. Struct.* **1996**, *25*, 163–195. <https://doi.org/10.1146/annurev.bb.25.060196.001115>.
- 61 Chen, H.; Viel, S.; Ziarelli, F.; Peng, L. ¹⁹F NMR: A Valuable Tool for Studying Biological Events. *Chem. Soc. Rev.* **2013**, *42* (20), 7971. <https://doi.org/10.1039/c3cs60129c>.
- 62 Gerig, J. T. Fluorine Nuclear Magnetic Resonance of Fluorinated Ligands. *Methods in Enzymology* **1989**, *177*, 3–23. [https://doi.org/10.1016/0076-6879\(89\)77003-8](https://doi.org/10.1016/0076-6879(89)77003-8).
- 63 Wüthrich, K. The Second Decade — into the Third Millennium. *Nat. Struct. Biol.* **1998**, *5* (7), 492–495. <https://doi.org/10.1038/728>.
- 64 Brünger, A. T. X-Ray Crystallography and NMR Reveal Complementary Views of Structure and Dynamics. *Nat. Struct. Biol.* **1997**, *4 Suppl*, 862–865.
- 65 Jin, Y.; Molt, R. W.; Walther, J. P.; Richards, N. G. J.; Blackburn, G. M. ¹⁹F NMR and DFT Analysis Reveal Structural and Electronic Transition State Features for RhoA-Catalyzed GTP Hydrolysis. *Angew. Chem. Int. Ed.* **2016**, *55* (10), 3318–3322. <https://doi.org/10.1002/anie.201509477>.
- 66 Grigorenko, B. L.; Kots, E. D.; Nemukhin, A. V. Diversity of Mechanisms in Ras–GAP Catalysis of Guanosine Triphosphate Hydrolysis Revealed by Molecular Modeling. *Org. Biomol. Chem.* **2019**, *17* (19), 4879–4891. <https://doi.org/10.1039/C9OB00463G>.
- 67 Khrenova, M. G.; Mironov, V. A.; Grigorenko, B. L.; Nemukhin, A. V. Modeling the Role of G12V and G13V Ras Mutations in the Ras-GAP-Catalyzed Hydrolysis Reaction of Guanosine Triphosphate. *Biochemistry* **2014**, *53* (45), 7093–7099. <https://doi.org/10.1021/bi5011333>.
- 68 Mironov, V. A.; Khrenova, M. G.; Lychko, L. A.; Nemukhin, A. V. Computational Characterization of the Chemical Step in the GTP Hydrolysis by Ras-GAP for the Wild-

-
- Type and G13V Mutated Ras. *Proteins Struct. Funct. Bioinforma.* **2015**, *83* (6), 1046–1053. <https://doi.org/10.1002/prot.24802>.
- 69 Grigorenko, B. L.; Nemukhin, A. V.; Cachau, R. E.; Topol, I. A.; Burt, S. K. Computational Study of a Transition State Analog of Phosphoryl Transfer in the Ras–RasGAP Complex: AlF_x versus MgF₃²⁻. *J. Mol. Model.* **2005**, *11* (6), 503–508. <https://doi.org/10.1007/s00894-005-0259-4>.
- 70 Gayer, K. H.; Thompson, L. C.; Zajicek, O. T. The solubility of aluminium hydroxide in acidic and basic media at 25°C. *Can. J. Chem.* **1958**, *36* (9), 1268–1271. <https://doi.org/10.1139/v58-184>.
- 71 Jin, Y.; Cliff, M. J.; Baxter, N. J.; Dannatt, H. R. W.; Hounslow, A. M.; Bowler, M. W.; Blackburn, G. M.; Walther, J. P. Charge-Balanced Metal Fluoride Complexes for Protein Kinase A with Adenosine Diphosphate and Substrate Peptide SP20. *Angew. Chem. Int. Ed.* **2012**, *51* (49), 12242–12245. <https://doi.org/10.1002/anie.201204266>.
- 72 Ahearn, I. M.; Haigis, K.; Bar-Sagi, D.; Philips, M. R. Regulating the Regulator: Post-Translational Modification of RAS. *Nat. Rev. Mol. Cell Biol.* **2012**, *13* (1), 39–51. <https://doi.org/10.1038/nrm3255>.
- 73 Abe, T.; Umeki, I.; Kanno, S.; Inoue, S.; Niihori, T.; Aoki, Y. LZTR1 Facilitates Polyubiquitination and Degradation of RAS-GTPases. *Cell Death Differ.* **2020**, *27* (3), 1023–1035. <https://doi.org/10.1038/s41418-019-0395-5>.
- 74 Casey, P. J. Lipid Modifications of G Proteins. *Curr. Opin. Cell Biol.* **1994**, *6* (2), 219–225. [https://doi.org/10.1016/0955-0674\(94\)90139-2](https://doi.org/10.1016/0955-0674(94)90139-2).
- 75 Chang, F.; Lemmon, C.; Lietha, D.; Eck, M.; Romer, L. Tyrosine Phosphorylation of Rac1: A Role in Regulation of Cell Spreading. *PLoS One* **2011**, *6* (12), e28587. <https://doi.org/10.1371/journal.pone.0028587>.
- 76 Ahearn, I.; Zhou, M.; Philips, M. R. Posttranslational Modifications of RAS Proteins. *Cold Spring Harb. Perspect. Med.* **2018**, *8* (11), a031484. <https://doi.org/10.1101/cshperspect.a031484>.
- 77 Greenstein, A. E.; Grundner, C.; Echols, N.; Gay, L. M.; Lombana, T. N.; Mieczkowski, C. A.; Pullen, K. E.; Sung, P.; Alber, T. Structure/Function Studies of Ser/Thr and Tyr Protein Phosphorylation in Mycobacterium Tuberculosis. *J. Mol. Microbiol. Biotechnol.* **2005**, *9* (3–4), 167–181. <https://doi.org/10.1159/000089645>.
- 78 Tu, S.; Wu, W. J.; Wang, J.; Cerione, R. A. Epidermal Growth Factor-Dependent Regulation of Cdc42 Is Mediated by the Src Tyrosine Kinase. *J. Biol. Chem.* **2003**, *278* (49), 49293–49300. <https://doi.org/10.1074/jbc.M307021200>.
- 79 Kwon, T.; Kwon, D. Y.; Chun, J.; Kim, J. H.; Kang, S. S. Akt Protein Kinase Inhibits Rac1-GTP Binding through Phosphorylation at Serine 71 of Rac1. *J. Biol. Chem.* **2000**, *275* (1), 423–428. <https://doi.org/10.1074/jbc.275.1.423>.
- 80 Yeatman, T. J. A Renaissance for SRC. *Nat. Rev. Cancer* **2004**, *4* (6), 470–480. <https://doi.org/10.1038/nrc1366>.
- 81 Bunda, S.; Heir, P.; Sri Kumar, T.; Cook, J. D.; Burrell, K.; Kano, Y.; Lee, J. E.; Zadeh, G.; Raught, B.; Ohh, M. Src Promotes GTPase Activity of Ras via Tyrosine 32 Phosphorylation. *Proc. Natl. Acad. Sci.* **2014**, *111* (36), E3785–E3794. <https://doi.org/10.1073/pnas.1406559111>.
- 82 Bunda, S.; Burrell, K.; Heir, P.; Zeng, L.; Alamsahebpour, A.; Kano, Y.; Raught, B.; Zhang, Z. Y.; Zadeh, G.; Ohh, M. Inhibition of SHP2-Mediated Dephosphorylation of

- Ras Suppresses Oncogenesis. *Nat. Commun.* **2015**, *6*, 1–12.
<https://doi.org/10.1038/ncomms9859>.
- 83 Kano, Y.; Gebregiworgis, T.; Marshall, C. B.; Radulovich, N.; Poon, B. P. K.; St-Germain, J.; Cook, J. D.; Valencia-Sama, I.; Grant, B. M. M.; Herrera, S. G.; Miao, J.; Raught, B.; Irwin, M. S.; Lee, J. E.; Yeh, J. J.; Zhang, Z.-Y.; Tsao, M.-S.; Ikura, M.; Ohh, M. Tyrosyl Phosphorylation of KRAS Stalls GTPase Cycle via Alteration of Switch I and II Conformation. *Nat. Commun.* **2019**, *10* (1), 224.
<https://doi.org/10.1038/s41467-018-08115-8>.
- 84 Mosaddeghzadeh, N.; Ahmadian, M. R. The RHO Family GTPases: Mechanisms of Regulation and Signaling. *Cells* **2021**, *10* (7), 1831.
<https://doi.org/10.3390/cells10071831>.
- 85 Clayton, N. S.; Ridley, A. J. Targeting Rho GTPase Signaling Networks in Cancer. *Front. Cell Dev. Biol.* **2020**, *8*. <https://doi.org/10.3389/fcell.2020.00222>.
- 86 Heasman, S. J.; Ridley, A. J. Mammalian Rho GTPases: New Insights into Their Functions from in Vivo Studies. *Nat. Rev. Mol. Cell Biol.* **2008**, *9* (9), 690–701.
<https://doi.org/10.1038/nrm2476>.
- 87 Mulloy, J. C.; Cancelas, J. A.; Filippi, M.-D.; Kalfa, T. A.; Guo, F.; Zheng, Y. Rho GTPases in Hematopoiesis and Hemopathies. *Blood* **2010**, *115* (5), 936–947.
<https://doi.org/10.1182/blood-2009-09-198127>.
- 88 Park, H.-O.; Bi, E. Central Roles of Small GTPases in the Development of Cell Polarity in Yeast and Beyond. *Microbiol. Mol. Biol. Rev.* **2007**, *71* (1), 48–96.
<https://doi.org/10.1128/MMBR.00028-06>.
- 89 Schlessinger, K.; Hall, A.; Tolwinski, N. Wnt Signaling Pathways Meet Rho GTPases. *Genes Dev.* **2009**, *23* (3), 265–277. <https://doi.org/10.1101/gad.1760809>.
- 90 Etienne-Manneville, S.; Hall, A. Rho GTPases in Cell Biology. *Nature* **2002**, *420* (6916), 629–635. <https://doi.org/10.1038/nature01148>.
- 91 Garcia-Mata, R.; Boulter, E.; Burridge, K. The “Invisible Hand”: Regulation of RHO GTPases by RhoGDI. *Nat. Rev. Mol. Cell Biol.* **2011**, *12* (8), 493–504.
<https://doi.org/10.1038/nrm3153>.
- 92 Hall, A. Rho Family GTPases. *Biochem. Soc. Trans.* **2012**, *40* (6), 1378–1382.
<https://doi.org/10.1042/BST20120103>.
- 93 Denk-Lobnig, M.; Martin, A. C. Modular Regulation of Rho Family GTPases in Development. *Small GTPases* **2019**, *10* (2), 122–129.
<https://doi.org/10.1080/21541248.2017.1294234>.
- 94 Hall, A. Rho GTPases and the Actin Cytoskeleton. *Science* **1998**, *279* (5350), 509–514. <https://doi.org/10.1126/science.279.5350.509>.
- 95 Vega, F. M.; Ridley, A. J. Rho GTPases in Cancer Cell Biology. *FEBS Lett.* **2008**, *582* (14), 2093–2101. <https://doi.org/10.1016/j.febslet.2008.04.039>.
- 96 Moore, K. J. M.; Webb, M. R.; Eccleston, J. F. Mechanism of GTP Hydrolysis by P21N-Ras Catalyzed by GAP: Studies with a Fluorescent GTP Analog. *Biochemistry* **1993**, *32* (29), 7451–7459. <https://doi.org/10.1021/bi00080a016>.
- 97 Barrett, T.; Xiao, B.; Dodson, E. J.; Dodson, G.; Ludbrook, S. B.; Nurmahomed, K.; Gamblin, S. J.; Musacchio, A.; Smerdon, S. J.; Eccleston, J. F. The Structure of the

-
- GTPase-Activating Domain from P50rhoGAP. *Nature* **1997**, 385 (6615), 458–461. <https://doi.org/10.1038/385458a0>.
- 98 Graham, D. L.; Lowe, P. N.; Grime, G. W.; Marsh, M.; Rittinger, K.; Smerdon, S. J.; Gamblin, S. J.; Eccleston, J. F. MgF₃⁻ as a Transition State Analog of Phosphoryl Transfer. *Chem. Biol.* **2002**, 9 (3), 375–381. [https://doi.org/10.1016/S1074-5521\(02\)00112-6](https://doi.org/10.1016/S1074-5521(02)00112-6).
- 99 Nassar, N.; Hoffman, G. R.; Manor, D.; Clardy, J. C.; Cerione, R. A. Structures of Cdc42 Bound to the Active and Catalytically Compromised Forms of Cdc42GAP. *Nat. Struct. Biol.* **1998**, 5 (12), 1047–1052. <https://doi.org/10.1038/4156>.
- 100 Pan, X.; Eathiraj, S.; Munson, M.; Lambright, D. G. TBC-Domain GAPs for Rab GTPases Accelerate GTP Hydrolysis by a Dual-Finger Mechanism. *Nature* **2006**, 442 (7100), 303–306. <https://doi.org/10.1038/nature04847>.
- 101 Bi, X.; Corpina, R. A.; Goldberg, J. Structure of the Sec23/24–Sar1 Pre-Budding Complex of the COPII Vesicle Coat. *Nature* **2002**, 419 (6904), 271–277. <https://doi.org/10.1038/nature01040>.
- 102 Leonard, D. A.; Lin, R.; Cerione, R. A.; Manor, D. Biochemical Studies of the Mechanism of Action of the Cdc42-GTPase-Activating Protein. *J. Biol. Chem.* **1998**, 273 (26), 16210–16215. <https://doi.org/10.1074/jbc.273.26.16210>.
- 103 Scrima, A.; Thomas, C.; Deaconescu, D.; Wittinghofer, A. The Rap–RapGAP Complex: GTP Hydrolysis without Catalytic Glutamine and Arginine Residues. *EMBO J.* **2008**, 27 (7), 1145–1153. <https://doi.org/10.1038/emboj.2008.30>.
- 104 Seewald, M. J.; Körner, C.; Wittinghofer, A.; Vetter, I. R. RanGAP Mediates GTP Hydrolysis without an Arginine Finger. *Nature* **2002**, 415 (6872), 662–666. <https://doi.org/10.1038/415662a>.
- 105 Głowacki, E. D.; Irimia-Vladu, M.; Bauer, S.; Sariciftci, N. S. Hydrogen-Bonds in Molecular Solids – from Biological Systems to Organic Electronics. *J. Mater. Chem. B* **2013**, 1 (31), 3742. <https://doi.org/10.1039/c3tb20193g>.
- 106 Meot-Ner, M. The Ionic Hydrogen Bond. *Chem. Rev.* **2005**, 105 (1), 213–284. <https://doi.org/10.1021/cr9411785>.
- 107 Emsley, J. Very Strong Hydrogen Bonding. *Chem. Soc. Rev.* **1980**, 9 (1), 91. <https://doi.org/10.1039/cs9800900091>.
- 108 Wendler, K.; Thar, J.; Zahn, S.; Kirchner, B. Estimating the Hydrogen Bond Energy. *J. Phys. Chem. A* **2010**, 114 (35), 9529–9536. <https://doi.org/10.1021/jp103470e>.
- 109 Bertolasi, V.; Gilli, P.; Ferretti, V.; Gilli, G. Evidence for Resonance-Assisted Hydrogen Bonding. 2. Intercorrelation between Crystal Structure and Spectroscopic Parameters in Eight Intramolecularly Hydrogen Bonded 1,3-Diaryl-1,3-Propanedione Enols. *J. Am. Chem. Soc.* **1991**, 113 (13), 4917–4925. <https://doi.org/10.1021/ja00013a030>.
- 110 Gilli, G.; Bellucci, F.; Ferretti, V.; Bertolasi, V. Evidence for Resonance-Assisted Hydrogen Bonding from Crystal-Structure Correlations on the Enol Form of the .Beta.-Diketone Fragment. *J. Am. Chem. Soc.* **1989**, 111 (3), 1023–1028. <https://doi.org/10.1021/ja00185a035>.
- 111 Weinhold, F.; Klein, R. A. What Is a Hydrogen Bond? Mutually Consistent Theoretical and Experimental Criteria for Characterizing H-Bonding Interactions. *Mol. Phys.* **2012**, 110 (9–10), 565–579. <https://doi.org/10.1080/00268976.2012.661478>.

-
- 112 Hoja, J.; Sax, A. F.; Szalewicz, K. Is Electrostatics Sufficient to Describe Hydrogen-Bonding Interactions? *Chem. - A Eur. J.* **2014**, *20* (8), 2292–2300. <https://doi.org/10.1002/chem.201303528>.
- 113 Herschlag, D.; Pinney, M. M. Hydrogen Bonds: Simple after All? *Biochemistry* **2018**, *57* (24), 3338–3352. <https://doi.org/10.1021/acs.biochem.8b00217>.
- 114 Cleland, W. W.; Frey, P. A.; Gerlt, J. A. The Low Barrier Hydrogen Bond in Enzymatic Catalysis. *J. Biol. Chem.* **1998**, *273* (40), 25529–25532. <https://doi.org/10.1074/jbc.273.40.25529>.
- 115 Steiner, T.; Saenger, W. Lengthening of the Covalent O–H Bond in O–H ... O Hydrogen Bonds Re-Examined from Low-Temperature Neutron Diffraction Data of Organic Compounds. *Acta Crystallogr. Sect. B Struct. Sci.* **1994**, *50* (3), 348–357. <https://doi.org/10.1107/S0108768193011966>.
- 116 Jaccaud, M.; Faron, R.; Devilliers, D.; Romano, R.; Riedel, S.; Pernice, H.; Fluorine. Ullmann's Encyclopedia of Industrial Chemistry; Wiley, **2020**; pp. 1–19. https://doi.org/10.1002/14356007.a11_293.pub2.
- 117 Wang, J.; Sánchez-Roselló, M.; Aceña, J. L.; del Pozo, C.; Sorochinsky, A. E.; Fustero, S.; Soloshonok, V. A.; Liu, H. Fluorine in Pharmaceutical Industry: Fluorine-Containing Drugs Introduced to the Market in the Last Decade (2001–2011). *Chem. Rev.* **2014**, *114* (4), 2432–2506. <https://doi.org/10.1021/cr4002879>.
- 118 Müller, K.; Faeh, C.; Diederich, F. Fluorine in Pharmaceuticals: Looking beyond Intuition. *Science* **2007**, *317* (5846), 1881–1886. <https://doi.org/10.1126/science.1131943>.
- 119 Alvarez, S. Van Der Waals Radii of Elements. *Inorg. Mater.* **2014**, *37* (9), 871–885. <https://doi.org/10.1023/A:1011625728803>.
- 120 Salwiczek, M.; Nyakatura, E. K.; Gerling, U. I. M.; Ye, S.; Koksch, B. Fluorinated Amino Acids: Compatibility with Native Protein Structures and Effects on Protein-Protein Interactions. *Chem. Soc. Rev.* **2012**, *41* (6), 2135–2171. <https://doi.org/10.1039/C1CS15241F>.
- 121 Jones, L. H.; Narayanan, A.; Hett, E. C. Understanding and Applying Tyrosine Biochemical Diversity. *Mol. Biosyst.* **2014**, *10* (5), 952–969. <https://doi.org/10.1039/c4mb00018h>.
- 122 Danielson, M. A.; Falke, J. J. Use of 19F NMR to Probe Protein Structure and Conformational Changes. *Annu. Rev. Biophys. Biomol. Struct.* **1996**, *25* (1), 163–195. <https://doi.org/10.1146/annurev.bb.25.060196.001115>.
- 123 Pace, C. J.; Gao, J. Exploring and Exploiting Polar-π Interactions with Fluorinated Aromatic Amino Acids. *Acc. Chem. Res.* **2013**, *46* (4), 907–915. <https://doi.org/10.1021/ar300086n>.
- 124 Seyedsayamdost, M. R.; Yee, C. S.; Stubbe, J. A. Site-Specific Incorporation of Fluorotyrosines into the R2 Subunit of *E. Coli* Ribonucleotide Reductase by Expressed Protein Ligation. *Nat. Protoc.* **2007**, *2* (5), 1225–1235. <https://doi.org/10.1038/nprot.2007.159>.
- 125 Hebel, D.; Furlano, D. C.; Phillips, R. S.; Koushik, S.; Creveling, C. R.; Kirk, K. L. An Enzymatic Synthesis of 2-Azido-L-Tyrosine. *Bioorg. Med. Chem. Lett.* **1992**, *2* (1), 41–44. [https://doi.org/10.1016/S0960-894X\(00\)80651-4](https://doi.org/10.1016/S0960-894X(00)80651-4).

-
- 126 Natarajan, A.; Schwans, J. P.; Herschlag, D. Using Unnatural Amino Acids to Probe the Energetics of Oxyanion Hole Hydrogen Bonds in the Ketosteroid Isomerase Active Site. *J. Am. Chem. Soc.* **2014**, *136* (21), 7643–7654. <https://doi.org/10.1021/ja413174b>.
- 127 Minnihan, E. C.; Young, D. D.; Schultz, P. G.; Stubbe, J. Incorporation of Fluorotyrosines into Ribonucleotide Reductase Using an Evolved, Polyspecific Aminoacyl-tRNA Synthetase. *J. Am. Chem. Soc.* **2011**, *133* (40), 15942–15945. <https://doi.org/10.1021/ja207719f>.
- 128 Yu, Y.; Lv, X.; Li, J.; Zhou, Q.; Cui, C.; Hosseinzadeh, P.; Mukherjee, A.; Nilges, M. J.; Wang, J.; Lu, Y. Defining the Role of Tyrosine and Rational Tuning of Oxidase Activity by Genetic Incorporation of Unnatural Tyrosine Analogs. *J. Am. Chem. Soc.* **2015**, *137* (14), 4594–4597. <https://doi.org/10.1021/ja5109936>.
- 129 Yu, Y.; Zhou, Q.; Wang, L.; Liu, X.; Zhang, W.; Hu, M.; Dong, J.; Li, J.; Lv, X.; Ouyang, H.; Li, H.; Gao, F.; Gong, W.; Lu, Y.; Wang, J. Significant Improvement of Oxidase Activity through the Genetic Incorporation of a Redox-Active Unnatural Amino Acid. *Chem. Sci.* **2015**, *6* (7), 3881–3885. <https://doi.org/10.1039/C5SC01126D>.
- 130 Oyala, P. H.; Ravichandran, K. R.; Funk, M. A.; Stucky, P. A.; Stich, T. A.; Drennan, C. L.; Britt, R. D.; Stubbe, J. Biophysical Characterization of Fluorotyrosine Probes Site-Specifically Incorporated into Enzymes: E. Coli Ribonucleotide Reductase As an Example. *J. Am. Chem. Soc.* **2016**, *138* (25), 7951–7964. <https://doi.org/10.1021/jacs.6b03605>.
- 131 Greene, B. L.; Stubbe, J.; Nocera, D. G. Photochemical Rescue of a Conformationally Inactivated Ribonucleotide Reductase. *J. Am. Chem. Soc.* **2018**, *140* (46), 15744–15752. <https://doi.org/10.1021/jacs.8b07902>.
- 132 Stubbe, J.; Nocera, D. G. Radicals in Biology: Your Life Is in Their Hands. *J. Am. Chem. Soc.* **2021**, *143* (34), 13463–13472. <https://doi.org/10.1021/jacs.1c05952>.
- 133 Gil, A. A.; Haigney, A.; Laptenok, S. P.; Brust, R.; Lukacs, A.; Iuliano, J. N.; Jeng, J.; Melief, E. H.; Zhao, R. K.; Yoon, E. Bin; Clark, I. P.; Towrie, M.; Greetham, G. M.; Ng, A.; Truglio, J. J.; French, J. B.; Meech, S. R.; Tonge, P. J. Mechanism of the AppABLUF Photocycle Probed by Site-Specific Incorporation of Fluorotyrosine Residues: Effect of the Y21 pKa on the Forward and Reverse Ground-State Reactions. *J. Am. Chem. Soc.* **2016**, *138* (3), 926–935. <https://doi.org/10.1021/jacs.5b11115>.
- 134 Gil, A. A.; Laptenok, S. P.; Iuliano, J. N.; Lukacs, A.; Verma, A.; Hall, C. R.; Yoon, G. E.; Brust, R.; Greetham, G. M.; Towrie, M.; French, J. B.; Meech, S. R.; Tonge, P. J. Photoactivation of the BLUF Protein PixD Probed by the Site-Specific Incorporation of Fluorotyrosine Residues. *J. Am. Chem. Soc.* **2017**, *139* (41), 14638–14648. <https://doi.org/10.1021/jacs.7b07849>.
- 135 Liu, X.; Jiang, L.; Li, J.; Wang, L.; Yu, Y.; Zhou, Q.; Lv, X.; Gong, W.; Lu, Y.; Wang, J. Significant Expansion of Fluorescent Protein Sensing Ability through the Genetic Incorporation of Superior Photo-Induced Electron-Transfer Quenchers. *J. Am. Chem. Soc.* **2014**, *136* (38), 13094–13097. <https://doi.org/10.1021/ja505219r>.
- 136 He, T.; Gershenson, A.; Eyles, S. J.; Lee, Y. J.; Liu, W. R.; Wang, J.; Gao, J.; Roberts, M. F. Fluorinated Aromatic Amino Acids Distinguish Cation-π Interactions from Membrane Insertion. *J. Biol. Chem.* **2015**, *290* (31), 19334–19342. <https://doi.org/10.1074/jbc.M115.668343>.

-
- 137 Yang, F.; Yu, X.; Liu, C.; Qu, C.-X.; Gong, Z.; Liu, H.-D.; Li, F.-H.; Wang, H.-M.; He, D.-F.; Yi, F.; Song, C.; Tian, C.-L.; Xiao, K.-H.; Wang, J.-Y.; Sun, J.-P. Phospho-Selective Mechanisms of Arrestin Conformations and Functions Revealed by Unnatural Amino Acid Incorporation and ¹⁹F-NMR. *Nat. Commun.* **2015**, *6* (1), 8202. <https://doi.org/10.1038/ncomms9202>.
- 138 Li, F.; Shi, P.; Li, J.; Yang, F.; Wang, T.; Zhang, W.; Gao, F.; Ding, W.; Li, D.; Li, J.; Xiong, Y.; Sun, J.; Gong, W.; Tian, C.; Wang, J. A Genetically Encoded ¹⁹F NMR Probe for Tyrosine Phosphorylation. *Angew. Chem. Int. Ed.* **2013**, *52* (14), 3958–3962. <https://doi.org/10.1002/anie.201300463>.
- 139 Villa, J. K.; Tran, H.-A.; Vipani, M.; Gianturco, S.; Bhasin, K.; Russell, B. L.; Harbron, E. J.; Young, D. D. Fluorescence Modulation of Green Fluorescent Protein Using Fluorinated Unnatural Amino Acids. *Molecules* **2017**, *22* (7), 1194. <https://doi.org/10.3390/molecules22071194>.
- 140 Romei, M. G.; Lin, C. Y.; Mathews, I. I.; Boxer, S. G. Electrostatic Control of Photoisomerization Pathways in Proteins. *Science* **2020**, *367* (6473), 76–79. <https://doi.org/10.1126/science.aax1898>.
- 141 Blatter, N.; Prokup, A.; Deiters, A.; Marx, A. Modulating the PK a of a Tyrosine in KlenTaq DNA Polymerase That Is Crucial for Abasic Site Bypass by in Vivo Incorporation of a Non-Canonical Amino Acid. *ChemBioChem* **2014**, *15* (12), 1735–1737. <https://doi.org/10.1002/cbic.201400051>.
- 142 O'Hagan, D.; Deng, H. Enzymatic Fluorination and Biotechnological Developments of the Fluorinase. *Chem. Rev.* **2015**, *115* (2), 634–649. <https://doi.org/10.1021/cr500209t>.
- 143 Li, J.; Griffith, W. P.; Davis, I.; Shin, I.; Wang, J.; Li, F.; Wang, Y.; Wherritt, D. J.; Liu, A. Cleavage of a Carbon–Fluorine Bond by an Engineered Cysteine Dioxygenase. *Nat. Chem. Biol.* **2018**, *14* (9), 853–860. <https://doi.org/10.1038/s41589-018-0085-5>.
- 144 Yu, Y.; Lv, X.; Li, J.; Zhou, Q.; Cui, C.; Hosseinzadeh, P.; Mukherjee, A.; Nilges, M. J.; Wang, J.; Lu, Y. Defining the Role of Tyrosine and Rational Tuning of Oxidase Activity by Genetic Incorporation of Unnatural Tyrosine Analogs. *J. Am. Chem. Soc.* **2015**, *137* (14), 4594–4597. <https://doi.org/10.1021/ja5109936>.
- 145 Prasad B, R.; Plotnikov, N. V.; Lameira, J.; Warshel, A. Quantitative Exploration of the Molecular Origin of the Activation of GTPase. *Proc. Natl. Acad. Sci.* **2013**, *110* (51), 20509–20514. <https://doi.org/10.1073/pnas.1319854110>.
- 146 Rubinson, K. A. Practical Corrections for p(H,D) Measurements in Mixed H₂O/D₂O Biological Buffers. *Anal. Methods* **2017**, *9* (18), 2744–2750. <https://doi.org/10.1039/C7AY00669A>.
- 147 Rosenau, C. P.; Jelier, B. J.; Gossert, A. D.; Togni, A. Exposing the Origins of Irreproducibility in Fluorine NMR Spectroscopy. *Angew. Chem. Int. Ed.* **2018**, *57* (30), 9528–9533. <https://doi.org/10.1002/anie.201802620>.
- 148 Krissinel, E.; Henrick, K. Inference of Macromolecular Assemblies from Crystalline State. *J. Mol. Biol.* **2007**, *372* (3), 774–797. <https://doi.org/10.1016/j.jmb.2007.05.022>.
- 149 Gill, S. C.; von Hippel, P. H. Calculation of Protein Extinction Coefficients from Amino Acid Sequence Data. *Anal. Biochem.* **1989**, *182* (2), 319–326. [https://doi.org/10.1016/0003-2697\(89\)90602-7](https://doi.org/10.1016/0003-2697(89)90602-7).

-
- 150 Walker, J. M. The Proteomics Protocols Handbook Humana Press, 1st edition, **2005**, p.571–606. <https://doi.org/10.1385/1592598900>.
- 151 Graham, D. L.; Eccleston, J. F.; Lowe, P. N. The Conserved Arginine in Rho-GTPase-Activating Protein Is Essential for Efficient Catalysis but Not for Complex Formation with Rho-GDP and Aluminium Fluoride. *Biochemistry* **1999**, 38 (3), 985–991. <https://doi.org/10.1021/bi9821770>.
- 152 Zhou, J.; Li, X.; Xia, J.; Wen, Y.; Zhou, J.; Yu, Z.; Tian, B. The Role of Temperature and Bivalent Ions in Preparing Competent Escherichia Coli. *3 Biotech* **2018**, 8 (5), 222. <https://doi.org/10.1007/s13205-018-1243-x>.
- 153 Norrander, J.; Kempe, T.; Messing, J. Construction of Improved M13 Vectors Using Oligodeoxynucleotide-Directed Mutagenesis. *Gene* **1983**, 26 (1), 101–106. [https://doi.org/10.1016/0378-1119\(83\)90040-9](https://doi.org/10.1016/0378-1119(83)90040-9).
- 154 Tucker, J.; Sczakiel, G.; Feuerstein, J.; John, J.; Goody, R. S.; Wittinghofer, A. Expression of P21 Proteins in Escherichia Coli and Stereochemistry of the Nucleotide-Binding Site. *EMBO J.* **1986**, 5 (6), 1351–1358.
- 155 Völkert, M.; Uwai, K.; Tebbe, A.; Popkirova, B.; Wagner, M.; Kuhlmann, J.; Waldmann, H. Synthesis and Biological Activity of Photoactivatable N -Ras Peptides and Proteins. *J. Am. Chem. Soc.* **2003**, 125 (42), 12749–12758. <https://doi.org/10.1021/ja036178d>.
- 156 Miyake-Stoner, S. J.; Refakis, C. A.; Hammill, J. T.; Lusic, H.; Hazen, J. L.; Deiters, A.; Mehl, R. A. Generating Permissive Site-Specific Unnatural Aminoacyl-tRNA Synthetases. *Biochemistry* **2010**, 49 (8), 1667–1677. <https://doi.org/10.1021/bi901947r>.
- 157 Jin, Y.; Molt, R. W.; Pellegrini, E.; Cliff, M. J.; Bowler, M. W.; Richards, N. G. J.; Blackburn, G. M.; Walther, J. P. Assessing the Influence of Mutation on GTPase Transition States by Using X-Ray Crystallography, ¹⁹F-NMR, and DFT Approaches. *Angew. Chemie Int. Ed.* **2017**, 56 (33), 9732–9735. <https://doi.org/10.1002/anie.201703074>.
- 158 Rittinger, K.; Walker, P. A.; Eccleston, J. F.; Smerdon, S. J.; Gamblin, S. J. Structure at 1.65 Å of RhoA and Its GTPase-Activating Protein in Complex with a Transition-State Analogue. *Nature* **1997**, 389 (6652), 758–762. <https://doi.org/10.1038/39651>.
- 159 Catanzariti, A.-M.; Soboleva, T. A.; Jans, D. A.; Board, P. G.; Baker, R. T. An Efficient System for High-Level Expression and Easy Purification of Authentic Recombinant Proteins. *Protein Sci.* **2004**, 13 (5), 1331–1339. <https://doi.org/10.1110/ps.04618904>.
- 160 Minnihan, E. C.; Young, D. D.; Schultz, P. G.; Stubbe, J. Incorporation of Fluorotyrosines into Ribonucleotide Reductase Using an Evolved, Polyspecific Aminoacyl-tRNA Synthetase. *J. Am. Chem. Soc.* **2011**, 133 (40), 15942–15945. <https://doi.org/10.1021/ja207719f>.
- 161 Demidkina, T. V.; Barbolina, M. V.; Faleev, N. G.; Sundararajus, B.; Gollnick, P. D.; Phillips, R. S. Threonine-124 and Phenylalanine-448 in Citrobacter freundii Tyrosine Phenol-Lyase Are Necessary for Activity with L-Tyrosine. *Biochem. J.* **2002**, 363 (3), 745–752. <https://doi.org/10.1042/0264-6021:3630745>.
- 162 Kim, K.; Cole, P. A.; Kinetic Analysis of a Protein Tyrosine Kinase Reaction Transition State in the Forward and Reverse Directions. *J. Am. Chem. Soc.* 1998, 120 (28), 6851–6858. <https://doi.org/10.1021/ja9808393>.

-
- 163 Gil, A. A.; Haigney, A.; Laptenok, S. P.; Brust, R.; Lukacs, A.; Iuliano, J. N.; Jeng, J.; Melief, E. H.; Zhao, R. K.; Yoon, E. Bin; Clark, I. P.; Townie, M.; Greetham, G. M.; Ng, A.; Truglio, J. J.; French, J. B.; Meech, S. R.; Tonge, P. J. Mechanism of the AppABLUF Photocycle Probed by Site-Specific Incorporation of Fluorotyrosine Residues: Effect of the Y21 PKa on the Forward and Reverse Ground-State Reactions. *J. Am. Chem. Soc.* **2016**, *138* (3), 926–935. <https://doi.org/10.1021/jacs.5b11115>.
- 164 Seeliger, M. A.; Young, M.; Henderson, M. N.; Pellicena, P.; King, D. S.; Falick, A. M.; Kuriyan, J. High Yield Bacterial Expression of Active C-Abl and c-Src Tyrosine Kinases. *Protein Sci.* **2005**, *14* (12), 3135–3139. <https://doi.org/10.1110/ps.051750905>.
- 165 D'Arcy, A.; Bergfors, T.; Cowan-Jacob, S. W.; Marsh, M. Microseed Matrix Screening for Optimization in Protein Crystallization: What Have We Learned? *Acta Crystallogr. Sect. F Struct. Biol. Commun.* **2014**, *70* (9), 1117–1126. <https://doi.org/10.1107/S2053230X14015507>.
- 166 Tickle, I. J.; Flensburg, C.; Keller, P.; Paciorek, W.; Sharff, A.; Vonrhein, C.; Bricogne, G. STARAN/ISO GLOBAL PHASING LTD: Cambridge, UK, **2018**. <http://staraniso.globalphasing.org/cgi-bin/staraniso.cgi>.
- 167 Winn, M. D.; Ballard, C. C.; Cowtan, K. D.; Dodson, E. J.; Emsley, P.; Evans, P. R.; Keegan, R. M.; Krissinel, E. B.; Leslie, A. G. W.; McCoy, A.; McNicholas, S. J.; Murshudov, G. N.; Pannu, N. S.; Potterton, E. A.; Powell, H. R.; Read, R. J.; Vagin, A.; Wilson, K. S. Overview of the CCP 4 Suite and Current Developments. *Acta Crystallogr. Sect. D Biol. Crystallogr.* **2011**, *67* (4), 235–242. <https://doi.org/10.1107/S0907444910045749>.
- 168 Vagin, A.; Teplyakov, A. MOLREP: An Automated Program for Molecular Replacement. *J. Appl. Crystallogr.* **1997**, *30* (6), 1022–1025. <https://doi.org/10.1107/S0021889897006766>.
- 169 Vagin, A. A.; Steiner, R. A.; Lebedev, A. A.; Potterton, L.; McNicholas, S.; Long, F.; Murshudov, G. N. REFMAC 5 Dictionary: Organization of Prior Chemical Knowledge and Guidelines for Its Use. *Acta Crystallogr. Sect. D Biol. Crystallogr.* **2004**, *60* (12), 2184–2195. <https://doi.org/10.1107/S0907444904023510>.
- 170 Lebedev, A. A.; Young, P.; Isupov, M. N.; Moroz, O. V.; Vagin, A. A.; Murshudov, G. N. JLigand: A Graphical Tool for the CCP 4 Template-Restraint Library. *Acta Crystallogr. Sect. D Biol. Crystallogr.* **2012**, *68* (4), 431–440. <https://doi.org/10.1107/S090744491200251X>.
- 171 Pretsch, E.; Bühlmann, P.; Badertscher, M.; Structure Determination of Organic Compounds; Springer, 4th edition, **2009**, p. 251.
- 172 Hansen, P. E. Isotope Effect on Chemical Shifts in Hydrogen-Bonded Systems. *J. Label. Compd. Radiopharm.* **2007**, *50* (11–12), 967–981. <https://doi.org/10.1002/jlcr.1440>.
- 173 Baxter, N. J.; Hounslow, A. M.; Bowler, M. W.; Williams, N. H.; Blackburn, G. M.; Walther, J. P. MgF₃⁻ and α-Galactose 1-Phosphate in the Active Site of β-Phosphoglucomutase Form a Transition State Analogue of Phosphoryl Transfer. *J. Am. Chem. Soc.* **2009**, *131* (45), 16334–16335. <https://doi.org/10.1021/ja905972m>.

-
- 174 Lee, C. R.; Park, Y. H.; Min, H.; Kim, Y. R.; Seok, Y. J. Determination of Protein Phosphorylation by Polyacrylamide Gel Electrophoresis. *J. Microbiol.* **2019**, *57* (2), 93–100. <https://doi.org/10.1007/s12275-019-9021-y>.
- 175 Wittinghofer, A.; Nassar, N. How Ras-Related Proteins Talk to Their Effectors. *Trends Biochem. Sci.* **1996**, *21* (12), 488–491. [https://doi.org/10.1016/S0968-0004\(96\)10064-5](https://doi.org/10.1016/S0968-0004(96)10064-5).
- 176 Spoerner, M.; Wittinghofer, A.; Kalbitzer, H. R. Perturbation of the Conformational Equilibria in Ras by Selective Mutations as Studied by ^{31}P NMR Spectroscopy. *FEBS Lett.* **2004**, *578* (3), 305–310. <https://doi.org/10.1016/j.febslet.2004.11.020>.
- 177 Matsumoto, S.; Miyano, N.; Baba, S.; Liao, J.; Kawamura, T.; Tsuda, C.; Takeda, A.; Yamamoto, M.; Kumasaka, T.; Kataoka, T.; Shima, F. Molecular Mechanism for Conformational Dynamics of Ras-GTP Elucidated from In-Situ Structural Transition in Crystal. *Sci. Rep.* **2016**, *6* (1), 25931. <https://doi.org/10.1038/srep25931>.
- 178 Sherekar, M.; Han, S.-W.; Ghirlando, R.; Messing, S.; Drew, M.; Rabara, D.; Waybright, T.; Juneja, P.; O'Neill, H.; Stanley, C. B.; Bhownik, D.; Ramanathan, A.; Subramaniam, S.; Nissley, D. V.; Gillette, W.; McCormick, F.; Esposito, D. Biochemical and Structural Analyses Reveal That the Tumor Suppressor Neurofibromin (NF1) Forms a High-Affinity Dimer. *J. Biol. Chem.* **2020**, *295* (4), 1105–1119. [https://doi.org/10.1016/S0021-9258\(17\)49919-4](https://doi.org/10.1016/S0021-9258(17)49919-4).
- 179 Wang, Y.; He, H.; Srivastava, N.; Vikarunnessa, S.; Chen, Y. -b.; Jiang, J.; Cowan, C. W.; Zhang, X. Plexins Are GTPase-Activating Proteins for Rap and Are Activated by Induced Dimerization. *Sci. Signal.* **2012**, *5* (207), ra6–ra6. <https://doi.org/10.1126/scisignal.2002636>.
- 180 Wang, Y.; He, H.; Srivastava, N.; Vikarunnessa, S.; Chen, Y.; Jiang, J.; Cowan, C. W.; Zhang, X. Plexins Are GTPase-Activating Proteins for Rap and Are Activated by Induced Dimerization. *Sci. Signal.* **2012**, *5* (207), ra6. <https://doi.org/10.1126/scisignal.2002636>.
- 181 Scheffzek, K.; Shivalingaiah, G. Ras-Specific GTPase-Activating Proteins—Structures, Mechanisms, and Interactions. *Cold Spring Harb. Perspect. Med.* **2019**, *9* (3), a031500. <https://doi.org/10.1101/cshperspect.a031500>.
- 182 Wang, F.; Qin, L.; Wong, P.; Gao, J. Facile Synthesis of Tetrafluorotyrosine and Its Application in pH Triggered Membrane Lysis. *Org. Lett.* **2011**, *13* (2), 236–239. <https://doi.org/10.1021/o102610q>.
- 183 Filler, R.; Ayyangar, N. R.; Gustowski, W.; Kang, H. H. New Reactions of Polyfluoroaromatic Compounds. Pentafluorophenylalanine and Tetrafluorotyrosine. *J. Org. Chem.* **1969**, *34* (3), 534–538. <https://doi.org/10.1021/jo01255a011>.
- 184 Seyedsayamdost, M. R.; Yee, C. S.; Stubbe, J. A. Site-Specific Incorporation of Fluorotyrosines into the R2 Subunit of E. Coli Ribonucleotide Reductase by Expressed Protein Ligation. *Nat. Protoc.* **2007**, *2* (5), 1225–1235. <https://doi.org/10.1038/nprot.2007.159>.
- 185 Milić, D.; Demidkina, T. V.; Faleev, N. G.; Matković-Čalogović, D.; Antson, A. A. Insights into the Catalytic Mechanism of Tyrosine Phenol-Lyase from X-Ray Structures of Quinonoid Intermediates. *J. Biol. Chem.* **2008**, *283* (43), 29206–29214. <https://doi.org/10.1074/jbc.M802061200>.

-
- 186 Kim, K.; Cole, P. A. Kinetic Analysis of a Protein Tyrosine Kinase Reaction Transition State in the Forward and Reverse Directions. *J. Am. Chem. Soc.* **1998**, *120* (28), 6851–6858. <https://doi.org/10.1021/ja9808393>.
- 187 Smolskaya, S.; Andreev, Y. Site-Specific Incorporation of Unnatural Amino Acids into Escherichia Coli Recombinant Protein: Methodology Development and Recent Achievement. *Biomolecules* **2019**, *9* (7), 255. <https://doi.org/10.3390/biom9070255>.
- 188 Seyedsayamdst, M. R.; Reece, S. Y.; Nocera, D. G.; Stubbe, J. A. Mono-, Di-, Tri-, and Tetra-Substituted Fluorotyrosines: New Probes for Enzymes That Use Tyrosyl Radicals in Catalysis. *J. Am. Chem. Soc.* **2006**, *128* (5), 1569–1579. <https://doi.org/10.1021/ja055926r>.
- 189 Oktaviani, N. A.; Pool, T. J.; Kamikubo, H.; Slager, J.; Scheek, R. M.; Kataoka, M.; Mulder, F. A. A. Comprehensive Determination of Protein Tyrosine pKa Values for Photoactive Yellow Protein Using Indirect ¹³C NMR Spectroscopy. *Biophys. J.* **2012**, *102* (3), 579–586. <https://doi.org/10.1016/j.bpj.2011.12.024>.
- 190 Stevens, J. S.; Coulter, S.; Jaye, C.; Fischer, D. A.; Schroeder, S. L. M. Core level spectroscopies locate hydrogen in the proton transfer pathway – identifying quasi-symmetrical hydrogen bonds in the solid state. *Phys. Chem. Chem. Phys.* **2020**, *22* (9), 4916–4923. <https://doi.org/10.1039/C9CP05677G>
- 191 Sanjuan-Szklarz, W. F.; Woińska, M.; Domagała, S.; Dominiak, P. M.; Grabowsky, S.; Jayatilaka, D.; Gutmann, M.; Woźniak, K. On the Accuracy and Precision of X-Ray and Neutron Diffraction Results as a Function of Resolution and the Electron Density Model. *IUCrJ* **2020**, *7* (5), 920–933. <https://doi.org/10.1107/S2052252520010441>.
- 192 Hodel, A.; Kim, S. H.; Brünger, A. T. Model Bias in Macromolecular Crystal Structures. *Acta Crystallogr. Sect. A Found. Crystallogr.* **1992**, *48* (6), 851–858. <https://doi.org/10.1107/S0108767392006044>.
- 193 Boudhraa, Z.; Carmona, E.; Provencher, D.; Mes-Masson, A.-M. Ran GTPase: A Key Player in Tumor Progression and Metastasis. *Front. Cell Dev. Biol.* **2020**, *8*. <https://doi.org/10.3389/fcell.2020.00345>.
- 194 Khrenova, M. G.; Grigorenko, B. L.; Nemukhin, A. V. Molecular Modeling Reveals the Mechanism of Ran-RanGAP-Catalyzed Guanosine Triphosphate Hydrolysis without an Arginine Finger. *ACS Catal.* **2021**, *11* (15), 8985–8998. <https://doi.org/10.1021/acscatal.1c00582>.
- 195 Phillips, R. A.; Hunter, J. L.; Eccleston, J. F.; Webb, M. R. The Mechanism of Ras GTPase Activation by Neurofibromin. *Biochemistry* **2003**, *42* (13), 3956–3965. <https://doi.org/10.1021/bi027316z>.
- 196 Moore, K. J. M.; Webb, M. R.; Eccleston, J. F. Mechanism of GTP Hydrolysis by P21N-Ras Catalyzed by GAP: Studies with a Fluorescent GTP Analog. *Biochemistry* **1993**, *32* (29), 7451–7459. <https://doi.org/10.1021/bi00080a016>.
- 197 Sermon, B. A.; Lowe, P. N.; Strom, M.; Eccleston, J. F. The Importance of Two Conserved Arginine Residues for Catalysis by the Ras GTPase-Activating Protein, Neurofibromin. *J. Biol. Chem.* **1998**, *273* (16), 9480–9485. <https://doi.org/10.1074/jbc.273.16.9480>.
- 198 Sermon, B. A.; Lowe, P. N.; Strom, M.; Eccleston, J. F. The Importance of Two Conserved Arginine Residues for Catalysis by the Ras GTPase-Activating Protein, Neurofibromin. *J. Biol. Chem.* **1998**, *273* (16), 9480–9485. <https://doi.org/10.1074/jbc.273.16.9480>.

-
- 199 Hoshino, M.; Clanton, D. J.; Shih, T. Y.; Kawakita, M.; Hattori, S. Interaction of Ras Oncogene Product P21 with Guanine Nucleotides. *J. Biochem.* **1987**, *102* (3), 503–511. <https://doi.org/10.1093/oxfordjournals.jbchem.a122082>.
- 200 Amin, E.; Jaiswal, M.; Derewenda, U.; Reis, K.; Nouri, K.; Koessmeier, K. T.; Aspenström, P.; Somlyo, A. V.; Dvorsky, R.; Ahmadian, M. R. Deciphering the Molecular and Functional Basis of RhoGAP Family Proteins: A Systematic Approach Toward selective Inactivation of Rho Family. *J. Biol. Chem.* **2016**, *291* (39), 20353–20371. <https://doi.org/10.1074/jbc.M116.736967>.
- 201 Lau, C. K. Y.; Ishida, H.; Liu, Z.; Vogel, H. J. Solution Structure of Escherichia Coli FeoA and Its Potential Role in Bacterial Ferrous Iron Transport. *J. Bacteriol.* **2013**, *195* (1), 46–55. <https://doi.org/10.1128/JB.01121-12>.
- 202 Kalbitzer, H. R.; Rosnizeck, I. C.; Munte, C. E.; Narayanan, S. P.; Kropf, V.; Spoerner, M. Intrinsic Allosteric Inhibition of Signaling Proteins by Targeting Rare Interaction States Detected by High-Pressure NMR Spectroscopy. *Angew. Chem. Int. Ed.* **2013**, *52* (52), 14242–14246. <https://doi.org/10.1002/anie.201305741>.
- 203 Foster, M. P.; McElroy, C. A.; Amero, C. D. Solution NMR of Large Molecules and Assemblies. *Biochemistry* **2007**, *46* (2), 331–340. <https://doi.org/10.1021/bi0621314>.
- 204 Atkins P.; Paula J.; Keeler J.; Atkins' Physical Chemistry, Oxford University Press, 11th edition, **2017**, p. 213–215.
- 205 Molt, R. W.; Pellegrini, E.; Jin, Y. A GAP-GTPase-GDP-Pi Intermediate Crystal Structure Analyzed by DFT Shows GTP Hydrolysis Involves Serial Proton Transfers. *Chem. – A Eur. J.* **2019**, *25* (36), 8484–8488. <https://doi.org/10.1002/chem.201901627>.
- 206 Bao, H.; Li, F.; Wang, C.; Wang, N.; Jiang, Y.; Tang, Y.; Wu, J.; Shi, Y. Structural Basis for the Specific Recognition of RhoA by the Dual GTPase-Activating Protein ARAP3. *J. Biol. Chem.* **2016**, *291* (32), 16709–16719. <https://doi.org/10.1074/jbc.M116.736140>.
- 207 Hall, B. E.; Bar-Sagi, D.; Nassar, N. The Structural Basis for the Transition from Ras-GTP to Ras-GDP. *Proc. Natl. Acad. Sci.* **2002**, *99* (19), 12138–12142. <https://doi.org/10.1073/pnas.192453199>.
- 208 Knihtila, R.; Holzapfel, G.; Weiss, K.; Meilleur, F.; Mattos, C. Neutron Crystal Structure of RAS GTPase Puts in Question the Protonation State of the GTP γ-Phosphate. *J. Biol. Chem.* **2015**, *290* (52), 31025–31036. <https://doi.org/10.1074/jbc.M115.679860>.
- 209 Menyhárd, D. K.; Pálfy, G.; Orgován, Z.; Vida, I.; Keserü, G. M.; Perczel, A. Structural Impact of GTP Binding on Downstream KRAS Signaling. *Chem. Sci.* **2020**, *11* (34), 9272–9289. <https://doi.org/10.1039/D0SC03441J>.
- 210 Khrenova, M. G.; Grigorenko, B. L.; Nemukhin, A. V. Molecular Modeling Reveals the Mechanism of Ran-RanGAP-Catalyzed Guanosine Triphosphate Hydrolysis without an Arginine Finger. *ACS Catal.* **2021**, *11* (15), 8985–8998. <https://doi.org/10.1021/acscatal.1c00582>.

7 Appendix

7.1 Protein Sequences

Single letter amino acid code is used for the protein sequences. A bold residue indicates a residue of interest. '*' indicates either a stop codon or a ncAA incorporation site.

7.1.1 HRas (1–166)

```
1      MTEYKLVVVG AGGVGKSAALT IQLIQNHFVD EYDPTIEDSY RKQVVIDGET
51     CLLDILDTAG QEEYSAMRDQ YMRTGEGFLC VFAINNTKSF EDIHQYREQI
101    KRVKDSDDPV MVLVGNKCDL AARTVESRQA QDLARSYGIP YIETSAKTRQ
151    GVEDAFYTLV REIRQH*
```

7.1.2 hSOS1 (564–1049)

```
1      EEQMRLPSAD VYRFAEPDSE ENIIFEENMQ PKAGIPIIKA GTVIKLIERL
51     TYHMYADPNF VRTFLTTYRS FCKPQELLSL IIERFEIPEP EPTEADRIAI
101    ENGDQPLSAE LKRFRKEYIQ PVQLRVLNVC RHWVEHHFYD FERDAYLLQR
151    MEEFIGTVRG KAMKKWVESI TKIIQRKKIA RDNGPGHNIT FQSSPPTVEW
201    HISRPGHIET FDLLTLHPIE IARQLTLLES DLYRAVQPSE LVGSVWTKE
251    KEINSPNLLK MIRHTTNLTL WFEKCIVETE NLEERVAVVS RIIIEILQVFQ
301    ELNNFNNGVLE VVSAMNSSPV YRLDHTFEQI PSRQKPILEE AHELSEDHYK
351    KYLAKLRSIN PPCVPFFGIY LTNILKTEEG NPEVLKRHGK ELINFSKRRK
401    VAEITGEIQQ YQNQPYCLRV ESDIKRFFEN LNPMGNSMEK EFTDYLFNKS
451    LEIEPRNPKP LPRFPKKSY PLKSPGVRPS NPPRPGT*
```

7.1.3 YoPH

```
1      MDLSLSDLHR QVSRLVQQES GDCTGKLRGN VAANKETTFQ GLTIASGARE
51     SEKVFAQTVL SHVANIVLTQ EDTAKLLQST VKHNLNNYEL RSVGNGNNSVL
101    VSLRSDQMTEL QDAKVLLEAA LRQESGARGH VSSHSHSVLH APGTPVREGL
151    RSHLDPRTPP LPPRERPHTS GHHGAGEARA TAPSTVSPYGY PEARAELSSR
201    LTTLRNTLAP ATNDPRYLQA CGGEKLNFR DIQCCRQTA V RADLNANYIQ
```

251 VGNTRTIACQ YPLQSQLESH FRMLAENRTP VLAVLASSSE IANQRFGMPD
301 YFRQSGTYGS ITVESKMTQQ VGLGDGIMAD MYTLTIREAG QKTISPVVH
351 VGNWPDQTAV SSEVTKALAS LVDQTAETKR NMYESKGSSA VADDSKLRPV
401 IHCRAGVGRT AQLIGAMCMN DSRNSQLSVE DMVSQMRVQR NGIMVQKDEQ
451 LDVLIKLAEG QGRPLLNS*

7.1.4 p120 RasGAP (714–1048)

1 GSMEKIMPEE EYSEFKELIL QKELHVYYAL SHVCQDRTL LASILLRIFL
51 HEKLESLLC TLNDREISME DEATTLFRAT TLASTLMEQY MKATATQFVH
101 HALKD SILKI MESKQSCELS PSKLEKNEDV NTNLTLLNI LSELVEKIFM
151 ASEILPPTLR YIYGCLQKSV QHKWPTNTTM RTRVVSGFVF LRLICPAI LN
201 PRMFNIISDS PSPIAARTLI LVAKSVQNL A NLVEFGAKEP YM EGVNPFIK
251 SNKHRMIMFL DELGNVPELP DTTEHSRTDL SRDLAALHEI CVAHSDELRT
301 LSNERGAQQH VLKKLLAIT LLQQKQNQYT KTNDVR*

7.1.5 USP2 (259–605)

1 MGSSHHHHHH SSGLVPRGSH MLEDPLLTKA KNSKSAQGLA GLRNLGNTCF
51 MNSILQCLSN TRELRDYCLQ RLYMRDLGHT SSAHTALMEE FAKLIQTIWT
101 SSPNDVVSPS EFKTQIQRYA PRFMGYNQQD AQEFLRFLLD GLHNEVNRVA
151 ARPKASPETL DHLPDEEKGR QMWRKYLERE DSRIGDLFVG QLKSSLTCTD
201 CGYCSTVFDP FWDLSLPIAK RGYPEVTLMD CMRLFTKEDI LDGDEKPTCC
251 RCRARKRCIK KFSVQRFPKI LVLHLKRFSE SRIRTSKLTT FVNFPRLDLD
301 LREFASENTN HAVYNLYAVS NHSGTTMGHH YTAYCRSPVT GEWHTFNDSS
351 VTPMSSSQVR TSDAYLLFYE LASPPSRM*

7.1.6 Trigger factor - Ubiquitin - RhoA

1 MGSSHHHHHH MQVSVETTQG LGRRVTITVA ADSIETAVKS ELVNVAKKVR
51 IDGFRKGKVP MNIVAQRYGA SVRQDVLDL MSRNFDIAII KEKINPAGAP
101 TYVPGEYKLG EDFTYSVEFE VYPEVELQGL EAIEVEKPIV EVTDADVDGM
151 LDTLRKQQAT WKEKDGAVEA EDRVTIDFTG SVDGEFFEGG KASDFVILAMG
201 QGRMIPGFED GIKGHKAGEE FTIDVTFPEE YHAESLKGKA AKFAINLKKV
251 EERELPELTA EFIGKRGVED GSVEGLRAEV RKNMERELKS AIRNRVKSQA

301 IEGLVKANDI DVPAALIDSE IDVLRRQAAQ RFGGNEKQAL ELPRELFEHQ
351 AKRRVVVGLL LGEVIRTNEL KADEERVKGL IEEMASAYED PKEVIEFYSK
401 NKELMNDMRN VALEEQAVERA VLAKAKVTEK ETTFNELMNQ QAQIFVKTLT
451 GKTITLEVEP SDTIENVKAK IQDKEGIPPD QQRLIFAGKQ LEDGRTLSY
501 NIQKESTLHL VLRLRGAAI RKKLVIVGDG ACGKTCLLIV NSKDQFPEVY
551 VPTVFENYVA DIEVDGKQVE LALWDTAGQE DYDRLRPLSY PDTDVILMCF
601 SIDSPDSLEN IPEKWTPEVK HFCPNVPIIL VGNKKDLRND EHTRRELAKM
651 KQECPVKPEEG RDMANRIGAF GYMECSAKTK DGVREVFEMA TRAALQARRG
701 KKKSGCLVL*

7.1.7 RhoA – F25N

1 AAIRKKLVIV GDGACGKTCL LIVNSKDQFP EVYVPTVFEN YVADIEVDGK
51 QVELALWDTA GQEDYDRILRP LSYPDTDVIL MCFSIDSPDS LENIPEKWTP
101 EVKHFCPNVP IILVGNKKDL RNDEHTRREL AKMKQEPVKP EERGRDMANRI
151 GAFGYMECSA KTKDGVREVF EMATRAALQA RRGKKKGCL VL*

7.1.8 sfGFP - N150TAG

1 MVSKGEELFT GVVPILVELD GDVNGHKFSV RGEGEGETDN GKLTLKFICT
51 TGKLPVPWPT LVTTLTGYVQ CFSRYPDHMK RHDFFKSAMP EGYVQERTIS
101 FKDDGTYKTR AEVKFEGDTL VNRIELKGID FKEDGNILGH KLEYNFNSH*
151 VYITADKQKN GIKANFKIRH NVEDGSVQLA DHYQQNTPIG DGPVLLPDNH
201 YLSTQSVL SK DPNEKRDHMV LLEFVTAAGI THGMDELYKG SHHHHHH*

7.1.9 hDbs (622–966)

1 MGEEEESLAI LRRHVMSELL DTERAYVEEL LCVLEGYAAE MDNPLMAHLL
51 STGLHNKKDV LFGNMEEIYH FHNRIFLREL ENYTDCEPELV GRCFLERMED
101 FQIYEKYCQN KPRSESLWRQ CSDCPFFQEC QRKLDHKLSL DSYLLKPVQR
151 ITKYQLLLKE MLKYSRNCEG AEDLQEALSS ILGILKAVND SMHLIAITGY
201 DGNLGDLGKL LMQGSFSVWT DHKRGHTKVK ELARFKPMQR HLFLHEKAVL
251 FCKKREENG GYEKAPSYSY KQSLNMAAVG ITENVKGDAK KFEIWYNARE
301 EVYIVQAPTP EIKAAWVNEI RKVLTSQQLQA CREASQHRAL EQSQSLLEHH
351 HHHH*

7.1.10 p50 RhoGAP(198–439) - R85A

1 GSHVKLEQLG IPLPVLKYDD FLKSTQKSPA TAPKPMPPRP PLPNQQFGVS
51 LQHLQEKNPE QEPIPIVLRE TVAYLQAHAL TTEGIF**A**RSA NTQVVREVQQ
101 KYNMGLPVDF DQYNELHLPV VILKTFREL PEPPLTFDLY PHVVGFLNID
151 ESQRVPATLQ VLQTLPEENY QVLRFLTAFL VQISAHSDQN KMTNTNLAVV
201 FGPNLLWAKD AAITLKAINP INTFTKFLLD HQGEFPSPD PSGL*

7.1.11 MjTyrRS – Y32L, L65G, H70N, D158S, I159Y, L162H

1 MDEFEMIKRN TSEIIISSEEEL REVLIKDEKS **A**LIGFEPSGK IHLGHYLQIK
51 KMIDLQNAGF DIIIGLADLN AYLNQKGELD EIRKIGDYNK KVFEAMGLKA
101 KYVYGSEFQL DKDYTLNVYR LALKTTLKRA RRSMELIARE DENPKVAEVI
151 YPIMQVN**SYH** YHGVDVAVGG MEQRKIHMLA RELLPKKVVC IHNPVLTGLD
201 GEGKMSSSKG NFIAVDDSPE EIRAKIKKAY CPAGVVEGNP IMEIAKYFLE
251 YPLTIKRPEK FGGDLTVNSY EELESLFKNK ELHPMDLKNA VAEELIKILE
301 PIRKRL*

7.1.12 TPL

1 MNYPAEPFRI KSVETVSMIP RDERLKKMQE AGYNTFLLNS KDIYIDL LTD
51 SGTNAMSDKQ WAGMMMGDEA YAGSENFYHL ERTVQELFGF KHIVPTHQGR
101 GAENLLSQLA IKPGQYVAGN MYFTTTRYHQ EKNGAVFVDI VRDEAHDA GL
151 NIAFKGDIDL KKLQQLIDEK GAENIAYICL AVTVNLAGGQ PVSMANMRAV
201 RELTEAHGIK VFYDATRCVE NAYFIKEQE**Q** GFENKSIAEI VHEMF SYADG
251 CTMSGKDCL VNIGGFLCMN DDEMFS SAKELVVVYEGMPS YGGLAGR DME
301 AMAIGLREAM QEYIEHRVK QVRYLGDKLK AAGVPIVEPV GGHAVFLDAR
351 RFCEHLTQDE FPAQSLAASI YVETGVRSME RGIIISAGRNN VTGEHHRPKL
401 ETVRLTIPRR VYTYAHMDVV ADGIIKLYQH KEDIRGLKFI YEPKQLRFFT
451 ARFDYI*

7.1.13 cSrc (251–533)

1 MGSSHHHHHH DYDIPTTENL YFQGHMQTQG LAKDAWEIPR ESLRLEV KLG
51 QGCFGEVWMG TWNGTTRVAI KTLKPGTMSP EAFLQEAQVM KKLRHEKLVQ

101 LYAVVSEEPI YIVTEYMSKG SLDFLKgem GKYLRLPQLV DMAAQIASGM
151 AYVERMNYVH RDLRAANILV GENLVCKVAD FGLARLIEDN EYTARQGAKF
201 PIKWTAPEAA LYGRFTIKSD VWSFGILLTE LTTKGRVPYP GMVNREVLDQ
251 VERGYRMPCP PECPESLHDL MCQCWRKDPE ERPTFEYLQA FLEDYFTSTE
301 PQYQPGENL*

7.2 Gene Sequences

7.2.1 Gene Fragment: USP2-cc

```
caattcccctctagaaataatttgttaactttaagaaggagatataccatggcag  
cagccatcatcatcatcacagcagcggcctggtgccgcggcagccatatgctc  
gaggatcctctgctcaccaaagccaagaattcaaagagtgcccagggtctggctggc  
ttcgaaaccttggaaacacacgtgctcatgaactcaattcttcagtgccctgagcaacac  
ccgagagctgagagattactgcctccagaggctgtacatgcgggacctcggccacacc  
agcagcgctcacacggccctcatggaagagttgcaaaaactaatccagaccatatgga  
cgtcgccccatgtatgtggtagccatctgagttcaagacccagatccagagata  
tgcgccacgcttcatggctataatcagcaggatgctcaggaattcctcgccccctt  
ctggatggctccacaatgaggtgaaccgggtggcagcaaggcctaaggccagccctg  
agacccttgcatctccctgatgaagaaaaaggggcgacagatgtggaggaagtatct  
ggaaagggaaagacagtcggattgggatcttcgttggcagctgaagagctccctc  
acatgcaccgattgtggctactgctctacagtcttcgatccctctggatctctcg  
tgcccatcgcaaagagaggttaccctgaggtgacgttaatggattgtatgaggcttt  
caccaaagaggacatattggatggtgatgagaagccaacttgctgcccgtccgagcc  
agaaaaacgatgcataaaaaagttctgtccagaggtccaaagatctggtgctcc  
acctgaagcgattctcagaatccaggatacgaaccagcaagctcacaacattgtgaa  
tttcccactaagagagacctggacttgagagaatttgcctcagaaaacaccaaccatgct  
gtttacaacctgtatgtgtccaatcactccggaaccaccatgggaggccactata  
cagcctactgccgaagtccggttacaggcgaatggcacacttcaatgattccagtgt  
cacacccatgtcctccagccaagtgcgcaccagcgcacgcctattgtcttatgaa  
ctggccagttccaccctccgtatgtaaggatccggctgctaacaagccgaaaggaa  
gctga
```

7.2.2 hSOS1

Purchased as PUC19-hSOS1. Restriction sites: BamHI, Xhol

```
GGATCCgaagaacaaatgcgtctgccgagcgcagatgttatcggtttgcagaaccgg  
atagcgaagaaaacatcatcttgaagaaaatatgcagccgaaagcaggcattccgat  
tatcaaagcaggtacagtgattaaactgattgaacgcctgacctatcatatgtatgca  
gatccgaatttgcgtaccttctgaccacctatcgtagctttgtaaaccgcaag  
aactgctgagcctgattattgaacgtttgaaattccggaaccggaaaccgaccgaagc  
agatcgtattgcaattgaaaatggtgatcagccgtgagcgcagaactgaaacgttt  
cgtaaagaatatccagccggttcagctgcgtgttctgaatgttgcgtcattggg  
ttgaacaccacttctatgatttgagcgtgatgcatactgcgtgcacgcgtatggaaga  
attcattggcaccgttcgtggtaaagcaatgaaaaatgggtgaaagcatcaccaaa  
atcatccagcgaaaaatgcacgtgataatggccgggtcataacattaccc  
agagcagccctccgaccgttgaatggcatattagccgtctggcatattgaaacctt  
tgatctgctgaccctgcattgcacgcgtgacactgctggaaagc
```

gatctgtatcgtgcagttcagccgagcgaactggttggtagcggttggaccaaagaag
ataaaagaaaattaacagccccgaacacctgctgaaaatgattcgcataccaccaatctgac
cctgtggttgaaaaatgtattgtggaaaccgagaatctggaagaacgtgtgcagtt
gttagccgcattattgaaattctgcaggtcttcaagagctgaacaattcaacgggt
ttctggaagttgtgagcgcaatgaatagcagtccggttatcgtctggatcatacctt
tgagcagattccgagccgtcagaaaaaaaaatcctggaagaaggcacacgaactgagcga
gatcattacaaaaatacctggcaaaactgcgcagcattaatccgccttgttccgt
ttttggtatctatctgaccaacatcctgaaaaccgaagaaggtaatccggaagttct
gaaacgtcatggtaaagaactgatcaactttagcaaacgtcgtaaagtgcagaaatt
accggtaattcagcagttatcagaatcagccgtattgtctgcgtgtgaaagcgata
ttaaacgcttttcgagaacctgaatccgatggtaatagcatggaaaaagaattcac
cgactacctgttaacaagagcctggaaattgaaccgcgtaatccgaaaccgctgcct
cgtttccgaaaaatacagctatccgctgaaaagtccgggtgtcgtccgagcaatc
cggtccggtacgtaaCTCGAG

7.2.3 hDbs

Purchased as PUC19-hDbs. Restriction sites: Ncol, Xhol

CCATGGggagaagaagaagaagcctggcaattctgcgtcgcatgttatgagcgaact
gctggataccgaacgtgcataatgttgaagaactgctgtgttctggaagggtatgca
gcagaaatggataatccgctgatggcacatctgctgagcaccggctgcataacaaaa
aagatgttctgtttggcaacatggaagagatctatcatttcacaaccgcattttct
gcgcgagctggaaaactataccgattgtccggaactggttggtcgtgtttctggaa
cgtatggaagatttcagatctacgagaaatattgccagaataaaccgcgtacgcggaa
gcctgtggcgtcagtgttagcgattgcccgttttcaagaatgtcagcgtaaactgg
tcacaaaactgagcctggatagttatctgctgaaaccgggtgcagcgtattaccaaata
cagctgctgtaaagagatgctgaaatatagccgtattgtgaaggtgcagaagatc
tgcaagaagactgagcagcattctgggtattctgaaagcagttatgatgatcatgca
tctgattgccattaccggttatgatggtatctgggtgatctggtaactgctgatc
cagggtagcttagcgttggaccgatcacaagcgtggcataccaaagttaagaac
tggcacgtttaaacctatgcagcgtcacctgtttctgcataaaaagccgtctgtt
ttgtaaaaaaacgcgaagaaaatggcgagggctatgagaaagcaccgagctatagtt
aaacagagcctgaatatggcagccgttggattaccgaaaatgttaaagggtgacgc
aaaagttcgagatctggtataatgcacgtgaagaggttatattgttcaggcaccgac
accggaaattaaagcagcatgggttaatgaaattcgcaaagttctgaccagccagctg

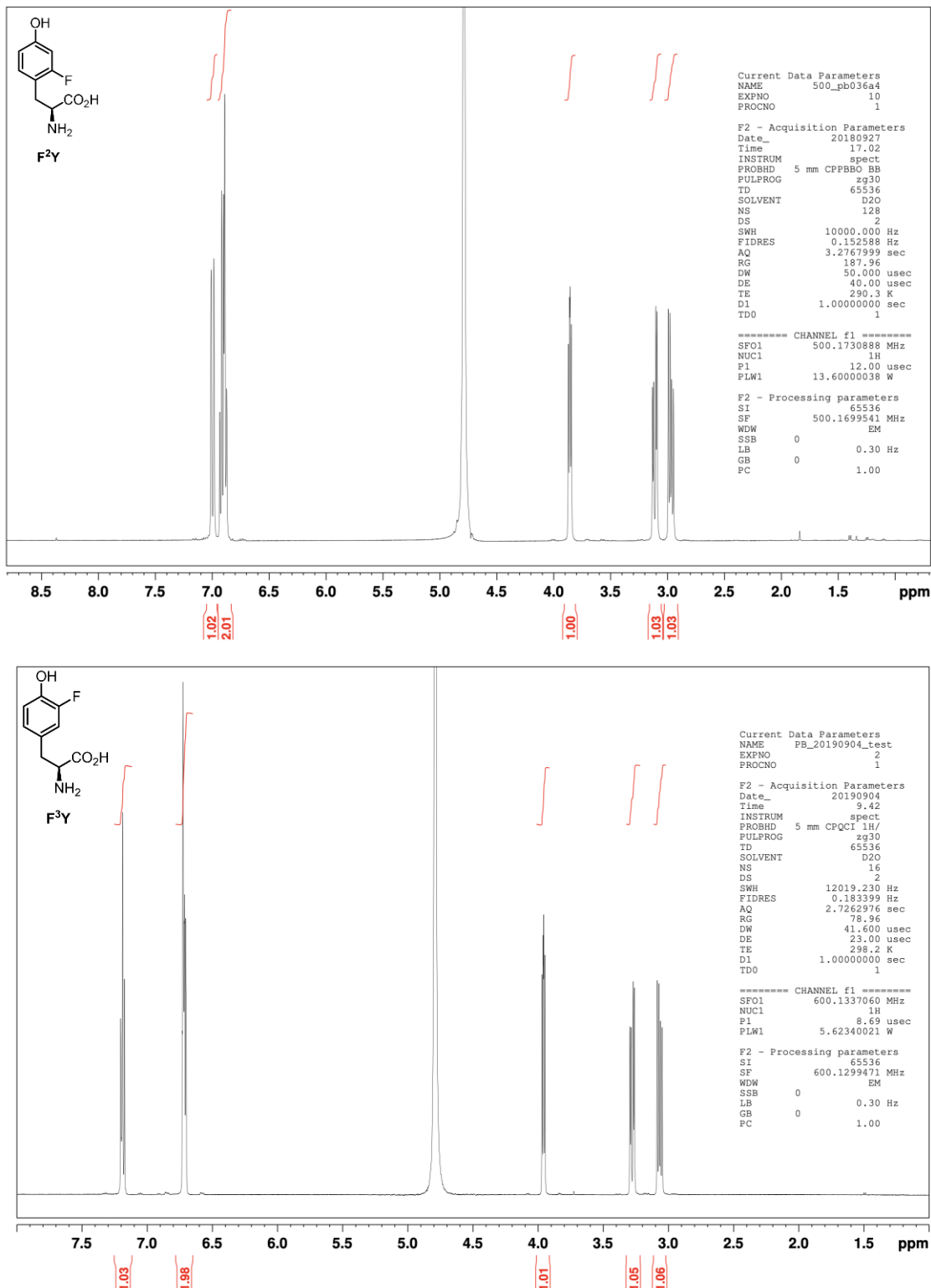
caggcatgtcgtgaagcaagccagcatcgtgcactggaacagagccagagcctgCTCG
AG

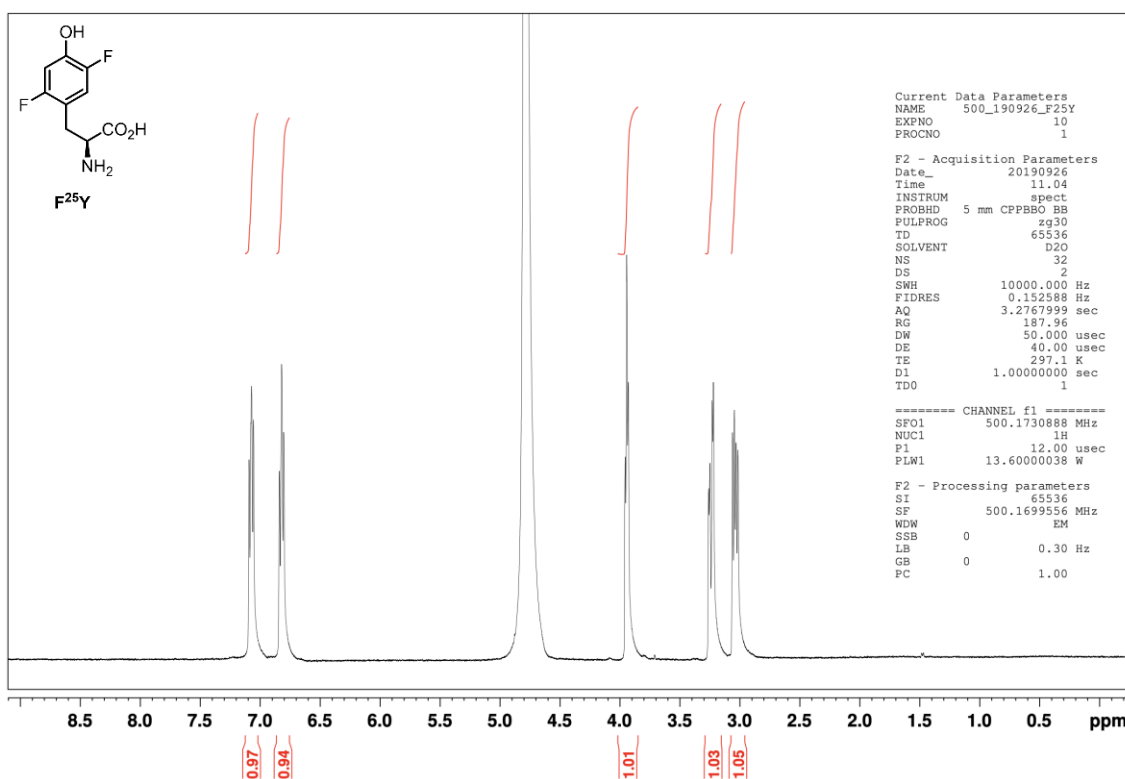
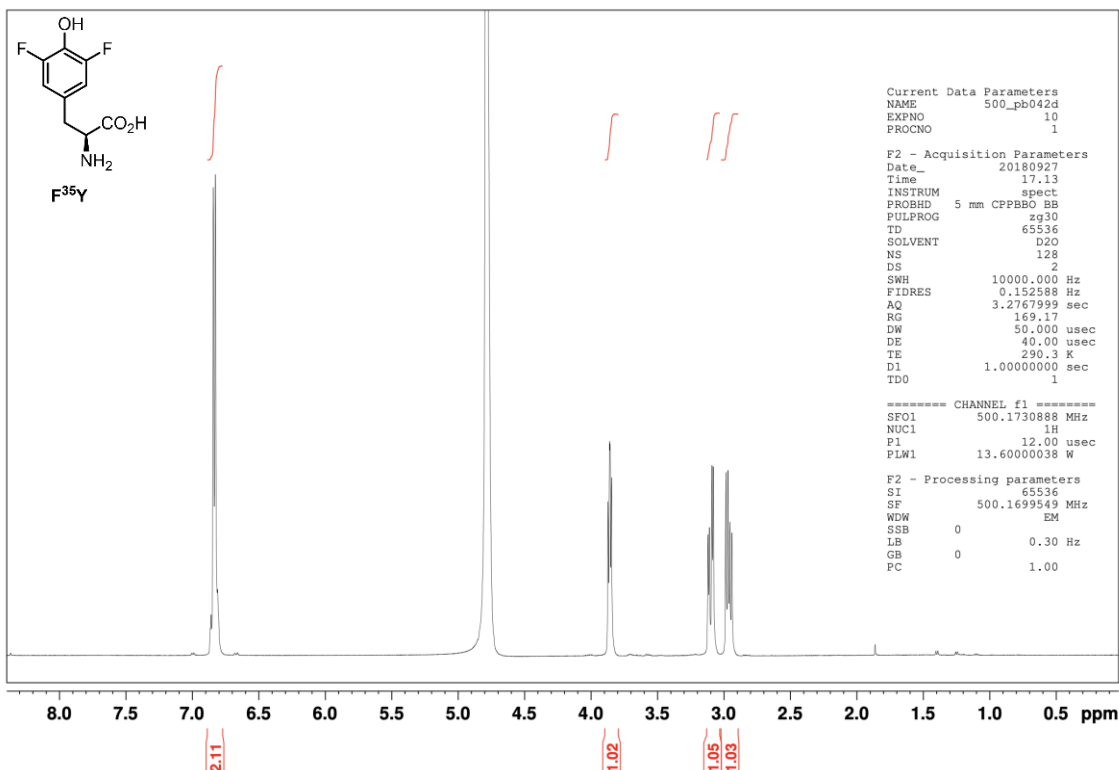
7.2.4 Gene Fragment: Trigger factor-Ubiquitin

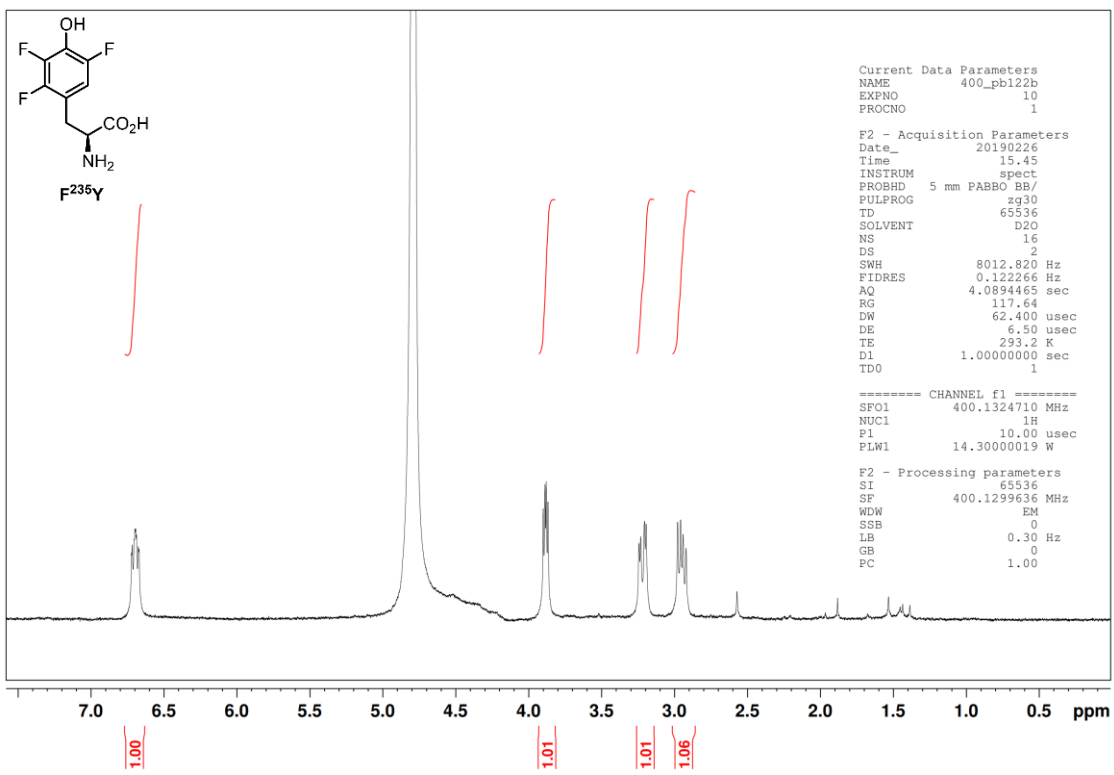
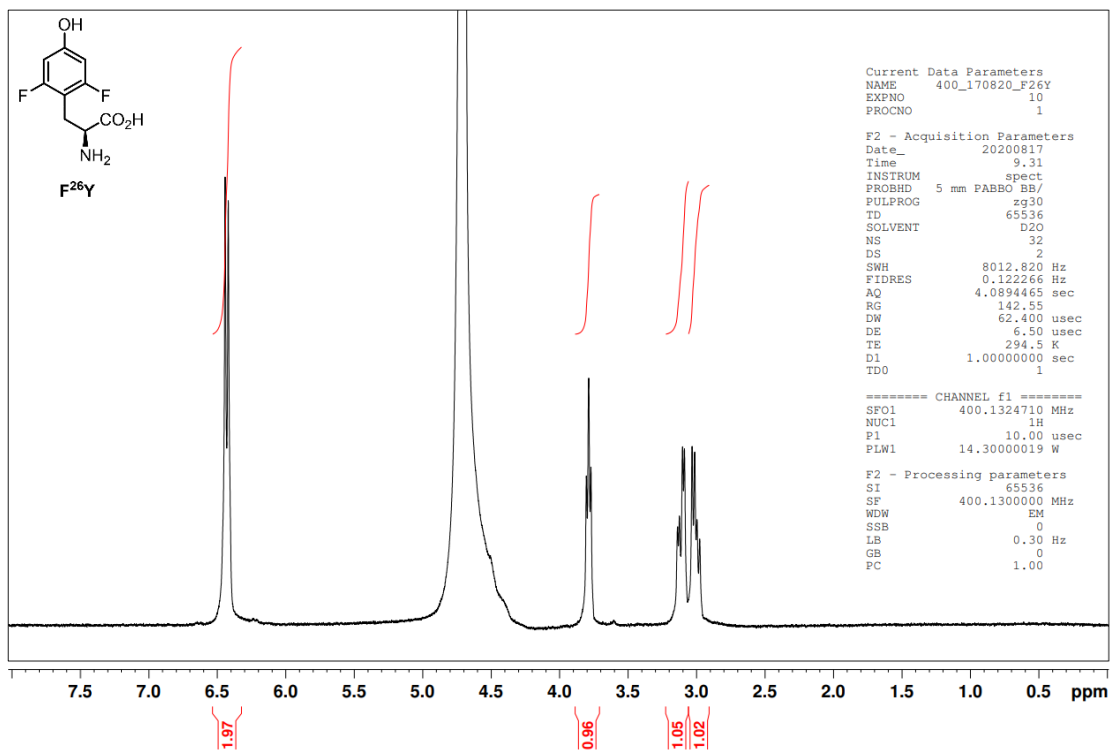
gaaggagatataccatgggcagcagccatcatcatcatcatcatatgcaagttttagt
tgaaccactcaaggcctggccggcgtaacgattactgtcgctgctgacagcatc
gagaccgctgttaaaagcgagctggtaacggtgcgaaaaaaagtacgtattgacggct
tccgcaaaggcaaagtgcataatgcattgcgttatggcgctgtac
ccaggacgttctgggtgacctgatgagccgttaacttcattgacgccatcattaaagaa
aaaatcaatccggctggcgaccgacttatgttccggcgaataacaagctgggtgaag
acttcacttactctgttagagttgaagttatccggaagttgaactgcagggtctgga
agcgatcgaagttgaaaaaccgatcggtgaatgtgaccgacgctgacgttgcacggcatg
ctggataactctgcgtaaacagcaggcgacctggaaagaaaaagacggcgctgttgaag
cagaagaccgcgttaaccatcgacttcaccggttctgttagacggcgaagagttcgaagg
cggttaaagcgtctgattcgtactggcgatggccagggtcgatgtatcccggcgtt
gaagacggtatcaaaggccacaaagctggcgaagagttcaccatcgacgtgaccttcc
cggaagaataccacgcagaaagcctgaaaggtaaagcagcgaattcgctatcaacct
gaagaaagttgaagagcgtgaactgccggaactgactgcagaattcatcaaacgttcc
ggcgttgaagatggttccgtagaaggtctgcgcgtgaagtgcgtaaaaacatggagc
gcgagctgaagagcgcctccgttaaccgcgttaagtctcaggcgatcgaaaggctggt
aaaagctaaccgacatcgacgtaccggctgcgtatcgacagcgaatcgacgttctg
cgccgcaggctgcacagcgttccgtggcaacgaaaaacaagctctggaactgcccgc
gcgaactgttcgaagaacaggctaaacgcgcgttagttgtggcctgctgctggcga
agttatccgcaccaacagcgtgaaagctgacgaggagcgcgtgaaaggcctgatcgaa
gagatggcttctgcgtacgaagatccgaaagaagttatcgagttctacagaaaaaca
aagaactgtatggacaacatgcgcaatgttgcgttgcgaaacagggctgttgaagctgt
actggcgaaagcgtaaagtgtactgaaaaaaaagaaaccactttcaacgagctgatgaaaccag
caggcgcagatctcgtaaaaccctgaccggcaagaccattaccctggaagtggAAC
cgagcgacaccatcgagaacgtgaaagcgaagatccaagacaaagaaggatccgc
ggatcagcaacgtctgattttgcgggcaagcagctggaggacggctgtaccctgagc
gattacaacatccaaaaagaaagcaccctgcatctggtgcgtctgcgtggcgttggcgt
ctgccattcgaaaaagcttg

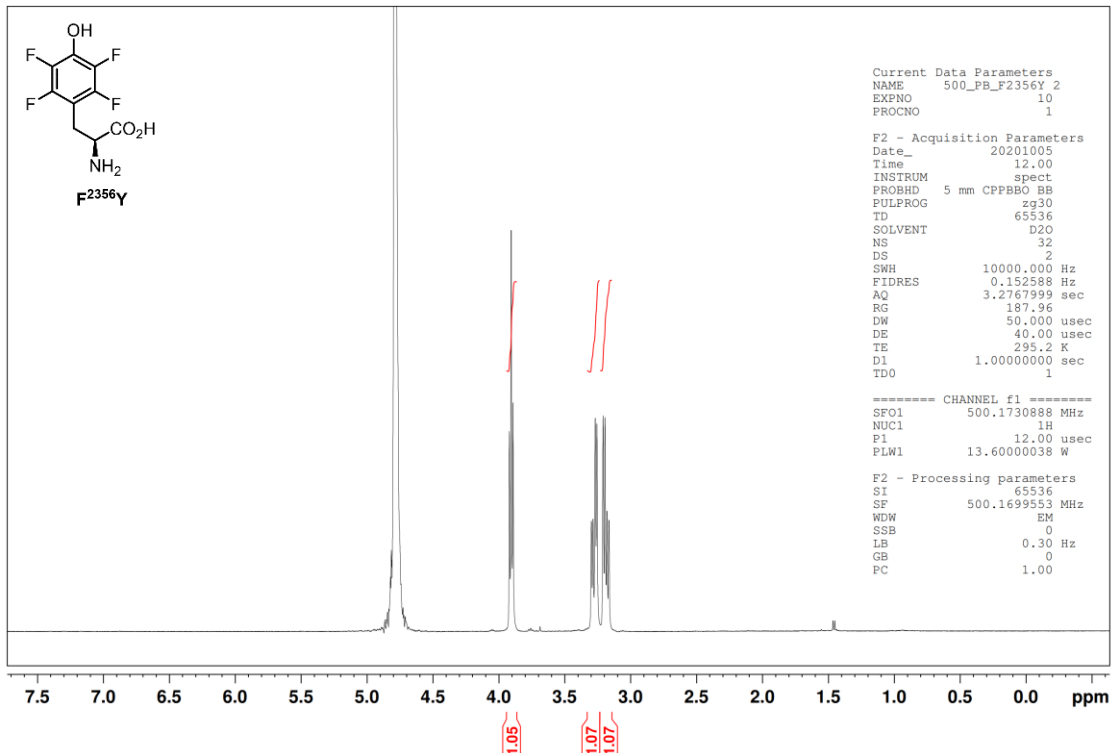
7.3 NMR Spectra

7.3.1 ^1H -NMR spectra of synthesised Fluorotyrosines



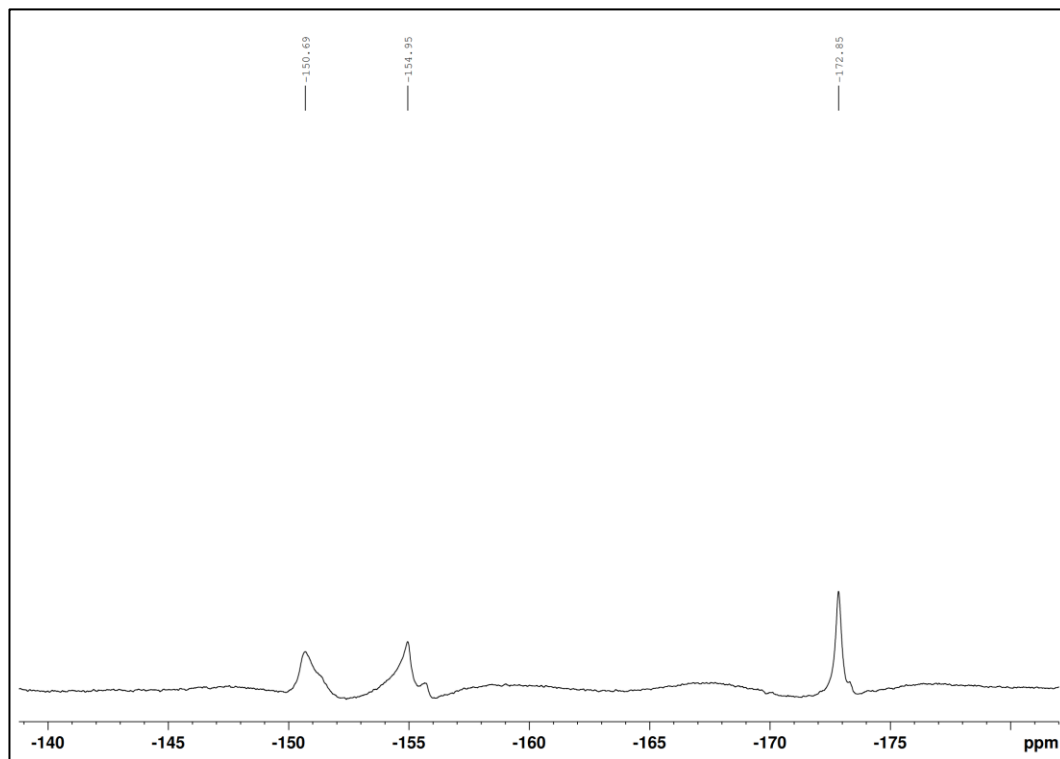




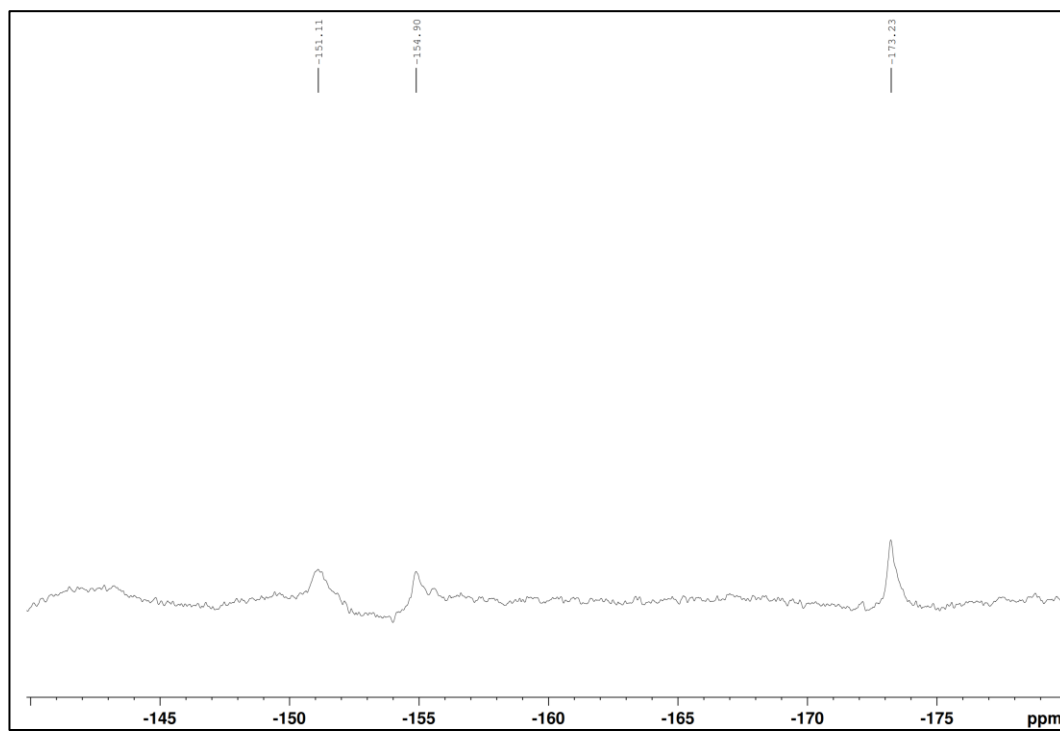


7.3.2 ^{19}F -NMR spectra of FY-RhoA/ MgF_3^- /RhoGAP^{R85A} TSA complexes

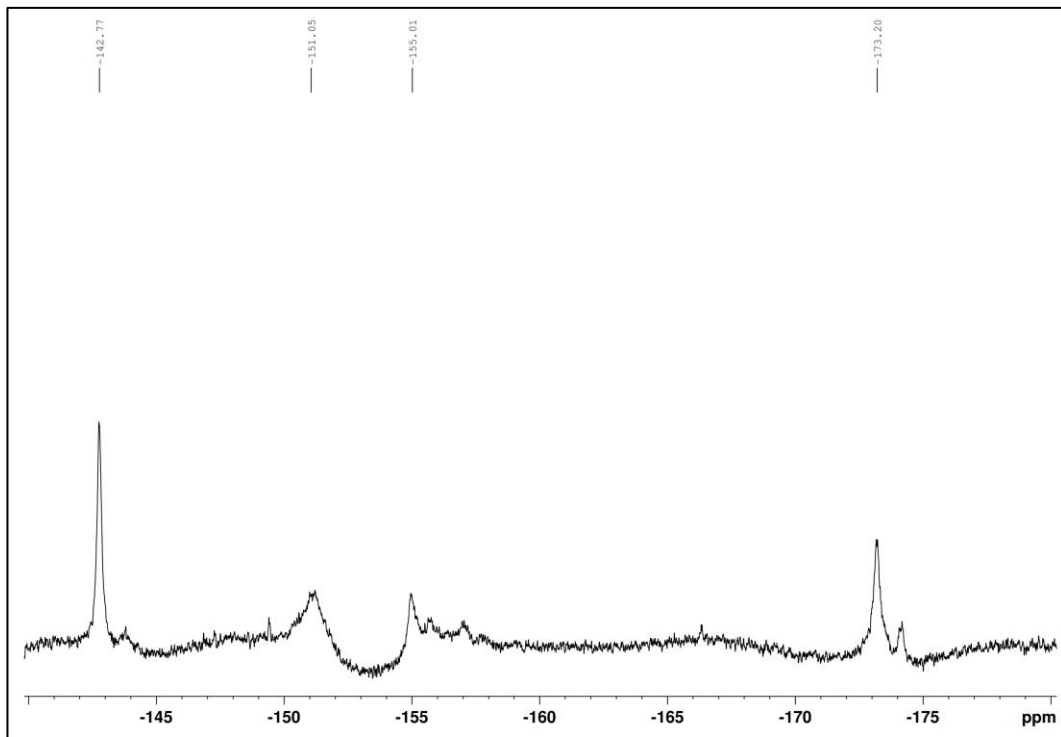
WT-RhoA/ MgF_3^- /RhoGAP^{R85A}



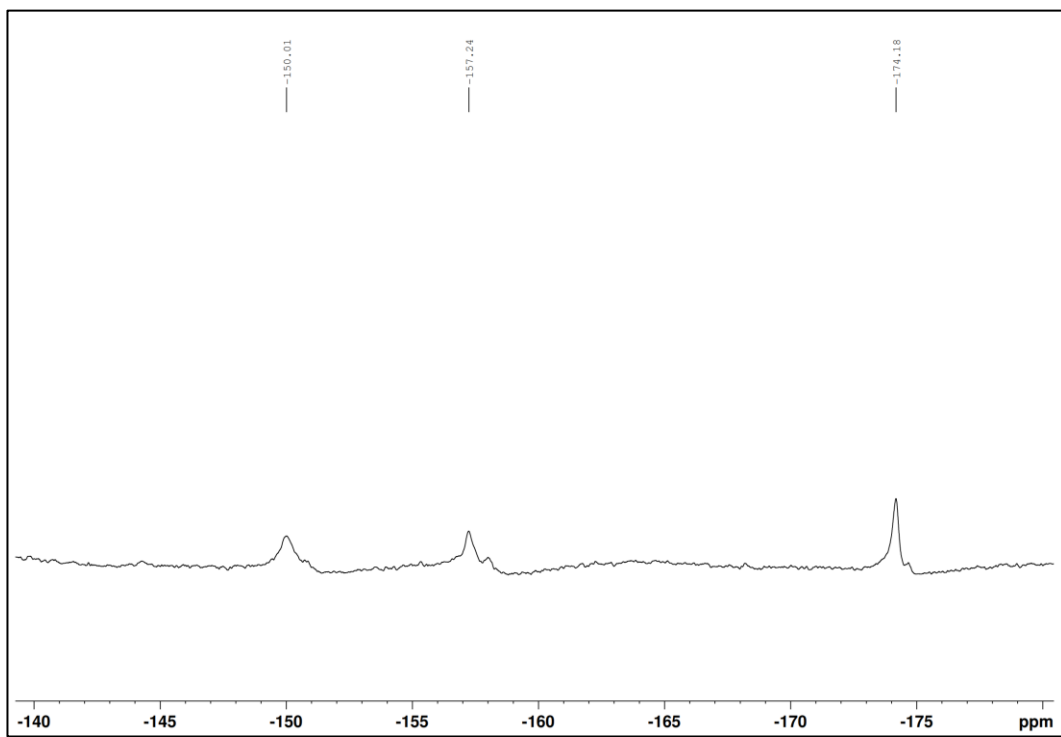
F³Y-RhoA/ MgF_3^- /RhoGAP^{R85A}



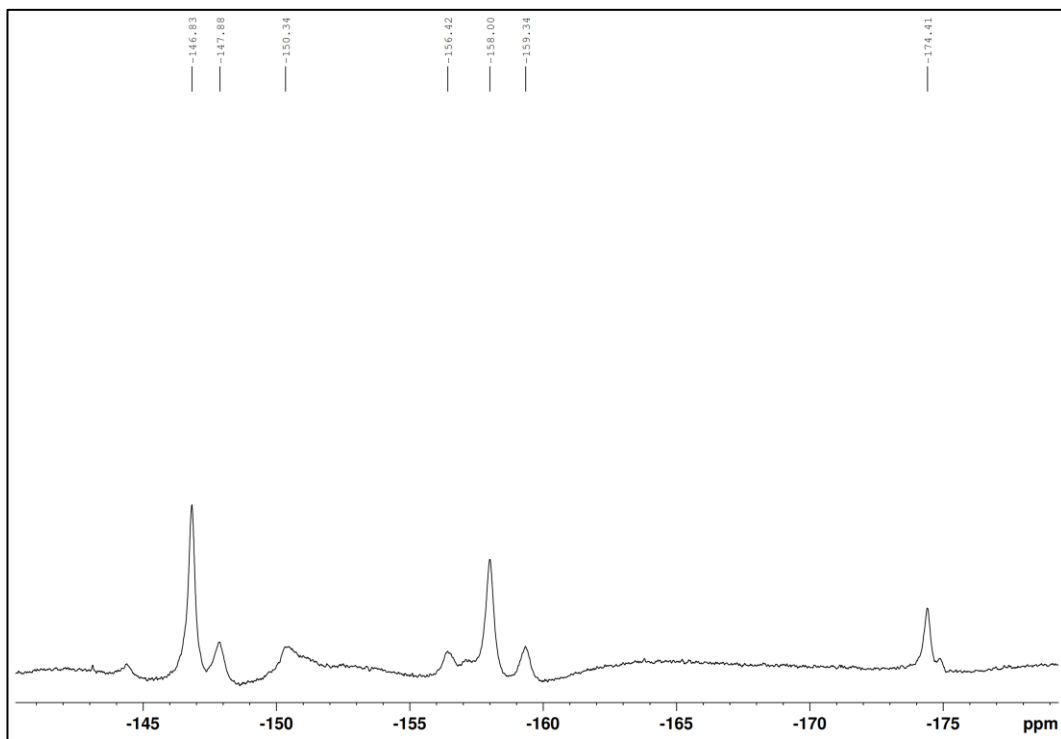
F²⁵Y-RhoA/MgF₃⁻/RhoGAP^{R85A}



F³⁵Y-RhoA/MgF₃⁻/RhoGAP^{R85A}

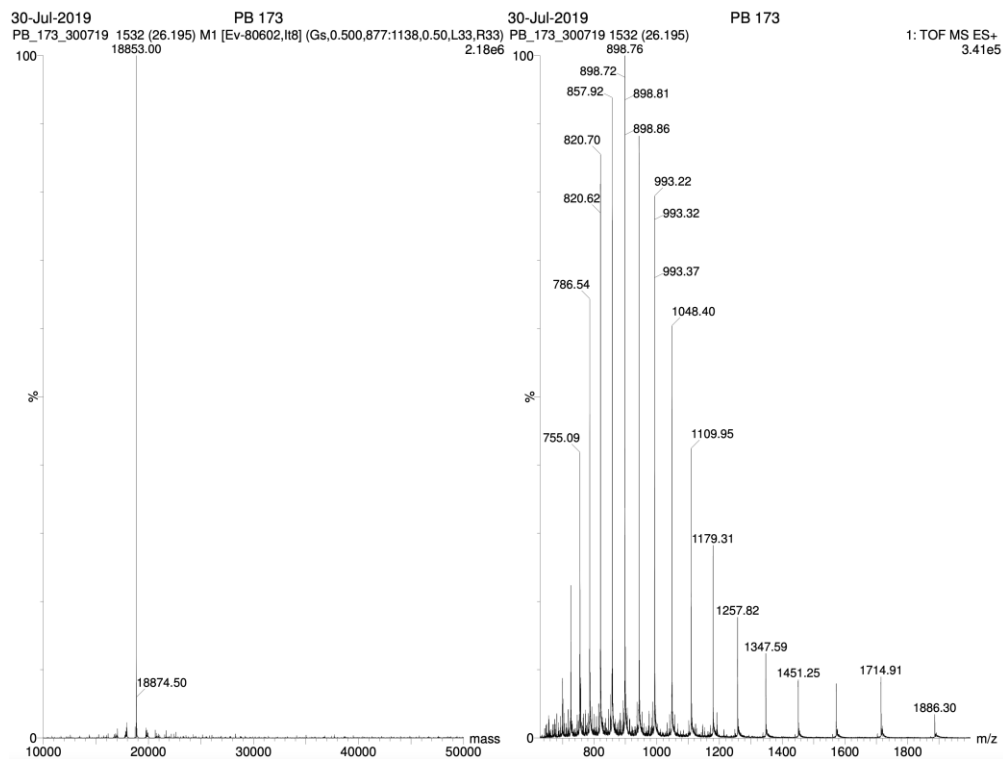


F²³⁵Y-RhoA/MgF₃⁻/RhoGAP^{R85A}

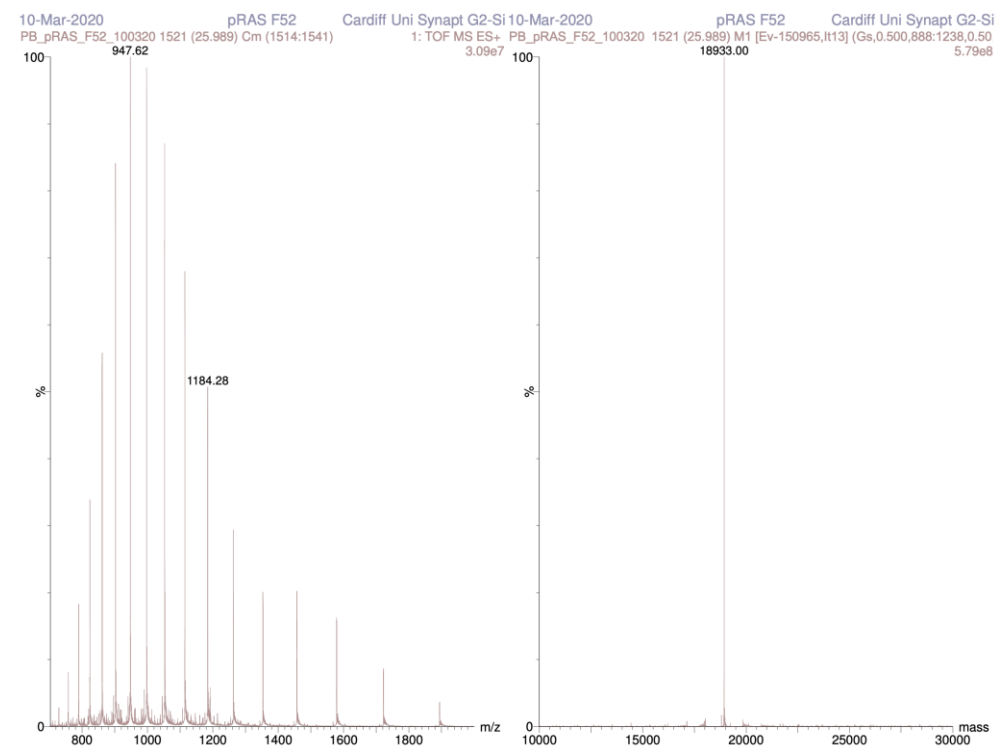


7.4 Mass Spectroscopy

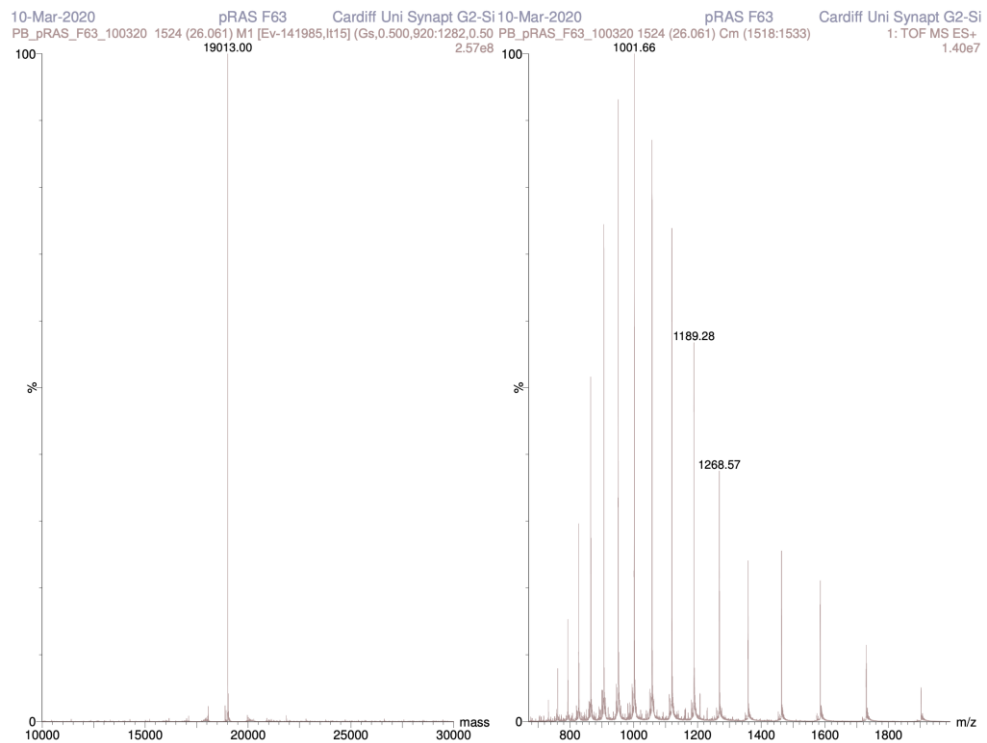
7.4.1 HRas(1–166)



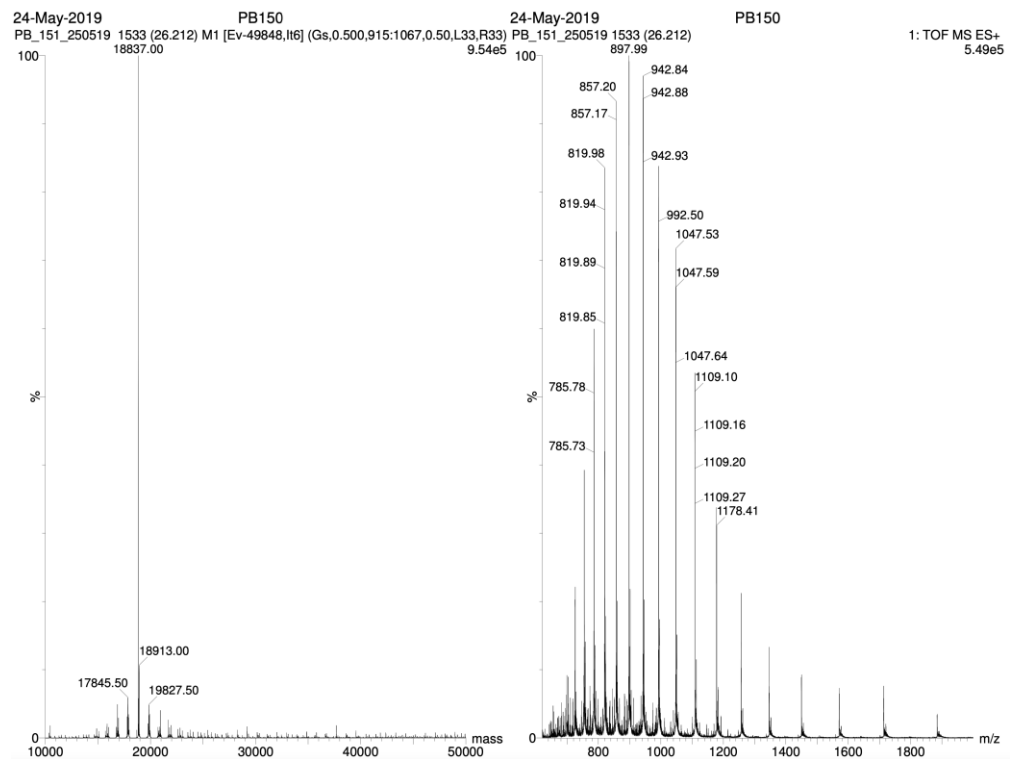
7.4.2 Monophosphorylated HRas(1–166)



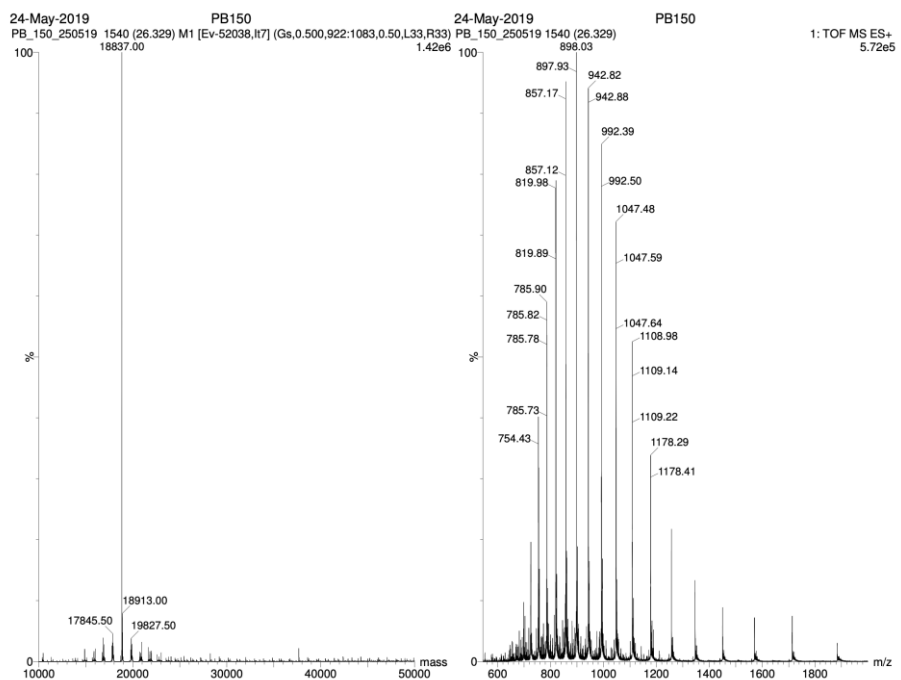
7.4.3 Diphosphorylated HRas(1–166)



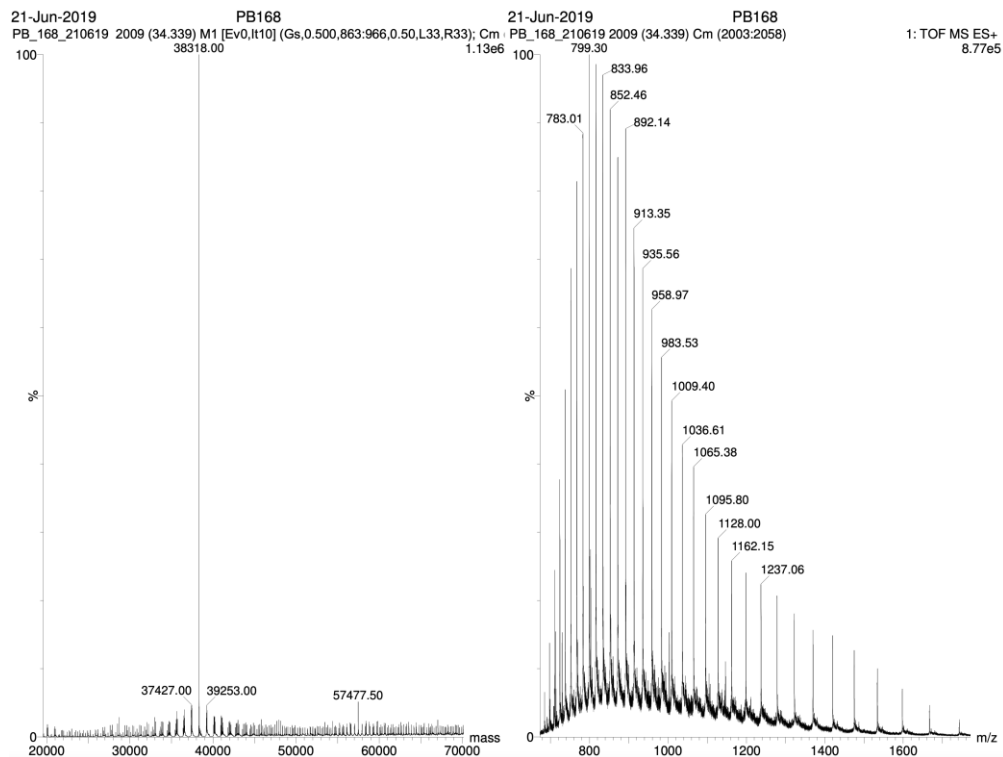
7.4.4 HRas(1–166)^{Y32F}



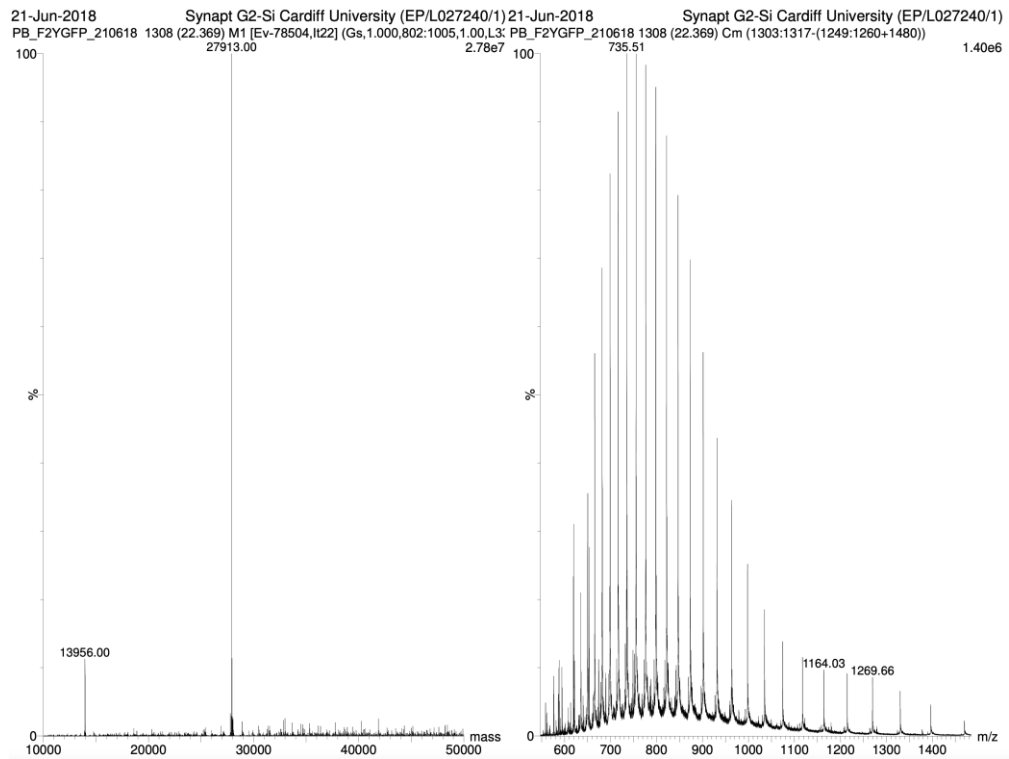
7.4.5 HRas(1–166)^{Y64F}



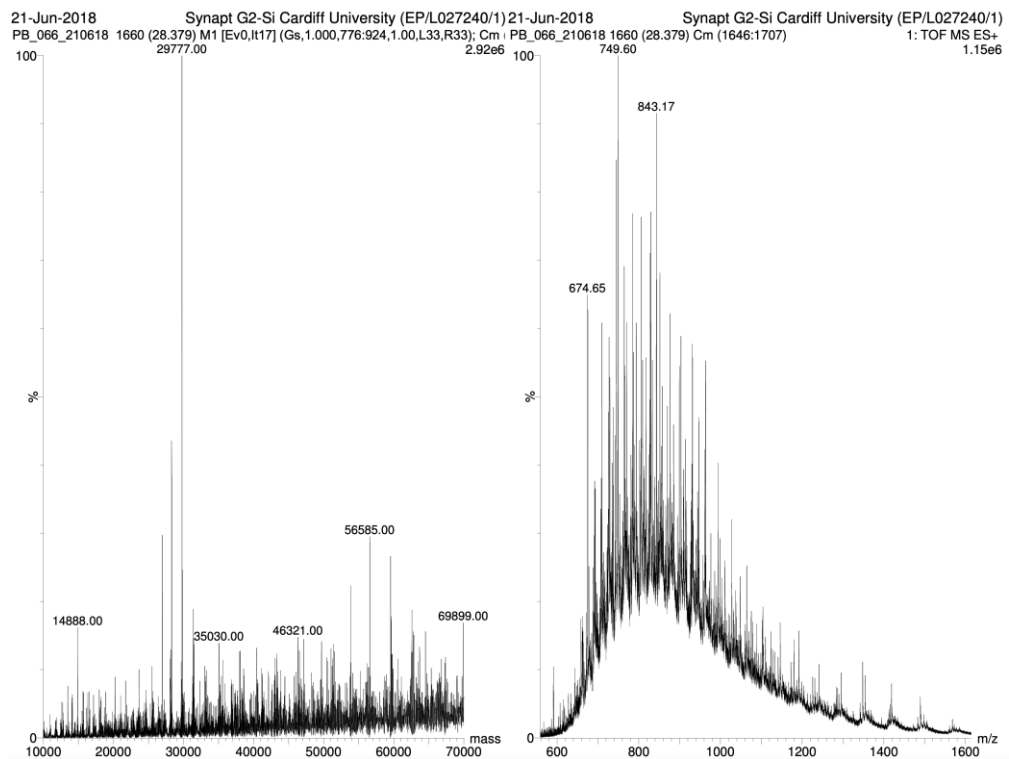
7.4.6 RasGAP (714–1047)



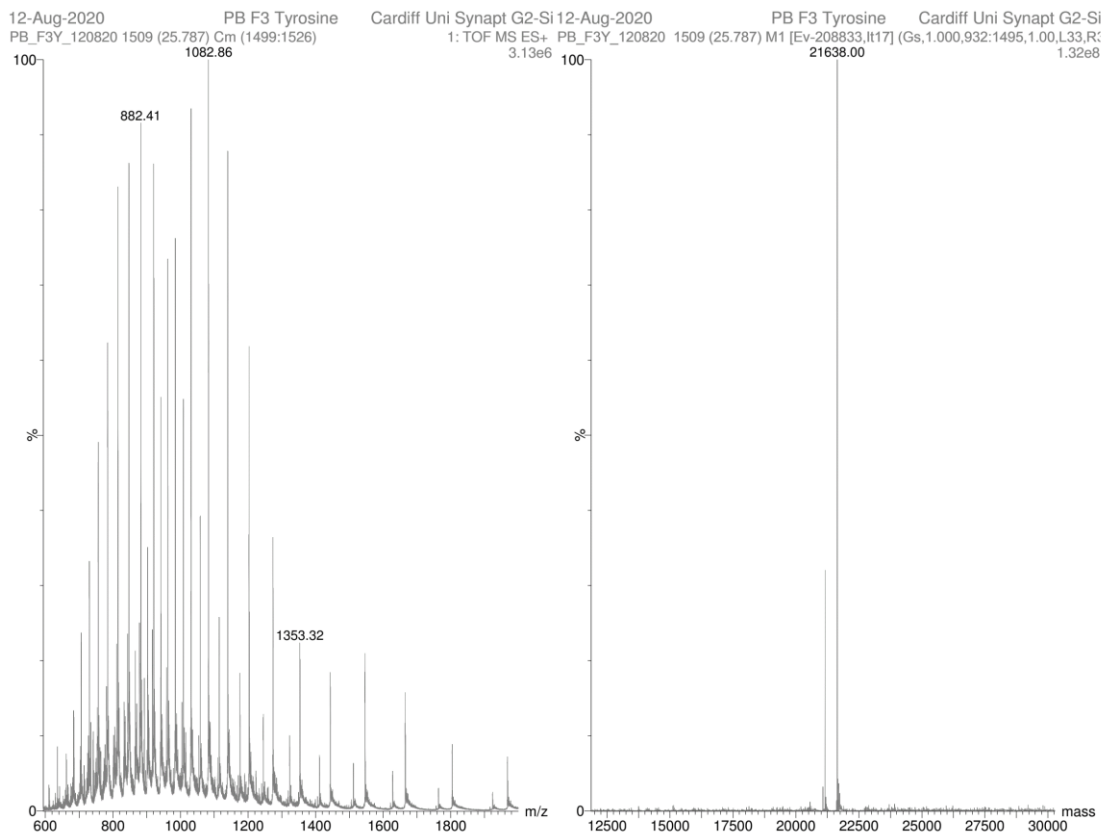
7.4.7 sfGFP-N150F³⁵Y



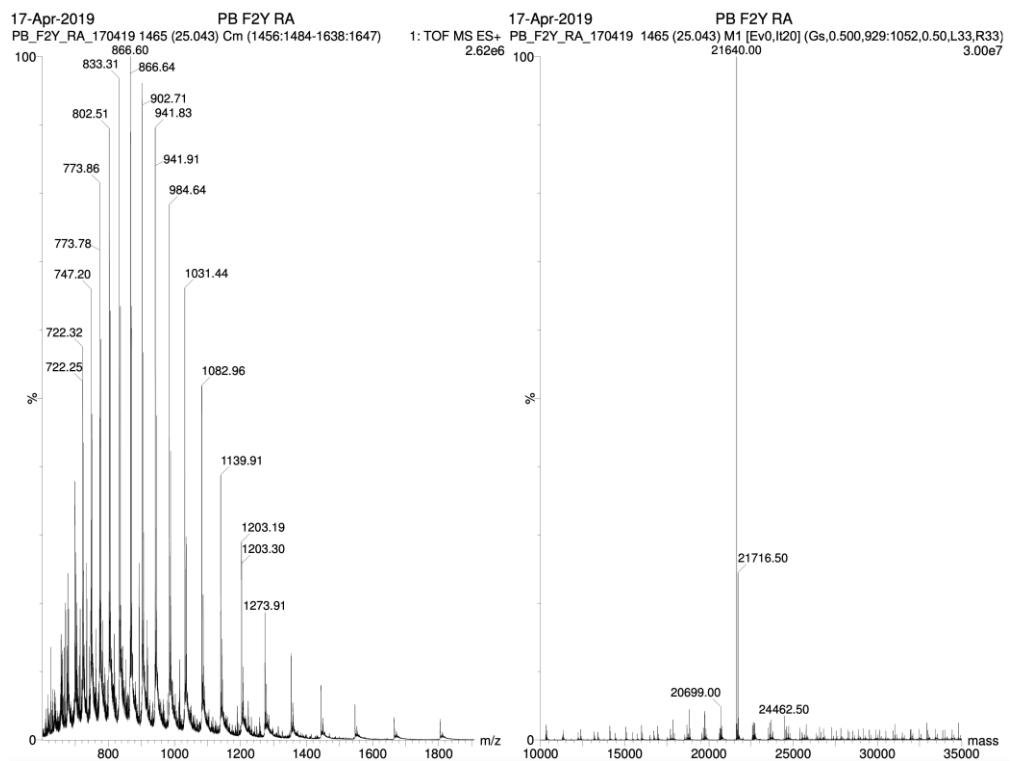
7.4.8 Truncated GST-RhoA



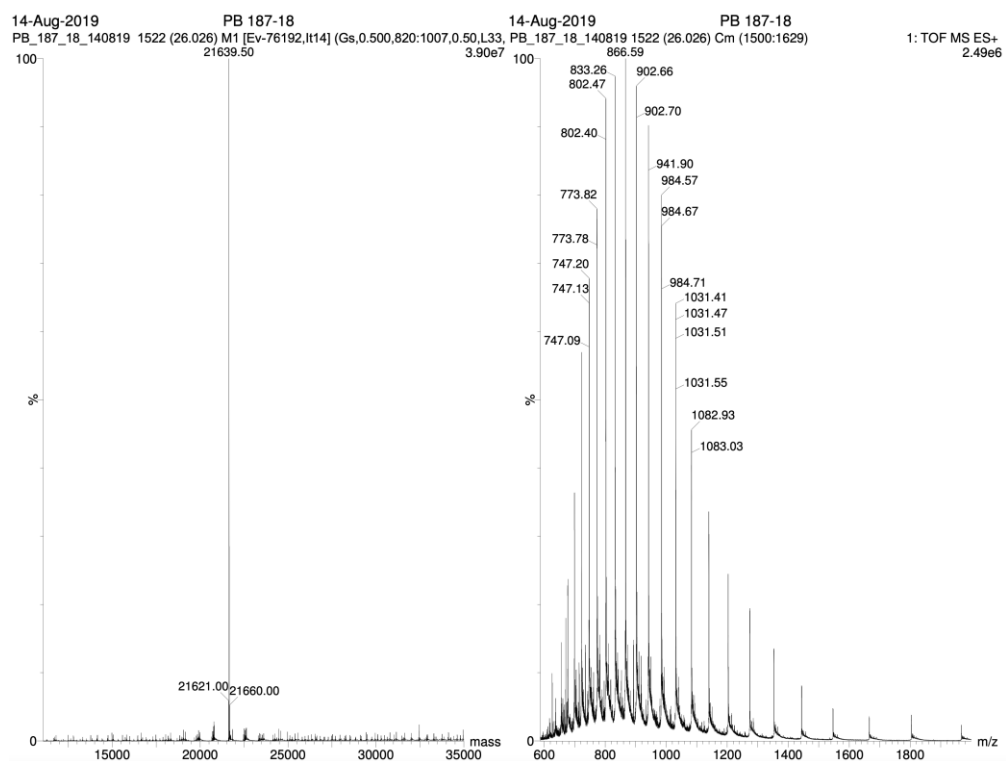
7.4.9 F³Y-RhoA



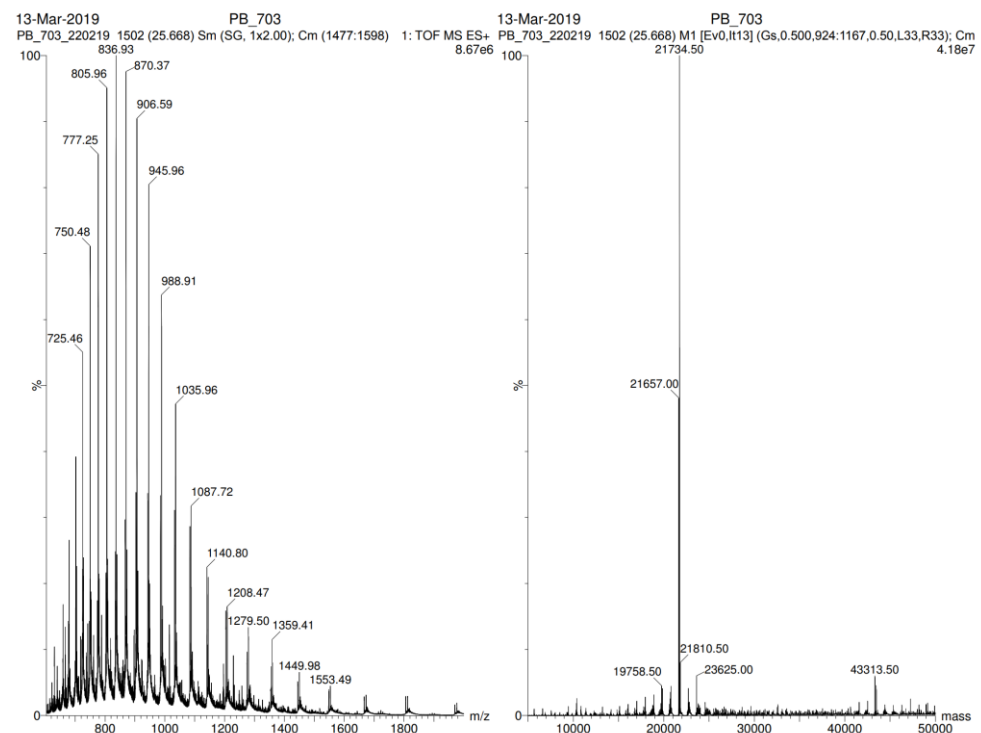
7.4.10 F³⁵Y-RhoA



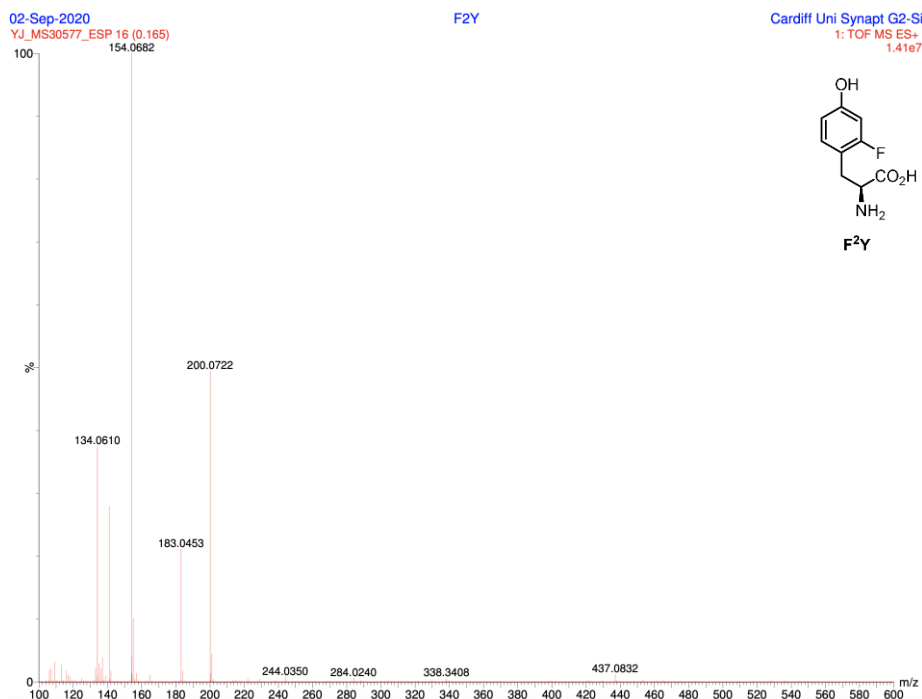
7.4.11 F²⁵Y-RhoA



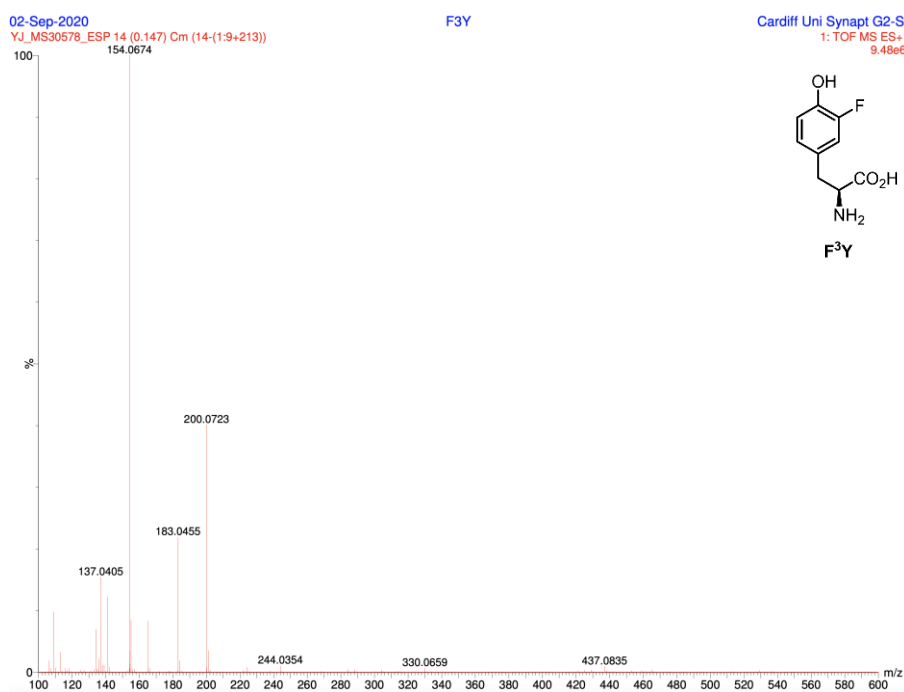
7.4.12 F²³⁵Y-RhoA



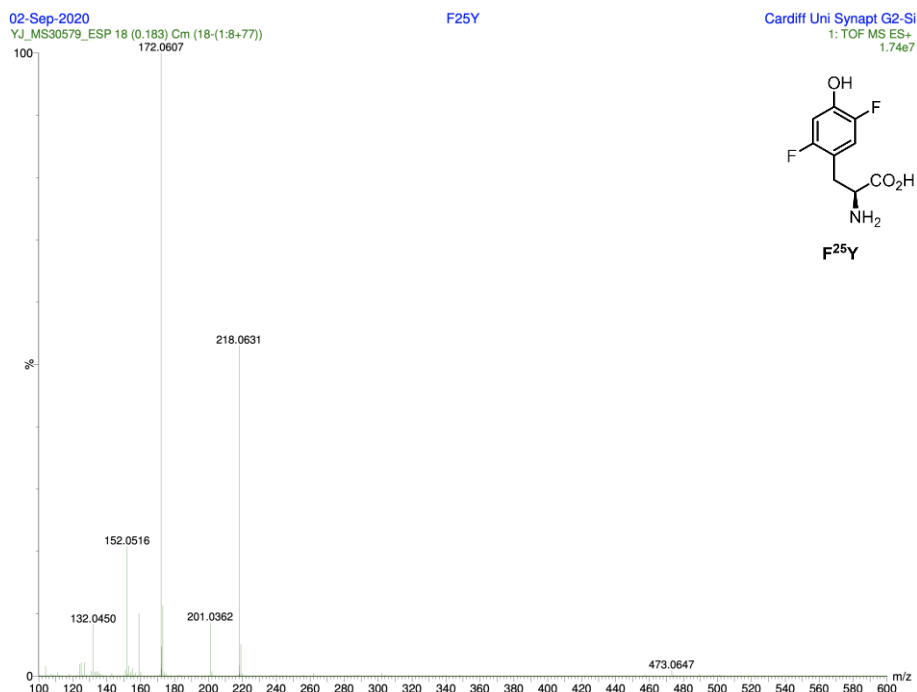
7.4.13 2-Fluorotyrosine (F²Y)



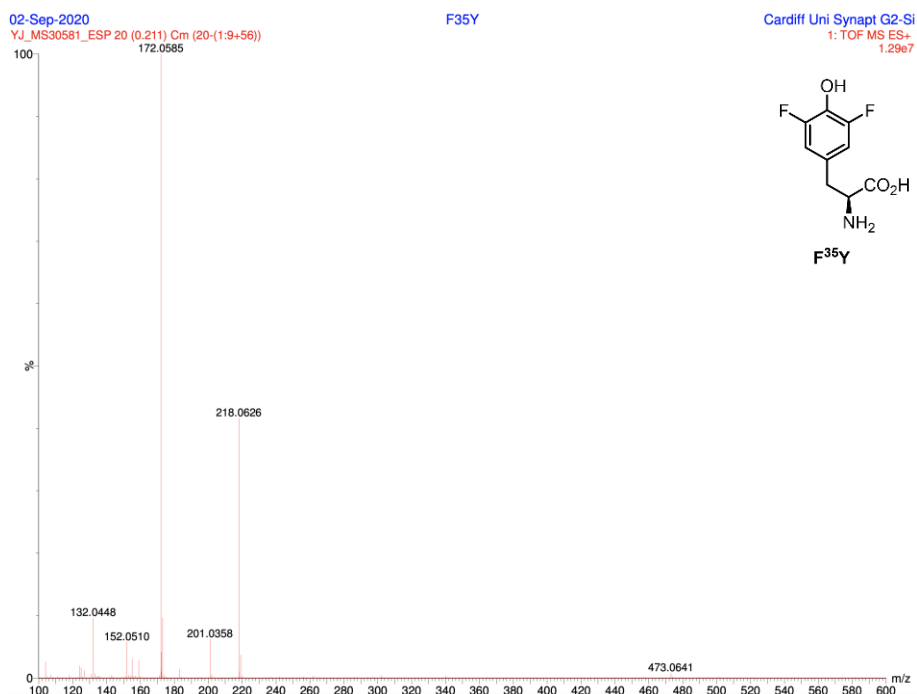
7.4.14 3-Fluorotyrosine (F³Y)



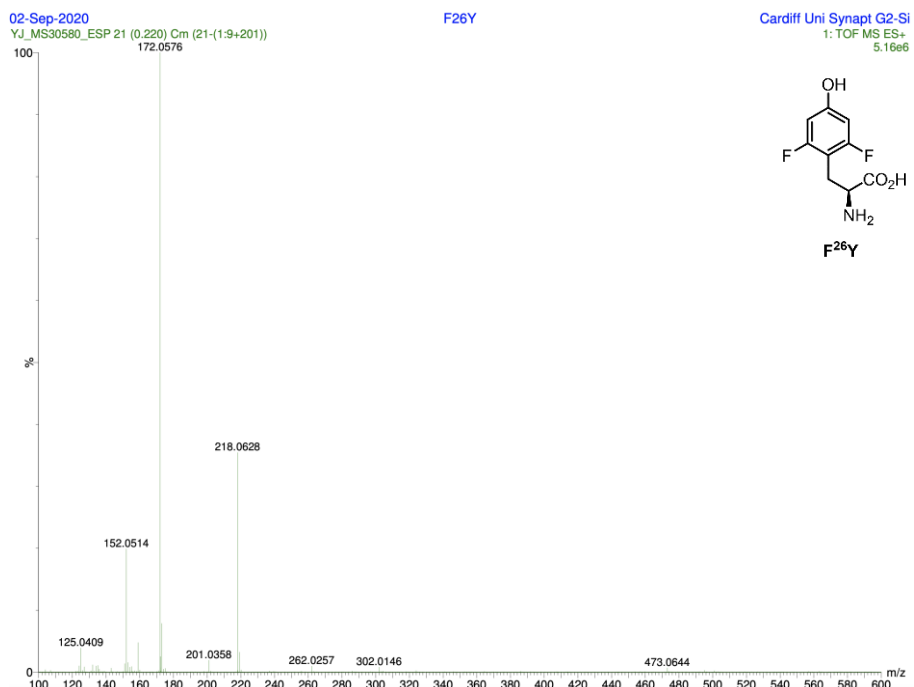
7.4.15 2,5-Difluorotyrosine ($F^{25}Y$)



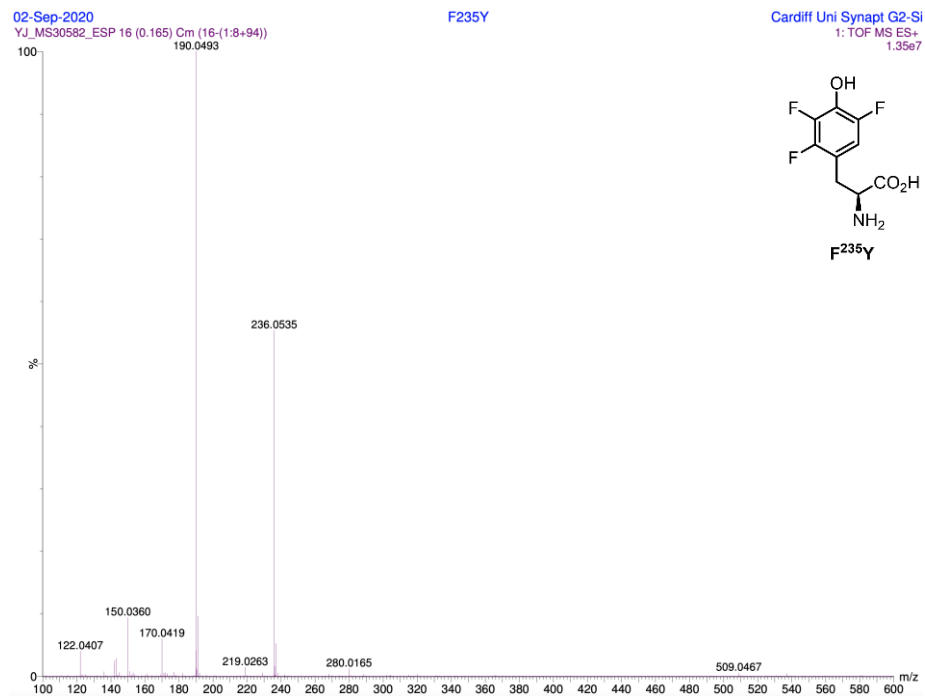
7.4.16 3,5-Difluorotyrosine ($F^{35}Y$)



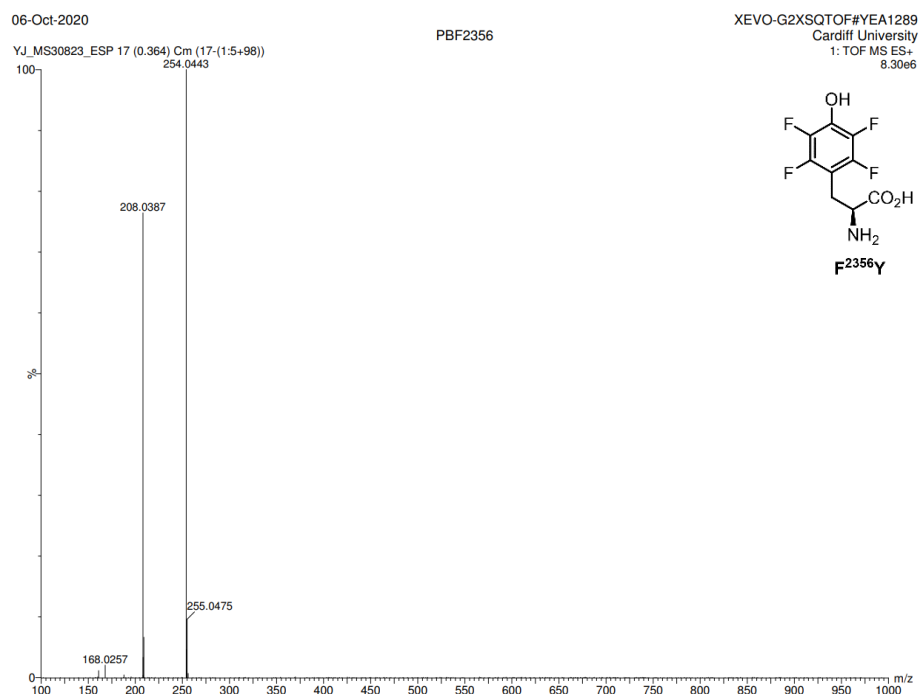
7.4.17 2,6-Difluorotyrosine ($F^{26}Y$)



7.4.18 2,3,5-Trifluorotyrosine ($F^{235}Y$)

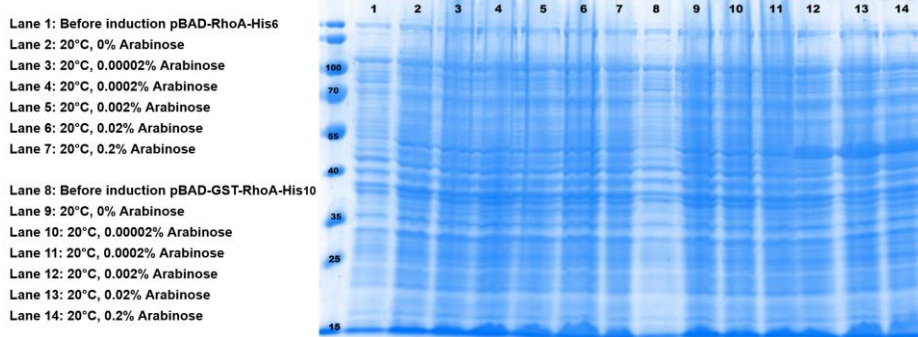


7.4.19 2,3,5,6-Tetrafluorotyrosine ($F^{2356}Y$)

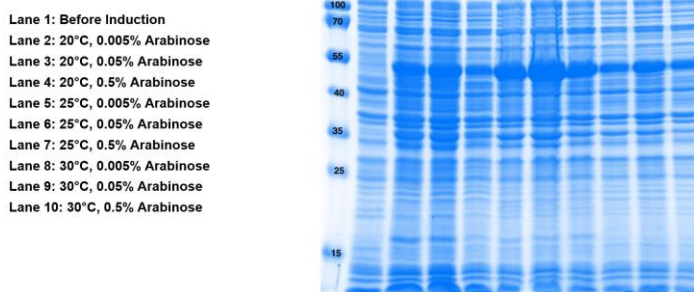


7.5 SDS-PAGE

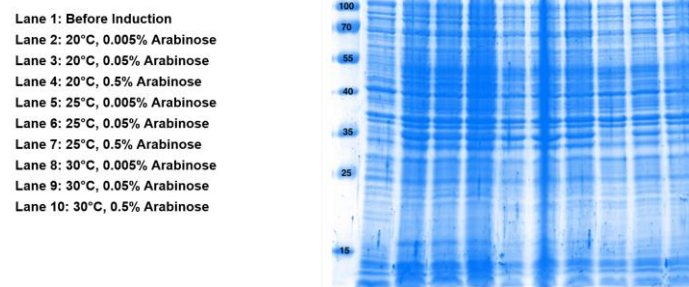
A



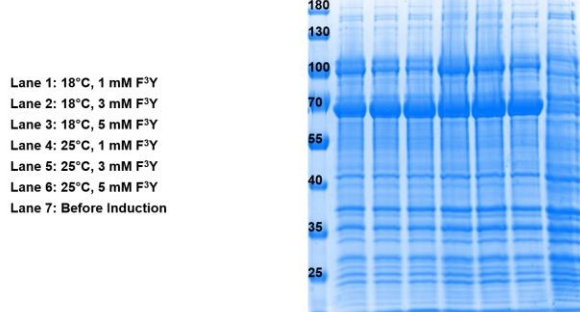
B



C

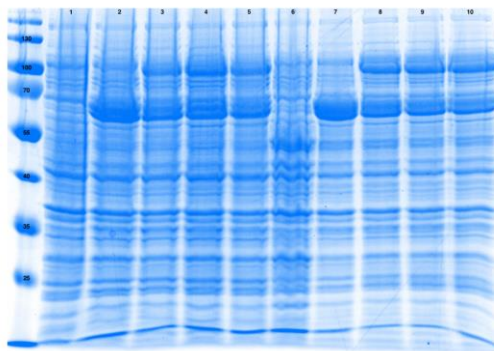


D



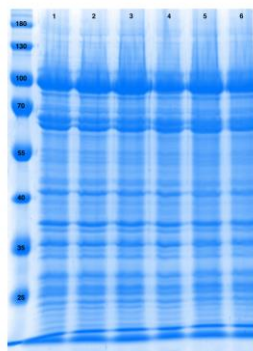
E

Lane 1: Before Induction
Lane 2: 18°C, 0 mM F³⁵Y
Lane 3: 18°C, 1 mM F³⁵Y
Lane 4: 18°C, 3 mM F³⁵Y
Lane 5: 18°C, 5 mM F³⁵Y
Lane 6: Before Induction
Lane 7: 25°C, 0 mM F³⁵Y
Lane 8: 25°C, 1 mM F³⁵Y
Lane 9: 25°C, 3 mM F³⁵Y
Lane 10: 25°C, 5 mM F³⁵Y



F

Lane 1: 18°C, 1 mM F²³⁵Y
Lane 2: 18°C, 3 mM F²³⁵Y
Lane 3: 18°C, 5 mM F²³⁵Y
Lane 4: 25°C, 1 mM F²³⁵Y
Lane 5: 25°C, 3 mM F²³⁵Y
Lane 6: 25°C, 5 mM F²³⁵Y
Lane 7: Before Induction



G

Lane 1: 18°C, 1 mM F²³⁵⁶Y
Lane 2: 18°C, 3 mM F²³⁵⁶Y
Lane 3: 18°C, 5 mM F²³⁵⁶Y
Lane 4: 25°C, 1 mM F²³⁵⁶Y
Lane 5: 25°C, 3 mM F²³⁵⁶Y
Lane 6: 25°C, 5 mM F²³⁵⁶Y
Lane 7: Before Induction

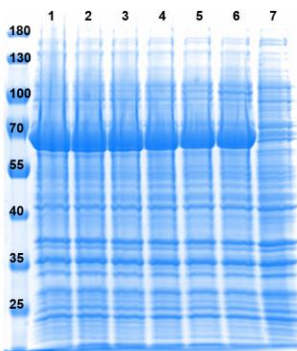


Figure 54: SDS-PAGE gels (**A**) and (**B**): Optimisation of expression conditions for non-fluorotyrosine labelled RhoA. (**C**) Representative SDS-PAGE gel of a failed fluorotyrosine incorporation. Expression trials for trigger factor construct in BL21(DE3) AI cells using (**D**) 3-fluorotyrosine, (**E**) 3,5-difluorotyrosine, (**F**) 2,3,5-trifluorotyrosine and (**G**) 2,3,5,6-tetrafluorotyrosine.

7.6 Measured and predicted Small Molecule ^{19}F -NMR Shifts

Table 15: Measured and predicted ^{19}F -NMR shifts of fluorophenols used in this work and their respective fluorotyrosine derivates.

$\Delta\delta$ in ppm	Predicted F_A	Observed F_A	Predicted F_B	Observed F_B	Predicted F_C	Observed F_C
	-113.9	-112.3				
	-137.4	-137.7				
	-120.5	-118.5	-144.0	-143.2		
	-135.4	-134.9				
	-111.9	-110.7				
	-142.0	-140.3	-143.7	-144.5	-158.9	-159.7
	-141.7	-144.9	-165.2	-166.2		
	-117.8	-115.8				
	-137.8	-136.6				

	-124.4	-122.1	-144.4	-142.2		
	-135.8	-134.2				
	-115.8	-115.0				
	-142.4	-139.5	-147.6	-147.2	-159.3	-159.2
	-145.65	-149.0	-165.6	-166.0		

7.7 Statistical Parameters for FY pK_a Determination

Table 16: Sigmoidal fit parameters for ¹⁹F-NMR signals for F²³⁵Y-RhoA.

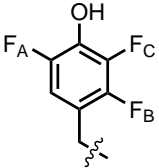
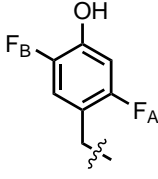
	F_A	F_B	F_C
Best-fit values			
Bottom	-138.7	-145.9	-156.5
Top	-140.6	-148.5	-160.5
pK _a	6.351	6.382	6.369
Span	1.873	2.601	4.008
95% CI			
Bottom	-138.3 to -138.9	-145.5 to -146.1	-156.0 to -156.8
Top	-140.3 to -142.1	-148.1 to -149.7	-159.9 to -162.6
pK _a	6.127 to 7.206	6.194 to 6.895	6.175 to 6.906
Goodness of Fit			
Degrees of Freedom	3	3	3
R squared	0.9961	0.9971	0.9967
Sum of Squares	0.01049	0.01495	0.04180
Sy.x	0.05913	0.07059	0.1180
Number of points			
# of X values	7	7	7
# Y values analysed	7	7	7

Table 17: Sigmoidal fit parameters for ^{19}F -NMR signal of F_A for F^{25}Y -RhoA. No significant pH dependant shift in ^{19}F NMR signal detected for F_B .

	F_A	F_B
Best-fit values		
Bottom	-138.7	-
Top	-140.6	-
$\text{p}K_\text{a}$	6.351	-
Span	1.873	-
95% CI		
Bottom	-138.3 to -138.9	-
Top	-140.3 to -142.1	-
$\text{p}K_\text{a}$	6.127 to 7.206	-
Goodness of Fit		
Degrees of Freedom	3	-
R squared	0.9961	-
Sum of Squares	0.01049	-
Sy.x	0.05913	-
Number of points		
# of X values	7	-
# Y values analysed	7	-

7.8 Pulse Programme for F⁻ Suppression in ¹⁹F-NMR Spectra

```
; zgpr
;avance-version (12/01/11)
;1D sequence with f1 presaturation
;${CLASS=HighRes
;${DIM=1D
;${TYPE=
;${SUBTYPE=
;${COMMENT=
#include <Avance.incl>
"d12=20u"
"acqt0=-p1*2/3.1416"

1 ze
2 30m
d12 p19:f1
d1 cw:f1 ph29
4u do:f1
d12 p11:f1
p1 ph1
go=2 ph31
30m mc #0 to 2 F0(zd)
exit

ph1=0 2 2 0 1 3 3 1
ph29=0
ph31=0 2 2 0 1 3 3 1
;p11 : f1 channel - power level for pulse (default)
;p19 : f1 channel - power level for presaturation
;p1 : f1 channel - 90 degree high power pulse
;d1 : relaxation delay; 1-5 * T1
;d12: delay for power switching [20 usec]
;ns: 1 * n, total number of scans: NS * TD0
;${Id: zgpr,v 1.11 2012/01/31 17:49:32 ber Exp $
```

7.9 Single-Turnover Kinetics of GTP-loaded FY-RhoA

7.9.1 RhoGAP^{R85A}-catalysed Hydrolysis of GTP-F³Y-RhoA

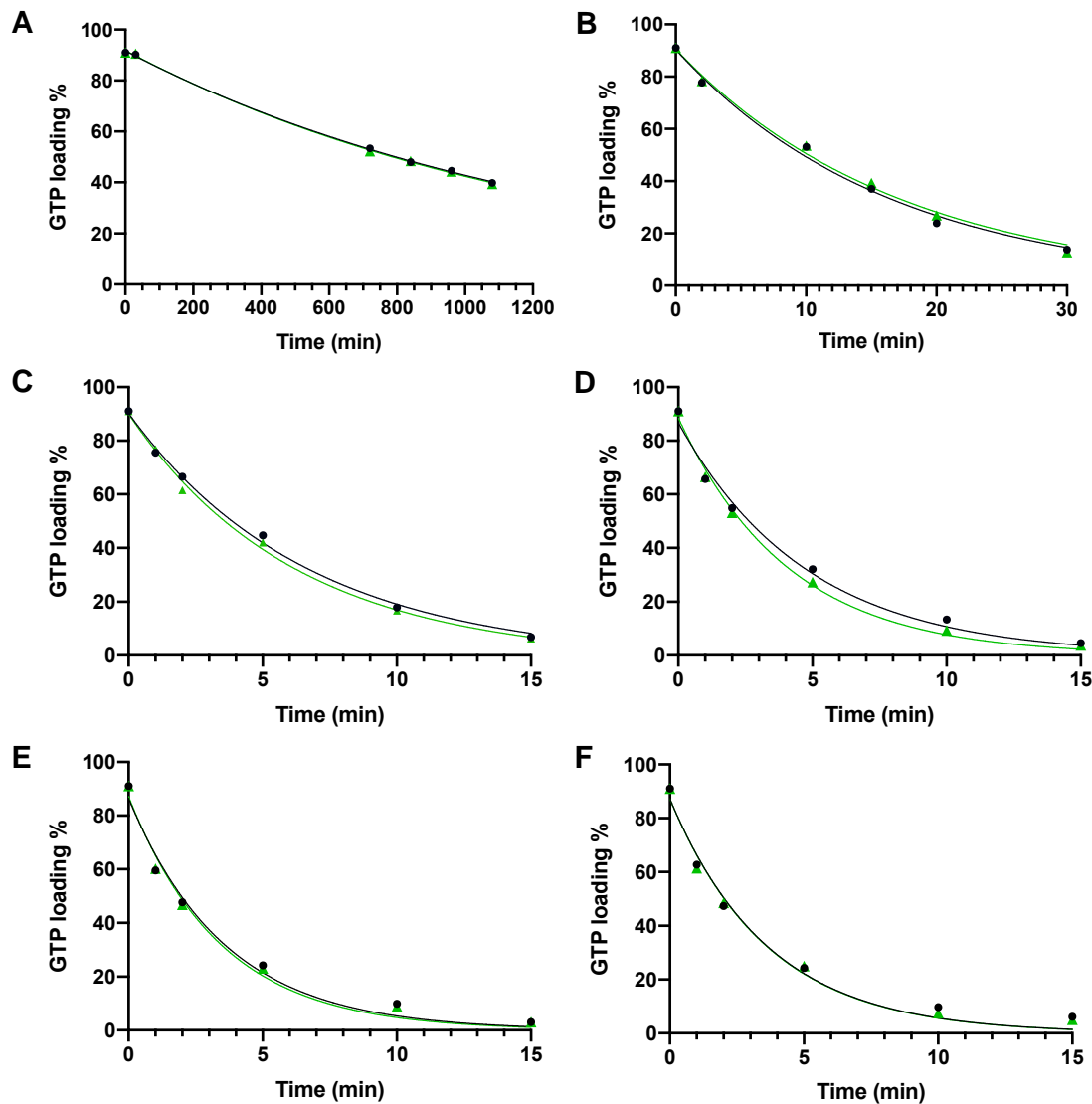


Figure 55: GTP-loading of F³Y-RhoA during the RhoGAP^{R85A}-catalysed hydrolysis of GTP. 50 µM of GTP-loaded F³Y-RhoA are turned over with (A) 0 µM, (B) 10 µM, (C) 25 µM, (D) 50 µM, (E) 100 µM or (F) 250 µM of RhoGAP^{R85A}. All runs were run in duplicates (1: ●, 2: ▲). Rates were obtained by fitting a two-exponent decay function (section 2.3.14).

7.9.2 RhoGAP^{R85A}-catalysed Hydrolysis of GTP-F²⁵Y-RhoA

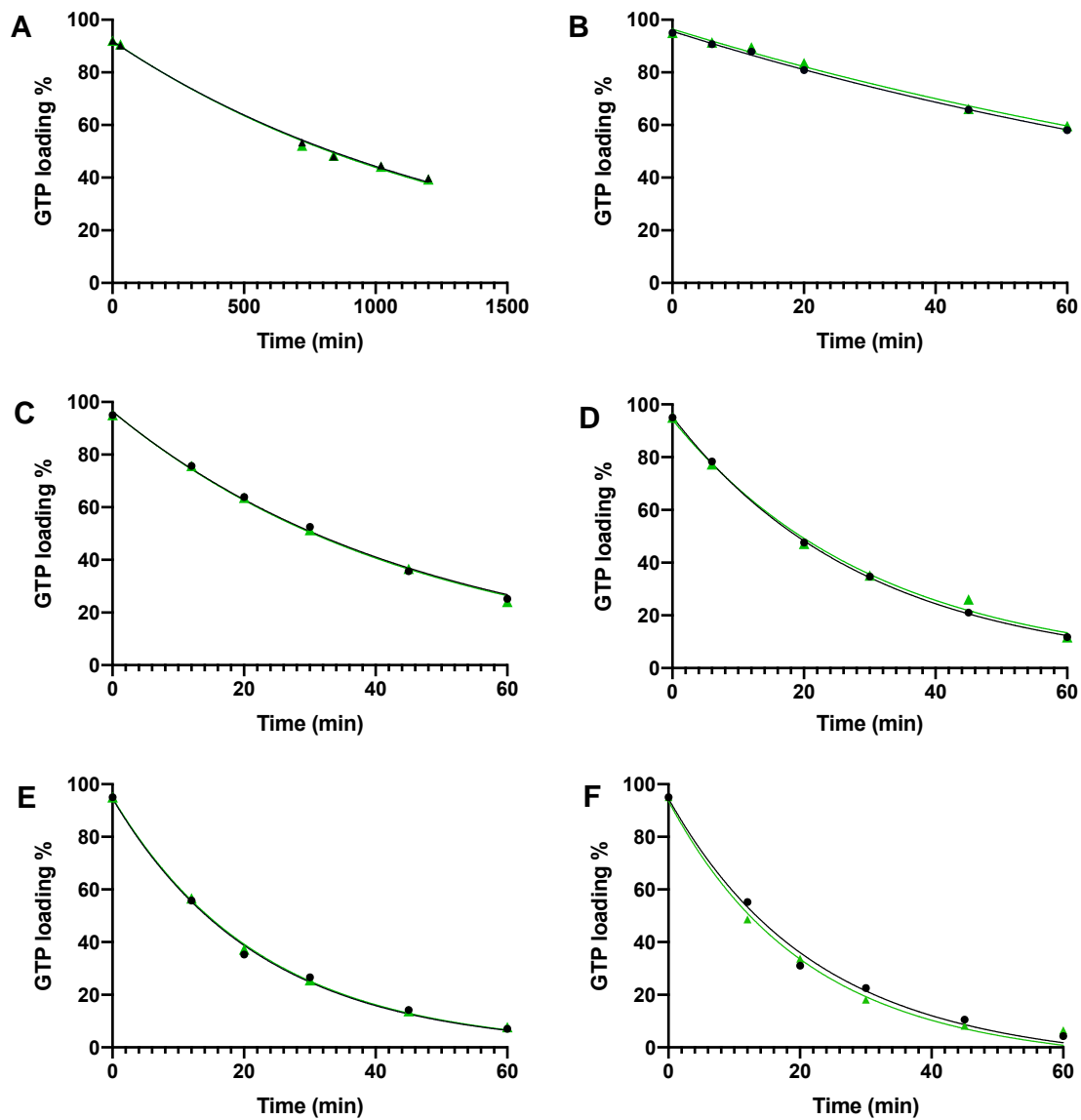


Figure 56: GTP-loading of F²⁵Y-RhoA during the RhoGAP^{R85A}-catalysed hydrolysis of GTP. 50 μM of GTP-loaded F²⁵Y-RhoA are turned over with (A) 0 μM, (B) 10 μM, (C) 25 μM, (D) 50 μM, (E) 100 μM or (F) 250 μM of RhoGAP^{R85A}. All runs were run in duplicates (1: ●, 2: ▲). Rates were obtained by fitting a two-exponent decay function (section 2.3.14).

7.9.3 RhoGAP^{R85A}-catalysed Hydrolysis of GTP-F³⁵Y-RhoA

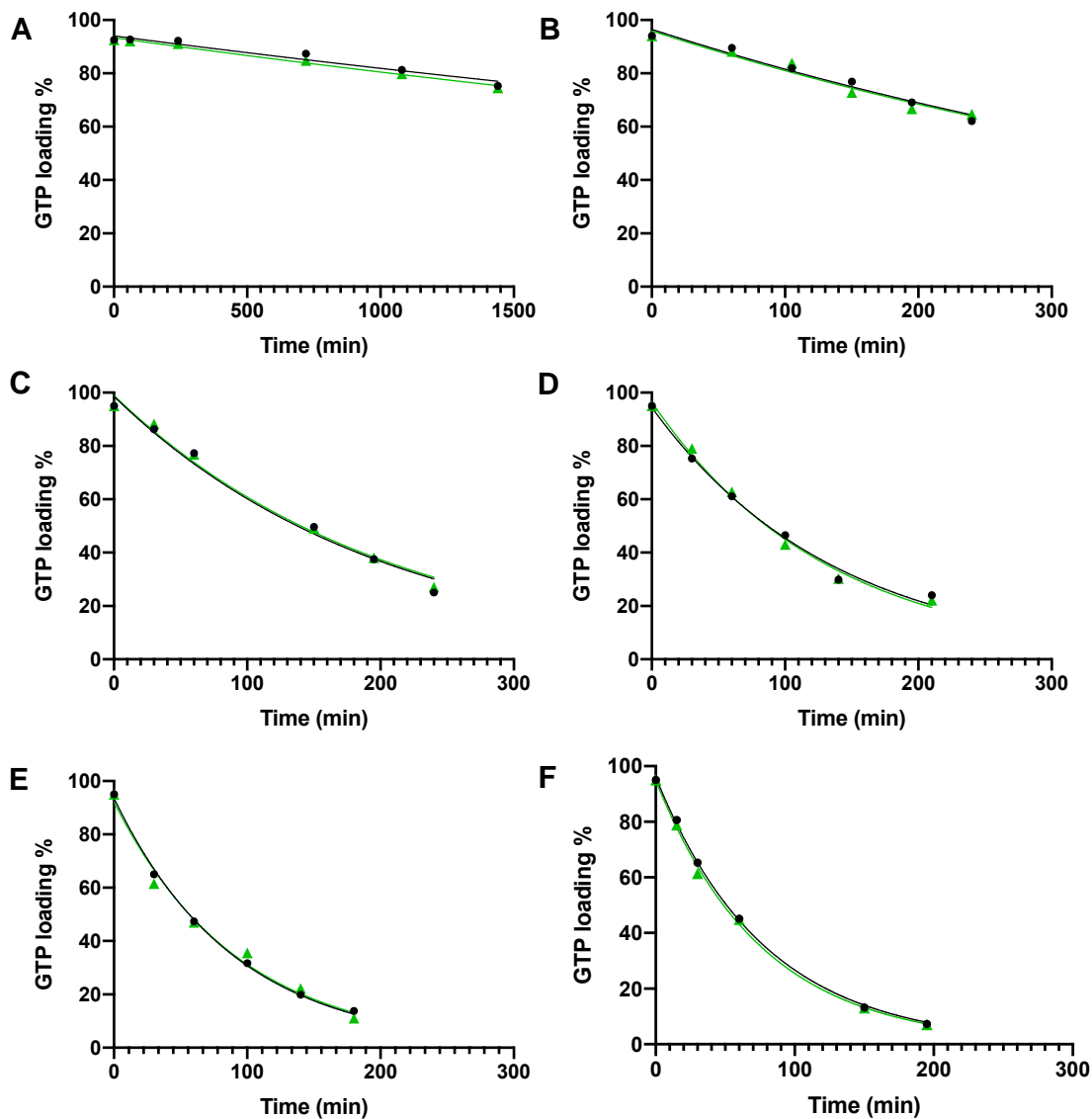


Figure 57: GTP-loading of F³⁵Y-RhoA during the RhoGAP^{R85A}-catalysed hydrolysis of GTP. 50 μM of GTP-loaded F³⁵Y-RhoA are turned over with (A) 0 μM, (B) 10 μM, (C) 25 μM, (D) 50 μM, (E) 100 μM or (F) 250 μM of RhoGAP^{R85A}. All runs were run in duplicates (1: ●, 2: ▲). Rates were obtained by fitting a two-exponent decay function (section 2.3.14).

7.9.4 RhoGAP^{R85A}-catalysed Hydrolysis of GTP-F^{235Y}-RhoA

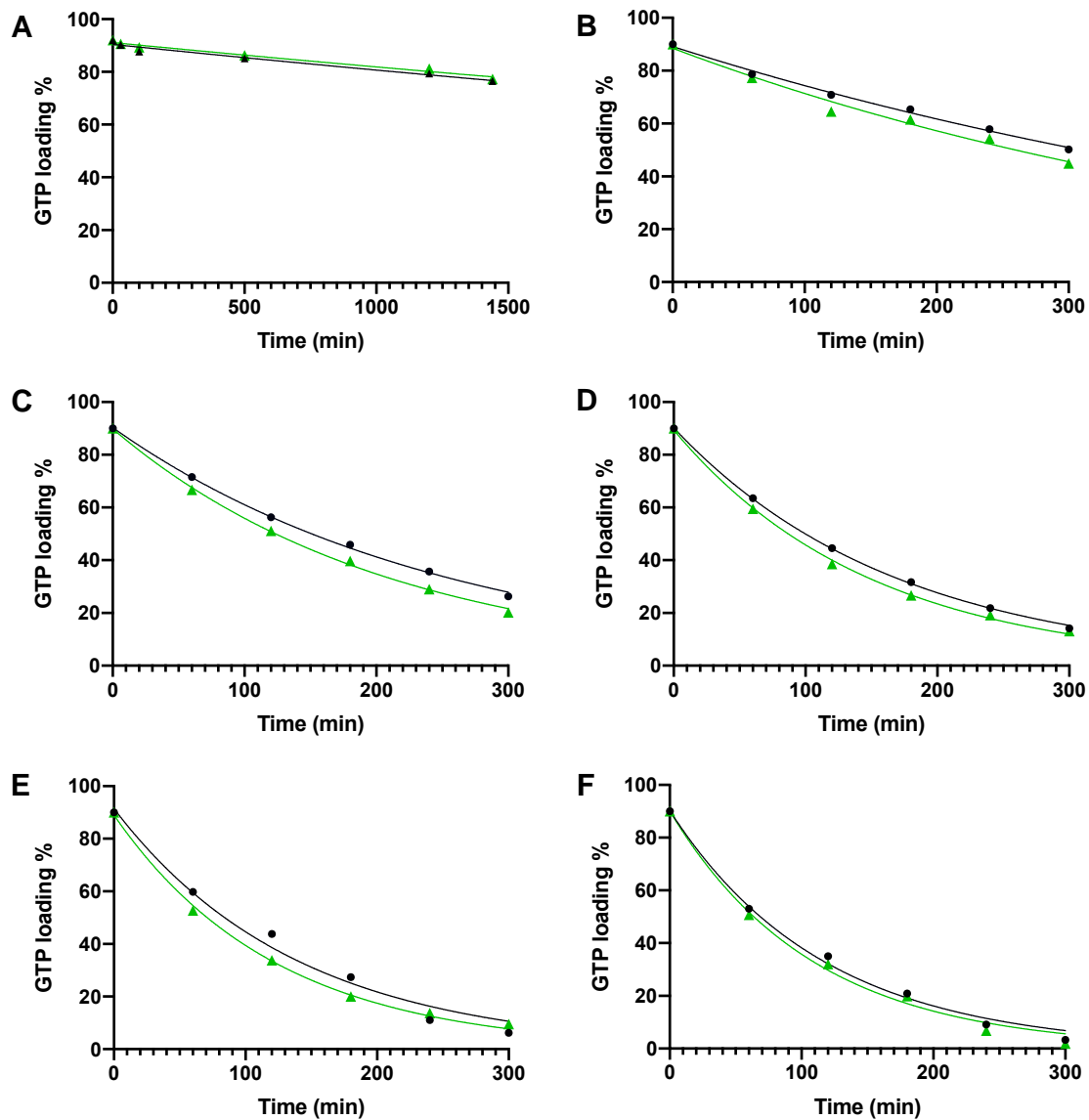


Figure 58: GTP-loading of F^{235Y}-RhoA during the RhoGAP^{R85A}-catalysed hydrolysis of GTP. 50 µM of GTP-loaded F^{235Y}-RhoA are turned over with (A) 0 µM, (B) 10 µM, (C) 25 µM, (D) 50 µM, (E) 100 µM or (F) 250 µM of RhoGAP^{R85A}. All runs were run in duplicates (1: ●, 2: ▲). Rates were obtained by fitting a two-exponent decay function (section 2.3.14).

7.10 Supplementary Data for HPLC Analysis of FY-RhoA-GTP Hydrolysis

Table 18: GTP-loading [%] for FY-RhoA at various timepoints

WT-RhoA	Time[min]	60	180	360	1200	1320
0 μ M RhoGAP ^{R85A}	Run1	83.3	71.2	59.5	20.6	14.3
	Run2	84.1	73.3	58.8	20.7	14.5
	Time[min]	1	3	5	10	30
10 μ M RhoGAP ^{R85A}	Run1	87.3	75.8	65.0	41.1	2.2
	Run2	85.0	67.7	61.5	38.6	0.9
	Time[min]	1	3	5	10	30
25 μ M RhoGAP ^{R85A}	Run1	87.3	75.8	65.0	41.1	2.2
	Run2	85.0	67.7	61.5	38.6	0.9
	Time[min]	1	3	5	10	30
50 μ M RhoGAP ^{R85A}	Run1	87.3	75.8	65.0	41.1	2.2
	Run2	85.0	67.7	61.5	38.6	0.9
	Time[min]	0.5	1	1.5	2	5
100 μ M RhoGAP ^{R85A}	Run1	83.3	71.2	59.5	20.6	14.3
	Run2	84.1	73.3	58.8	20.7	14.5
	Time[min]	0.25	0.5	2	3	5
250 μ M RhoGAP ^{R85A}	Run1	83.3	71.2	59.5	20.6	14.3
	Run2	84.1	73.3	58.8	20.7	14.5
	Time[min]					
F ³ Y-RhoA	Time[min]	30	720	840	960	1080
0 μ M RhoGAP ^{R85A}	Run1	90.2	53.4	48.4	44.6	39.8
	Run2	90.6	52.2	48.0	44.2	39.4
	Time[min]	2	10	15	20	30
10 μ M RhoGAP ^{R85A}	Run1	77.7	53.1	37.0	23.9	12.8
	Run2	78.4	53.5	39.3	26.9	13.8
	Time[min]	1	2	5	10	15
25 μ M RhoGAP ^{R85A}	Run1	75.5	66.5	44.7	17.9	6.8
	Run2	76.8	61.5	42.0	16.7	6.3
	Time[min]	1	2	5	10	15
50 μ M RhoGAP ^{R85A}	Run1	65.7	54.9	32.1	13.4	4.5
	Run2	66.5	53.1	27.3	9.3	3.7
	Time[min]	1	2	5	10	15
100 μ M RhoGAP ^{R85A}	Run1	59.5	47.7	24.2	9.9	3.0
	Run2	60.2	46.8	23.0	8.9	2.9
	Time[min]	1	2	5	10	15
250 μ M RhoGAP ^{R85A}	Run1	62.7	47.4	24.3	9.7	6.1
	Run2	61.4	48.5	25.0	7.5	5.0
	Time[min]					
F ²⁵ Y-RhoA	Time[min]	30	720	840	1020	1200
0 μ M RhoGAP ^{R85A}	Run1	90.2	53.4	48.4	44.6	39.8
	Run2	90.6	52.2	48.0	44.2	39.4
	Time[min]	6	12	20	45	60
10 μ M RhoGAP ^{R85A}	Run1	90.7	87.9	80.9	65.8	58.0
	Run2	91.4	89.5	83.5	66.1	59.6
	Time[min]	12	20	30	45	60
25 μ M RhoGAP ^{R85A}	Run1	75.7	63.9	52.5	35.7	25.2
	Run2	75.7	63.6	51.4	36.6	24.0
	Time[min]	6	20	30	45	60
50 μ M RhoGAP ^{R85A}	Run1	78.4	47.6	34.7	21.0	11.8
	Run2	77.3	47.1	35.1	26.0	11.7
	Time[min]					

100 μM RhoGAP ^{R85A}	Time[min]	12	20	30	45	60
	Run1	55.8	35.3	26.6	14.2	7.0
	Run2	56.6	40.2	24.5	13.8	7.7
250 μM RhoGAP ^{R85A}	Time[min]	12	20	30	45	60
	Run1	55.2	31	22.5	10.5	4.3
	Run2	48.6	33.7	18.1	8.2	6.5
F³⁵Y-RhoA						
0 μM RhoGAP ^{R85A}	Time[min]	60	240	720	1080	1440
	Run1	92.7	92.2	87.4	81.3	75.3
	Run2	92.1	91.1	84.8	79.8	74.5
10 μM RhoGAP ^{R85A}	Time[min]	60	105	150	195	240
	Run1	89.5	81.9	76.9	69.1	62.1
	Run2	88.2	83.9	72.8	66.7	64.7
25 μM RhoGAP ^{R85A}	Time[min]	30	60	150	195	240
	Run1	86.3	77.3	49.6	37.5	25.0
	Run2	88.3	76.9	49.1	38.1	27.3
50 μM RhoGAP ^{R85A}	Time[min]	30	60	100	140	210
	Run1	75.3	61.1	46.5	29.9	24.0
	Run2	79	62.8	43	30.3	22.1
100 μM RhoGAP ^{R85A}	Time[min]	60	105	150	195	240
	Run1	65	47.4	31.7	19.9	13.8
	Run2	61.5	47	35.5	22.2	11
250 μM RhoGAP ^{R85A}	Time[min]	15	30	60	150	195
	Run1	80.6	65.3	45.1	13.2	7.3
	Run2	78.9	61.4	44.9	13.0	7.0
F²³⁵Y-RhoA						
0 μM RhoGAP ^{R85A}	Time[min]	30	100	500	1200	1440
	Run1	90.2	87.7	85.1	79.4	76.5
	Run2	90.6	89.3	86.3	81.2	77.3
10 μM RhoGAP ^{R85A}	Time[min]	60	120	180	240	300
	Run1	78.7	70.9	65.4	57.9	50.2
	Run2	77.3	64.5	61.5	54.3	44.9
25 μM RhoGAP ^{R85A}	Time[min]	60	120	180	240	300
	Run1	71.5	56.3	45.9	35.7	26.3
	Run2	66.7	51.1	39.7	29.0	20.2
50 μM RhoGAP ^{R85A}	Time[min]	60	120	180	240	300
	Run1	63.5	44.6	31.7	21.9	14.2
	Run2	59.5	38.6	26.7	19.2	13.1
100 μM RhoGAP ^{R85A}	Time[min]	60	120	180	240	300
	Run1	59.8	43.8	27.4	11.0	6.2
	Run2	52.7	33.8	20.0	13.7	9.5
250 μM RhoGAP ^{R85A}	Time[min]	60	120	180	240	300
	Run1	53.0	35.0	20.9	9.1	3.3
	Run2	50.7	32.0	19.9	6.8	1.9

Table 19: Curve fit parameters for the intrinsic hydrolysis of FY-RhoA-GTP

Run1	WT-RhoA	F ³ Y-RhoA	F ²⁵ Y-RhoA	F ³⁵ Y-RhoA	F ²³⁵ Y-RhoA
Best-fit values					
Y0	91.23	91.65	91.86	94.05	90.42
Plateau	= 0.000	= 0.000	= 0.000	= 0.000	= 0.000
k	0.00129	0.00076	0.0007292	0.0001386	0.0001141
Half Life	537.7	911	950.6	5000	6074
Tau	775.7	1314	1371	7214	8764
Span	= 91.23	= 91.65	= 91.86	= 94.05	= 90.42
95% CI					
Y0	87.62 to 94.88	90.40 to 92.90	89.15 to 94.58	91.02 to 97.10	88.52 to 92.33
k	0.001145 to 0.001452	0.0007347 to 0.0007872	0.0006749 to 0.0007845	9.471e-005 to 0.0001831	8.526e-005 to 0.0001433
Half Life	477.5 to 605.5	880.5 to 943.4	883.5 to 1027	3785 to 7319	4836 to 8130
Tau	688.8 to 873.5	1270 to 1361	1275 to 1482	5460 to 10559	6977 to 11729
Goodness of Fit					
Deg. of Freedom	4	4	4	4	4
R squared	0.9972	0.9994	0.9973	0.9516	0.9689
Sum of Squares	14.63	1.557	7.354	12.55	5.819
Sy.x	1.913	0.6238	1.356	1.772	1.206
Constraints					
Plateau	Plateau = 0	Plateau = 0	Plateau = 0	Plateau = 0	Plateau = 0
# X values	6	6	6	6	6
# Y values	6	6	6	6	6

Run2	WT-RhoA	F ³ Y-RhoA	F ²⁵ Y-RhoA	F ³⁵ Y-RhoA	F ²³⁵ Y-RhoA
Best-fit values					
Y0	91.93	91.82	92.03	93.36	91.12
Plateau	= 0.000	= 0.000	= 0.000	= 0.000	= 0.000
k	0.00129	0.00077	0.0007402	0.0001484	0.0001070
Half Life	537.1	897.5	936.5	4669	6480
Tau	774.9	1295	1351	6737	9348
Span	= 91.93	= 91.82	= 92.03	= 93.36	= 91.12
95% CI					
Y0	89.16 to 94.72	90.32 to 93.33	89.22 to 94.85	91.72 to 95.00	89.68 to 92.56
K	0.001179 to 0.001412	0.0007407 to 0.0008042	0.0006835 to 0.0007981	0.0001243 to 0.0001727	8.544e-005 to 0.0001287
Half Life	490.9 to 587.7	861.9 to 935.8	868.5 to 1014	4013 to 5574	5385 to 8113
Tau	708.2 to 847.9	1243 to 1350	1253 to 1463	5789 to 8042	7770 to 11704
Goodness of Fit					
Deg. of Freedom	4	4	4	4	4
R squared	0.9984	0.9992	0.9972	0.9869	0.9800
Sum of Squares	8.558	2.254	7.933	3.626	3.331
Sy.x	1.463	0.7507	1.408	0.9522	0.9126
Constraints	Plateau = 0	Plateau = 0	Plateau = 0	Plateau = 0	Plateau = 0
Plateau					
# X values	6	6	6	6	6
# Y values	6	6	6	6	6

Table 20: Curve fit parameters for the RhoGAP^{R85A} catalysed hydrolysis of WT-RhoA-GTP

Run 1	10 μM RhoGAP ^{R85A}	25 μM RhoGAP ^{R85A}	50 μM RhoGAP ^{R85A}	100 μM RhoGAP ^{R85A}	250 μM RhoGAP ^{R85A}
Best-fit values					
Y0	94.87	93.64	90.79	90.12	89.88
K	0.08369	0.2396	0.3024	0.3522	0.3919
Kint	= 0.001287	= 0.001287	= 0.001287	= 0.001287	= 0.001287
95% CI					
Y0	88.16 to 101.8	86.93 to 100.5	84.72 to 96.93	83.68 to 96.75	84.93 to 94.91
K	0.06647 to 0.1039	0.2014 to 0.2833	0.2564 to 0.3552	0.2859 to 0.4261	0.3394 to 0.4504
Goodness of Fit					
Degrees of Freedom	4	4	4	4	4
R squared	0.9915	0.9952	0.9961	0.9896	0.9951
Sum of Squares	48.75	32.94	24.12	33.04	20.83
Sy.x	3.491	2.870	2.456	2.874	2.282
Constraints					
Kint	Kint = 0.00128699865 160858	Kint = 0.00128699865 160858	Kint = 0.00128699865 160858	Kint = 0.00128699865 160858	Kint = 0.00128699865 160858
Number of points					
# X values	6	6	6	6	6
# Y values	6	6	6	6	6

Run 2	10 μM RhoGAP ^{R85A}	25 μM RhoGAP ^{R85A}	50 μM RhoGAP ^{R85A}	100 μM RhoGAP ^{R85A}	250 μM RhoGAP ^{R85A}
Best-fit values					
Y0	92.58	92.66	90.43	89.29	89.74
K	0.09145	0.2669	0.3300	0.3659	0.3617
Kint	= 0.001287	= 0.001287	= 0.001287	= 0.001287	= 0.001287
95% CI					
Y0	86.07 to 99.26	89.81 to 95.52	83.77 to 97.18	82.71 to 96.08	83.62 to 95.98
K	0.07302 to 0.1130	0.2480 to 0.2870	0.2759 to 0.3934	0.2960 to 0.4438	0.3013 to 0.4305
Goodness of Fit					
Degrees of Freedom	4	4	4	4	4
R squared	0.9923	0.9991	0.9955	0.9895	0.9918
Sum of Squares	43.59	5.588	28.63	34.08	33.06
Sy.x	3.301	1.182	2.675	2.919	2.875
Constraints					
Kint	Kint = 0.00128699865 160858	Kint = 0.00128699865 160858	Kint = 0.00128699865 160858	Kint = 0.00128699865 160858	Kint = 0.00128699865 160858
Number of points					
# X values	6	6	6	6	6
# Y values	6	6	6	6	6

Table 21: Curve fit parameters for the RhoGAP^{R85A} catalysed hydrolysis of F³Y-RhoA-GTP

Run 1	10 μM RhoGAP ^{R85A}	25 μM RhoGAP ^{R85A}	50 μM RhoGAP ^{R85A}	100 μM RhoGAP ^{R85A}	250 μM RhoGAP ^{R85A}
Best-fit values					
Y ₀	90.35	90.24	86.72	86.44	87.26
K	0.06072	0.1517	0.2091	0.2784	0.2733
Kint	= 0.0007609	= 0.0007609	= 0.0007609	= 0.0007609	= 0.0007609
95% CI					
Y ₀	84.44 to 96.30	86.13 to 94.41	78.33 to 95.46	74.85 to 98.65	76.37 to 98.66
K	0.05229 to 0.07004	0.1343 to 0.1712	0.1598 to 0.2736	0.1899 to 0.4033	0.1911 to 0.3858
Goodness of Fit					
Degrees of Freedom	4	4	4	4	4
R squared	0.9934	0.9972	0.9898	0.9837	0.9855
Sum of Squares	30.37	15.73	55.18	90.43	79.56
Sy.x	2.755	1.983	3.714	4.755	4.460
Constraints					
Kint	Kint = 0.00076087542 8033615	Kint = 0.00076087542 8033615			
Number of points					
# X values	6	6	6	6	6
# Y values	6	6	6	6	6

Run 2	10 μM RhoGAP ^{R85A}	25 μM RhoGAP ^{R85A}	50 μM RhoGAP ^{R85A}	100 μM RhoGAP ^{R85A}	250 μM RhoGAP ^{R85A}
Best-fit values					
Y ₀	90.53	89.98	88.55	87.15	87.18
K	0.05837	0.1630	0.2443	0.2913	0.2746
Kint	= 0.0007609	= 0.0007609	= 0.0007609	= 0.0007609	= 0.0007609
95% CI					
Y ₀	85.06 to 96.05	85.40 to 94.64	83.06 to 94.17	76.77 to 97.99	77.28 to 97.50
K	0.05081 to 0.06664	0.1421 to 0.1868	0.2065 to 0.2887	0.2082 to 0.4027	0.1997 to 0.3741
Goodness of Fit					
Degrees of Freedom	4	4	4	4	4
R squared	0.9942	0.9966	0.9963	0.9875	0.9882
Sum of Squares	26.38	18.79	21.78	70.89	66.52
Sy.x	2.568	2.167	2.333	4.210	4.078
Constraints					
Kint	Kint = 0.00076087542 8033615	Kint = 0.00076087542 8033615			
Number of points					
# X values	6	6	6	6	6
# Y values	6	6	6	6	6

Table 22: Curve fit parameters for the RhoGAP^{R85A} catalysed hydrolysis of F²⁵Y-RhoA-GTP

Run 1	10 μM RhoGAP ^{R85A}	25 μM RhoGAP ^{R85A}	50 μM RhoGAP ^{R85A}	100 μM RhoGAP ^{R85A}	250 μM RhoGAP ^{R85A}
Best-fit values					
Y ₀	95.61	96.39	95.35	94.54	94.56
K	0.008261	0.02130	0.03402	0.04456	0.04636
Kint	= 0.0007347	= 0.0007347	= 0.0007347	= 0.0007347	= 0.0007347
95% CI					
Y ₀	94.25 to 96.99	92.54 to 100.3	93.90 to 96.80	88.94 to 100.2	86.31 to 102.9
K	0.007698 to 0.008831	0.01940 to 0.02325	0.03293 to 0.03514	0.03978 to 0.04977	0.03925 to 0.05448
Goodness of Fit					
Degrees of Freedom	4	4	4	4	4
R squared	0.9979	0.9968	0.9997	0.9965	0.9931
Sum of Squares	2.266	10.79	1.594	18.11	39.62
Sy.x	0.7527	1.642	0.6312	2.128	3.147
Constraints					
Kint	Kint = 0.00073465696 9533713	Kint = 0.00073465696 9533713	Kint = 0.00073465696 9533713	Kint = 0.00073465696 9533713	Kint = 0.00073465696 9533713
Number of points					
# X values	6	6	6	6	6
# Y values	6	6	6	6	6

Run 2	10 μM RhoGAP ^{R85A}	25 μM RhoGAP ^{R85A}	50 μM RhoGAP ^{R85A}	100 μM RhoGAP ^{R85A}	250 μM RhoGAP ^{R85A}
Best-fit values					
Y ₀	96.45	96.43	94.23	95.04	93.64
K	0.007991	0.02156	0.03245	0.04347	0.04932
Kint	= 0.0007347	= 0.0007347	= 0.0007347	= 0.0007347	= 0.0007347
95% CI					
Y ₀	93.73 to 99.18	92.51 to 100.4	88.48 to 100.0	92.97 to 97.12	85.01 to 102.3
K	0.006897 to 0.009112	0.01962 to 0.02357	0.02834 to 0.03699	0.04172 to 0.04528	0.04129 to 0.05862
Goodness of Fit					
Degrees of Freedom	4	4	4	4	4
R squared	0.9915	0.9967	0.9949	0.9995	0.9924
Sum of Squares	9.039	11.20	25.57	2.508	42.41
Sy.x	1.503	1.673	2.528	0.7918	3.256
Constraints					
Kint	Kint = 0.00073465696 9533713	Kint = 0.00073465696 9533713	Kint = 0.00073465696 9533713	Kint = 0.00073465696 9533713	Kint = 0.00073465696 9533713
Number of points					
# X values	6	6	6	6	6
# Y values	6	6	6	6	6

Table 23: Curve fit parameters for the RhoGAP^{R85A} catalysed hydrolysis of F³⁵Y-RhoA-GTP

Run 1	10 µM RhoGAP ^{R85A}	25 µM RhoGAP ^{R85A}	50 µM RhoGAP ^{R85A}	100 µM RhoGAP ^{R85A}	250 µM RhoGAP ^{R85A}
Best-fit values					
Y0	96.51	98.60	94.45	93.68	96.07
K	0.001681	0.004931	0.007299	0.01113	0.01280
Kint	= 0.0001265	= 0.0001265	= 0.0001265	= 0.0001265	= 0.0001265
95% CI					
Y0	91.35 to 101.7	90.28 to 107.1	88.02 to 101.0	90.03 to 97.35	93.79 to 98.37
K	0.001272 to 0.002092	0.003958 to 0.006006	0.006198 to 0.008492	0.01027 to 0.01203	0.01202 to 0.01362
Goodness of Fit					
Degrees of Freedom	4	4	4	4	4
R squared	0.9703	0.9843	0.9915	0.9981	0.9993
Sum of Squares	21.76	63.47	31.45	8.800	4.280
Sy.x	2.332	3.984	2.804	1.483	1.034
Constraints					
Kint	Kint = 0.00012646602 5363908	Kint = 0.00012646602 5363908			
Number of points					
# X values	6	6	6	6	6
# Y values	6	6	6	6	6

Run 2	10 µM RhoGAP ^{R85A}	25 µM RhoGAP ^{R85A}	50 µM RhoGAP ^{R85A}	100 µM RhoGAP ^{R85A}	250 µM RhoGAP ^{R85A}
Best-fit values					
Y0	95.92	98.98	96.49	92.22	94.85
K	0.001687	0.004864	0.007623	0.01082	0.01313
Kint	= 0.0001265	= 0.0001265	= 0.0001265	= 0.0001265	= 0.0001265
95% CI					
Y0	90.13 to 101.8	91.70 to 106.4	90.23 to 102.8	82.62 to 102.0	91.19 to 98.57
K	0.001223 to 0.002154	0.004016 to 0.005787	0.006549 to 0.008782	0.008671 to 0.01332	0.01185 to 0.01455
Goodness of Fit					
Degrees of Freedom	4	4	4	4	4
R squared	0.9623	0.9877	0.9927	0.9863	0.9983
Sum of Squares	27.32	48.64	29.61	62.11	10.88
Sy.x	2.614	3.487	2.721	3.941	1.649
Constraints					
Kint	Kint = 0.00012646602 5363908	Kint = 0.00012646602 5363908			
Number of points					
# X values	6	6	6	6	6
# Y values	6	6	6	6	6

Table 24: Curve fit parameters for the RhoGAP^{R85A} catalysed hydrolysis of F²³⁵Y-RhoA-GTP

Run 1	10 µM RhoGAP ^{R85A}	25 µM RhoGAP ^{R85A}	50 µM RhoGAP ^{R85A}	100 µM RhoGAP ^{R85A}	250 µM RhoGAP ^{R85A}
Best-fit values					
Y0	89.15	90.30	90.24	91.51	90.25
K	0.001686	0.003913	0.005906	0.007173	0.008589
Kint	= 0.0001073	= 0.0001073	= 0.0001073	= 0.0001073	= 0.0001073
95% CI					
Y0	86.56 to 91.75	87.82 to 92.79	88.64 to 91.85	80.21 to 103.0	83.21 to 97.36
K	0.001498 to 0.001875	0.003677 to 0.004154	0.005707 to 0.006110	0.005668 to 0.008957	0.007425 to 0.009914
Goodness of Fit					
Degrees of Freedom	4	4	4	4	4
R squared	0.9945	0.9984	0.9996	0.9838	0.9943
Sum of Squares	5.698	4.430	1.673	81.57	29.68
Sy.x	1.194	1.052	0.6467	4.516	2.724
Constraints					
Kint	Kint = 0.00010725828 595012	Kint = 0.00010725828 595012			
Number of points					
# X values	6	6	6	6	6
# Y values	6	6	6	6	6

Run 2	10 µM RhoGAP ^{R85A}	25 µM RhoGAP ^{R85A}	50 µM RhoGAP ^{R85A}	100 µM RhoGAP ^{R85A}	250 µM RhoGAP ^{R85A}
Best-fit values					
Y0	88.49	89.81	89.43	89.08	90.10
K	0.002015	0.004738	0.006682	0.008138	0.009232
Kint	= 0.0001073	= 0.0001073	= 0.0001073	= 0.0001073	= 0.0001073
95% CI					
Y0	83.06 to 93.98	87.09 to 92.55	86.47 to 92.40	85.08 to 93.10	82.17 to 98.11
K	0.001603 to 0.002436	0.004448 to 0.005037	0.006271 to 0.007111	0.007472 to 0.008855	0.007828 to 0.01087
Goodness of Fit					
Degrees of Freedom	4	4	4	4	4
R squared	0.9813	0.9985	0.9987	0.9980	0.9931
Sum of Squares	24.42	5.093	5.437	9.435	37.02
Sy.x	2.471	1.128	1.166	1.536	3.042
Constraints					
Kint	Kint = 0.00010725828 595012	Kint = 0.00010725828 595012			
Number of points					
# X values	6	6	6	6	6
# Y values	6	6	6	6	6

Table 25: Sigmoidal fit parameters for $\log_{10}(k_{\text{cat}} \times 10^4)$ against Tyr34 p K_a

Best-fit values	
Bottom	0.2397
Top	1.862
Inflection Point	7.787
Span	1.622
Goodness of Fit	
Degrees of Freedom	1
R squared	0.9990
Sum of Squares	0.002217
Sy.x	0.04709
Number of points	
# X values	5
# Y values	5